EFFECTS OF CLIMATIC BOUNDARY CONDITIONS ON CURING AND SET GRADIENT OF CONCRETE

A Dissertation

by

ALIREZA JOSHAGHANI

Submitted to the Office of Graduate and Professional Studies of
Texas A&M University
In partial fulfillment of the requirements for the degree of

DOCTOR OF PHILOSOPHY

Chair of Committee,	Dan G. Zollinger
Committee Members,	Robert L. Lytton
	Zachry C. Grasley
	Mohammed Haque
Head of Department,	Yunlong Zhang

December 2020

Major Subject: Civil Engineering

ABSTRACT

The main purpose of this dissertation was to assess the effect of curing practices on early-age concrete pavement behavior with respect to the development of the set gradient based on the laboratory and field experiments. Several methods were used to relate measured aspects of curing to the concrete properties in the laboratory. The purpose of the laboratory experiments was to show the viability of identified curing quality indicators. Then, the preliminary laboratory testing for the field program was conducted to examine the quality of curing under different ranges of curing combinations. These experiments facilitated the determination of an appropriate application rate for a given curing compound under different ranges of ambient environmental conditions. This assessment appeared to be a feasible method of monitoring curing quality performance under different circumstances and over broad areas of concrete pavement construction. Then, concrete curing evaluations were conducted in several field experiments to collect data from the test slabs' placement. Concrete slabs were placed and cured under different conditions to create different states of stress and creep behavior during and after hardening. The evaluation principally consisted of parameters to evaluate the curing quality and early-age concrete behavior. The concrete temperature and moisture history were important factors that influence the slab curling/warping behavior as well as the set gradient in concrete slabs. These factors were influenced by variations of ambient weather and the curing conditions, which in turn were found to be important with respect to the induced gradients and set in concrete slabs. In this dissertation, the amount of the set or permanent curling/warping built into the test slabs was represented by the difference between the theoretical and the measured strains. Moreover, in a series of field tests, the application of ground-penetrating radar (GPR) provided the basis for justifying the curing effectiveness of the test results in terms of the application rate of the curing compounds and uniformity.

DEDICATION

To my beloved wife and her love and continuous support throughout my life

and to my beloved parents for their endless patience and unconditional encouragement

ACKNOWLEDGMENT

I am incredibly grateful to many people who helped me. There are far too many, to mention all of them; but I would like to thank several here.

I would like to express my sincere gratitude to my advisor, Dr. Dan Zollinger, for his advice, valuable encouragement, and precious guidance throughout this research. His support has been beyond invaluable both for his technical expertise and his overall nurturing of me as a researcher. Without him, this work would never been accomplished. I would like to thank Dr. Zachry Grasley, Dr. Robert Lytton, and Dr. Mohammed Haque for serving as the advisory committee members. They provided me with their deep understanding on the subject. Finally, thanks to my fellow researchers and everyone who helped me during my research and experiments.

TABLE OF CONTENTS

Page

LIST OF FIGURES

Page

LIST OF TABLES

Page

1 INTRODUCTION

This chapter focuses on defining the basic concepts, problem statement, main objectives, and the dissertation structure. The motivation behind this research will also be elaborated in this chapter.

The effects of ambient conditions on curing procedures used in construction can significantly impact the performance of a given concrete pavement system. The main objective of curing is to provide adequate conditions, i.e., an appropriate level of moisture content in concrete, or keep concrete in a suitable configuration (such as reducing shrinkage and curling) during the service life. Curing quality should be evaluated with respect to the production of durable concrete as the excessive evaporation of surface moisture (lack of appropriate curing practice) can lead to different distress types. Therefore, an evaluation of curing quality under different ranges of environmental conditions (i.e., temperature, relative humidity, and wind velocity) and curing practices is required.

In this study, a series of laboratory tests were conducted to develop a database of the main factors involved in determining curing effectiveness. The relations among these parameters were analyzed. These relationships were validated to make up an evaluation process. This kind of development helped identify the proper curing practice (amount, type, and timing) for any given project conditions. Some methods have been tested to relate measured aspects of curing to the characteristics of concrete. The experimental studies in the laboratory consisted of testing different curing compounds under different situations. Two forms of indicators were defined to evaluate the curing: direct and indirect measurements. These indicators were tested for a given curing situation by measuring numerous factors, such as surface moisture loss, surface abrasion resistance, porosity on the top surface, electrical conductivity, and drying shrinkage. Also, a method was proposed in accordance with concrete maturity concepts. The temperature-based maturity was conventionally an index that depended solely on time and the concrete temperature.

Since this form of maturity was not an effective indicator of the curing quality, a moisture-based maturity equation was utilized. This approach stated how the curing has progressed based on the moisture, temperature, and time. In the updated form, the maturity was quantified based on both temperature and moisture to develop an effectiveness index (EI). Additionally, the dielectric constant (DC) was used as a rapid means to extend the application of measuring curing effectiveness since it showed an excellent sensitivity to free moisture content. To validate the utility and the efficacy of these methods, the correlations between indirect and direct measures were calculated using the Pearson coefficient of the correlation function.

The laboratory and field characterizations were inherently empirical, but the process was calibrated to ensure the accuracy of the estimates of the application rate. Thus, a series of preliminary tests were conducted before field experiments. Curing performance was evaluated by comparing curing quality in each condition to establish reference curves covering the range of curing conditions expected under the field conditions. By considering the probable ambient conditions, the application rate was adjusted to facilitate the analysis of curing situations in each placement. Since the environmental conditions and various curing practices affected the concrete properties, the relationship between EI and DC was able to represent the moisture retention capability and the strength development of concrete (i.e., maturity). To generate reference curves, the ambient conditions, the type of curing compound, and the application rate were considered, as shown in Figure 1-1. The solid and dashed lines represent the wax-based and resin-based curing compounds, respectively, which imply that curing compound types affected the performance. The chart shows the correlation between these parameters as a prediction of the required application rate. Thus, by knowing the water-to-cement (w/c) ratio (mixture conditions), potential evaporation (ambient conditions), and the desired EI, an appropriate application rate was able to be determined. Besides the laboratory experiments, field data collections were needed to verify curing compound evaluation test methods. The main purpose of reference curves was to establish a relationship between the laboratory and

field conditions, and then extend that relationship to the moisture and temperature gradients in a concrete slab.

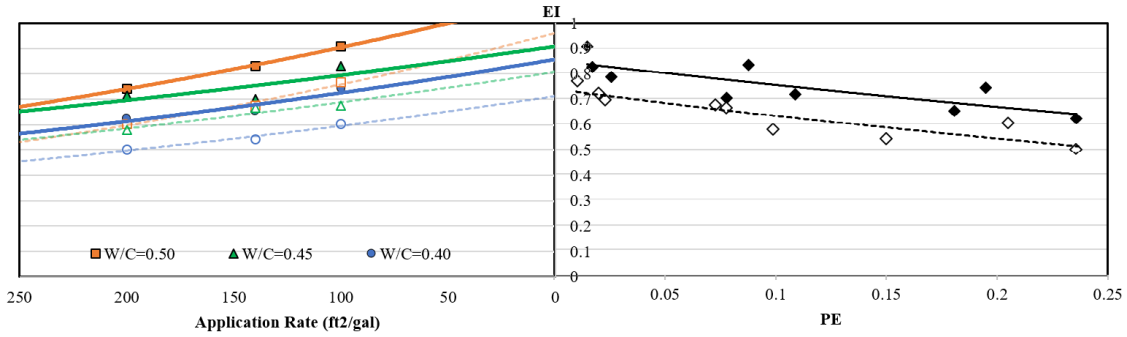

Figure 1-1. EI vs. Potential Evaporation (PE) in the Laboratory

(Solid: Wax-based, Dashed: Resin-based)

To assess the effect of curing practices on concrete slab behaviors, several studies commenced under actual circumstances. The primary purpose was to examine the effects of curing methods on the set gradient of newly constructed concrete slabs. Two series of field investigations were conducted at the Florida Department of Transportation (FDOT) SMO in Gainesville, FL to investigate the early-age concrete pavement properties with variable thicknesses, curing practices, and times of placement. In Phase I of this study, four test slabs were placed and cured under different conditions to show the viability of the concept that the concrete curing conditions were able to influence the set. Early-age concrete temperature and moisture history were key factors affecting the set based on slab curling and warping behavior. The variations of the ambient conditions, the curing compound type, and the application rate induced temperature and moisture gradients inside the slab, which caused concrete slabs to curl and warp. It was anticipated that the capability to pre-select a value of a built-in set gradient for design purposes was significantly dependent upon the capability to control curing practices. The objective of Phase II was to achieve a specific set value for the curing conditions anticipated at the time of placement. In this phase, the variables were the time of placement and the

application rate. The set value of a -10 ˚F, as used in the AASHTOWare Pavement ME (mechanistic-empirical pavement design guide) software as the ideal set for design purposes, was the target set in one slab. Accordingly, considering the probable placement conditions, the required task was to predict the application rate for a given curing compound prior to concrete placement. The probabilistic models were used to evaluate the relationship between the target set gradient and the environmental effects and curing practices.

The ground-penetrating radar (GPR) was used in different field studies to measure dielectric properties. Under environmental field conditions, dielectric readings provided a method to extend the curing assessment besides the maturity meter system over a wider paving area rather than a single position. A better curing operation depended on many factors, such as the type of the curing compound, application rate, uniformity of the curing application, and timing of the application. By running GPR in the field experiments, the quality of a curing operation was examined. Several field investigations were conducted in a series of test sections during concrete placement at paving projects in Victoria, TX; Itasca, IL; and Jacksonville, FL. GPR was the leading equipment in these field studies. One of the significant steps in this part of the research was to validate the prevailing application rate of the curing compound sprayed at the test sections. The application of GPR provided the basis for justifying the curing effectiveness of the test results in terms of the application rate of the curing compounds and uniformity.

1.1 Research Motivations

Although American Society for Testing and Materials (ASTM) C 156 characterized a laboratory practice to check the water retention capability of different curing compounds under controlled laboratory conditions, the drawbacks of this method prevent the use of this standard under different ranges of field conditions [1, 2]. Thus, the current standard is only practical under the limited conditions of the laboratory. Also, no

common, transferable, or functional indication has been drawn between the field and the laboratory. Finally, current standards fail to specify the application rate of a given curing compound to satisfy variable field environment conditions.

The main factors that affect concrete pavements are temperature and moisture gradients between the top and the bottom of slabs. The MEPDG as an analysis/design tool included the temperature and moisture gradients in the design inputs. Also, MEPDG enveloped mechanisms that could influence pavement performance. The primary purpose was to estimate the quantities of jointed plain concrete pavement (JPCP) distresses at any given time. For the design procedure, it is important to understand the slab configuration at the loading time accurately. In order to characterize the shape of slabs due to curling/warping, the effective temperature gradient (based on the stress condition) can be used. This parameter has three components, as shown in Eq. (1-1): the built-in equivalent linear temperature gradient ($\Delta T_{built-in}$), the drying shrinkage equivalent linear temperature gradient ($\Delta T_{shrinkage}$), and the creep relaxation equivalent linear temperature gradient (ΔT_{creep}).

$$\Delta T_{curling/warping} = \Delta T_{built-in} + \Delta T_{shrinkage} - \Delta T_{creep} \quad (1\text{-}1)$$

In the moment that the built-in gradients ($\Delta T_{built-in}$) are formed into slabs, the amount of stress is zero. The zero-stress temperature gradient, which happens shortly after the final setting time, can have a substantial impact on the shape of the slab [3]. Some researchers reported that as slabs are fully saturated during the hardening process after the final set, the influence of the moisture gradients on the slab configuration can be disregarded [4]. $\Delta T_{shrinkage}$ is the irrecoverable differential drying shrinkage that ultimately stabilizes over time. The equivalent moisture-related temperature gradients are defined based on the changes of the relative humidity in the slab [5]. ΔT_{creep} is the effect of the creep relaxation that can negate the impacts of $\Delta T_{curling/warping}$ when slab ages.

Concrete slabs depend on the conditions can curl either upward (corners lift up) or downward (middle lifts up) rather than be in a flat position [6, 7]. A positive temperature gradient makes the slab expand more at the top surface compared to the bottom, which

mostly happens in the daytime. However, a concrete slab deforms into a concave configuration when the pavement is subjected to a resultant negative composite gradient of temperature and moisture effects through the thickness, such as nighttime. If the net negative gradients are high enough to offset warping effects, the interfacial tensile strength may be exceeded, and the slab edge or corner may separate from the underlying base. In this case, slabs can separate from the sub-layer that can cause high deflections and pumping [8]. In the upward situation, the dead-weight of the slab with heavy traffic load repetitions can induce tensile stresses, which likely causes fatigue damages and top-down cracking. The top-down cracking is much likely under a combination of upward curling and repeated heavy-vehicle loadings [9]. Besides the temperature gradient, the relative humidity gradient can also control the configuration of concrete slabs by inducing non-uniform shrinkage strains in the slab [10]. The reason for the non-uniformity in shrinkage is the exposure of slabs to ambient conditions from the surface, which makes the concrete much more prone to drying. However, the bottom of the slab remains saturated.

The set gradient is formed due to the environmental effects during the first days after placement within a fully supported concrete slab. It is speculated that some of the strains contributing to a built-in set occur after the hardening process is irreversible. Other strains (especially drying shrinkage) develop as further volume changes take place. These strains are reversible and can fluctuate with the ambient relative humidity changes. However, irreversible shrinkage in the slab concrete, which is a time-dependent deformation, only occurs once the slab can sustain tensile and compressive stress, such as when slab lift-off occurs. Thus, depending on the cause, warping can be permanent (due to the built-in set) or reversible (due to the seasonal variations).

In the design guide of Pavement ME, the permanent curling/warping (i.e., $\Delta T_{curling/warping}$) has been considered as one of the design inputs. Pavement ME recommends -10 ˚F for the equivalent linear temperature gradient of permanent curling/warping. This number is the nationwide average for the temperature gradient of the concrete slabs for all climatic regions. To achieve this value, Pavement ME used about 200 JPCP sections in 24 states to investigate a mechanistic-empirical method to predict

the transverse cracking percentages. Nassiri *et al.* [11] conducted a comprehensive parametric study to assess the sensitivity of various performance design inputs. They found that $\Delta T_{curling/warping}$ plays a key role on the transverse cracking prediction. The greater negative temperature gradient will appear in the higher slab lift-up. By changing $\Delta T_{curling/warping}$ (from -10 ˚F to 0 ˚F) the predicted transverse cracking is changing as well.

In another study, a group of researchers at Iowa State University evaluated the sensitivity of different factors in $\Delta T_{curling/warping}$ [12]. They assessed a wider range of this parameter on the transverse cracking. As shown in Figure 1-2, changing the level of $\Delta T_{curling/warping}$ from -10 ˚F (the nationwide average value) to 0 ˚F, -20 ˚F and -30 ˚F will influence the predicted transverse cracking percentage considerably. Thus, they reported that the distress predicted by the Pavement ME correlated with the permanent curling/warping amount.

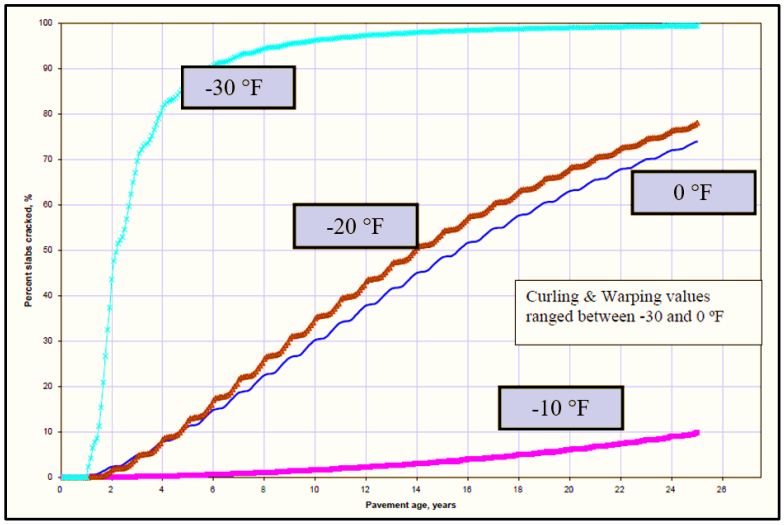

Figure 1-2. Dependence of Transverse Cracking to Equivalent Temperature Gradient

Although Pavement ME suggests using the default value, adjusting the value according to the local calibrations is available [13]. Gutierrez attempted to compare the

Pavement ME predicted performance results with the performance history data [14]. The researcher found that using -10 ˚F for $\Delta T_{curling/warping}$ in Pavement ME design yielded to more accurate predictions of pavement distress (transverse cracking). Vandenbossche *et al.* [15] studied the contribution of environmental conditions, traffic loading, and structural properties on $\Delta T_{curling/warping}$ in order to minimize the transverse cracking percentage in JPCP (predicted with Pavement ME). They found the most reasonable performance prediction generate from Pavement ME with typical traffic patterns in normal climatic conditions is the default value of -10 ˚F. Thus, different parameters including the pavement mixture, geometry, restraint types, curing and climatic conditions can directly change the magnitude of $\Delta T_{curling/warping}$, during and after the paving operations. The value of the permanent curling/warping temperature gradient can be different from -10 ˚F depends on the projects. A calibration based on the local data can result in more accurate predictions of concrete pavement performance. There are only limited studies that have been done on the effects of variable conditions on the permanent curling/warping and the set gradients. Thus, more endeavors are needed to estimate this gradient under the complicated combination of factors in concrete slabs.

1.2 Problem Statement

The present standard methods for curing materials have some constraints in the curing efficiency evaluation. Also, the current assessments inhibit their applications to be implemented in the field under different ambient conditions. Therefore, an approach should be taken to study the quality of any curing compound, as well as the curing practices to deploy a given compound in the laboratory and the field. Such assessments should be applicable to a range of weather conditions, curing compounds, and application rates. Furthermore, a method is also needed to extend the curing evaluation over a wide area of paving to determine the adequacy of the application rate of a curing compound and its effectiveness in an ongoing construction project. Considerable moisture evaporation

occurs at the surface of an early-age rigid pavement during construction. As the dielectric constant can be used as an indicator of the unbound free moisture, it is anticipated and recommended that a GPR was able to be implemented to achieve this purpose under field conditions. Lack of appropriate technologies may have been a factor in the design or specification stages of curing practices. Therefore, a technical development is needed to delineate the performance of curing under the impact of specific field conditions, such as a variety of combinations of the temperature, the relative humidity, the solar radiation, and the wind.

To account for the effects of climatic factors and curing performance on the setting, it was convenient to consider the lift-off displacement behavior of the slab's corner due to induced strain composed of thermal, shrinkage, and creep effects. Comparing the actual measurements against the theoretical displacements (or strains) provided a method to assess the built-in set in concrete slabs. This difference can be used to reflect the curing quality.

By definition, the zero-stress temperature is the temperature of the concrete shortly after the final set time. It is commonly believed that this temperature is the point from which the concrete starts to experience stress from climatically induced strains. However, this assumption ignores the effect of creep strain (which is both age and moisture dependent) on the zero-stress temperature. The set gradient depends not only on the time of placement but also the curing quality and the ambient conditions at the time the concrete is placed. A key aspect of the set gradient is its inclusion in AASHTOWare Pavement ME software with a default value of a -10 ˚F in the design process. However, considering a default value in different regions with variable climatic conditions is not a reasonable assumption. Thus, various design situations and calibrations should be implemented where an increase or decrease in this factor may be warranted. Calibration of performance for design purposes should inherently address the effect of climate on fatigue cracking of concrete slabs. Even though the interaction of the climate with performance is complex, curing effectiveness affects slab support and ultimately affects the critical slab stresses and cracking. Not only do diurnal moisture and temperature gradients through the slab

affect the slab cracking, but they also affect the permanent built-in curling and warping that occurs during construction.

1.3 Research Objectives

The main objective of this research is to calculate the set based on the built-in gradient. Concrete pavements can be subjected to different climatic conditions depends on the zone and placement time. Moreover, the curing conditions are different by implementing various curing compound types, application rates, and spraying methods. Thus, investigating the impacts of environmental and curing factors on the set gradient is the primary purpose of this study.

To achieve this goal, it is important to understand the behavior of concrete under different conditions. This research includes four major modules, which focus on establishing:

1) Evaluating concrete curing effectiveness under the laboratory conditions,

2) Conducting preliminary laboratory testing for the field program,

3) Collecting data to assess the curing quality and slab setting characteristics, and

4) Analyzing the impacts of the most important factor on the set gradient.

The modules of this work are illustrated in a schematic flowchart, as shown in Figure 1-3.

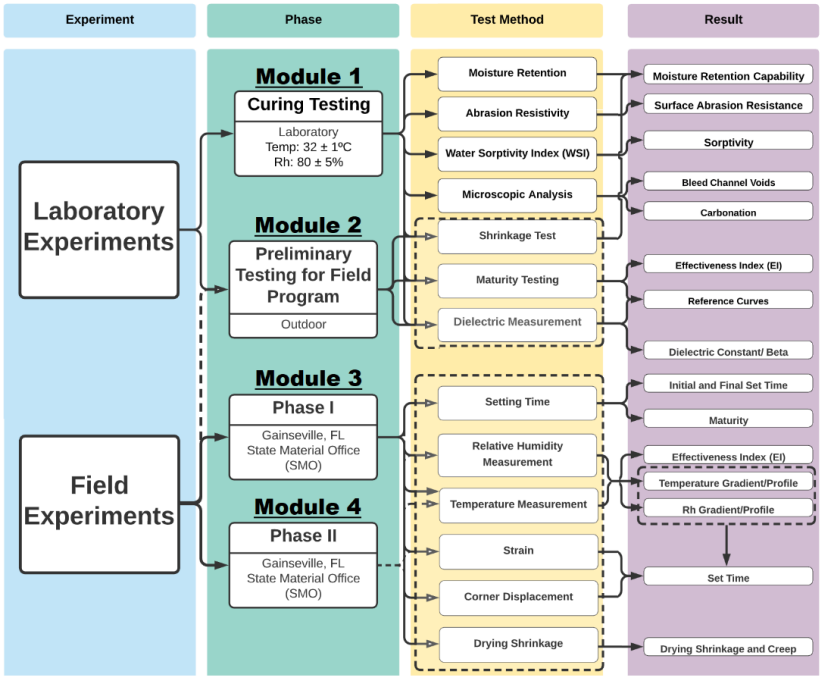

Figure 1-3. Schematic Illustration of Modules Implemented in the Research

To find the main factors in curing evaluation, Module 1 in Figure 1-3, several test methods were used to relate measured aspects of curing to the concrete properties, such as strength, permeability, maturity, and conductivity. The experimental study in the laboratory consisted of testing a given curing compound under different situations to evaluate its performance. The main purpose of the laboratory experiments is to show the viability of identified curing quality indicators.

To establish the reference curves, Module 2 in Figure 1-3, the preliminary laboratory testing for the field program was conducted under different ranges of curing combinations. The variables included the compound's type, application rate, and time of placing. Curing compound performance was evaluated to establish laboratory reference curves covering the range of curing conditions expected under field testing. The effects of the placement time on EI, the final set, and the gradients were investigated in the preliminary laboratory testing.

To measure the set gradient, Module 3 in Figure 1-3, four slabs were placed and tested in February to study the different curing conditions and placement times. Several instruments and sensors were used on the slabs to collect data and understand the set behavior of concrete slabs under different curing conditions. This data set was used to validate the findings from the previous calibration work.

To achieve the predetermined set gradient, Module 4 in Figure 1-3, a preliminary data collection (Module 2) was conducted before the actual field investigation. The preliminary laboratory testing and reference curves were used to determine the rates and types of curing in the slab testing. The target set gradient for one slab in Phase II placement was -10 ˚F, which is the assumed set gradient used in the AASHTOWare Pavement ME software. This number is the nationwide average for the equivalent linear temperature difference between the top and the bottom of the slab for all climatic regions. Therefore, by considering the probable ambient conditions, the application rate for each compound was established to facilitate the prediction of the set in a given placement. Moreover, the effects of different factors, such as time of placement, the curing compound type, and the application rate, on the set gradient were analyzed.

1.4 Structure of Dissertation

This dissertation is organized into six chapters. Each chapter has a specific purpose. Chapter 1 presents a brief introduction, the problem statement of this research, and the structure of the dissertation.

Chapter 2 involves a literature review of concrete curing, such as methods. Here, this part primarily reviews the liquid membrane-forming curing compounds method and characterization. Then, factors that affect curing quality are discussed. After that, the application of the dielectric constant is explained. The early-age behavior of concrete, such as temperature and moisture gradients, and the set (built-in) gradient are described. The

objective of this chapter is to conduct a comprehensive and focused review of information on current and emerging concrete curing and the set gradient by considering the early-age performance of concrete slabs.

In Chapter 3, the experimental study in the laboratory is explained, which consists of testing a given curing compound under different situations to evaluate the curing performance. Two types of indicators are defined to evaluate the curing practices. The purpose of this chapter is to show the viability of curing quality indicators. Then, the results from a series of laboratory tests are presented. The results were used to validate relationships that could make up an evaluation protocol. In this part, characteristics of the mortar mixture, as well as the curing compound's application rate and the ambient conditions, affected these test results.

Chapter 4 presents all the field data collection programs from two separate field trials to show the impacts of different curing conditions and placement times on early-age concrete properties. One of the key objectives of the slab monitoring was to collect data to assess the slab setting characteristics relative to the quality of curing provided for each slab. Then, results from two separate field trials of slab placements are discussed to represent different combinations of curing conditions and placement times. Additionally, using GPR as a practical approach to assess the curing effectiveness in three field data collections is discussed.

Chapter 5 presents the impacts of different factors on the set gradient. Then, the set gradient or the built-in gradient is defined. In this chapter, the set calculations in both Phase I and Phase II are explained. Based on the findings and interpretation, calibration of performance for design purposes was conducted to address the effect of climate on fatigue cracking of concrete slabs. Then, the correlation of the set with other characteristics of concrete slabs, such as creep, EI, and cracking probabilities, are discussed. Finally, a specification development is discussed, included how to predict the required application rate based on the probabilistic models by considering the ambient condition and the curing quality.

Chapter 6 summarizes the outcomes of this dissertation. Additionally, this chapter provides the general conclusions of the research findings.

APPENDIX describes the process of the set determination with tables and figures in ten steps for a single slab. Finally, the equivalent set gradient is expressed in terms of temperature.

2 LITERATURE REVIEW

This chapter presents a wide-ranging literature review on several subjects that are pertinent to concrete curing, early-age concrete behavior, and concrete set gradient behavior characterizations. In the curing section, the curing compound and wet curing methods are discussed in detail. Then, the application of the dielectric constant in monitoring the curing quality is explained. The early-age behavior of concrete, such as temperature and moisture gradients, and the set (built-in) gradient are described. The factors that can influence the permanent curling/warping gradient are discussed. This chapter's main purpose is to present a comprehensive and focused review on current and emerging concrete curing and set gradient procedures based on early-age concrete behavior.

2.1 Background of Concrete Curing

Concrete hydration is a fundamental part of curing practices. In this section, the purposes of different types of curing methods are introduced. Additionally, the possible distress types of concrete pavements due to deficient curing methods are mentioned. Finally, the current curing membrane effectiveness is evaluated, and its defects are explained.

2.1.1 Concrete Hydration

Understanding the need for concrete curing, one of the primary elements in pavement construction, is essential to understanding concrete hydration. Therefore, the application of a proper curing method in pavement construction is required to facilitate

the concrete hydration process and mitigate moisture loss that induces distresses. Concrete hydration is a consequence of physical and chemical reactions between cementitious materials and water [16, 17]. In the hydration of cementitious materials process, the power of the internal bonding between the particles will increase in intensity, and the porosity percentage will reduce [18]. In addition, the cementitious materials' surfaces are densely covered with random oriented hydration products due to the chemical reactions in the presence of water [19, 20]. These hydration products, such as calcium silicate hydrate (C-S-H), can improve the concrete strength considerably, and also have significant impacts on the concrete durability and performance [17]. The process of strength development is initiated by filling the spaces between cement particles with hydration products [19, 20].

The rate of hydration is defined based on the rate of cement hydration development within a given period. The external factors, such as ambient conditions, can influence the hydration rate. For example, the low relative humidity condition can keep the rate of cement hydration at a low level. Generally, the rate of cementitious materials' hydration under an environment of 80% relative humidity is not significant (about 10% of the hydration under an environment of 100% relative humidity) [21]. The reason of low rate of hydration under the low relative humidity is that a sufficient amount of moisture content is necessary to achieve a higher level of concrete hydration rate.

There are two kinds of water in the early-age concrete: (1) non-evaporable water (gel water) and (2) evaporable water (capillary water). The first type physically reacts to the interlayer voids of the hydration products. The second type is the available water that is used for forming hydration products [22]. As concrete pavements typically have a high surface-area-to-volume ratio, the rate of evaporation is relatively high from the exposed surface to environmental conditions. In this case, significant moisture loss on concrete pavement surfaces is very likely at early-age. Thus, in order to keep water inside concrete and optimize chemical reactions, providing a suitable temperature and relative humidity in the curing process seems necessary to prevent excessive water loss through the surface of concrete during the hydration process [23-25]. Considering the inevitable role of water

in the hydration reactions, excessive amounts of moisture loss can result in unfavorable consequences in terms of strength and durability.

2.1.2 The Need for Curing Practices

It is well-known that ambient conditions, such as temperature and relative humidity, can affect mechanical and durability-related properties of concrete during the service life of concrete structures. There are many pavement distress types that relate to inadequate curing.

2.1.2.1 Drying Shrinkage

A frequent curing-related distress is shrinkage, which is likely to occur in dry, warm, and windy environments. Under these circumstances, the moisture evaporation amount at the surface is greater than the moisture absorption amount for cement hydration. In this case, the concrete can fail to endure stresses that are caused by concrete volumetric contraction due to moisture loss before adequate tensile strength [26]. Plastic shrinkage can emerge as tiny cracks on top surfaces or penetrate the concrete slab deeply. On the other hand, some curing methods may have negative impacts on drying shrinkage. Perenchio reported that drying shrinkage was increased by wet curing during the first seven days [27]. The duration of the curing is important regarding the drying shrinkage rate. Several researchers found that a shorter curing time might result in a faster drying rate [28, 29].

2.1.2.2 Curling

Researchers observed that either temperature or moisture could cause curling in concrete pavements. The faster drying rate due to moisture loss can minimize internal moisture gradients and reduce curling caused by drying shrinkage [30]. When a slab is

wet cured, water can penetrate through the surface and collect in the base. The excess water, which makes the bottom of the slab saturated, can cause the slab bottom to expand and curl. Hajibabaee and Ley found that a longer period of wet curing could increase curling as only one surface is drying [31, 32]. However, Suprenant reported that a more extended moist-curing period may have negligible impacts on drying shrinkage and curling [33]. Hajibabaee observed that the extra water supplied by the wet curing does not seem to impact the magnitude of the curling, only the drying rate and the amount needed to reach the maximum amount of curling [30]. Using water-retaining coverings delay curling while in place (usually for a week); however, curling will begin shortly after removal. Finally, as curing compounds can retain moisture, they can delay curling for a longer period.

2.1.2.3 Delamination

Another common concrete pavement distress related to the lack of effective curing is delamination on the top surface due to the vertical moisture gradient. The moisture differences between the top and the bottom of concrete slabs induce horizontal stresses [34]. These stresses can induce a horizontal break plane close to the concrete surface. The outcome might be the deterioration of the concrete surface and the reduction of horizontal stresses resistance [35]. As the horizontal stresses exceed the amount of concrete shear strength, delamination emerges on the shallow surface of concrete. In the case of poor curing, the moisture evaporation from the exposed surface is considerably higher than the internal moisture of the concrete. The degree of this moisture gradient (or delamination) is influenced by the ambient conditions and the curing quality. As a result of the delamination, other issues can happen. For example, the spalling of concrete pavement can deteriorate the riding quality. In conclusion, the unwanted excessive moisture loss due to evaporation is one of the main purposes of concrete curing.

2.2 Concrete Curing

The principal objective of concrete curing is to preserve acceptable conditions that allow the desired concrete properties to develop [18]. There are several functions for concrete curing in pavements: (1) preserving mixing water in concrete at early-age; (2) reducing the water loss from the exposed surface of concrete pavements; and (3) accelerating strength gain [36]. Based on the American Concrete Institute (ACI) Committee 308 guide [18], the concrete curing process usually has two main parts: (1) initial curing, which consists of practices that should be done between concrete placement and the surface finishing; and (2) final curing, referring to the practices that must be applied after the surface finishing of concrete is done [18, 37]. The most important purposes for initial curing are to check the bleeding water on the surface and prevent excessive evaporation of water in capillaries [37, 38].

In this section, different methods of concrete curing are introduced briefly. Then, the differences between these methods are discussed. The wet curing and the curing compounds are the two most common methods in concrete curing. These two methods are elaborated in detail.

2.2.1 Methods for Concrete Curing

Depending on the project circumstances and limitations, different curing methods are recommended. The common methods of curing are as follow:

- Spraying: Spraying is recommended when the environment temperature is greater than freezing and the humidity is low. This method can minimize plastic shrinkage before the setting of concrete. Although this method is considered an excellent method for curing, the high expense of delivering water in regions with water shortages and the freezing conditions are drawbacks that hinder the usage of this method.

- Ponding: Ponding can typically be used on surfaces with small areas. Thus, this method is suitable in the laboratory for the curing of concrete test specimens. Water

temperature should be no more than 20 ˚C and colder than the concrete surface temperature to avoid cracking due to thermal stresses.

- Saturated Wet Coverings: Saturated wet coverings must be applied after the final set time of concrete to prevent surface damages. These coverings always need to remain wet.

- Left-in-place Forms: These types of forms typically provide adequate protection against moisture loss from concrete surfaces. Forms should be placed on concrete surfaces as long as the construction plan allows. If the wooden forms are used, they have to be kept wet all the time, especially during hot and dry weather.

- Covering with Impervious Sheets: Impervious sheets must be used on fresh concrete after the final set time to prevent damaging the surface. As this method is not ideal with regard to time and money for wide concrete surface areas, it is only feasible for small surface areas.

- Membrane-forming Curing Compounds: There are different sorts of curing compounds that form a membrane to reduce moisture evaporation from the exposed surface of concrete pavement. These compounds can be either clear or white-pigmented. White-pigmented compounds are usually recommended for dry and sunny areas to reflect solar radiation. Typically, curing compounds should be sprayed right after the final finishing. Among the different curing practices, using curing compounds is regarded as one of the most cost-effective techniques for curing concrete pavements. Due to a large surface-area-to-volume ratio of concrete pavement and being readily available, this method has become the most commonly used method for curing concrete pavements [39].

- High-pressure Steam: Using high-pressure steam in autoclaves is a method of curing to prepare satisfactory conditions for concrete quickly. The steam temperature at atmospheric pressure must be kept at 140 ˚F or less until the required concrete strength is attained.

- Electrical Elements: Heated coils are generally used as embedded elements close to the top surface to protect concrete from freezing in cold regions. Also, electrical heated forms or pads can be used in precast concrete production.

- Insulation Blankets: Concrete insulation blankets are usually used to cover concrete surfaces that are subjected to freezing temperatures. This method should be applied while concrete is hard enough to prevent surface damage.

2.2.2 Wet Curing Methods

Wet curing as a curing method can preserve moisture inside concrete and maintain the temperature at a constant level. Due to extra water, this method can promote hydration at early-age. Moreover, researchers observed that wet curing could enhance concrete durability, abrasion resistance, and strength [40-43]. One of the disadvantages of this method is the non-uniform moisture distribution after the curing period causing shrinkage and curling. The intensity of this deformation might be under control if the drying happens from all sides of a member [44].

Wet curing can decrease the porosity and permeability of cement paste. The reduction of the size and density of capillaries inside the concrete paste increases the degree of saturation at any given relative humidity. Based on Kelvin's equation, the water content is directly related to the vapor pressure in the paste of concrete [45]. The greater the vapor pressure, the higher the amount of condensed water. The wet curing can cause a higher degree of saturation, and the results will be an increase in the pores' pressure [46].

Hajibabaee [30] found that wet curing increased the rate of shrinkage and the time needed to reach the maximum amount of curling. In another study, Perenchio showed that the drying shrinkage increased for wet cured samples. The reduction in permeability makes the moisture loss from drying unlikely. This lower moisture loss will make the time to reach their maximum amount of curling longer [28].

2.2.3 The Liquid-Applied Membrane-Forming Curing Compounds

This section primarily reviews the method of liquid membrane-forming curing compounds because it has a significant role in concrete curing. The curing compounds' characterization, specifications, standards, and assessment are presented in the following paragraphs. The current curing membrane assessment procedure is often dictated by ASTM C 156 [47], "Standard Test Method of Water Retention by Concrete Curing Materials." However, this standard cannot be used under different ranges of environmental conditions and curing practices. One of the reasons is that the quality of any curing compound and the curing operation are considered independent of each other. Thus, a single test method cannot reflect the differences.

2.2.3.1 Curing Compounds Characterization

Generally, curing compounds are in a liquid form. They are applied as a coating on the concrete pavement surface to mitigate the rate of moisture evaporation from the exposed surface. Additionally, the white-pigmented curing compounds can reflect solar radiation and decrease heat. Curing compounds can create beneficial moisture and temperature conditions for concrete hydration [48].

Different considerations are used for curing compounds. For example, ASTM C 309 categorizes compounds based on color: clear with no dye, clear with fugitive dye, and white-pigmented [49]. Another criterion is the base of compounds that can be the solids dissolved in the compounds or resin-based composition [50]. Also, ASTM C 1315 specifies compound properties, such as water retention potential, reflectance characteristics, drying time, and other general requirements [51].

2.2.3.1.1 Reflectance Property

The reflectance of white-pigmented curing compounds is specified in ASTM C 309 and ASTM C 1315 [50, 51]. This property refers to the capability of compounds to

reflect solar radiation. This characteristic can control concrete temperature after and during the hydration period and reduce early-age possible stresses [52].

2.2.3.1.2 Water Retention Capability

Water retention potential is explained in both ASTM C 309 and ASTM C 1315 [50, 51]. Some departments of transportation (DOT)s set the maximum moisture loss limit to 0.40-0.55 kg/m^2 for cured specimens within the first 72 hours. Generally, the amount of moisture loss of a concrete sample is measured during a fixed period under controlled laboratory environments according to ASTM C 156 [53]. Based on the requirements of this standard, a chamber with fixed ambient conditions, with a PE rate of 0.135-0.220 $lb/ft^2/hr$, should be used. Although this method is not complicated, the precision is not reliable due to variable conditions. This level of uncertainty can affect the curing compound testing because of factors such as ambient temperature, relative humidity, wind velocity, time of curing application, and the application rate of curing compounds that can change the results [37]. Moreover, the constant environmental conditions and single application rate should be noted along with the deficiency of precision, while field environments are subjected to different conditions.

2.2.3.1.3 Drying Time

Drying time is another principal factor in curing compound properties. Checking the concrete workability and setting time for determining the joint sawing time after spraying the curing compounds is essential. Compounds are prone to be washed away by water under rainy days. Both ASTM C 309 and ASTM C 1315 indicate that the drying period must be less than 4 hours [50, 51].

2.2.3.2 Factors Affecting Curing Quality

Several factors can influence curing quality that need to be considered in each project, such as implantation time, application rate, and the uniformity of the application [54-56].

2.2.3.2.1 Time of Application

The determination of the curing compound application time has been an issue in pavement construction for many years. The timing of the curing compound application can impact the results if it is applied too late or too soon. A delay in curing compound application could cause excessive moisture loss from the exposed surface due to evaporation; however, an early application can cause degradation of the concrete quality due to the mixing of curing compounds with the bleeding water [18].

The time of the curing compound application depends on the surface bleeding. Several standards and specifications dictate that curing compounds have to be sprayed when the sheen on the concrete pavement surface has disappeared [37]. Several DOTs stated that the time of spraying curing should be right after the concrete surface operation is done [57-59]. However, ACI 308 indicated that the best possible time for spraying curing compounds is when the rate of water evaporation on the surface surpasses the concrete bleeding rate [18]. Determining the rate of moisture evaporation, whether it is greater than the bleeding rate on a newly placed concrete slab, is a challenge [54]. On the other hand, applying curing compounds before the disappearance of the bleeding sheen on concrete pavements can prevent a major bleeding event at the early-age.

2.2.3.2.2 Application Rate

Choosing the correct application rate for the curing compound can improve the curing process significantly. Based on the previous experiments, the application rate ranges from 100 ft^2/gal to 210 ft^2/gal on pavement constructions [39]. However,

suggesting a limited range for the application rate by disregarding the project situations is not appropriate. As some DOTs have their constraints and considerations for the curing compound application rate, most of them stated that the required application should not be more than 150 ft^2/gal [57-59]. Usually, contractors use 200 ft^2/gal in a single pass with a hand-spray machine to cover all areas [37]. Nevertheless, ACI 308 specifications stated that a double-coat of curing compounds with a total rate of 200 ft^2/gal is enough for the curing purposes [18]. Also, in concrete pavements with a textured surface, the application rate can be doubled, i.e., two passes of 200 ft^2/gal. Thus, Eq. (2-1) was used for modifying the application rate for the textured pavement surfaces to balance the additional area:

$$AR = (AR_{ungrooved}) \frac{(S+W)}{(S+2D+W)} \quad (2\text{-}1)$$

where

AR = the modified application rate (ft^2/gal),

$AR_{ungrooved}$ = the specific application rate for an un-grooved surface (ft^2/gal),

S = the spacing between the grooves (inch),

W = the width of the grooves (inch), and

D = the depth of the grooves (inch)

2.2.3.2.3 Uniformity of Application

The uniformity of the curing application is one of the most critical factors that can affect curing effectiveness. To achieve better application uniformity, some paving companies use curing machines spanning over the pavement's length to provide a more consistent curing application practice. However, the curing compound is manually sprayed in most field applications, which creates many non-uniform spots.

Minnesota Department of Transportation (MnDOT) reported that the curing compound uniformity is directly influenced by the curing compound spraying method [58]. In the curing machines, the wears, and damages of any parts can lead to non-uniform coverage. Thus, regular checkups on the spray machines and nozzles are needed for proper

spraying practice [55]. The factors that influence the curing application of curing machines are [55, 60]:

1. Nozzle type: It consists of different requirements, such as spray form, droplet size, spray angle, pump pressure, and flow

2. Nozzle spacing and boom height: Based on MnDOT recommendation [55], the nozzle and boom need to be adjusted for at least 30% overlap

3. Nozzle orientation

4. Windshield

5. Cart speed: The cart speed can be calculated using Eq. (2-2):

$$v = \frac{Coeff \times F}{C \times w} \tag{2-2}$$

where

v = cart speed (km/h, or miles/h),

$Coeff$ = 6 for SI units (0.136 for metrics units),

F = flow rate for each nozzle (L/min, or gal/min),

C = required coverage (L/m^2, or gal/ft^2), and

w = nozzle spacing (cm, or inch)

Flow for spray nozzles depends on compound specifications (provided from the factory). The flow can be from 0.1 gal/min to 1.2 gal/min. Most sprayers are equipped with a 0.5 gal/min (1.9 L/min) spray nozzle and a 0.1 gal/min (0.38 L/min) nozzle to produce an even spray pattern.

One of the advantages of white-pigmented curing compounds compared to non-pigmented is that the uniformity can be verified by visual inspections. The areas with less white appearances are a sign of non-uniform application [37]. Another way to detect the uniformity is by using a portable reflectometer to quantify the intensity of light reflectance from the cured surface [61]. The reflected light intensity is measured based on the brightness of the white-pigmented compounds. The brighter surface can reflect more light,

which indicates the higher application rate of curing compounds on the concrete pavement surface [61].

2.2.4 Comparison of Different Curing Methods

There are different types of concrete curing. Depending on the project conditions and circumstances, each method is recommended. Two general classifications of curing methods are wet and sealed. The mechanisms of these methods in controlling the moisture loss, shrinkage rate, and curling are different.

2.2.4.1 Moisture Loss

Wet curing can increase the specimens' mass due to capillary and osmotic suction; however, the sealed curing usually does not affect the mass during curing. The rate of moisture loss in these two methods is different. There is a high rate of water loss for the initial days in the wet cured samples, and this rate is becoming lower gradually over time. However, the sealed cured samples lose moisture at a similar rate regardless of the curing length. Also, samples treated with curing compounds had the lowest amount of curling compared to the control samples and wet curing method.

Hajibabaee and Ley [31] reported that the wet cured samples could have a high amount of moisture loss in the first 72 hours due to the loss of the excessive water added. The amount of moisture loss was less than the control samples with no curing. Also, samples with curing compounds showed less weight loss compared to the wet curing method. The amount of weight loss between the sealed and wet cured samples had a huge difference; however, the corresponding deformations (such as curling) caused by drying was quite similar.

2.2.4.2 Curling

Another difference between the sealed and the wet curing methods is the effects of curing on curling. Researchers found that the maximum curling height is increasing with the curing time [30, 31]. In the wet curing method, there is an increased drying rate before maximum curling due to the loss of the additional water added during the wet curing. However, the magnitude of the maximum curling is similar between the wet and sealed cured samples [30]. The main reason is that the extra water from wet curing can dry without causing subsequent curling and shrinkage.

2.2.4.3 Shrinkage

In the wet curing method, there is a greater capillary pressure inside the concrete specimens that causes a higher rate of drying shrinkage and curling deflection [62]. However, using curing compounds is an acceptable technique for structures, such as concrete pavements, which are susceptible to relative humidity gradients.

2.3 Dielectric Properties

In the electrical terminology, materials can be classified as either conductor or dielectric materials. The conductor materials can transmit electric currents, such as aluminum or copper. However, the dielectric materials (such as most construction materials) do not conduct electric currents but can create an electric field. The electrical characteristics that govern the propagation of electromagnetic waves in materials are electrical conductivity and the dielectric values [63]. The theory of radar wave propagation in solid objects was simplified for functional structural testing purposes in pavements. Thus, dielectric properties of concrete pavements can be implemented in materials behavior evaluation.

In order to use electromagnetic results in the pavement assessment, information about the dielectric properties of concrete over a wideband of frequencies is required. The signal velocity is taken to be inversely proportional to the square root of the relative permittivity (ε_r), which ranges from 1.0 (air) to 81 (water). A dielectric constant value shows both electric and magnetic properties, which describe the permittivity and the permeability of materials, respectively [2]. Since the magnetic permeability of materials is not substantial, this property can be ignored. The remaining electrical permittivity is one of the investigation interests pertaining to dielectric materials among pavement engineers [64]. The permittivity in dielectric materials is defined based on the ability to allow the passage of electric fields (or a current). Also, the permittivity of free space is combined with the electric flux density as described in Eq. (2-3) [65, 66]:

$$D = \varepsilon_0 E + P \tag{2-3}$$

where

D = electric flux density (C/m^2),

ε_0 = permittivity of free space, 8.85×10^{-12} (F/m),

E = electric field intensity or strength (V/m), and

P = induced polarization (C/m^2)

If a material is considered isotropic through the electric field, the proportional relationship between the electric field and the induced polarization is defined as [67]:

$$P = \chi_e \varepsilon_0 E \tag{2-4}$$

where

χ_e = dimensionless electric susceptibility

$$D = \varepsilon_0 (1 - \chi_e) E \tag{2-5}$$

It is also known that:

$$D = \varepsilon E \tag{2-6}$$

Therefore:

$$\varepsilon_r = \frac{\varepsilon}{\varepsilon_0} = (1 - \chi_e) \quad (2\text{-}7)$$

ε_r = relative complex permittivity (dielectric constant), and

ε = complex permittivity of a material

The sensitivity of the dielectric property of a given material to water content is a critical factor in identifying the free moisture variation. The speed of the electromagnetic waves is reduced with an increase in the dielectric constant. The velocity of electromagnetic waves through non-magnetic materials, such as water or soils, is directly related to the signal velocity, the velocity of light (0.3 m/ns), and the relative dielectric constant [63]. Usually, the average velocity values on concrete pavements vary between 0.11-0.13 m/ns. This range for aggregate and water is 0.05-0.13 m/ns and 0.033 m/ns, respectively. Standard ranges of the signal velocity in the construction materials are listed in Table 2-1.

2.3.1 Dielectric Constant on Concrete

Some experimental studies have tested the impacts of materials' properties, including moisture conditions, temperature, compaction, and chloride content at particular frequencies. Typical dielectric values of pavement materials are given in Table 2-1 [68]. One of the main influences of moisture on permittivity and conductivity of concrete emerges in aggregates. For example, concrete mix design with lightweight aggregates has higher relative permittivity and conductivity values due to the moisture in the aggregate particles [69]. The electrical conductivity has the greatest impact on the signal attenuation degree, i.e., the signal's penetration depth. The higher the conductivity, the greater the attenuation, and the penetration depth may be less [63]. The attenuation is also getting higher with the wave frequency that is propagating through the medium. Thus, a high-frequency investigation cannot be a suitable condition to test the penetration of wet materials.

Table 2-1. Dielectric Ranges for Typical Pavement Materials

Materials	Dielectric Constant	Velocity (m ns^{-1})
Air	1.0	0.3
Water	80 - 82	0.033
Sand	3.0 - 6.0	0.06 - 0.07
Gravel	5.8 - 6.5	0.05 - 0.13
Cement	3.6 - 4.0	0.09 - 0.15
Hydration Products	4.0 - 5.0	0.07 - 0.091
Bituminous Bound	2.0 - 12.0	0.15 - 0.21

As shown in Table 2-1, water has the greatest dielectric value compared with the other materials. Thus, the dielectric properties can be used as an index of free moisture. Due to the differences in the material conditions, dielectric constant values differ with changing position in samples, regardless of having the same material type [70].

Concrete, as a composite material, is a combination of several constituents that have different properties. Although each part keeps its individual properties, the reactions between cement particles and water during the hydration can impact the distinct properties of materials [71]. Figure 2-1 displays the volumetric conversions of different portions of concrete due to hydration [72]. During the hydration reactions, free water reacts with cementitious materials and forms different hydrated products. During these chemical reactions, free water content is getting reduced, and subsequently, hydration products are getting increased.

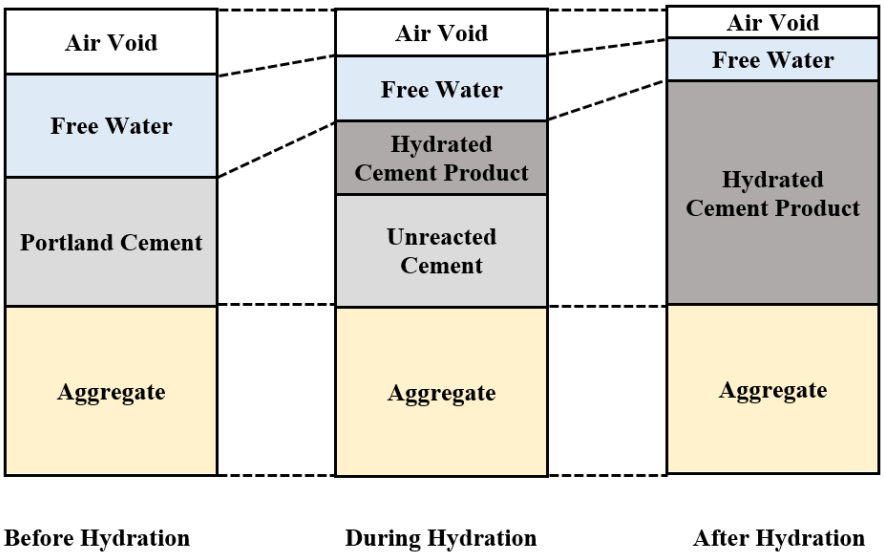

Figure 2-1. The Conversion of Concrete Constituents Due to Hydration

2.3.2 Moisture Content Measurement with Dielectric Constant

Considering the chemical reactions (hydration) and time, the portion of each part would change. The capillaries inside the concrete are reduced with self-desiccation because of the evaporation and hydration [73]. Some research studies have been published on estimating the water content of fresh concrete by using dielectric measurements. Typical relative dielectric permittivity values lie in the range of 5-6 in dry conditions and upwards of 14 in wet conditions [74].

The major variation is predominantly governed by moisture content and signal frequency [17]. A micro-analytical model was proposed by Lee *et al.* to evaluate the composite nature of concrete pavement materials to account for the contribution of each component on dielectric behavior. The dielectric constant value of each material in a composite varies according to the specific dielectric and volume fractions of that specific material [75]. This formulation can relate the dielectric constant of each component to its volume portion [76]. The proposed method in previous studies minimizes the possible systematic errors in empirical approaches [77]. This approach was a calibration process that corrects the dielectric constant of each component based on the data collection. This

method produced correct outcomes with no other hypotheses for the intrinsic constituent dielectric characteristics [75]. A general form that is being used in this technique is Eq. (2-8):

$$\sum_{i=1}^{n} v_i \left(\frac{\varepsilon_i - \varepsilon}{\varepsilon_i + 2\varepsilon}\right) = 0 \qquad (2\text{-}8)$$

where

n = number of components in a composite material (such as concrete),

v_i = volume fraction of component i ($\sum v_i = 1.0$),

ε_i = dielectric constant of component i, and

ε = composite dielectric constant

Based on the proposed model, cementitious materials during the hydration are defined as a five-phase system including available water, hydrated cement products, unreacted cement, aggregate particles, and air voids. Water is one of the inherent parts of the hydration products and gel that keeps changing its amount versus time [75]. Figure 2-2 shows the weight-volumetric relationship in a fresh concrete.

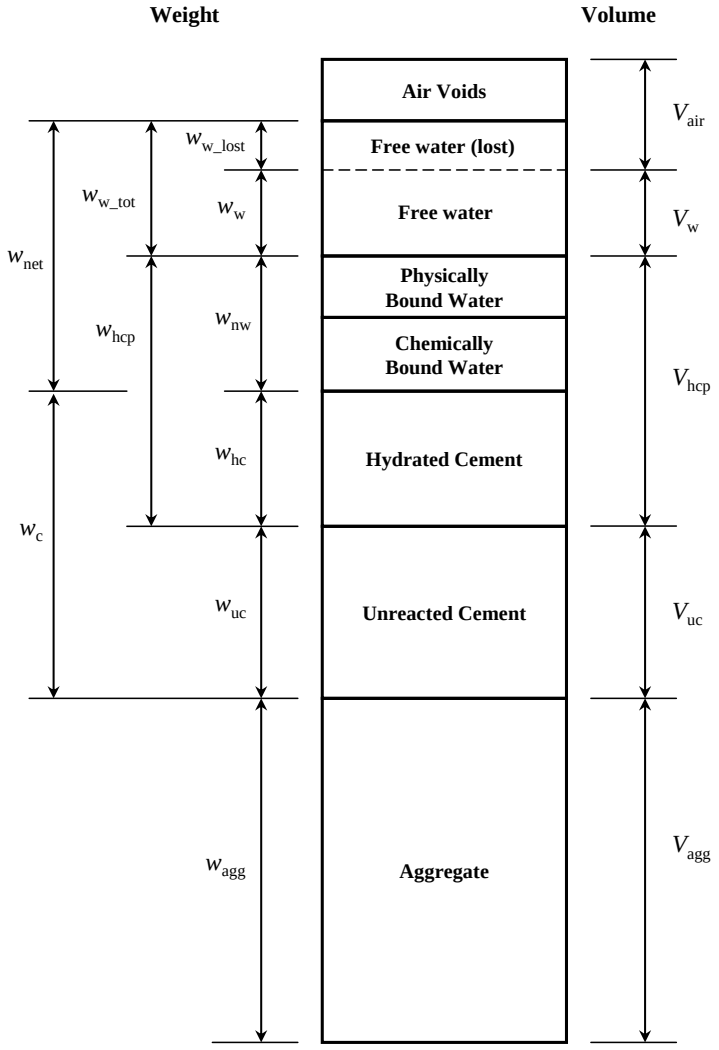

Figure 2-2. Weight-Volume Proportions of Fresh Concrete [2, 78]

Eq. (2-8) can be applied to portland cement concrete (PCC), based on the volumetric relationship of concrete in Eq. (2-9).

$$\theta_w \frac{\varepsilon_1-\varepsilon}{\varepsilon_1+2\varepsilon} + \theta_{hcp} \frac{\varepsilon_2-\varepsilon}{\varepsilon_2+2\varepsilon} + \theta_{uc} \frac{\varepsilon_3-\varepsilon}{\varepsilon_3+2\varepsilon} + \theta_{agg} \frac{\varepsilon_4-\varepsilon}{\varepsilon_4+2\varepsilon} + \theta_{air} \frac{\varepsilon_5-\varepsilon}{\varepsilon_5+2\varepsilon} = 0 \quad (2\text{-}9)$$

where

θ_w = volumetric content of free water,

θ_{hcp} = volumetric content of hydrated cement paste,

θ_{uc} = volumetric content of unreacted cement,

θ_{agg} = volumetric content of aggregate particle,

θ_{air} = volumetric content of air void,

ε_1 = dielectric constant of water,

ε_2 = dielectric constant of hydrated cement paste,

ε_3 = dielectric constant of unreacted cement,

ε_4 = dielectric constant of aggregate particle, and

ε_5 = dielectric constant of air (= 1.0)

The first step in this model is to measure the dielectric constant of concrete (composite). Then, the volume portion of each element can be back-calculated. The forward calculation should be implemented to compute the volume ratio of the components based on the composite dielectric constant measured for the further intervals.

2.3.3 Application of Dielectric in Curing Method

The dielectric constant of free water is approximately 81 at 20 ˚C, which is significantly higher than that of solid materials, such as aggregate, cement, and hydration products. Shen *et al.* [79] found that free water content was linked to capillary pores at early-age. Dielectric measurements reflected the capillaries' density. Shen *et al.* [79] also observed that there was a linear correlation between free water content and dielectric of the concrete. Thus, this relationship could enable users to estimate water content in a fresh concrete mixture.

Several studies explored the changes of concrete dielectric while the changes of free water content were significant during the hydration [80]. Researchers observed that the dielectric value strongly tied up to the free water content in the concrete mixture [81]. Lee and Zollinger proposed a method to calculate the portion of the different phases, such as moisture content, based on the volumetric relationship of a fresh concrete. They validated data by comparing the results with the laboratory test results [76]. The higher

dielectric constant values were detected at the first few hours. The hydration and moisture evaporation reduced the water content over time [72].

A new laboratory protocol was proposed by Sun and Zollinger to measure and evaluate concrete curing quality [38]. They measured the dielectric at the surface of mortar specimens. A correlation was reported between the dielectric constant and the efficiency of a given curing compound in terms of the moisture retention capability. Thus, the dielectric measurements showed the quality of curing compounds under different environmental conditions and different w/c values. They also found that changing the application rates of curing compounds did not substantially influence the dielectric values.

2.3.3.1 Ground-Penetrating Radar (GPR)

The dielectric measurements in the field investigation can be conducted after concrete setting. GPR can determine dielectric constant in concrete pavements under different conditions. In most applications of GPR in concrete pavements, a constant value of 6.5 for the dielectric (the real part of the complex permittivity) of concrete has been assigned [82]. The permittivity depends on the temperature, moisture content, salt content, pore structure, and pulse frequency. The permittivity of dry and moist concrete is 5-8 and 8-16, respectively. By using GPR, the dielectric values of the pavement layers can be measured by comparing the amplitude of a reflected signal from the surface to the amplitude of a signal reflected from a metal plate (as the reference) [83]. Nevertheless, upper layers of the pavement are usually investigated and are multi-layered with different compositions, which might lead to errors due to interference of surface reflected and direct (transmitter to receiver) waves [84, 85]. Typically, the range of signal frequencies of GPR is within a 400 MHz to 2 GHz for investigations with different purposes. Higher frequency leads to better resolution with a lower penetration depth [86].

The configuration of the GPR system allows for an extensive evaluation of the curing effectiveness over the entire concrete-paved area within a short period. Also, the GPR system is useful to suggest both the global and local curing uniformity based on the

dielectric measurements. The composite dielectric of pavement materials is determined from GPR. The analysis is conducted based on reflected signal amplitudes or correlation with other data. The dielectric constant value does not characterize the pavement materials per se. However, the dielectric properties of the pavement materials principally show useful information, such as the velocity of the radar pulse, times of reflections, and the depth of layers. The GPR system entails the propagation of electromagnetic pulses ($t<1$ ns) reflected in varying sharp variations in the electromagnetic properties of the medium, including the magnetic permittivity, electric conductivity, and dielectric permittivity [87].

2.3.3.2 Percent Within Limits (PWL) in Concrete Pavements

Specifications for quality control and quality assurance (QC/QA) are important aspects of construction and can be useful in determining the pay factor for work done on a project. In the early 1990's, many agencies concentrated on creating statistical-based quality control standards considering the allowable variability [88-90]. The percent within limits (PWL) and percent defective (PD) are recommended quality indicators. One of the advantages of these quality measures is incorporating mean and standard deviation. Thus, they enable users to measure the center and spread to calculate the percentage that is within or outside of the specification limits [91]. PWL is the preferred statistical method that the Federal Highway Administration (FHWA) and Federal Aviation Administration (FAA) recommend to the state agencies [92-94]. PWL is used as a pay factor for determining the statistical consistency of pavement density on a project. However, it is not necessary and practical to calculate the actual standard deviation and the average of all the samples. An alternate approach was used by the U.S. Department of Defense to approximate the surface area under the normal distribution graph based on the limited samples [95].

Burati *et al*. analyzed different techniques and procedures for developing quality assurance specifications and recommended PWL as the best quality measure. The PWL method uses the mean and standard deviation of the samples to estimate the percentage of the population that is within specified limits [90]. Almost 25 state agencies have replaced

their quality control specifications for flexible concrete pavements with PWL and some state DOT's, such as Michigan, Oklahoma, and Florida, adopted this method even for their rigid pavement quality specifications.

In a different study, Trost evaluated the PWL quality specification laid out by the Oklahoma Department of Transportation (ODOT). Researchers found that the testing precision of the data did not significantly alter the PWL specifications and suggested establishing target limits for all PWL quality characteristics [96]. The PWL quality specifications are used to determine conformance with a given requirement and are also known as the Acceptance Quality Characteristic (AQC). Generally, compressive strength, thickness, slump loss, and ride quality are the most often used AQCs for the concrete pavements. The AQCs related to performance should be chosen for better results.

2.4 Development of Set in Concrete

The zero-stress temperature is the point from which the concrete starts to experience stresses from climatically induced strains (usually after the final set time). Consequently, the set gradient not only depends on the time of placement but also the curing quality and the ambient conditions at the time the concrete is placed [8]. In other words, the set gradient is a function of the exposure of the slab to specific environmental conditions, which consists of a wide range of temperature and moisture variations. This situation can cause a concrete slab to be subjected to irreversible warping shortly after or during placement [97].

2.4.1 Environmental Stresses

Climatic factors, such as temperature and moisture, can induce stresses inside concrete slabs. The effect of the thermal strains can be dominant in the total stress of the

early-age concrete pavement. However, researchers usually have not taken moisture-related strain into account for the early-age stress calculation due to the minor drying shrinkage in the treated concrete pavements at the early-age. In a field project, researchers found that the moisture loss was less than 3% at the top surface (5 mm), and it was insignificant at depths (12.5 mm) [98]. Moreover, the autogenous shrinkage has been neglected in many cases due to the moderate w/c [99].

The temperature profile along the depth of the concrete pavements is non-linear at the early-age, which can be separated into three components (Eq. 2-10): the axial temperature, equivalent linear temperature difference, and the temperature affiliated with the self-equilibrating strain, as shown in Figure 2-3.

$$T_z = T_{axial} + T_{linear} + T_{ses} \tag{2-10}$$

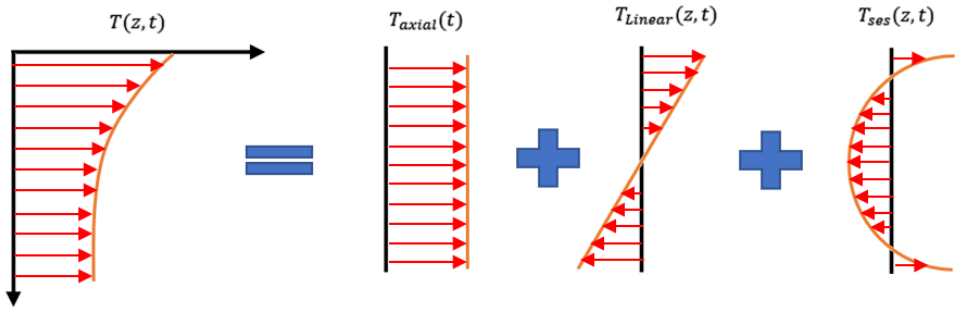

Figure 2-3. Distribution of Temperature into Concrete Pavements

The axial temperature (T_{axial}) is a uniform temperature that can induce strains in concrete. Although the axial temperature gradient strain is generally overlooked, this presumption is not quite right at the early-age of concrete slabs. The equivalent linear temperature gradient (T_{linear}) causes the bending moment. The non-linear component (T_{ses}) does not influence the slab deflection [100]. Researchers used polynomial (quadratic or third-order) models to characterize the actual non-linear temperature profile [101, 102].

2.4.2 Built-in Gradient

Curling and warping are some of the terminologies that are used interchangeably throughout the current literature. Curling is generally associated with the effects of temperature gradients and warping with moisture gradients. However, in most cases, curling and warping were referred to as merely curling regardless of the cause. Due to the built-in temperature gradients during the concrete setting, rigid pavements usually experience a permanent upward curling irrespective to the cyclical temperature [103]. Although the extent of the curling fluctuates with cyclical temperature/moisture gradients in the slab, a specific level of permanent built-in curling always remains in the slab. Rao and Roesler [104] reported a -20 ˚C linear effective built-in temperature difference for an un-doweled full-scale test in Palmdale, California (desert climate). They also observed that slabs with restraints had lower built-in curl levels. Hiller and Roesler studied the fatigue damage level for seven climatic regions with different built-in curling levels. As shown in Figure 2-4, the absolute fatigue damage levels minimize between built-in curl levels of -16 ˚C and -20 ˚C. The total damage of fatigue loading reduced by increasing the set gradient to a point, and then it increased beyond that.

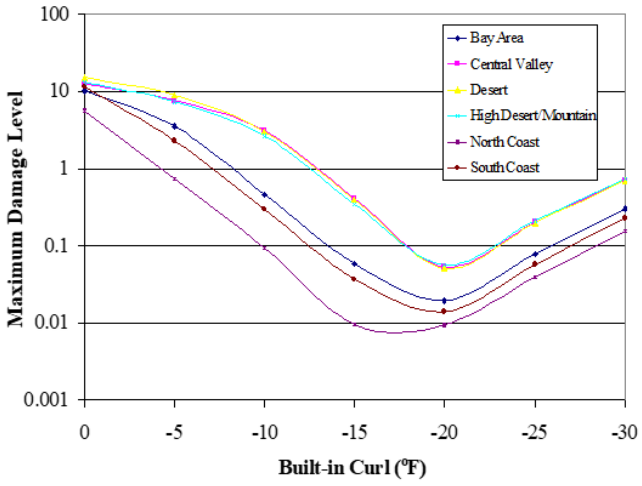

Figure 2-4. Fatigue Damage versus Effective Built-in Temperature Difference

When the concrete is set, the slab is flat and in full contact position with the sub-layer. Even though temperature and moisture gradients exist, there is no stress inside the concrete because the concrete is not in the plastic phase. Then, the thermal exchange of concrete with the adjacent atmosphere will start in different ways, such as hydration, convection, evaporation, radiation, and irradiation. Thus, the ambient temperature can subject concrete slabs into different gradients. The concrete slab at the final set is considered as a zero-stress state. At this moment, the concrete slab is flat just before becoming solid. Then, this state (zero temperature gradient) is regarded as a reference point. The slab turns into a concave condition with a negative temperature gradient, as illustrated in Figure 2-5. A positive temperature gradient is formed by placing the concrete during the daytime hours. In this case, the top surface temperature is higher than the bottom after the concrete has set. However, a negative temperature gradient is built-in the slab. So, the slab will form into a concave shape under a negative temperature gradient [15].

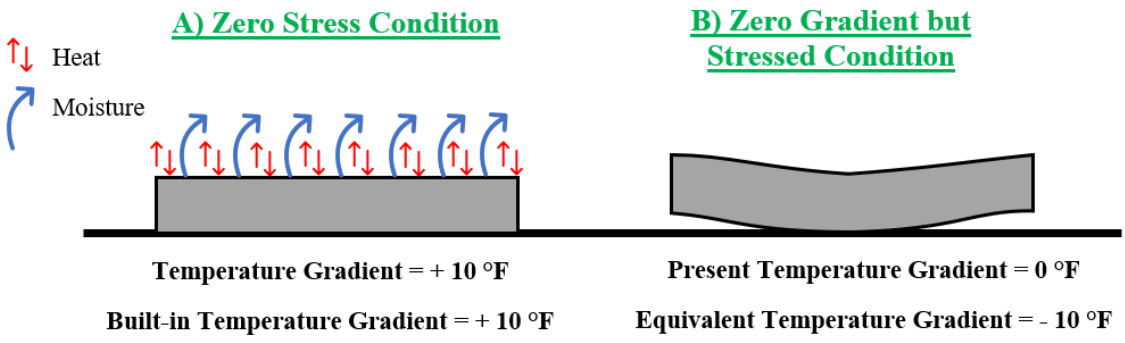

Figure 2-5. The Effective Built-In Temperature Gradient

Many researchers tried to show that $\Delta T_{built-in}$ is an important parameter in the prediction of JPCP-related performance [12, 14, 105-107]. As many factors influence the $\Delta T_{built-in}$, Pavement ME let the users to choose $\Delta T_{built-in}$ based on the given

assumption/information. The default value of $\Delta T_{built-in}$ in Pavement ME (i.e., -10 ˚F) was supposed to include not only the temperature and moisture gradients at the set time, but also the irrecoverable element of the drying shrinkage ($\Delta T_{shrinkage}$), the creep effect (ΔT_{creep}), and slab support [7, 107]. This single default value for $\Delta T_{built-in}$ was derived from the Pavement ME calibration to minimize the contrast between the predicted and the actual distresses [15]. Although this constant is advised for the general use in JPCP design, users should choose the appropriate value for $\Delta T_{built-in}$ based on the actual site-specific properties.

A part of the drying shrinkage strains (usually caused by seasonal variation) in concrete is recoverable by rewetting. However, the irrecoverable part of the shrinkage is accountable for the permanent curling/warping ($\Delta T_{curling/warping}$) in concrete slabs. Creep (ΔT_{creep}) has complicated impacts on the permanent curling/warping gradients in concrete slabs due to the non-constant state of stress in the slab. Another reason that makes the evaluation of the permanent curling/warping difficult is that there are numerous influential variables involved. Thus, only a few studies have been worked on the effects of the creep on the permanent curling/warping.

2.4.2.1 Drying Shrinkage

Several factors can influence the permanent curling/warping ($\Delta_{shrinkage}$), such as the geometry of the section, age, concrete mix design, environmental conditions, and the curing procedure. The irrecoverable portion of the drying shrinkage happens in a longer course of time. In many studies, researchers stated that the ultimate drying shrinkage might take about 3-5 years to occur. Also, the ambient relative humidity can change the rate of the irrecoverable drying shrinkage. For example, dry climates can make the irreversible drying shrinkage portion greater rather than the normal environments [108]. Irreversible drying shrinkage is directly related to the porosity of concrete, which is dependent on water content in the concrete mixture [109]. Additionally, concrete mixtures with a higher amount of cementitious materials show more shrinkage [110].

Due to the high surface-to-volume ratio of concrete pavements, the top surface of the slabs is prone to have a higher rate of drying than the bottom of slab. This non-uniform drying shrinkage distribution will cause a non-linear moisture gradient inside the slab. This challenging task can be settled by transforming the non-linear moisture gradient in the slab into the linear form. Some researchers have used this concept to model the slab strain due to the non-linear moisture gradients [111]. This gradient can be shown a moment in a beam because of the drying shrinkage gradient, as shown in Eq. (2-11).

$$\Delta t = \frac{6 \times t \times \varepsilon_s (h - h_s)}{\alpha h^3} \tag{2-11}$$

where Δt is the linear temperature gradient (˚F/in), ε_s is the drying shrinkage, h is the slab thickness (inches), h_s is the maximum depth that shrinkage occurs (inches), and α is the coefficient of thermal expansion (1/˚F). In order to calculate the temperature difference equivalent at any time after placement, Eq (2-11) from Pavement ME was used [97].

Pavement ME used the same approach to replace the drying shrinkage with an equivalent linear temperature gradient. Also, Pavement ME considers the impacts of seasonal changes on warping in terms of an equivalent temperature gradient (ETG) (see Eq. 2-11) [97]:

$$ETG_{shrinkage,t} = \frac{Age}{n + Age} ETG_{shrinkage,i} \tag{2-12}$$

$$ETG_{shrinkage,i} = \frac{3(\varphi . \varepsilon_{ult})(S_i - S_{ave}) h_s (\frac{h}{2} - \frac{h_s}{3})}{\alpha h^3} \tag{2-13}$$

where

$ETG_{shrinkage,t}$ = the equivalent temperature gradient (˚F/in) at time *t*,

Age = the concrete age from the placement (days), and

n = the time to reach 50% of ε_{ult} (days)

φ = the reversible shrinkage factor (Pavement ME recommended 0.5),

ε_{ult} = the ultimate drying shrinkage,

S_i = the relative humidity (RH) factor for each month, and

S_{ave} = the annual average RH factor

In Eq. (2-13), the S_i and ε_{ult} are defined as:

$$S_i = \begin{cases} 1.1 \times RH_a & RH_a < 30\% \\ 1.4 - 0.01 \times RH_a & 30\% < RH_a < 80\% \\ 3 - 0.03 \times RH_a & RH_a > 80\% \end{cases}$$

$$\varepsilon_{ult} = C_1 C_2 [0.02 w^{2.1} (f'c)^{-0.28} + 270] \quad (2\text{-}14)$$

where

RH_a = the ambient relative humidity,

C_1 = the cement type constant (1.0 for type I),

C_2 = the curing compound constant (1.2 for the curing compound treatment),

w = the water content in the concrete mix (kg/m^3), and

$f'c$ = the 28-day compressive strength (MPa)

The ultimate drying shrinkage (ε_{ult}) can be derived from a laboratory test method or an empirical method (such as Eq. 2-14).

The CEB MC90 model [112] predicts the drying shrinkage of a concrete slab. The model form is hyperbolic versus time based on the mixture proportioning and environment conditions with some noted assumptions:

1) Pertains to normal weight and strength concretes (compressive strength in the range of 20 MPa <f_{cm28}< 90 MPa)
2) Cured at normal temperatures (5 to 30℃) and
3) Exposed to a mean ambient relative humidity (40 to 100%).

The total shrinkage strains of concrete $\varepsilon_{sh}(t, t_c)$ is calculated from:

$$\varepsilon_{sh}(t, t_c) = \varepsilon_{CSO} \beta_{s,T}(t - t_c) \quad (2\text{-}15)$$

where ε_{CSO} is the notional shrinkage coefficient, $\beta_s(t - t_c)$ is the coefficient describing the development of shrinkage with time of drying, t is the age of concrete (days), t_c is the age of concrete at the beginning of drying (days), and $(t - t_c)$ is the duration of drying (days). The notional shrinkage coefficient is obtained from the following equations:

$$\varepsilon_{CSO} = \varepsilon_S(f_{cm28})\beta_{RH,T}(h) \tag{2-16}$$

$$\varepsilon_S(f_{cm28}) = [160 + 10\beta_{SC}\left(9 - \frac{f_{cm28}}{f_{cmo}}\right)] \times 10^{-6} \tag{2-17}$$

$$\beta_{RH,T}(h) = \beta_{RH}(h)[1 + (\frac{0.08}{1.03-\frac{h}{h_0}})(\frac{\frac{T}{T_0}-20}{40})] \tag{2-18}$$

$$\beta_{RH}(h) = -1.55[1 - (\frac{h}{h_0})^3] \tag{2-19}$$

where f_{cm28} is the mean compressive cylinder strength of concrete at the age of 28 days (MPa), f_{cmo} is equal to 10 MPa, β_{SC} is a coefficient that depends on the type of cement, h is the ambient relative humidity as a fraction, and h_0 is assumed to be 1. The parameter $\beta_{RH,T}(h)$ is the relative humidity parameter, which is corrected in terms of temperature. Also, T is the ambient temperature (˚C), and T_0 is assumed to be 1.

$$\beta_{s,T}(t - t_c) = [\frac{\frac{t-t_c}{t_1}}{350[\frac{\frac{V}{S}}{(\frac{V}{S})_0}]^2 \exp[-0.06(18.778\frac{T}{T_0}-37.778)]+\frac{t-t_c}{t_1}}]^{0.5} \tag{2-20}$$

where $(t - t_c)$ is the duration of drying (days), t_1 is equal to 1 day, $\frac{V}{S}$ is the volume-surface ratio (mm), and $\left(\frac{V}{S}\right)_0$ is equal to 50 mm.

2.4.2.2 Creep at Early-Age

Concrete, as a composite material, behaves as both an instantaneous and a viscous material under loading. Drying shrinkage and drying creep in concrete are tied together as common factors that can affect the concrete properties. Concrete creep and shrinkage strain consist of different components: basic creep, drying creep, and drying shrinkage (see Figure 2-6). Basic creep occurs due to constant ambient moisture/temperature conditions. Basic creep can be measured in the laboratory using a sealed specimen. Another component that has a role in the drying process is the drying creep [113]. Figure 2-6 confirms that the creep amount is getting higher over time at a decreasing rate.

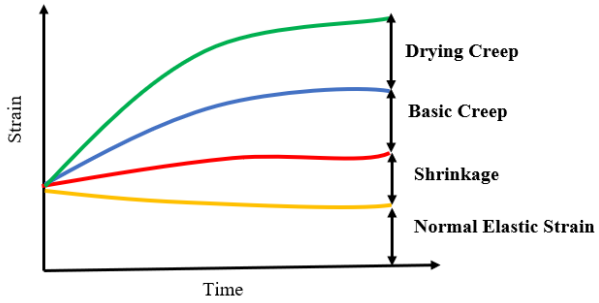

Figure 2-6. Components of Drying Shrinkage and Creep

Limited studies have been done to evaluate the concrete built-in gradient. Rao *et al.* [114] measured the curling of the slabs' corner for the short-term and long-term. The researchers predicted the form of the slab due to the temperature gradients. Then, the difference between the predicted values and the measurements were compared. They named this term the built-in that contains shrinkage and creep. They reported that the equivalent gradient is reduced by about 33% in the first two weeks. Also, this value reached to 50% after 40 days. They stated that the main cause of this reduction in the short-term and long-term was attributed to drying shrinkage and creep, respectively.

2.4.2.2.1 Creep Activation Energy

Usually, creep is defined as a thermally activated process based on the activation energy. The influence of age and moisture content on this creep mechanism can be taken into consideration in a reasonable way (such as maturity). The impacts of coupling temperature and moisture on the early-age concrete creep properties are well-known. The internal drying and the heat development of hydration can change the impact of these couplings. Thus, the creep of concrete can be modeled based on the age and the thermal activation (governed by the Arrhenius principle) [115]. The hydration development can reduce the rate of creep. However, the thermal activation might increase the rate of creep

by changing the viscosity. The maturity principle is used to calculate the hydration. To keep moisture included, an adjustment was applied on this calculation. The activation energy of concrete creep strongly varies with the moisture content. The creep activation energy is known to depend on moisture in a linear fashion [116]. The heat of hydration of concrete (Q_h) is the amount of heat which is released near the concrete pavement due to the hydration process. Type of the cementitious materials can change the activation energy values (usually range from 42,000 to 68,000 /mol) [117]. The heat of hydration is mathematically defined based on the equivalent age (t_e) [34].

$$Q_h = H_u C\alpha \frac{\lambda_1 \kappa_1}{t_1} \frac{[ln(\tau)]^{-(1+\kappa_1)}}{\tau} \cdot \beta_T \quad (2\text{-}21)$$

where

H_u = total heat of hydration (J/g),

C = cement content (g/cm^2),

λ_1, κ_1, t_1= hydration shape and time parameters,

τ = age parameter $= 1 + \frac{t_e}{t_1}$,

t_e = equivalent age (hours),

α = degree of hydration,

$$\beta_T = exp\left[-\frac{E_a}{R}\left(\frac{1}{T+273} - \frac{1}{T_r+273}\right)\right] \quad (2\text{-}22)$$

Hansen and Pederson defined the equivalent age based on an Arrhenius equation, to relate the chemical reactions to concrete temperature, as shown in Eq. (2-23) [118].

$$t_e = \sum_0^t exp\left[-\frac{E_a}{R}\left(\frac{1}{T+273} - \frac{1}{T_r+273}\right)\right] \quad (2\text{-}23)$$

E_a = activation energy (J/mol),

R = universal gas constant (= 8.314 J/mol/˚K),

T = concrete temperature (˚C), and

T_r = reference temperature (= 20 ˚C)

A technique for estimating the creep's dependence on time, temperature history, and moisture history was proposed. Degree of hydration, $\alpha(t_e)$, can be expressed in several ways, such as the ratio of current strength over the ultimate strength. This term is characterized by Eq. (2-24):

$$\alpha(t_e) = \alpha_u \cdot exp\left(-\left({}^{\tau}/_{t_e}\right)^{\beta}\right) \quad (2\text{-}24)$$

where

α_u = ultimate degree of hydration,

τ = hydration time parameter (hours), and

β = hydration shape parameter

These hydration parameters can be obtained from the mixture design information [119]. Since the heat generation rate and the self-desiccation rate are dependent on the derivative of the degree of hydration with respect to time, this derivative is presented in Eq. (2-25) for further use.

$$\frac{\partial \alpha}{\partial t} = \frac{(\tau/t_e)^{\beta}\beta_T\beta_{RH}\alpha}{t_e} \quad (2\text{-}25)$$

where β_{RH} was the adjustment factor for the numerical calculation of the effects of moisture on the equivalent age (Eq. 2-26), and β_T was recommended by Hansen and Pederson according with the Arrhenius equation (Eq. 2-22) [120].

$$\beta_{RH} = [1 + (a - a \times RH)^b]^{-1} \quad (2\text{-}26)$$

where

RH = the relative humidity of concrete,

a = coefficient constant changing from 5 to 7.5, and

b = coefficient constant, which is 1

Bazant [121] suggested *a* = 7.5 and *b* = 4, while Jeong *et al.* [122] found that *a*=5 and *b*=1 had better conformity with data. Thus, the latter suggestion was used in this study.

Finally, the creep deformation of concrete at a given time is as Eq. (2-27):

$$\varepsilon = \dot{\varepsilon_0} \exp\left(-\frac{E_a}{RT}\right).\sinh\left(\frac{V\sigma}{RT}\right) \quad (2\text{-}27)$$

where ε_0, E_a and V are materials parameters that depend on the w/c ratio, degree of hydration and water content. However, the creep deformation can be calculated quantitatively by means of Eq. (2-27).

2.4.2.2.2 Compliance

Creep compliance has been used in many studies to describe the creep behavior in terms of the total strain $\varepsilon(t)$ and the sustained stress, as shown in Eq. (2-28).

$$\varepsilon(t, t_0) = J(t, t_0)\sigma(t_0) \quad (2\text{-}28)$$

The compliance function $J(t, t_0)$ that characterizes the total stress-dependent strain by unit stress is given by

$$J(t, t_0) = \frac{1}{E_{cm28}}[\eta(t_0) + \phi_{28}(t, t_0)] = \frac{1}{E_{cmto}} + \frac{\phi_{28}(t,t_0)}{E_{cm28}} \quad (2\text{-}29)$$

where $\eta(t_0) = E_{cm28}/E_{cmto}$, E_{cm28} is the average of a 28-day concrete modulus of elasticity (MPa), and E_{cmto} is the modulus of elasticity at the time of loading (MPa). The dimensionless 28-day creep coefficient $\phi_{28}(t, t_0)$ gives the ratio of the creep strain from the start of loading at the age t_0 to the elastic strain (constant stress applied to concrete at age 28 days) [123]. Thus, $\frac{1}{E_{cmto}}$ is the initial strain per unit stress at loading. For the prediction of the creep function, the initial strain is based on the tangent modulus of elasticity at the time of loading. The modulus of elasticity of concrete at a concrete age *t* different than 28 days may be estimated from Eq. (2-30):

$$E_{cmt} = E_{cm28} exp\left[\frac{s}{2}\left(1 - \sqrt{\frac{28}{\frac{t}{t_1}}}\right)\right] \quad (2\text{-}30)$$

where E_{cm28} is the modulus of elasticity of concrete at the age of 28-day; the coefficient s is associated with the cement type and the compressive strength of concrete. The modulus of elasticity at the age of 28-day E_{cm28} (MPa) can be estimated from the compressive strength of concrete. The effects of temperature on the modulus of elasticity of concrete, at the 28-day age without the exchange of moisture, can be shown with Eq. (2-31):

$$E_{cm28} = 21{,}500\sqrt[3]{\frac{f_{cm28}}{f_{cmo}}}\left(1.06 - 0.003\frac{T}{T_0}\right) \tag{2-31}$$

2.4.2.2.3 Creep Coefficient

Within the range of concrete service stresses (less than 40% of the mean concrete strength f_{cmto} at the time of loading t_0) [123], the 28-day creep coefficient $\phi_{28}(t, t_0)$ is calculated from Eq. (2-32):

$$\phi_{28}(t, t_0) = \phi_o \beta_c(t - t_0) \tag{2-32}$$

where ϕ_o is the notional creep coefficient, $\beta_c(t - t_0)$ is the coefficient that describes the development of creep with time after loading, t is the concrete age (days) at the moment considered, and t_0 is the concrete age at time of loading (days). The notional creep coefficient ϕ_o can be determined from Eq. (2-33):

$$\phi_o = \phi_{RH}(h)\beta(f_{cm28})\beta(t_0) \tag{2-33}$$

$$\phi_{RH}(h) = \left[1 + \frac{1 - \frac{h}{h_0}}{\sqrt[3]{0.1\frac{\frac{V}{S}}{\left(\frac{V}{S}\right)_0}}}\alpha_1\right]\alpha_2 \tag{2-34}$$

$$\beta(f_{cm28}) = \frac{5.3}{\sqrt{\frac{f_{cm28}}{f_{cmo}}}} \tag{2-35}$$

$$\beta(t_0) = \frac{1}{0.1 + \left(\frac{t_0}{t_1}\right)^{0.2}} \tag{2-36}$$

$$\alpha_1 = \left[\frac{3.5 f_{cmo}}{f_{cm28}}\right]^{0.7} \quad (2\text{-}37)$$

$$\alpha_2 = \left[\frac{3.5 f_{cmo}}{f_{cm28}}\right]^{0.2} \quad (2\text{-}38)$$

The coefficient $\beta_c(t - t_0)$ that highlights the development of creep with time after loading may be determined from Eq. (2-39):

$$\beta_c(t - t_0) = \left[\frac{(t-t_0)/t_1}{\beta_H + (t-t_0)/t_1}\right]^{0.3} \quad (2\text{-}39)$$

$$\beta_H = 150\left[1 + \left(1.2\frac{h}{h_0}\right)^{18}\right]\frac{\frac{V}{S}}{\left(\frac{V}{S}\right)_0} + 250\alpha_3 \quad (2\text{-}40)$$

$$\alpha_3 = \left[\frac{3.5 f_{cmo}}{f_{cm28}}\right]^{0.5} \quad (2\text{-}41)$$

2.4.3 Zero-Stress Temperature

Right after concrete placement, concrete slabs experience an increase in volume (expansion) and temperature due to the cement hydration. Although there is a gradient inside the concrete, there is no stress because the concrete has not been solid yet. The zero-stress temperature in concrete slabs depends on multiple variables, such as environmental conditions, curing practices, concrete mixture, and pavement structure. This structural property of slabs can be impacted by the construction operations significantly. Several studies have reported that zero-stress temperature has considerable effects on short-term and long-term concrete pavement performance [124, 125]. One of the results was that the low zero-stress temperature would induce smaller crack widths and increase slab stiffness within concrete pavements. Schindler *et al.* [126] found that zero-stress temperature can affect the design of the reinforced concrete. Increasing the steel amount of reinforcement may control the transverse cracking.

Concrete slabs are not allowed to move because of different restraints, such as the frictional base layer and dead-weight. The result of these restraints form stresses after the

set time. Figure 2-7 shows an example of the ambient temperature, the concrete temperature, and the conceptual determination of the zero-stress state. The concrete temperature will be higher after the setting time. Then, the increase in temperature causes the compressive stress (expansion) in the slab until the maximum temperature is reached. Placing concrete in the hot weather can intensify the induced stress. The concrete temperature decreases after the maximum temperature, and the compressive stress is reduced until it reaches zero. The temperature corresponding to this point is called zero-stress temperature (the second zero-stress point after the concrete placement) [127]. By assuming there is no shrinkage and creep inside the concrete, the zero-stress temperature could be the same as the final set temperature [99]. Depending on the concrete temperature placement, the zero-stress temperature can be either higher (in hot weather) or lower (in cold weather) than the setting temperature.

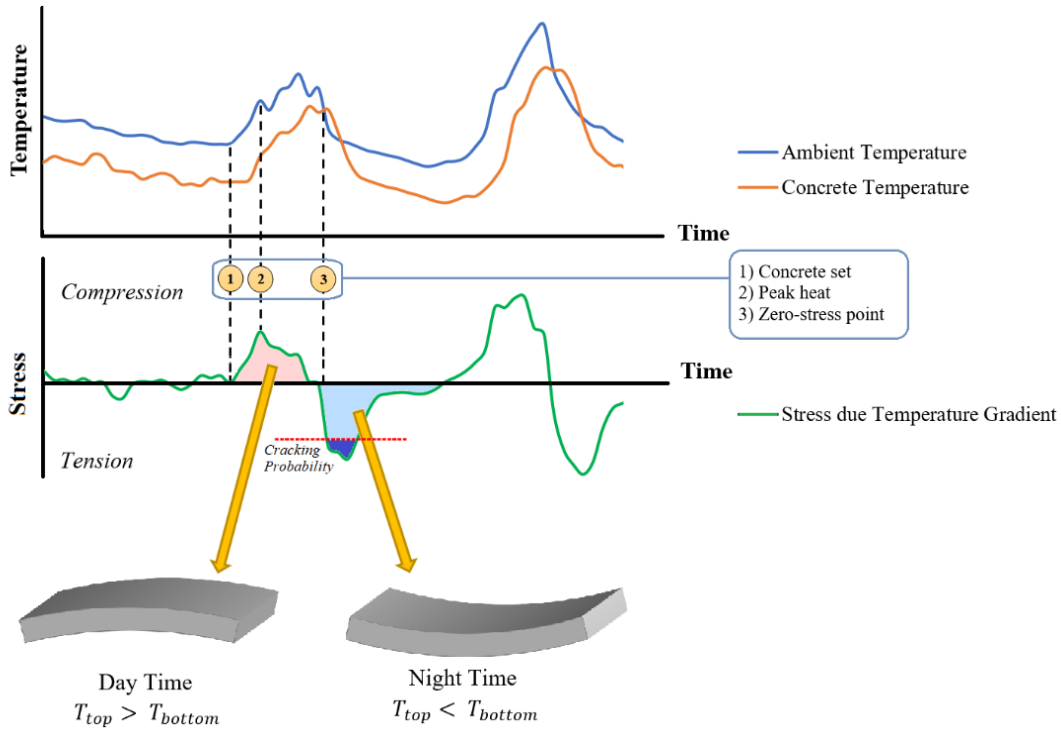

Figure 2-7. Relationship of Air and Concrete Temperatures to Stress

Accurate approaches for predicting the zero-stress temperature under different conditions have not been studied very much. Pavement ME uses an empirical method to estimate the zero-stress temperature by considering monthly temperature and cement content [128]. However, these two parameters cannot cover all the key factors. Due to these constraints, researchers tried to measure the zero-stress temperature [98, 124, 125, 129]. Hansen *et al.* [124] measured the zero-stress temperature by coupling the early-age concrete temperature and stress of a fully-restrained concrete. Schindler *et al.* [126] proposed a numerical analysis to estimate concrete temperature profiles and related stress to establish zero-stress temperature. Schindler *et al.* reported that the zero-stress temperature is about 92-94% of the maximum temperature if the thermal stress is uniform through the cross-section. Yeon *et al.* [98] determined this percentage is about 88.9-99.8% of the early-age maximum concrete temperature. In this research, climatic and curing conditions are the main parameters that will be discussed in the further paragraphs in detail. Climatic conditions can change the rate of hydration, which ultimately influence the set time. The maturity function can link hydration to the set by considering both time and temperature of concrete [130].

Once the slab sets, the set gradient is considered the reference concrete gradient during its service life. In other words, gradients above the zero-stress gradient (positive built-in gradient) will cause a convex shape, and gradients that are below the zero-stress gradient will cause a concave shape. These cases can induce critical stresses at the slabs' bottom and surface [8, 131]. Under these circumstances, concrete is prone to have cracks due to the difference between the zero-stress temperature and the actual concrete temperature. In addition, Hu *et al.* found that the positive gradient changes to the negative gradient gradually, and the gradient of zero-stress temperature tends to decrease during the life of concrete pavement [132]. Ali and Urgessa reported that using the zero-stress temperature profile can measure the extent of built-in curl in concrete pavements [133].

2.4.4 Concrete Setting

The set has been characterized when concrete changes from a liquid phase to a rigid form [134, 135]. ASTM C 403 considers different penetration resistance levels in concrete to determine the initial and final set in concrete [136]. As the degree of hydration is defined based on the rate of gaining strength, this term can be tied to the set times [137]. Although the built-in gradient must be determined according to the zero-stress state, a few studies showed a correlation between the degree of hydration and the built-in gradient [138]. In many studies, the built-in temperature gradient was considered as the temperature gradient in the concrete slab at the final set [3, 7, 9, 119, 139-141].

2.4.5 The Set Gradient

Early-age curling/warping due to temperature and moisture gradients have two significant consequences. First, curling/warping can cause a contact loss from the base layer along the edges and corners of slabs. Second, curling/warping can induce restraint stresses inside concrete slabs as their dead-weight inhibits unrestrained deformations. Thus, restraint stresses are made within the slab. A concrete slab experiences volumetric changes due to the climatic conditions, such as temperature and moisture. The induced strains can promote either contraction or expansion of the concrete during hardening and afterward. As shown in Figure 2-8, the moisture difference usually represents upward warping as a consequence of the slab top surface being drier than the bottom of the slab. Due to the dominant effects of drying shrinkage, the set gradient is likely large enough to shape the concrete slab in a concave configuration and separate it from the substrate along the edges and the corners of the slab [139]. Subsequent temperature and relative humidity differences will either add to or subtract from the stresses and strains associated with the set gradient. The corner displacements curl up in the morning and curl down in the afternoon. These strains create a combination of restrained and irreversible strains leading to deformation and tensile stresses within the pavement. Upward slab curling in this manner may cause tensile stress at the top of the slab, which can lead to top-down cracking

in slabs. Once these conditions develop, the slab also tends to exhibit time-dependent deformation referred to as creep. Creep strains are greater early on and ultimately diminish over time but will still affect the final set condition of the slab. As a consequence, the set gradient is principally a warp related strain [97].

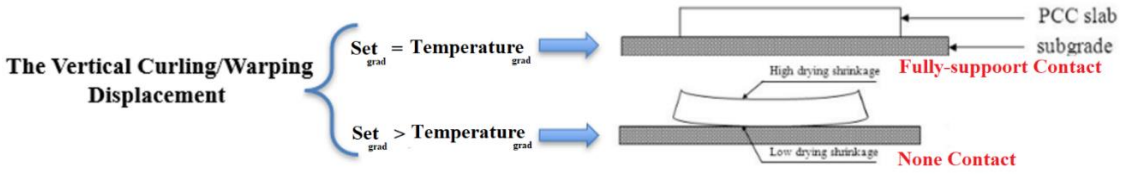

Figure 2-8. Diagram of Concrete Slab Warping

Huang *et al.* [142] studied the effects of the heat of hydration and water evaporation at the early-age on the set gradient of concrete slabs. They used a one-dimensional heat conductivity and moisture diffusivity model to estimate the temperature and moisture profiles in concrete slabs. In another study, Sun and Zollinger [143] used the heat and moisture models to take curing quality and the boundary conditions in calculating the set gradient. They studied the impacts of curing quality on the set gradient and long-term performance by conducting laboratory and field experiments. Springenschmid and Hiller [144] reported that the application of the impervious plastic sheets and insulation blankets as the curing methods could cause a higher set gradient. McCracken analyzed the response of a JPCP to seasonal loads, and in the unrestrained slabs found that there was a higher set gradient due to lack of full support [145]. Taghavighalesari *et al.* [146] used the non-linear built-in (set) temperature profile in the modeling of the effect of thermal loads on the concrete pavement. The authors considered the effective temperature profile to calculate the residual thermal stress distribution. Thus, they assumed the slab should be modeled as a plate with linear elastic and isotropic material behavior to be totally restrained against deformation. Zollinger and Fernando [147] proposed a method to

increase the accuracy of fatigue damage calibration coefficients by considering the effects of the set gradient on the long-term performance.

By modeling the slab curling/warping, the set gradient behavior can be predicted in a concrete slab in relation to the separation along the subbase/slab interface. Of particular interest is the effect of moisture in the behavior of concrete slabs as it can be manifested in concrete drying shrinkage and creep rate during the hydration. These slabs' properties are of interest with respect to early-age concrete slab deformations along the edges and corners. These displacements influence the cracking propagation and horizontal delamination. Furthermore, material-related and moisture transport properties (such as permeability and diffusivity) are important in the scientific modeling of stress and strain because of drying shrinkage and creep [148]. The time-dependent deformations (i.e., creep) or the stress relaxation under different environmental conditions can be quantitatively calculated as a part of representing the physical processes involved [149].

3 LABORATORY TESTING AND DATA COLLECTION PROGRAM

This chapter presents the data collection methods and results from a series of laboratory tests that were conducted to develop a database of the main factors involved in the determination of the curing effectiveness as well as to validate relationships that could be used to make up an evaluation protocol. Several test methods were used to relate measured aspects of curing to the concrete properties, such as strength, permeability, maturity, and conductivity. Figure 3-1 shows the proposed laboratory program as a flowchart, which consists of using several methods to assess the concrete curing effectiveness. The experimental study in the laboratory consisted of testing a given curing compound under different situations to evaluate the curing compound's performance. The ambient conditions were considered in this evaluation. The main purpose of the laboratory experiments was to show the viability of identified curing quality indicators. Two types of indicators were defined to evaluate the curing practices: direct and indirect. These indicators were determined by measuring several factors, such as moisture loss, surface abrasion resistance, surface porosity, and drying shrinkage. The quality of a given curing compound was evaluated using a concrete moisture-based maturity and developing a new index. In addition, the dielectric measurements were utilized as non-destructive tests to assess curing quality. Laboratory test results subsequently showed that the direct measures had a significant correlation with the indirect methods, EI and DC. Consequently, the mortar mixture characteristics, as well as the curing compound's application rate and the ambient conditions, affected these test results. In the next step, a series of preliminary testing was conducted to examine the quality of curing methods under different ranges of curing combinations. Results were used to establish laboratory reference curves that cover the range of curing conditions expected under field testing. This chapter consists of materials, laboratory test methods, analysis, and curing evaluation procedures.

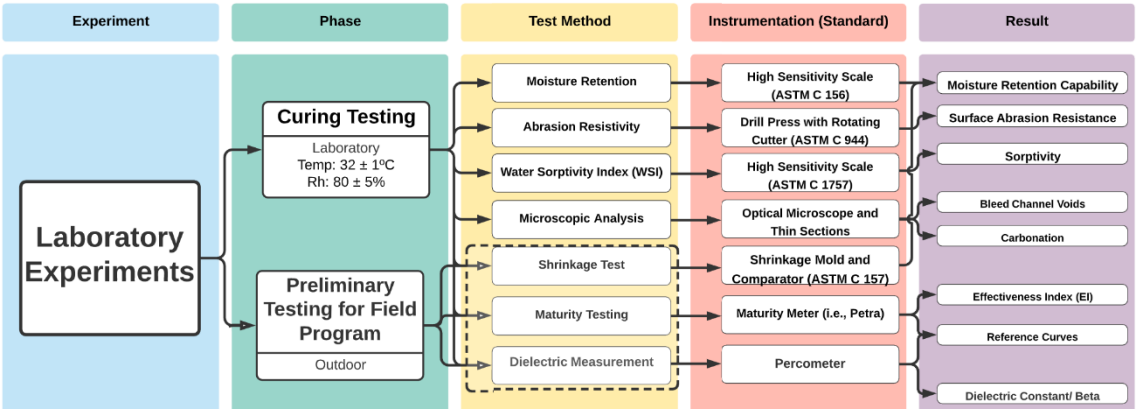

Figure 3-1. Laboratory Research Program Flowchart

3.1 Materials and Mixtures

The test specimens that were prepared in this research consisted of mortar. Materials for mixing and molding the mortar specimens were cement, fine aggregate, and water. All specimens were made with Type I Ordinary Portland cement. The specific area of the cement was 345 cm^2/kg. River sand was used as the fine aggregate in all specimens in this study with a specific gravity of 2.61 g/cm^3 and fineness modulus of 2.45. The fine aggregate conformed to the requirements for graded standard sand in specification ASTM C 778 [150]. Table 3-1 and Figure 3-2 show the sieve analysis of fine aggregates.

Table 3-1. Sieved Fine Aggregates in Accordance with ASTM C 778

IS Sieve Designation	Sieve Opening (mm)	Weight Retained (gm)	Percent Weight Retained (%)	Percent Weight Passing (%)
No. 4	4.76	4.00	0.82	99.18
No. 8	2.38	36.00	7.36	91.82
No. 16	1.19	106.00	21.68	70.14
No. 30	0.60	88.00	18.00	52.15
No. 50	0.30	115.00	23.52	28.63
No. 100	0.15	108.00	22.09	6.54
No. 200	0.08	32.00	6.54	0.00

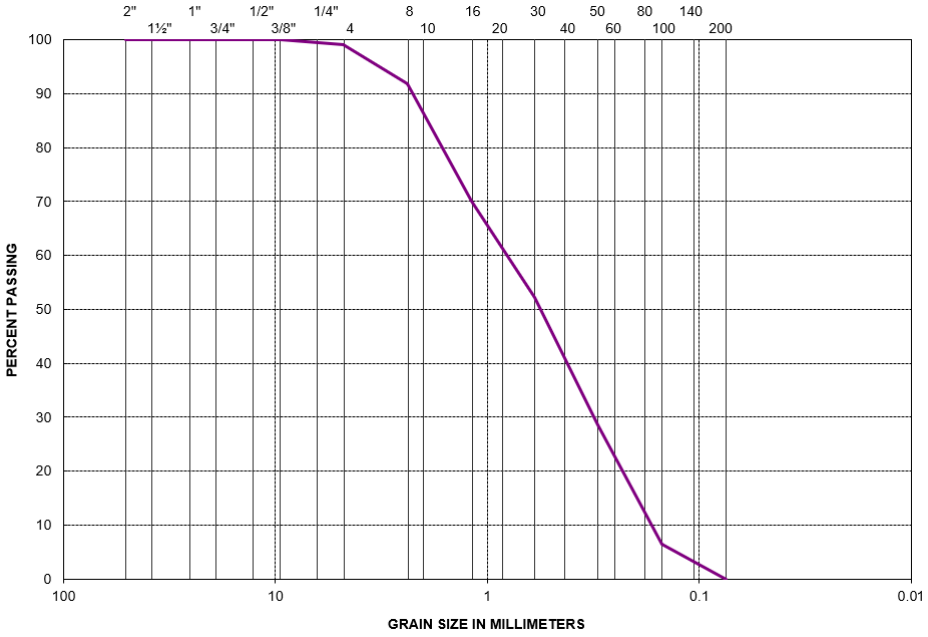

Figure 3-2. Grain Size Distribution Graph of Fine Aggregate (River Sand)

A single w/c ratio was selected in this study. An electrical-mechanical mixer was used to prepare a consistent mortar mixture for specimens according to ASTM C 305, "Standard Practice for Mechanical Mixing of Hydraulic Cement Pastes and Mortars of Plastic Consistency" [151]. Based on ASTM C 109, the proportions of materials for the standard mortar were 1:2.75 by mass [152]. Mixture proportions of the mortar are presented in Table 3-2. Water content for cementitious materials was set at a sufficient amount to obtain a flow of 110±5 in 25 drops of the flow table [152]. Depending on each test, three or four specimens were made from a batch of mortar for each test age, and the average was reported.

Table 3-2. Mortar Mixture Proportions

Mixture	W/C	Unit Weight (lb/ft^3)		
		Water	Cement	Sand
	0.4	14.1	35.25	96.93

Four different application rates were used to assess specimen sensitivity to changing curing conditions. The curing compound types were wax-based and white-pigmented. The curing compound formed a membrane that optimized the water retention, as shown in Figure 3-3a. An electric paint sprayer was used to treat samples with the application rates of 100, 140, 200, and 240 ft^2/gal (see Figure 3-3b). A control sample that was prepared for testing consisted of no curing compound to benchmark the curing level. The samples were kept in an environmental chamber. The temperature and relative humidity were held constant at 32±1 ˚C and in 50±5%, respectively. Specimens were kept in front of an industrial fan with different wind speed levels of 0, 5, 10, and 15 mph.

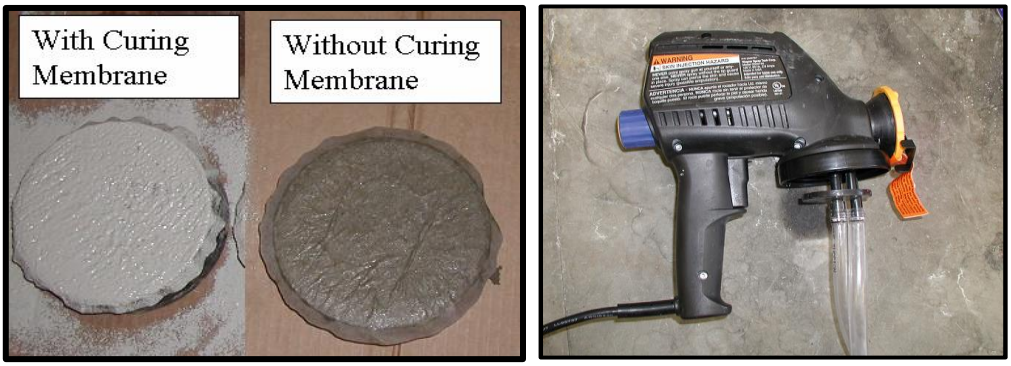

A) White-pigmented Curing Compound Treatment; B) Using Electric Paint Sprayer for Curing Application

Figure 3-3. Applying the Curing Compound on the Samples

3.2 Test Methods

The non-destructive tests (e.g., maturity and electrical conductivity) for measuring curing quality indicators were carried out to validate the utility of such measures in the selected mortar properties, such as moisture loss, abrasion resistance, sorptivity, porosity, and shrinkage. These direct measures of the mortar were identified as a practical way to ensure its utility.

3.2.1 Direct Indicators

The direct tests were carried out to verify the utility of measured moisture loss, surface abrasion resistance, sorptivity, porosity, and shrinkage. The results of these tests were used to directly interpret the effect of free moisture content changes in mortar specimens under different curing conditions. Measurements of direct indicators at the surface showed strong relationships with the change of moisture in the mortar specimens.

3.2.1.1 Moisture Retention Test

The moisture retention test measured the amount of moisture loss from the mortar specimens within a given period using a high sensitivity scale. This test was carried out in accordance with the ASTM C 156 [47], which was related to the capability of a curing compound to minimize evaporation (see Figure 3-4). The specimens' weights were recorded at specific time intervals after spraying the curing compound for 72 hours. The mold dimensions were 6×12 inches inside area and 1 7/8 inches depth. To assure the accuracy of the test, three specimens were tested, and the average of the moisture loss was reported. Since moisture loss was nearly constant after a while, whether the mortar was cured or not, the most critical time to measure moisture loss measurement was in the first 36 hours.

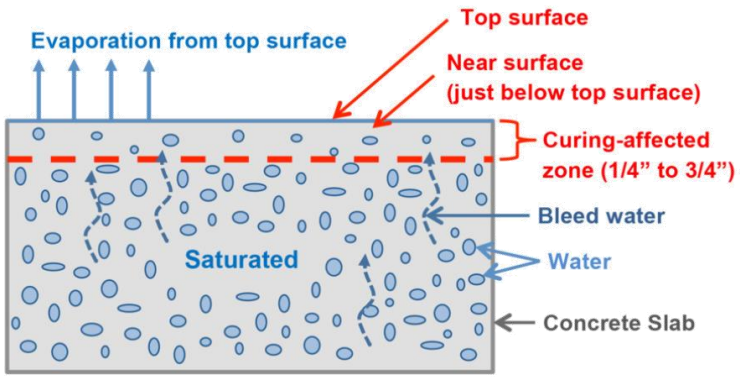

Figure 3-4. Water Retention Capability by Measuring the Moisture Loss

3.2.1.2 Abrasion Resistivity Test

An important characteristic of a concrete pavement surface is its abrasion resistance. In order to test curing effects on surface strength, the abrasion resistance of the top 5 mm of the mortar surface was tested. The results of the abrasion resistance reflected the influences of the curing treatment on the strength of the top surface. Surface abrasion resistance was evaluated by measuring the abraded weight loss based on the ASTM C 944 test method [153], as shown in Figure 3-5. In this procedure, a cutter rotated at 200 rpm for two minutes. During this test, a constant force of 22 lbs was applied to the test specimen surface. The mortar specimen was weighed before and after the test to determine the weight loss percentage. By dividing the weight loss of the mortar by the initial weight of the specimen, the abrasion resistance index was determined [154].

Figure 3-5. Abrasion Resistance Test Based on ASTM C 944

3.2.1.3 Water Sorptivity Index (WSI) Test

There are different methods to evaluate the absorption of mortar specimens. One of the quickest methods to measure the sorptivity is Water Sorptivity Index (WSI). The sorptivity can be defined as the rate of water movement through a porous material under

capillary actions. Preconditioned mortar samples were placed on the saturated layers of absorbent material. The mass gained of mortar specimens was monitored at prescribed time intervals. The opposite side of the samples was sealed to measure uniaxial absorption (see Figure 3-6). The WSI, which was interpreted as the rate of water penetration ($\mathrm{mm}/\sqrt{\mathrm{h}}$), was calculated by using the dimensions, porosity, and absorption rate of the samples. The typical range of these test results is 8.5 $\mathrm{mm}/\sqrt{\mathrm{h}}$ or less (for superior quality) to 15 $\mathrm{mm}/\sqrt{\mathrm{h}}$ or more (for low-quality) [155]. The sorptivity was calculated using Eq. (3-1):

$$S = \frac{\Delta M_t}{t^{1/2}} \times \frac{d}{(M_{sat} - M_{dry})} \tag{3-1}$$

where

S = sorptivity ($m/s^{1/2}$),

ΔM_t = mass of water absorbed at time 't' (kg),

t = time (s),

d = specimen thickness (m),

M_{sat} = saturated mass (kg),

M_{dry} = initial mass (kg), and

$\frac{\Delta M_t}{t^{1/2}}$ = slope of the best-fit line for the mass of water absorbed versus square root of time graph

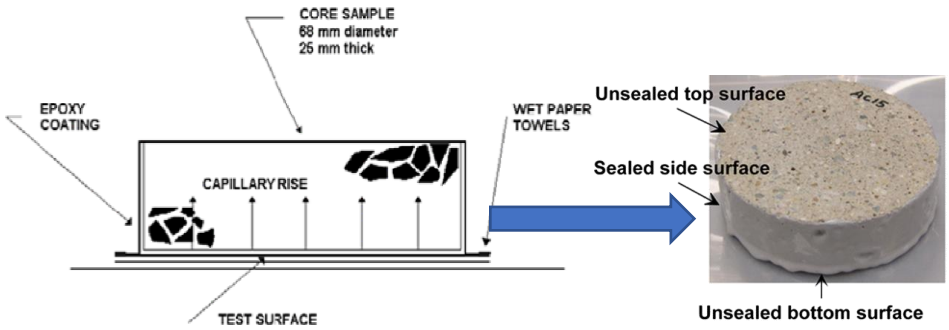

Figure 3-6. Water Sorptivity Index (WSI) Test

3.2.1.4 Microscopic Analysis (Thin Sections)

A direct indicator of curing effectiveness was based on microstructural characterization of a mortar surface using thin section-based transmitted light optical microscopy (TLOM). The curing compound limited excessive moisture loss from an exposed mortar surface either by sealing the surface or by forming a membrane over the mortar surface. These surface interactions led to different pore structures and size distributions at or near the surface of the cured specimens, as compared to the uncured (control) sample. Thin section examination under TLOM allowed for the detection of microstructural changes due to curing methods and provided direct evidence related to curing effectiveness.

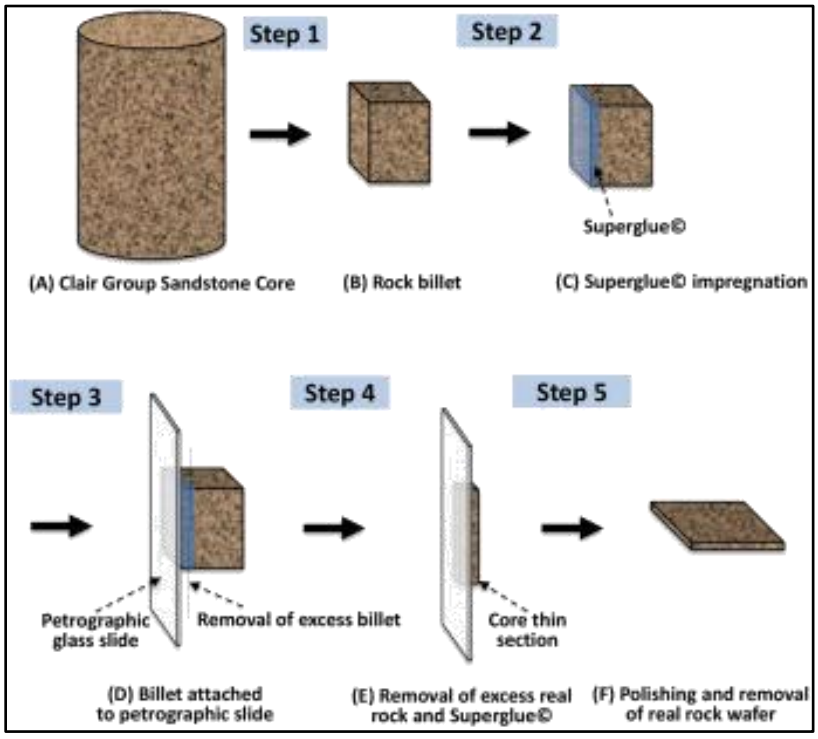

Figure 3-7. The Process of Thin Section Samples Preparation

Thin section images of size 50×75 mm with 20-micron thickness were prepared from 28-day old mortar specimens experiencing four different application rates. Using blue-dye epoxy in the thin sections allowed the pores, voids, and micro-cracks to be highlighted by the blue color. Parameters included in this study were interconnected capillary voids, bleeding channels, and carbonation at the top surface (15 mm) of the mortar. These characteristics at the surface were used as direct indicators of moisture loss.

3.2.1.5 Shrinkage Test

During and after hardening, mortar typically began to shrink as water was not being consumed in the cement hydration process. The shrinkage characteristics of a mortar mixture were determined by ASTM C 596 [156]. This test method allowed for the determination of the changes in length of mortar bars cured with curing compounds. The lengths and weights at specific time intervals were recorded up to 90 days by using a length comparator and a digital scale, respectively (see Figure 3-8).

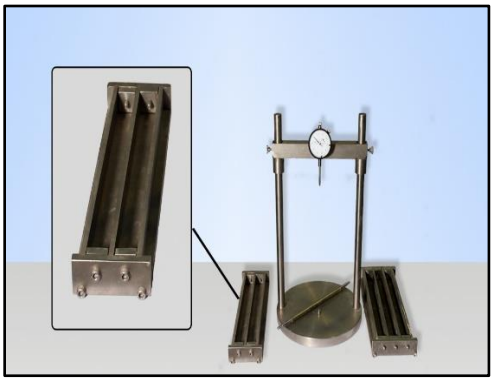

Figure 3-8. Determining the Length Changes of Mortar Bars with a Comparator

3.2.2 Indirect Indicators

Two parameters were identified as being indirectly related to the free moisture content and the degree of hydration of the mortar specimens. Thus, by observing the

changes in the measured moisture content and a moisture-based maturity with time, the correlation between indirect and direct indicators could be facilitated. The rate of changes reflected the effectiveness of an applied curing compound. The indirect indicators provided a way to measure the effectiveness of the curing compounds without damaging the curing compound membrane applied at the surface of the specimens.

3.2.2.1 Effectiveness Index (EI)

The quality of a given curing compound was evaluated using a moisture-based maturity according with dew point temperature measurements. This data was obtained by using a maturity meter. A detailed view of this unit is shown in Figure 3-9. This device was able to measure temperature data pertinent to the relative humidity under different environmental conditions. A high-performance data acquisition system provided an instantaneous display of the measurements and computations of the curing process.

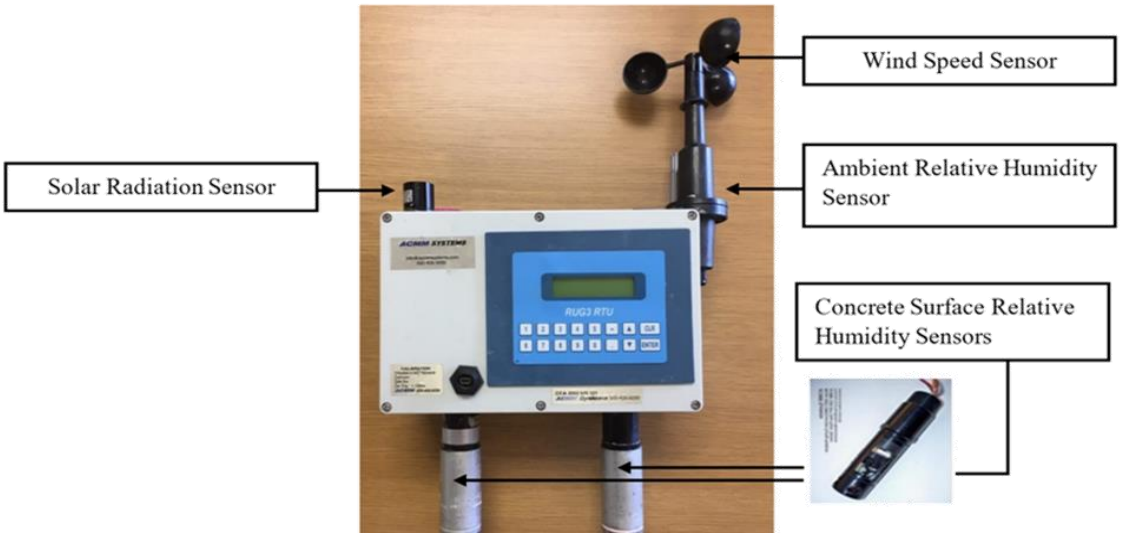

Figure 3-9. The Maturity Meter Unit with the Climatic and Chamber Sensors

Chilled-mirror dew point sensors were used to measure the curing process. For this purpose, algorithms were developed to verify the optimal moisture-based maturity of the curing environment. These sensors provided an absolute value for relative humidity, contrary to common relative humidity sensors, which strictly depend upon the ambient temperature. Thus, implanting chilled-mirror dew point sensors eliminated a large margin of error due to temperature fluctuations.

The maturity system was able to measure relative humidity inside the two separate chambers of a curing plate (which was placed on top of bare mortar), as shown in Figure 3-10. The measurements within each chamber consisted of the dew point and dry bulb temperatures, which were used to calculate the relative humidity. One of the dual dew point sensors was positioned in a sealed chamber configuration within the base plate. As moisture migrated from the mortar into the chamber, the moisture equilibrated to a consistent level within the chamber to the vapor pressure within the pores of the surface mortar. The second dew point sensor was positioned in another chamber configured within the monitoring plate that was filtered via a membrane formed by the curing medium. This type of measurement represented the vapor pressure immediately below the curing medium. To assess the curing quality of a compound, a comparison between the conditions inside the sealed chamber and the conditions inside the filtered chamber was conducted.

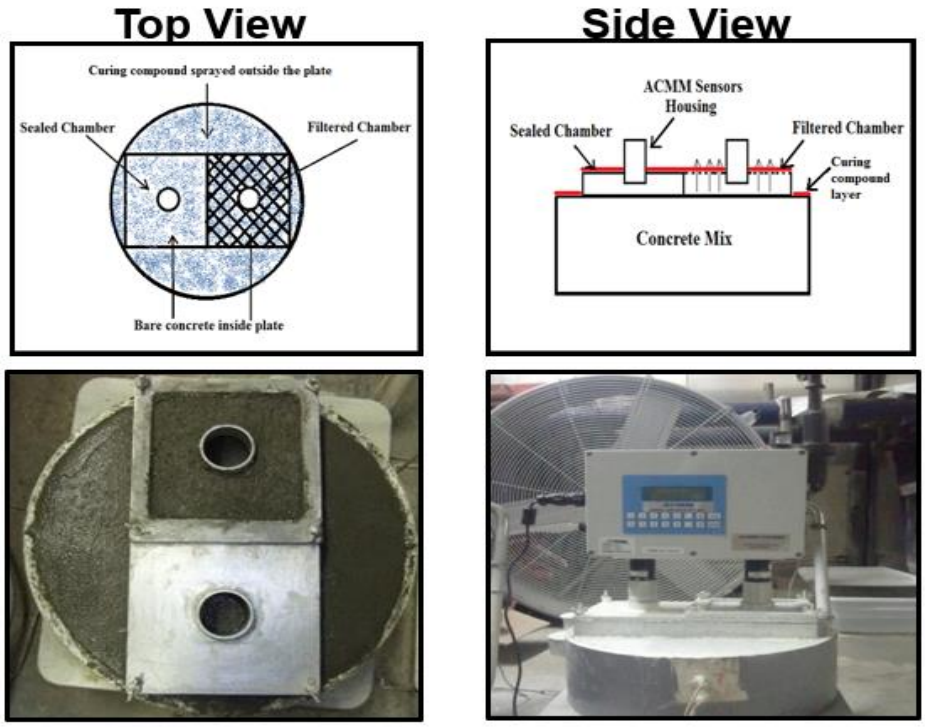

Figure 3-10. Top and Side Views of Sealed and Filtered Chambers

3.2.2.2 Dielectric Measurement

As previously alluded to, one purpose of curing is to hold surface moisture for the hydration process. The amount of free water at the mortar surface was an index to assess the effectiveness of a given curing compound. The dielectric constant is directly related to the free moisture content and the degree of hydration [83, 157]. Thus, by establishing a relationship between the dielectric constant and the capability of curing compounds to maintain free moisture at mortar surface, a reliable index was defined to show the effectiveness of curing conditions. In the laboratory experiments, the permittivity parameters (dielectric constant and conductivity) were measured by a percometer, as shown in Figure 3-11. The device had two segments: A probe that was used to measure the dielectric constant (by generating an electric field and receiving), and the body of the device. The specifications of the percometer are listed in Table 3-3. Permittivity was measured by the changes in the electrical capacity of the electrode (probe) due to the

influence of the measured material at a frequency of 40-50 MHz [158]. During the dielectric measurements at each planned time, three random locations on the sample were tested and the average of DC measurement was reported.

Figure 3-11. The Percometer Body and the Probe for the Dielectric Measurements

Table 3-3. Specifications of the Percometer in the Dielectric Measurements

Probe Type	Dielectric Constant (ε_r)	Electrical Conductivity (μs/m)	Temperature (˚C)	Accuracy
Surface Probe	1 ~ 31	0 ~ 2000	-50 ~ +85	± 0.1+2%

The dielectric constant was measured on 6-inch diameter specimens in the laboratory. A special set of chambers were placed on the mortar surface with no curing compound, as shown in Figure 3-12. The chamber was sealed onto the mortar surface. A screen mesh was provided as support for a thin layer of mortar and the curing compound. The dielectric constant of the mortar specimens was measured directly by removing the cap and inserting the probe into the chamber to access the bare mortar. This setup provided a direct way to measure the dielectric constant of the cured sample without damaging the curing compound membrane.

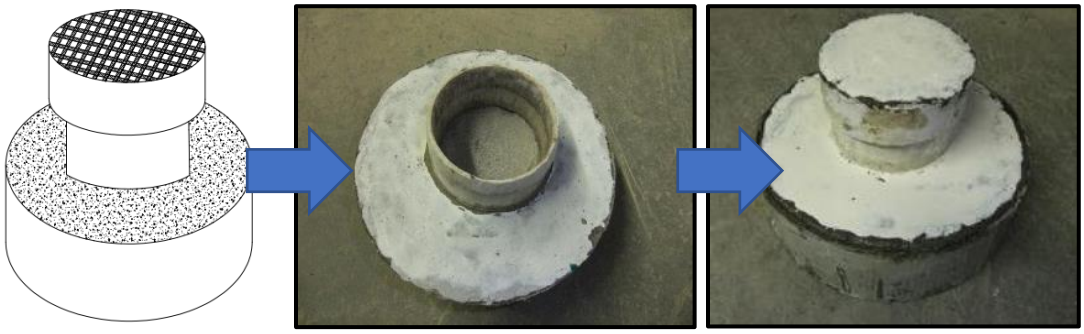

Figure 3-12. Dielectric Constant Measurement Setup for the Cured Samples

3.3 Laboratory Findings and Interpretation

To evaluate curing performance, direct and indirect indicators were introduced. Direct measurements were tested on the mortar specimens. These test methods measured moisture loss, surface abrasion resistance, surface porosity, electrical conductivity, and drying shrinkage. However, indirect indicators evaluated the curing effectiveness indirectly. Direct measurements were found to have a significant correlation with indirect indexes.

3.3.1 Moisture Loss Trends

The duration of the moisture loss measurement was 72 hours. The weight loss of mixtures with four different application rates and four wind speed levels is shown in Figure 3-13. The maximum amount of moisture loss allowed by the AASHTO and ASTM specification is 0.055 g/cm^2 [53]. The results indicated that with a mortar specimen cured with a higher application rate (100 ft^2/gal), significant moisture loss was prevented. This low moisture loss rate was achieved by limiting water transmission due to low moisture diffusion.

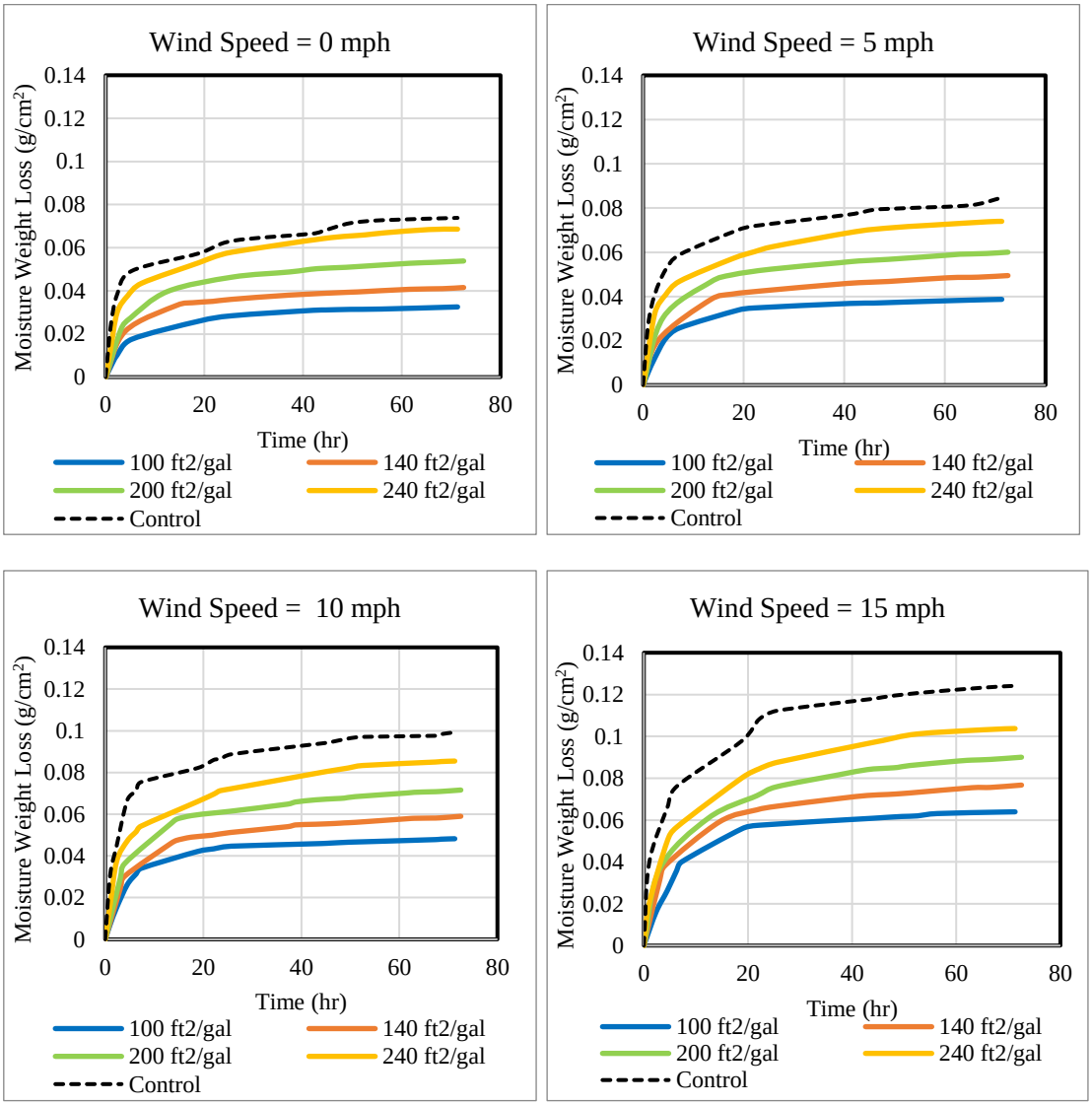

Figure 3-13. Weight Loss Results Under Different Wind Speed Situations

As displayed in Figure 3-13, the higher wind speed increased the moisture weight loss amount. The rate of evaporation from mortar depends directly on wind velocity. For example, in the treated sample, the range of moisture loss in samples with no-wind was 0.03-0.07 g/cm^2 at 72 hours. In all cases, the value of moisture loss in the control samples was more than the standard recommendation (i.e., 0.055 g/cm^2). Also, treated samples

with the higher application rate (100 ft^2/gal) kept the moisture loss under the limit for many cases. Under 15 mph wind conditions, which was the most severe condition for the water evaporation, no treated samples met the standard requirement. Thus, this standard's inability to address the ambient conditions makes it an inappropriate method for testing the curing quality under the field conditions.

3.3.2 Abrasion Resistance Trends

The weight loss percentage from the abrasion resistance testing of the specimens with four different application rates and four wind speed levels is shown in Figure 3-14. The rate of changes in treated samples with a higher application rate was lower than the untreated (or less treated) samples.

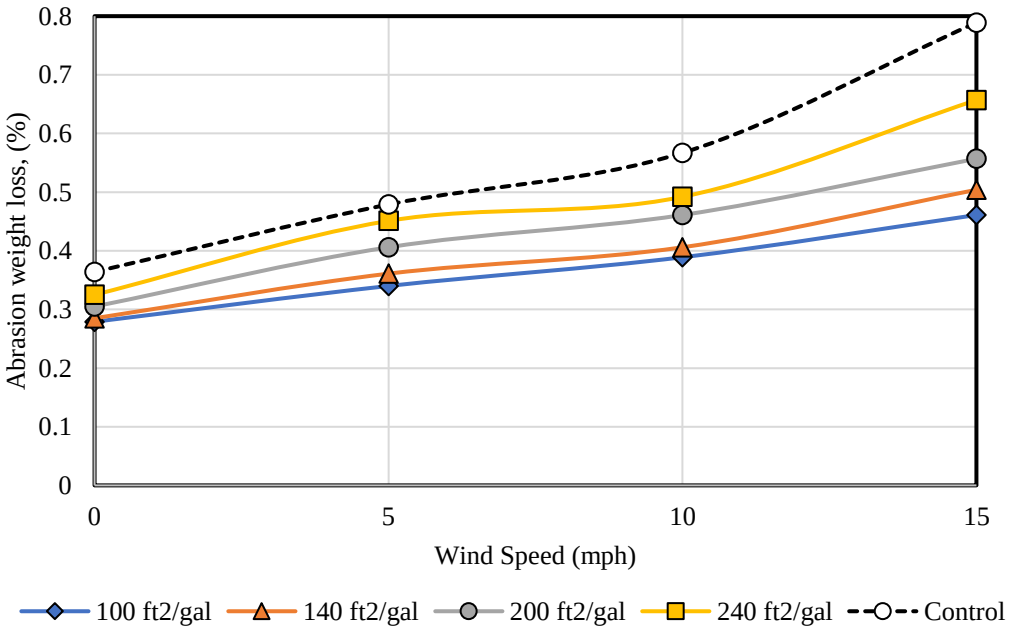

Figure 3-14. Weight Loss in the Abrasion Resistance Test

In higher application rates, as the strength of surface mortar increased, the resistance to abrasion also increased. Therefore, a lower weight loss of the abrasion test indicated a higher strength of surface mortar (or concrete), which was probably due to a better curing quality. The higher wind speed levels (15 mph) resulted in a greater abrasion weight loss compared with a no-wind cured condition.

3.3.3 Water Sorptivity Index (WSI) Test

For measuring transport performance, the water absorption of the mortar specimens was measured, as displayed in Figure 3-15. Differences in trends were observed for the WSI due to sensitivity to the properties of the specimen surfaces. The results showed that exposure to wind resulted in a substantial increase of this index, which was considered an indication of poor curing quality.

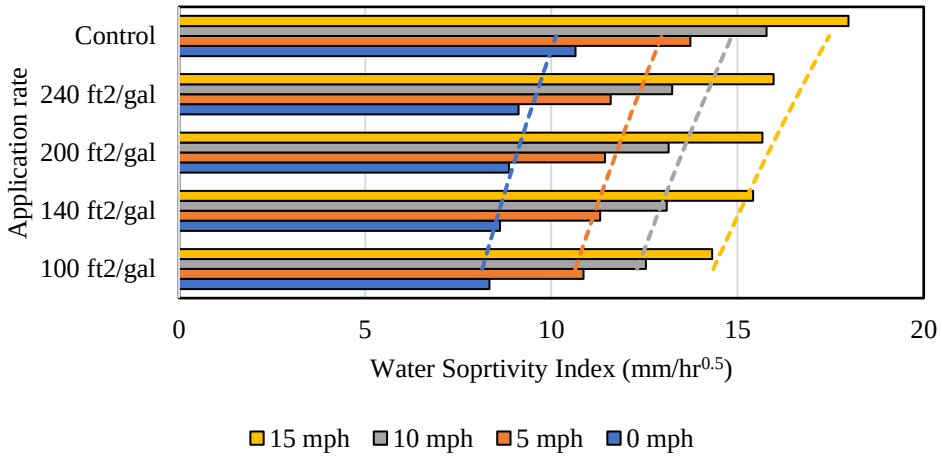

A) 3 days

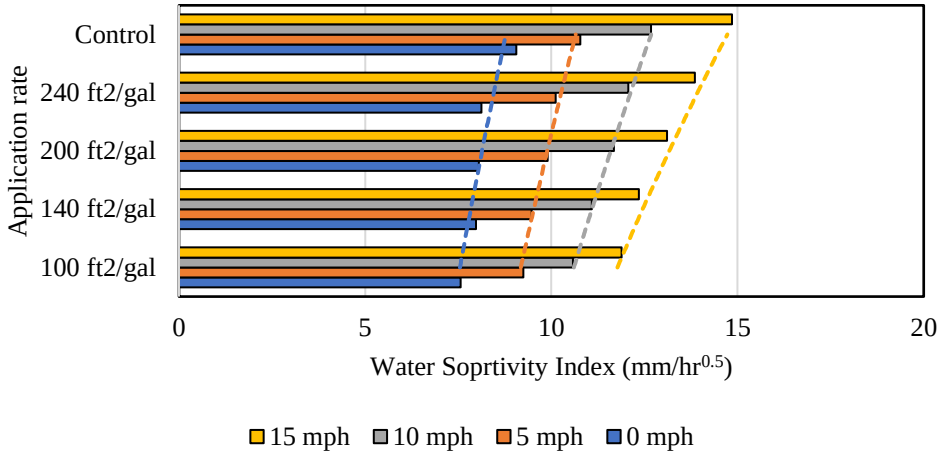

B) 7 days

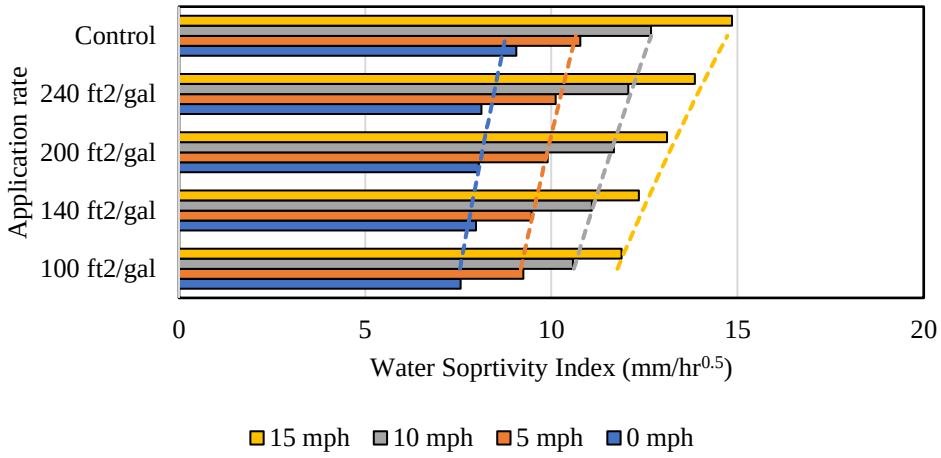

C) 28 days

Figure 3-15. WSI Results After 3, 7, and 28 Days

The lower wind speed level (0 mph) showed lower WSI numbers, which indicated better quality. Mortar samples that were cured for three days performed poorly, especially at lower application rates (240 ft^2/gal) and the control samples (no treatment), while results obtained from specimens that were cured with 100 ft^2/gal were generally similar or better. In older ages, the differences between the specimens were fewer than the early-aged ones. The fewer differences indicated that an adequate curing period (28 days) ensured that the

mortar had a sufficiently dense microstructure, enabling it to retain its moisture and benefit from the more rapid rates of hydration at higher temperatures.

3.3.4 Thin Section-Based Petrographic Investigation

As hydration progresses, two types of void systems come to prominence in a typically hardened concrete paste: capillary pores (50 nm-10 μm) and bleed water voids (greater than 100 μm). In this test, interconnected capillary pores and bleed channels were analyzed as they were thought to be related to curing effectiveness. Better curing resulted in a lower percentage of capillary pores and bleed channels at the surface.

Thin section images were analyzed with a microscopy imaging computer program that gave the quantity and density of pores and voids found in the image field area. The quantitative analysis of the samples consisted of the identification and measurement of the area of voids and their number density in the images [131]. The area of the voids was compared with the total area of the thin section to get a percentage of void space in the mortar. The petrographic examination also provided information on the sample's amount of carbonation. A better-cured mortar tended to show less carbonation as there was a limited path for atmospheric CO_2 to travel through the microstructure. The qualitative analysis of the sample thin sections that was carried out was done with respect to the presence of carbonation and the following parameters as a function of curing effectiveness.

3.3.4.1 Interconnected Capillary Voids

Interconnected capillary voids were defined as a porous region of paste in the thin sections with major dimensions less than 100 μm and higher. Blue-dye impregnated areas in the thin sections were analyzed as they showed the porous regions. These porous areas were more prevalent in samples treated at low application rates of curing compounds, as shown in Figure 3-16. Since dimensions of capillary pores were beyond the resolution of

an optical microscope, this study focused on interconnected capillary voids in thin sections.

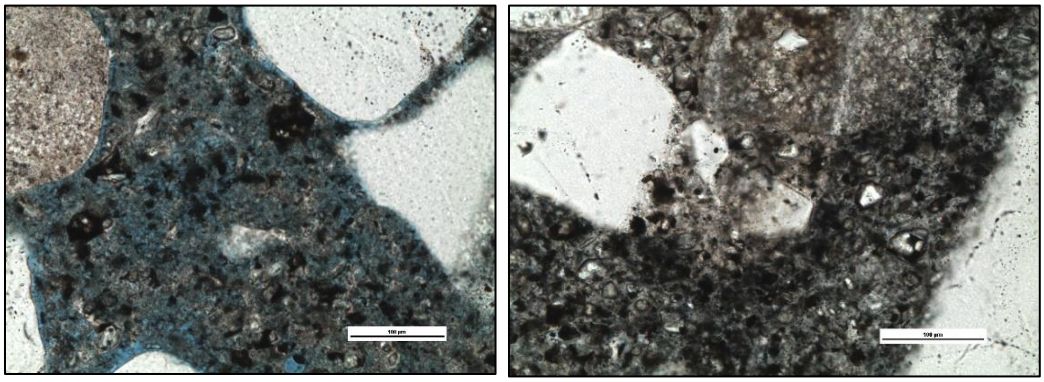

Figure 3-16. Interconnected Capillary Pores (Left) and Best Cured Sample (Right)

3.3.4.2 Bleed Water Voids

Bleed channels, the irregularly shaped voids that were created in the paste by bleed water, were prevented from rising to the surface by aggregate particles or the hardening of the paste. These porous voids usually occur along aggregate boundaries. As previously noted, the control samples used for reference in this study were not cured with a curing compound. As shown in Figure 3-17, using a higher application rate of curing compounds decreased the percentage of bleeding channels. The basis of this observation was attributed to the amount of bleeding that occurred in accordance with the inability of the curing compound to check evaporation completely at the lower application rates.

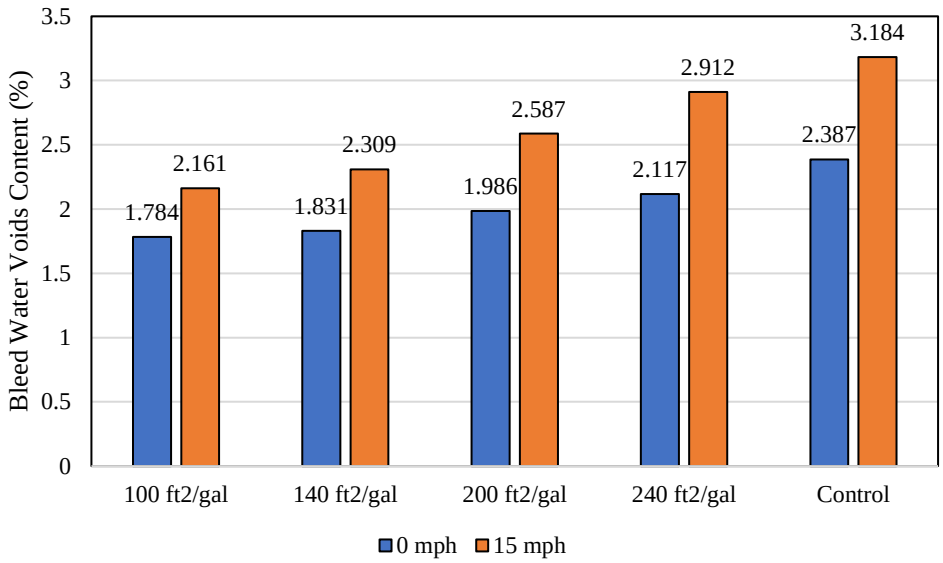

Figure 3-17. Bleed Water Voids Content for Different Application Rates

3.3.4.3 Carbonation

Carbonation started at the surface and diffused deeper into the mortar. All the samples showed carbonation mainly in the vicinity of the surface, which decreased with depth, as shown in Figure 3-18. Carbonation products (calcite) have a tendency to block the surface pores and may lead to a slight decrease in permeability [159]. The occurrence of carbonated areas was more frequent for samples cured at low application rates, making it a viable parameter to assess curing quality.

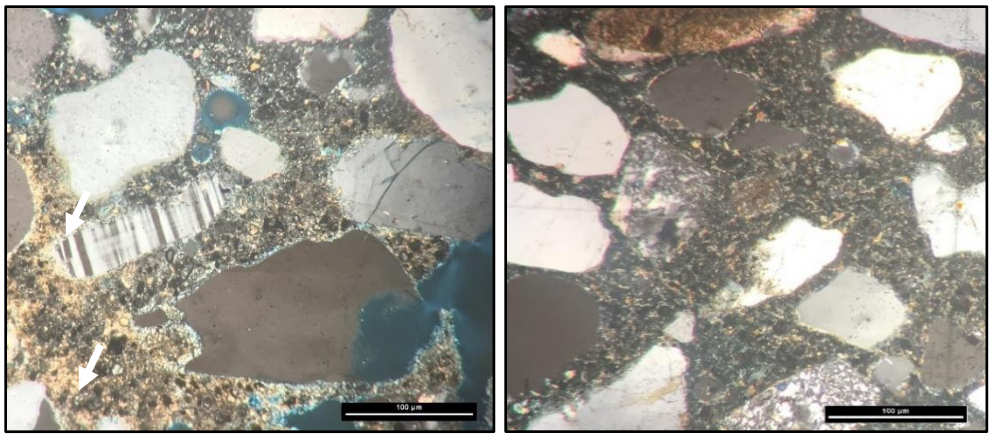

Figure 3-18. Carbonated Surface (Left) vs. Non-Carbonated Interiors (Right)

**Note: The Whole Paste Between Fine Aggregates in the Left Image Is Carbonated.*

3.3.5 Drying Shrinkage

As shown in Figure 3-19, the results indicated the shrinkage potential with elapsed time under different curing conditions. These moisture-induced volume changes were characteristics of mortar moisture-induced behavior. Since drying shrinkage was related to moisture loss from the mortar, the shrinkage was influenced by external factors, such as wind speed and the rate of curing. The length change of each specimen at each age was expressed as millionths and as the percent of the effective gauge length. The higher application rate (100 ft^2/gal) prevented moisture loss and mitigated the adverse effects of shrinkage. Thus, specimens treated accordingly had lower shrinkage trends. The drying shrinkage of mortar specimens was increased by elevating the wind speed level. Shrinkage specimens subjected to a 15 mph wind speed had up to 44% higher shrinkage than those subjected to a no-wind condition. The treated samples had a fewer shrinkage increase under the wind conditions.

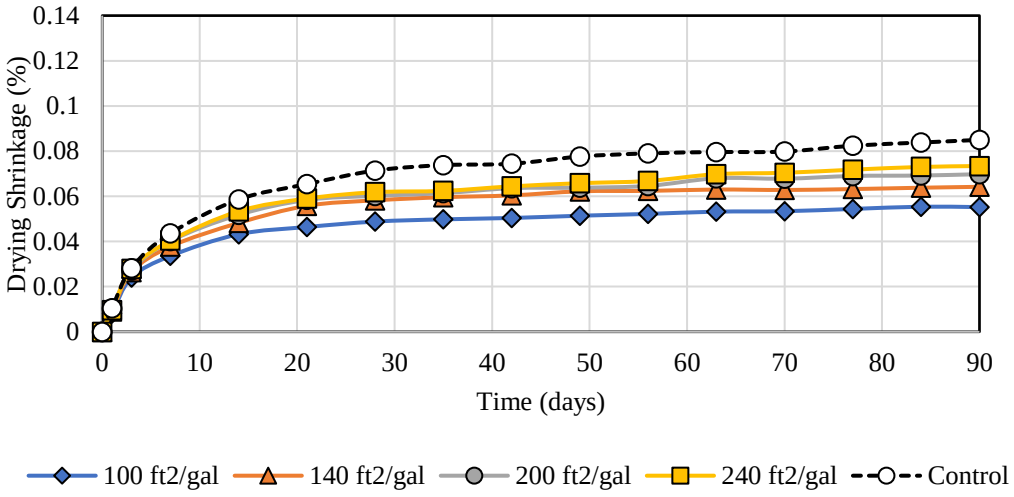

A) Wind Speed = 0 mph

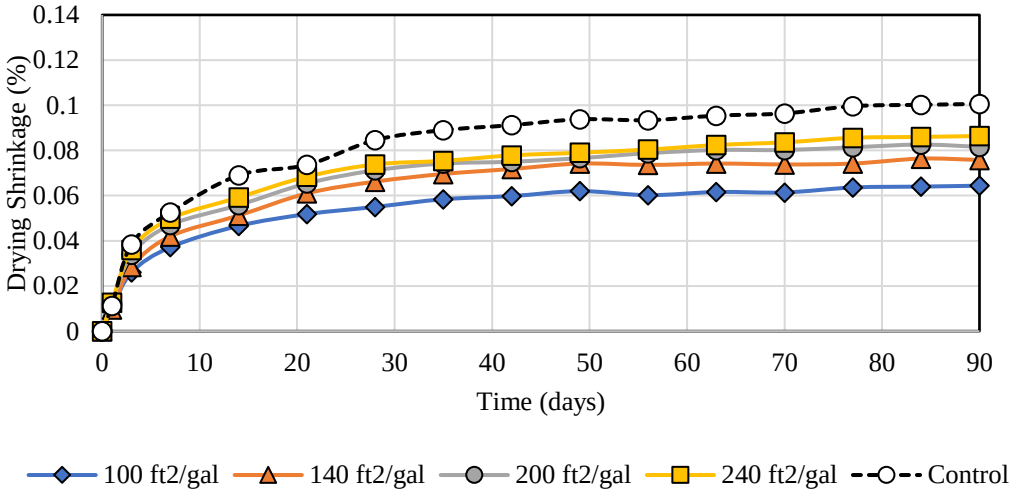

B) Wind Speed = 5 mph

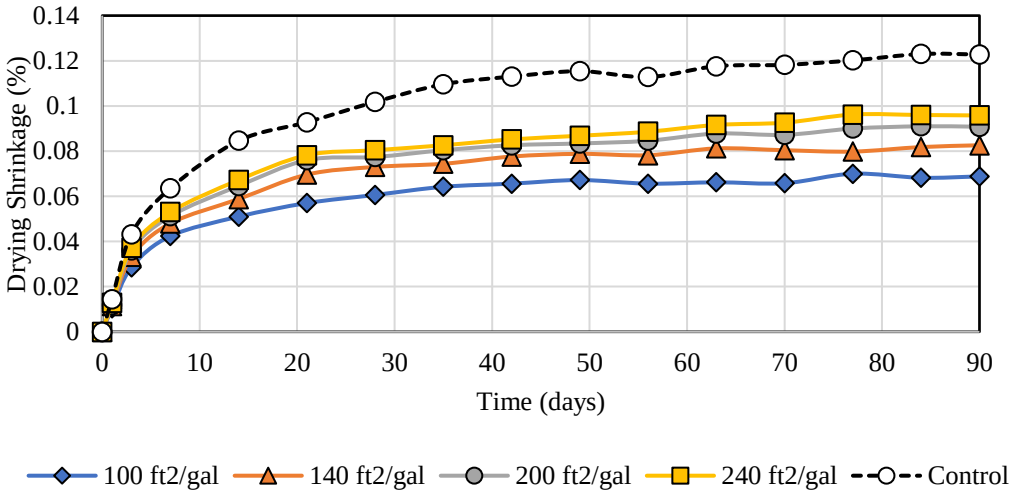

C) Wind Speed = 10 mph

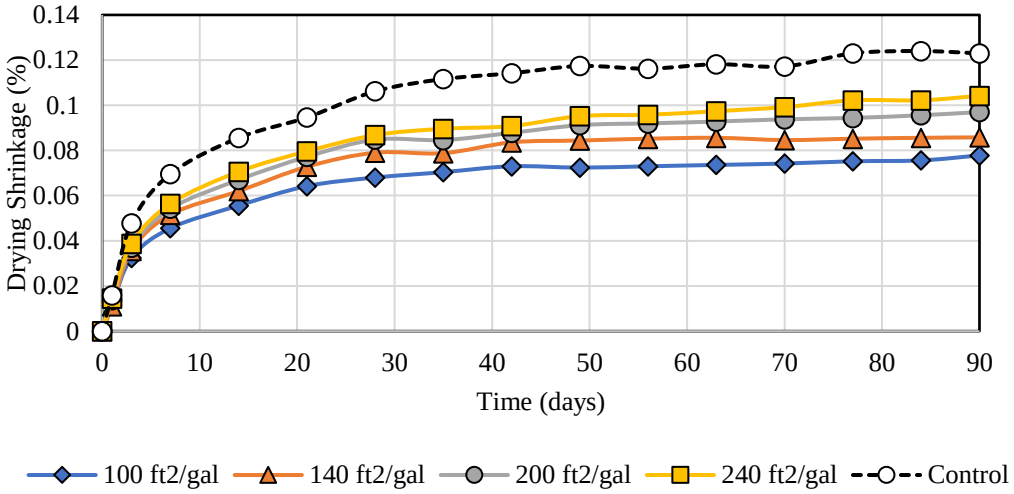

D) Wind Speed = 15 mph

Figure 3-19. Effect of Application Rate and Wind Speed on Drying Shrinkage

3.3.6 EI Measurements

The moisture-based maturity is a parameter that indicates how the curing has progressed based on its relationship to moisture, temperature, age, and strength gain.

Accordingly, the temperature-based maturity is considered conventionally as an index that depends only on time and the temperature. Since this form of maturity is not an effective indicator of the curing quality, a moisture-modified factor was utilized. This adjustment factor was considered for the numerical calculation of the effects of moisture on the equivalent age, as shown in Eq. (3-2):

$$\beta_{RH} = [1 + (a - a \times RH)^b]^{-1} \quad (3\text{-}2)$$

where

RH = the relative humidity of mortar (or concrete),

a = coefficient constant changing from 5 to 7.5, and

b = coefficient constant, which is 1

Bazant [121] suggested *a* = 7.5 and *b* = 4, while Jeong *et al.* [122] found that *a*=5 and *b*=1 had better conformity with data. Thus, the latter suggestion was used in this study. This modification factor was used to modify the maturity index as Eq. (3-3):

$$M_H = \beta_{RH} \sum_0^t (T - T_0)\Delta t = \frac{\sum_0^t (T - T_0)\Delta t}{1 + (5 - 5.RH)} \quad (3\text{-}3)$$

where

M_H = the moisture-modified maturity at age *t* of mortar (or concrete),

t = elapsed time (hours or days),

Δt = time interval (hours or days),

T = the average mortar (or concrete) temperature during Δt (˚C), and

T_0 = datum temperature (usually taken to be -10 ˚C)

The equivalent age is an essential concept, which can be described as Eq. (3-4):

$$t_e = \int_0^t \beta_T \beta_{RH} dt \quad (3\text{-}4)$$

where

t_e = equivalent age (hours or days),

β_T = temperature weighing factor, and

β_{RH} = the moisture modification factor

Eq. (3-4) can be expressed as:

$$t_e = \beta_{RH} \times \sum_0^t \frac{(T-T_0)}{T_{rm}-T_0} \times \Delta t = \frac{1}{1+(5-5\times RH)} \sum_0^t \frac{(T-T_0)}{T_{rm}-T_0} \times \Delta t \quad (3\text{-}5)$$

All data required for calculating the equivalent age of mortar (or concrete) under different curing conditions (sealed, filtered, and ambient) were recorded by using the maturity meter unit. To evaluate the effectiveness of curing compounds, EI was introduced as an index based on the adjusted maturity model, as shown in Eq. (3-6):

$$EI = \frac{t_f - t_a}{t_s - t_a} \quad (3\text{-}6)$$

where

t_f = the equivalent age under filtered curing conditions,

t_s = the equivalent age under sealed curing conditions, and

t_a = the equivalent age under ambient curing conditions

EI is a number between 0 and 1. The better the effectiveness of the curing compound, the longer the relative humidity level in the filtered side remained at a higher level. Therefore, EI was higher under this condition [38]. Usually, the value of EI is calculated for 72 hours under different curing conditions.

The assessed EI values were plotted in Figure 3-20 against time to illustrate its efficacy as an evaluation index. A higher EI indicated a higher moisture-modified maturity on the filtered side of the plate. Relative humidity on the filtered side was influenced by the amount of the applied curing compound and the ambient environment (temperature, moisture, and wind condition).

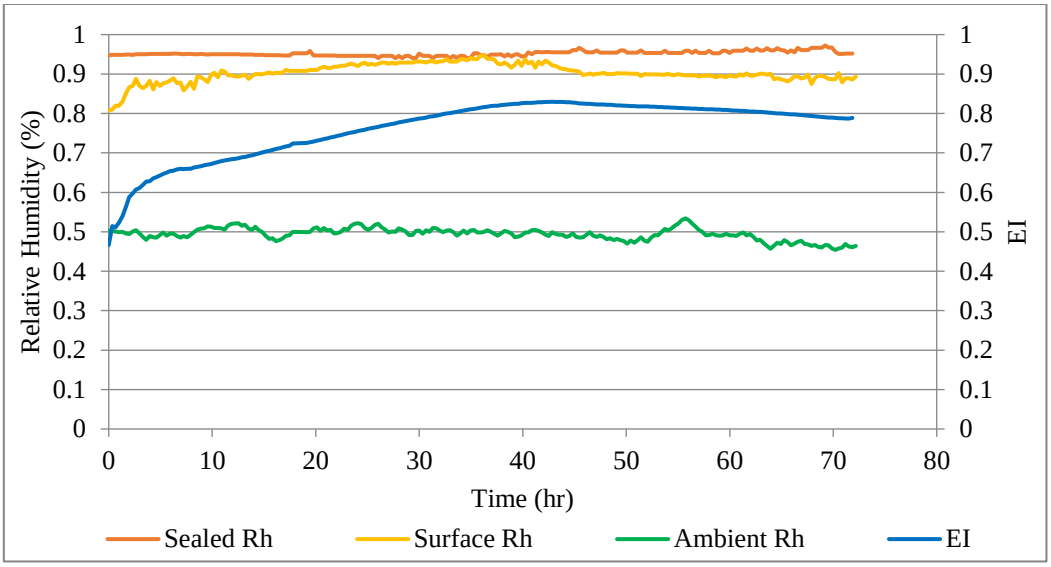

Figure 3-20. Sample of EI Measurement Based on the Updated Maturity Concept

** Note: Curing with An Application Rate of 200 ft²/gal*

The filtered relative humidity started to reduce after a given period, which much depended on the quality of the curing conditions and mixture design. As shown in Figure 3-21, the better the quality of the curing conditions, the longer the relative humidity in the filtered side remained at a high level.

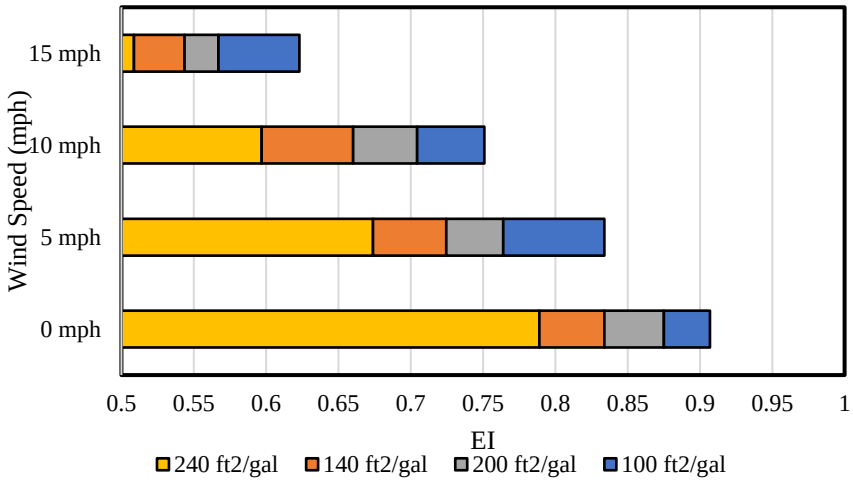

Figure 3-21. EI Measurements Under Different Wind Speed Values

The application rate of 100 ft^2/gal held water at a greater rate than lower application rates where this moisture water was released gradually and resulting in a higher EI. Specimens subjected to wind currents experienced a greater moisture loss and a drop in the filtered relative humidity, yielding a lower EI. As shown in Figure 3-21, the high wind speed (15 mph) affected the EI values for all application rates significantly. Even by using 100 ft^2/gal, which was the highest application rate, the yielded EI was 0.621. However, in the milder conditions, the curing compound did control the moisture loss well.

3.3.7 Dielectric Constant Measurements

At early ages, when the volumetric moisture content in the mortar specimens was high, DC measurements were at their highest levels. After initial setting, the DC measurements decreased over a 72-hour period. The rates of change in DC values for all specimens subjected to wind conditions were higher compared to non-windy conditions due to their sensitivity to the moisture conditions at the surface. In Figure 3-22, the sensitivity of DC measurements to various curing practices is illustrated. Furthermore, trends in the test data indicate that the better the curing practice (the higher application rates), the longer it took for DC to drop to lower levels. Water evaporated from the mortar surface, and DC values decreased accordingly since DC measurements were highly associated with the moisture content at the mortar surface.

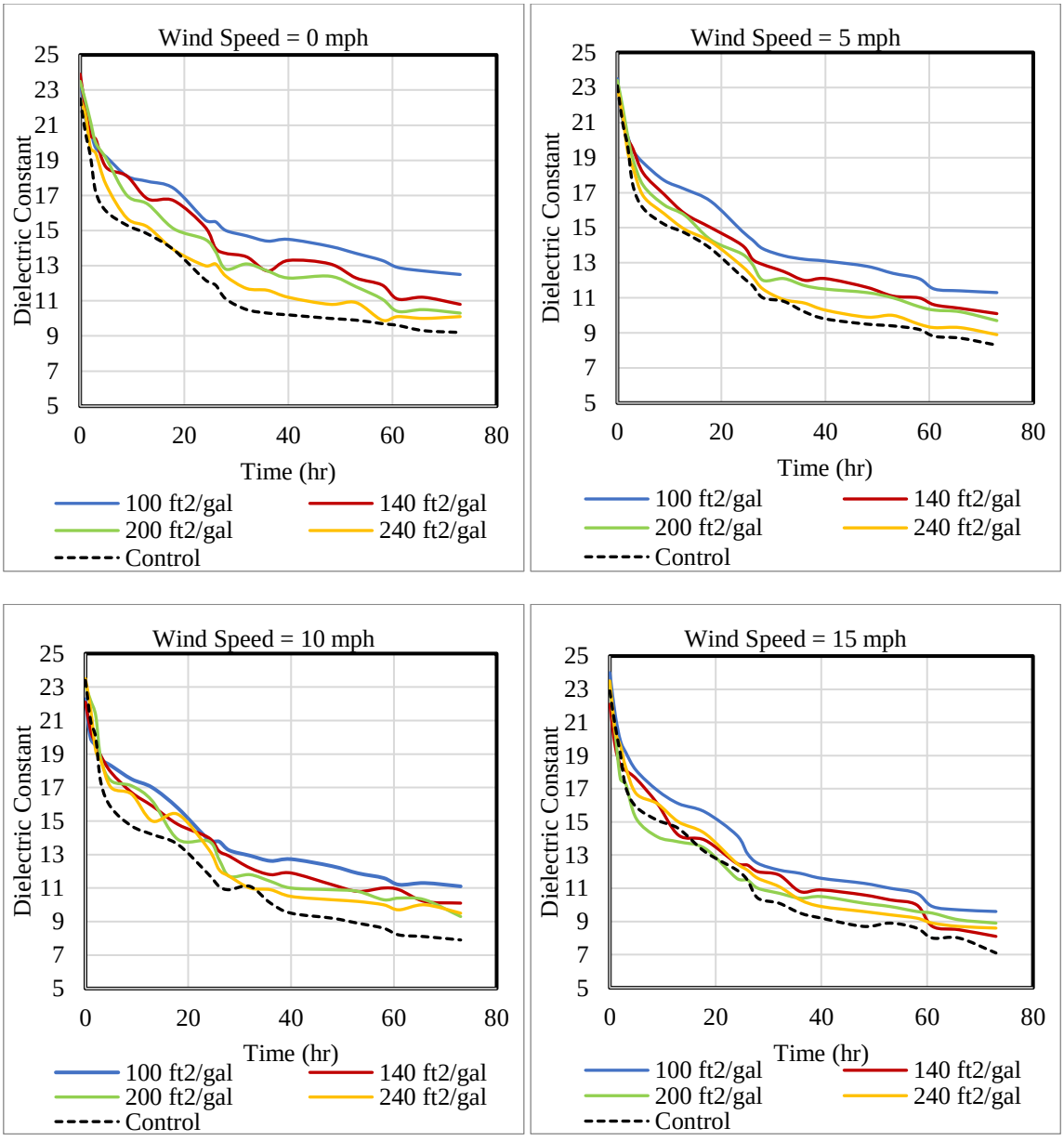

Figure 3-22. DC in Different Application Rates and Wind Speed Levels

A modified Weibull distribution function was used to represent expected trends in DC measurements with time [143]. In probability theory and statistics, the Weibull distribution is a continuous probability distribution. The values of DC measured from the

final set is governed by the probabilistic relationship that is affected by time. The $\overline{DC}$ is the mean value of measurement for each spot and is shown as Eq. (3-7):

$$\overline{DC} = \int_1^\infty p(x)dx \tag{3-7}$$

where $p(x)$ is a probability density function that was an appropriate way to model DC data. Generally, $p(x)$ is a log-normal, Gumbel, or Weibull distribution, which is described below:

$$p(x) = \gamma\lambda(\gamma x)^{\gamma-1} \exp -(\lambda x)^\gamma \tag{3-8}$$

In which the $\gamma\ and\ \lambda$ are shape and scale parameters, respectively. The cumulative probability distribution function $P(x)$, which corresponds to the Weibull probability density function and fits through the data points relating $\overline{DC}$ and time from the final set, is indicated in Eq. (3-9):

$$P(x) = 1 - \ exp[-(\lambda x)^\gamma] \tag{3-9}$$

When γ = 1, the Weibull probability density function reduces to the exponential model, with α=1/λ. Depending on the value of the shape parameter γ, the Weibull model can empirically fit a wide range of data histogram shapes to appropriate mathematical equations. A modified Weibull distribution function in Eq. (3-10) was used to generate regression curves for the DC measurements.

$$\overline{\varepsilon_r} = \tau\left[1 - e^{-\left(\frac{t}{\alpha}\right)^\beta}\right] \tag{3-10}$$

where

$\overline{\varepsilon_r}$ = the average value of dielectric constant,

t = the elapsed time (hours),

τ = the amplifying parameter and the ultimate value of $\overline{\varepsilon_r}$,

α = the scaling factor, and

β = the shape parameter that depends on the decreasing rate

Among the parameters in Eq. (3-10), β is a regression parameter that represents the negative slope of a DC curve over time. Decreasing DC with a lower rate is associated

with a lower value of beta, which shows higher moisture content. Thus, the utility of using the parameter beta to qualify the curing practice is validated. Furthermore, trends in the test data can indicate that the better the curing practice, the longer it takes for DC to drop to lower levels. Also, α is a time parameter related to the duration of curing effectiveness (the greater the quality, the lower the value). This parameter can show how long DC can remain at the higher levels at the initial hours. In other words, α (referred to the residence time of the curing) indicates the degradation trend.

The dielectric constant was used to determine the moisture content at the surface of the mortar or concrete. Thus, the relationship between the dielectric constant and water content provides a rapid method of assessing the evaporation rate under laboratory and field conditions. Water evaporates from the surface, and DC values decrease accordingly since DC measurements are positively associated with moisture content at the concrete or mortar surface. Therefore, the utility of DC measurements can show the moisture retention capability for various methods of curing. Table 3-4 lists the beta regression parameter. The decreasing DC with a lower rate was associated with a lower value of beta, which showed higher moisture contents.

Table 3-4. Beta Parameter from the Adjusted Weibull Distribution Model

	0 mph	**5 mph**	**10 mph**	**15 mph**
100 ft^2/gal	0.435	0.467	0.494	0.534
140 ft^2/gal	0.438	0.441	0.506	0.549
200 ft^2/gal	0.448	0.505	0.525	0.588
240 ft^2/gal	0.471	0.529	0.553	0.644
Control	0.483	0.546	0.593	0.716

3.3.8 Correlation

In the laboratory test program, the main two parameters were the wind speed and the application rate (each had four different levels). The influence of these factors on the results of different test methods should be determined to find an effective procedure in

controlling the curing quality. The initial step is to compare the test results by checking the sensitivity of outcomes to each variable. As all test methods were dependent on the time, all results were compared at a constant time frame, i.e., 72 hours after the spraying application. Contour plots were created with Minitab software [160] to show the relationship between a fitted response and two continuous variables (application rate and wind speed). As the magnitude range of each test method is different, Image J software [161] was used to convert the contours into a 3D plot with the same scale (used interactive 3D Surface Plot Plugin), as shown in Figure 3-23. In these plots, the *x* and *y* axes show the wind speed and the application rate, respectively. The *z*-axis displays the results of the tests. The light color represents the lower values, and the dark color indicates the higher magnitudes. By observing these plots, similar patterns can be found, specifically on tests that were associated with the moisture retention capability.

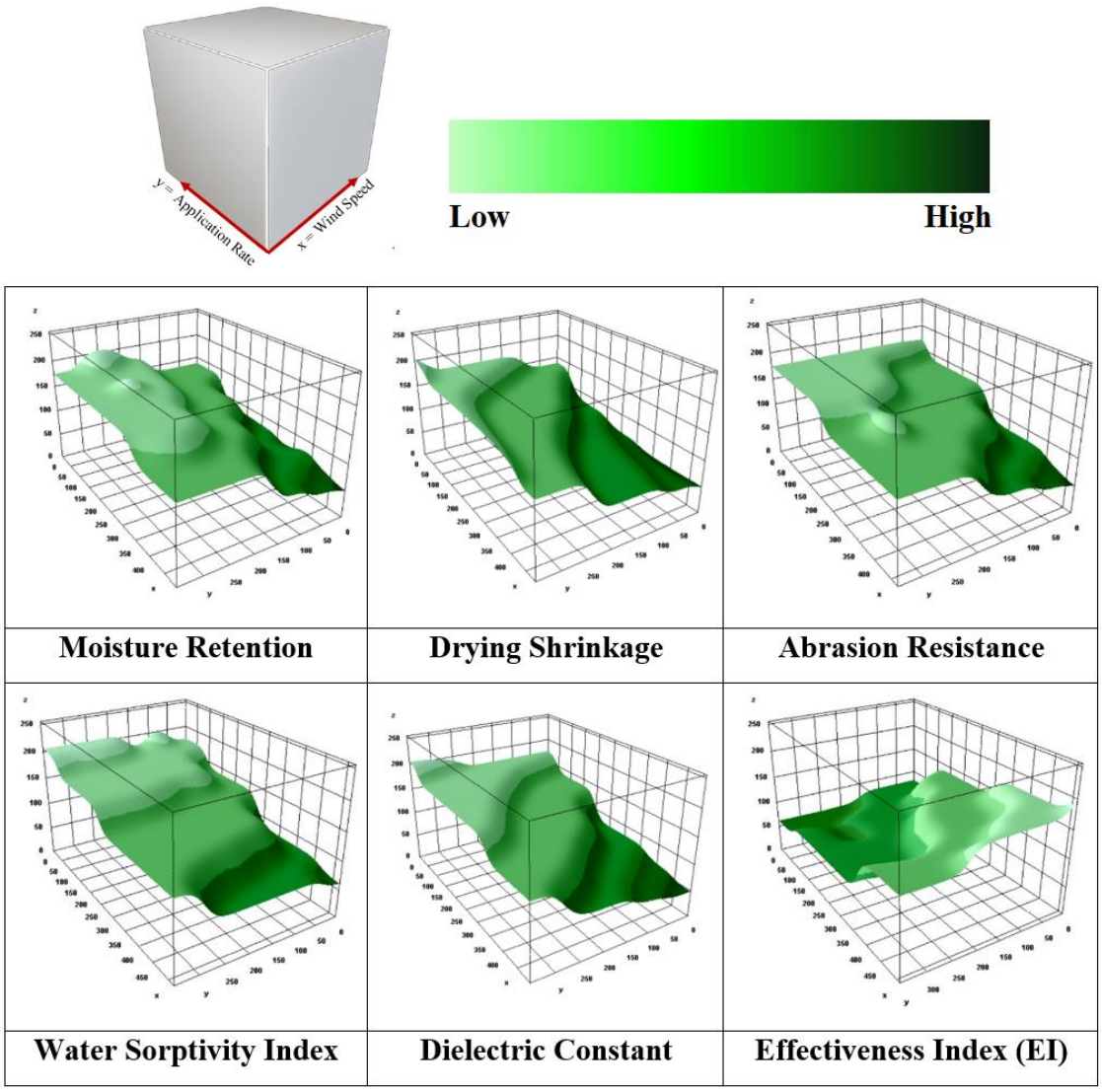

Figure 3-23. The Sensitivity of Test Results to Variables in 3D Plots

In order to validate the utility and verify the efficacy of this procedure, the correlations between indirect and direct measures were conducted using the Pearson coefficient of the correlation function, as shown in Table 3-5. The correlation coefficient (a value between -1 and +1) identified how strongly two variables were related to each other. A correlation coefficient of +1 and -1 indicated a perfect positive and negative

correlation respectively. If a correlation coefficient was greater than 0.8, it was classified as a strong correlation. Whereas a correlation coefficient less than 0.5 would be classified as a weak correlation.

Table 3-5. Correlation Coefficients of Mortar Properties

	Moisture Loss	**Abrasion**	**Sorptivity**	**Interconnected Voids**	**Shrinkage**	**EI**	**DC (β)**
Moisture Loss	1	-	-	-	-	-	-
Abrasion	0.976	1	-	-	-	-	-
Sorptivity	0.980	0.724	1	-	-	-	-
Interconnected Voids	0.932	0.865	0.952	1	-	-	-
Shrinkage	0.975	0.884	0.855	0.926	1	-	-
EI	-0.895	-0.721	-0.871	-0.809	-0.859	1	-
DC (β)	0.964	0.775	0.860	0.928	0.908	-0.853	1

The correlation coefficients between the moisture dependent factors, such as moisture loss, sorptivity, shrinkage, and DC, were more than 0.8, which indicated a strong correlation. The abrasion was not strongly correlated with other mortar properties. The correlations between the direct and indirect measures were strong. The correlation coefficient between EI and the moisture weight loss measurements was -0.895. This correlation was considered as a strong negative relationship. By increasing EI, moisture loss would be decreased. It can be concluded as curing quality improved (as indicated by EI), hydration was improved. This improvement resulted in higher surface strength and a diminution in moisture weight.

3.4 Preliminary Program

The purpose of the preliminary laboratory testing for the field program was to examine the quality of curing methods under different ranges of curing combinations. Curing compounds were selected and tested under different situations to predetermine the rates and types of curing in the slab testing. The variables included the compound's type, application rate, and time of placing. Curing compound performance was evaluated to establish laboratory reference curves that cover the range of curing conditions expected under field testing. The ambient conditions, such as relative humidity and temperature measurements, were used for this evaluation.

3.4.1 Preliminary Test Method

To obtain various levels of curing performance in the test slab, the curing effectiveness was checked for different application rates of WRM-1150 and WRM-1625 curing compounds. The characteristics of these compounds are listed below:

a) WRM-1150 was a water-emulsion and resin-based concrete curing compound that appeared white when wet, but clear when dried.

b) WRM-1625 was a wax-based and white-pigmented concrete curing compound. The white pigment was able to reflect the solar radiation to prevent excessive heat buildup.

Two different application rates were used to check the sensitivity of the curing effectiveness in changing curing conditions. To simulate climate conditions, samples were kept outdoors to be subjected to ambient temperature, relative humidity, and wind (see Figure 3-24).

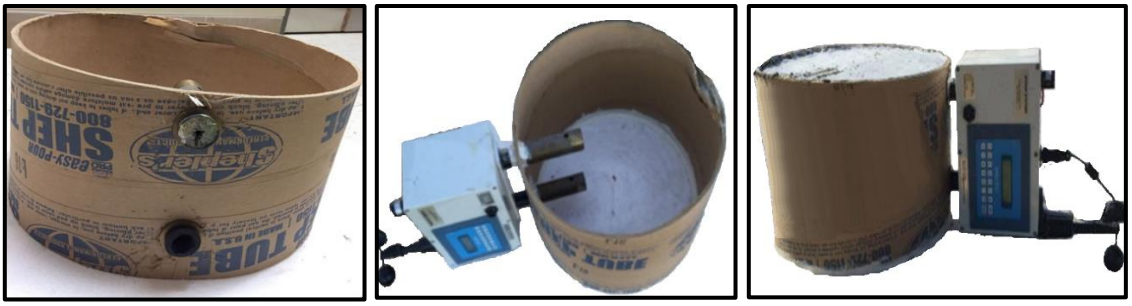

Figure 3-24. Experimental Setup for Preliminary Testing

**Note: The Maturity Meter Device and The Cylinder Mold Before and After Casting*

A summary of the design variables is shown in Table 3-6. The application rates used were 250 ft^2/gal and 180 ft^2/gal to project the lower and higher quality of curing. Since the performance of curing was influenced by the environmental conditions, two separate times (one in the morning and the other in the afternoon) were selected to start the test. Monitoring the curing compounds' effectiveness was carried out with two objectives: (1) to measure the performance under the actual situations, and (2) to find a consistent correlation between laboratory and field results to establish reference curves.

Table 3-6. Different Levels of the Design Parameters

Variable	Level 1	Level 2
Application Rate (ft^2/gal)	180	250
Time of Placement	9 AM	3 PM
Curing Compound Type	WRM-1150	WRM-1625

3.4.2 Preliminary Program Interpretation

In the preliminary testing for the field program, WRM-1150 and WRM-1625 curing compounds were evaluated. EI trends were established under different curing conditions to determine the relationship between the application rate and the evaporative

conditions. After the laboratory program data analysis section, reference curves that covered the range of PEs and EIs expected under the field conditions were established.

3.4.2.1 EI Measurements

Preliminary testing was conducted to assess the effectiveness of the curing compounds with respect to application rate and time of placement. The purpose was to determine the required application rate for the slab placements. Each specimen was tested for a 72-hour period. EI measurements of specimens with two different application rates (180 and 250 ft^2/gal) and two times of placement (9 AM and 3 PM) are shown in Figure 3-25. As displayed in Figure 3-25, the loss of EI with time in the morning placement was higher than the evening placement. Additionally, a high-quality compound (WRM-1625) kept EI at a higher range for a longer period. Figure 3-25 confirmed this fact and indicated that the rate of EI loss in curing compounds with lower quality (WRM-1150) was high. Although the low-quality curing compound (WRM-1150) yielded a lower EI, placing concrete in the evening provided a better quality (i.e., moisture retention capability), at least for this period.

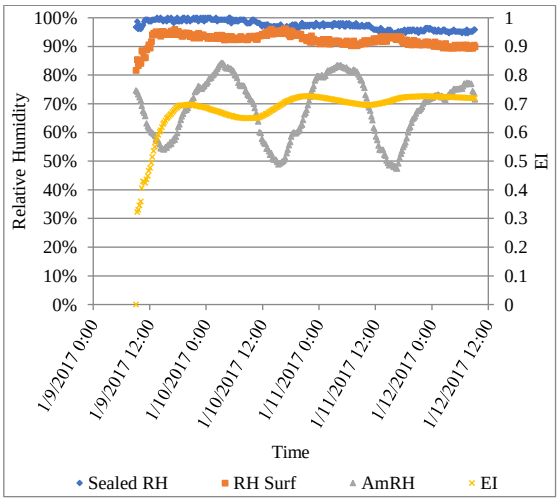

A) WRM-1625 – AR 180 ft^2/gal – 9 AM.

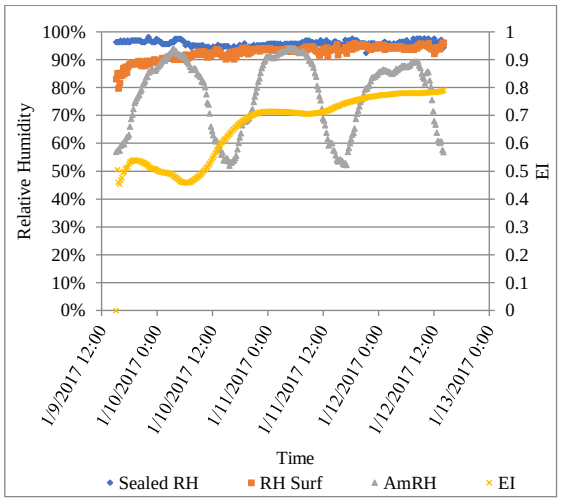

B) WRM-1625 – AR 180 ft^2/gal – 3 PM.

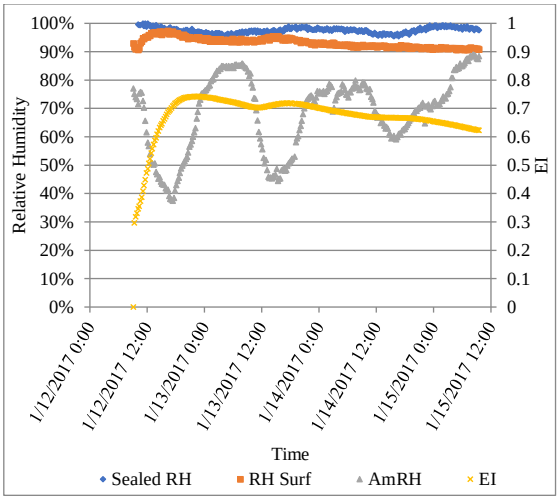

C) WRM-1625 – AR 250 ft^2/gal – 9 AM.

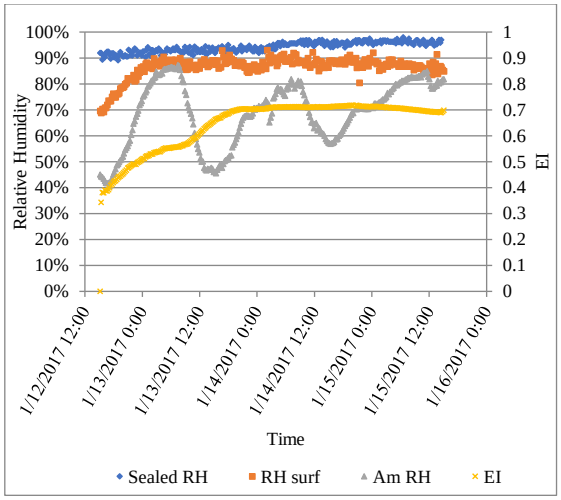

D) WRM-1625 – AR 250 ft^2/gal – 3 PM.

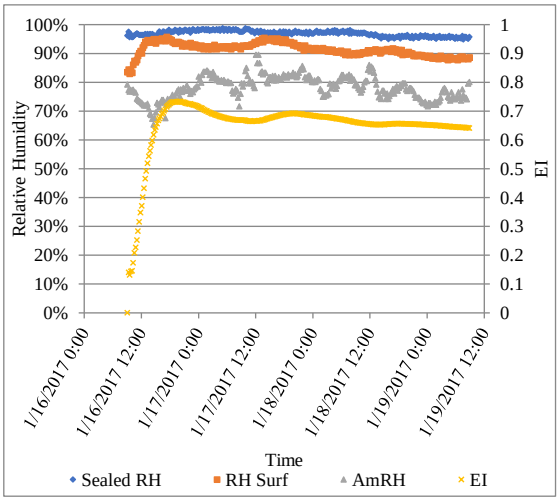

E) WRM-1150 – AR 180 ft^2/gal – 9 AM.

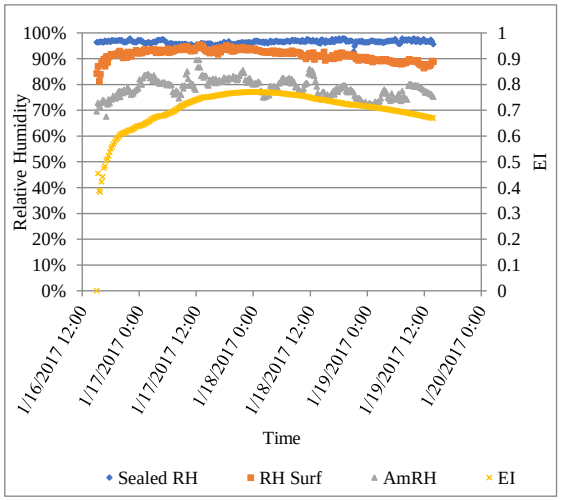

F) WRM-1150 – AR 180 ft^2/gal – 3 PM.

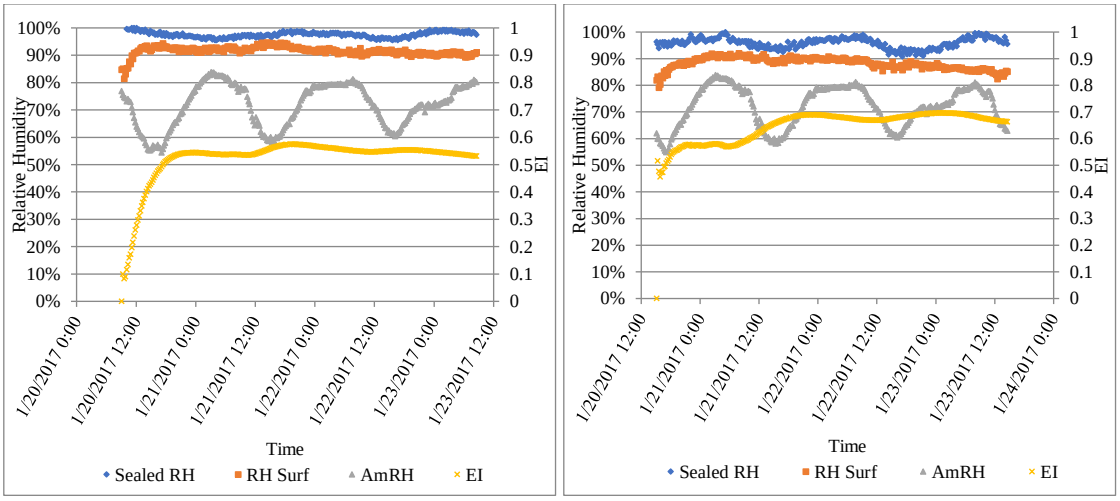

G) WRM-1150 – AR 250 ft²/gal – 9 AM. H) WRM-1150 – AR 250 ft²/gal – 3 PM.

Figure 3-25. EI versus Different Application Rates and Placement Times

3.4.2.2 Dielectric Constant Measurements

DC measurements over time are shown in Figure 3-26. A higher decreasing rate of DC measurement was observed in specimens with WRM-1150 compound and 9 AM placements compared to WRM-1625 and 3 PM placements.

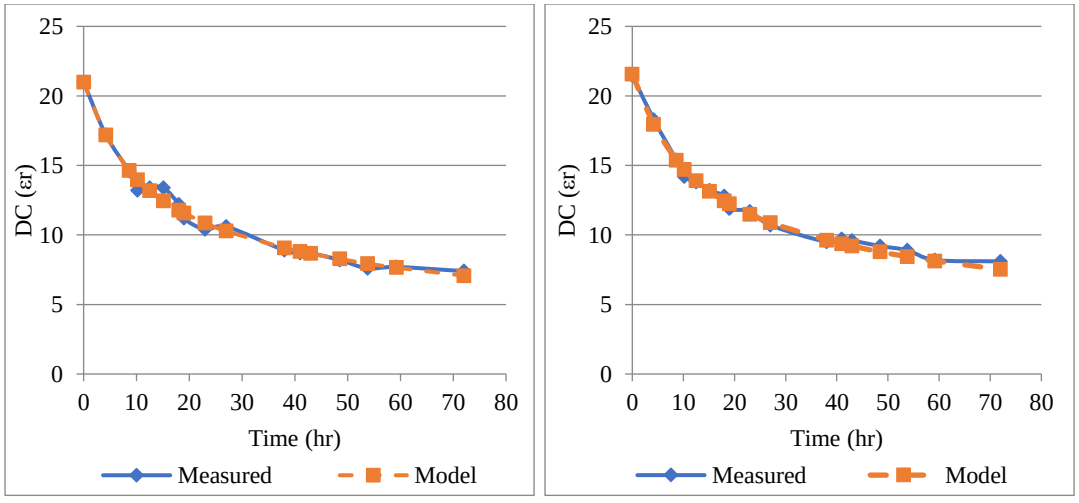

A) WRM-1625 – AR 180 ft²/gal – 9 AM. B) WRM-1625 – AR 180 ft²/gal – 3 PM.

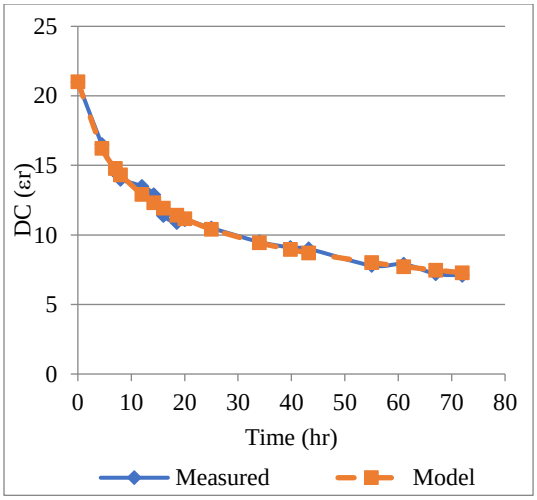

C) WRM-1625 – AR 250 ft^2/gal – 9 AM.

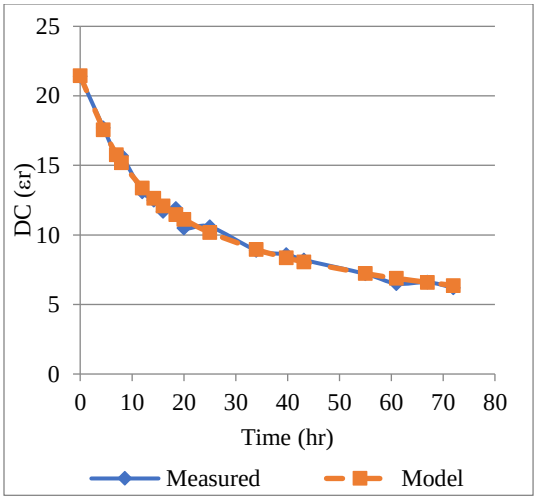

D) WRM-1625 – AR 250 ft^2/gal – 3 PM.

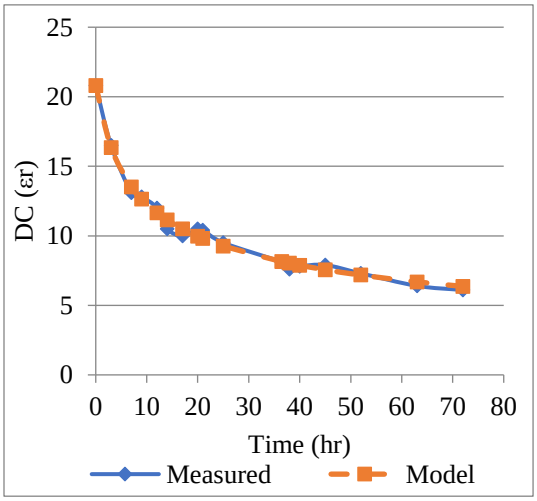

E) WRM-1150 – AR 180 ft^2/gal – 9 AM.

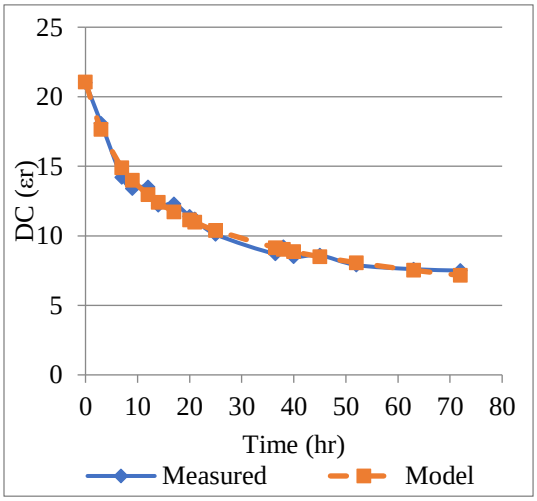

F) WRM-1150 – AR 180 ft^2/gal – 3 PM.

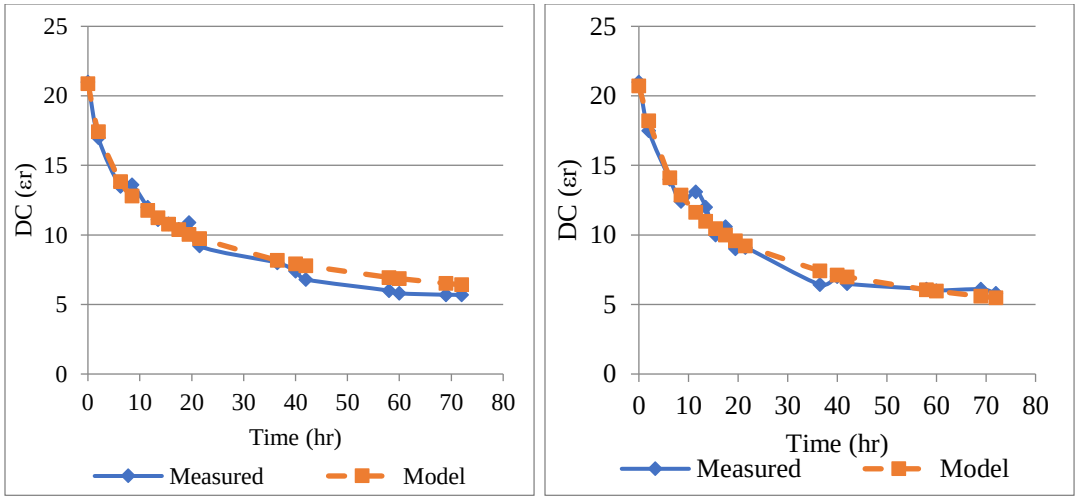

G) WRM-1150 – AR 250 ft^2/gal – 9 AM. H) WRM-1150 – AR 250 ft^2/gal – 3 PM.

Figure 3-26. DC with Different Application Rates and Placement Times

Using compounds with higher application rates resulted in higher EI magnitudes. As expected, WRM-1625 showed a better performance than WRM-1150 under the same conditions. The effects of placement time on EI were investigated. It was observed that EI for evening placements was consistently higher than morning placements irrespective of the application rate of curing. Figure 3-27 shows EI versus β in application rates of 180 ft^2/gal and 250 ft^2/gal. A direct correlation was found between EI and β. Using 180 ft^2/gal as an application rate resulted in higher values for EI.

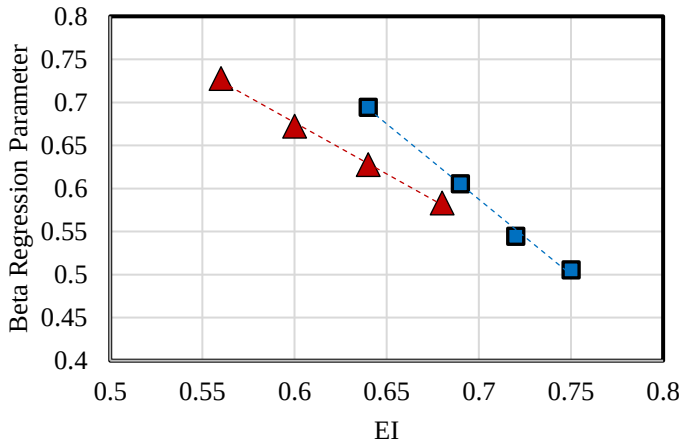

Figure 3-27. EI Measurements vs. Beta in the Preliminary Testing

A higher EI was generally associated with a lower β, which represented a lower rate of DC decreasing. It was required to select appropriate application rates for different curing compounds to have acceptable EI values in the field testing. This preliminary testing was the best opportunity to determine the required curing compound and application rate.

3.4.2.3 Shrinkage Test

The purpose of shrinkage testing was to find the effects of a curing method on the shrinkage rate. Curing compounds limited moisture loss and mitigated the unfavorable effects of drying depending on the type and application rate. This test method showed that the changes in length on the drying of the treated mortar bars were cured with different curing compounds and application rates. Mortar mixtures were prepared in the laboratory under a relative humidity of 50±5%. In Figure 3-28, shrinkage is plotted for WRM-1150 and WRM-1625 curing compounds in two application rates of 180 ft^2/gal and 250 ft^2/gal.

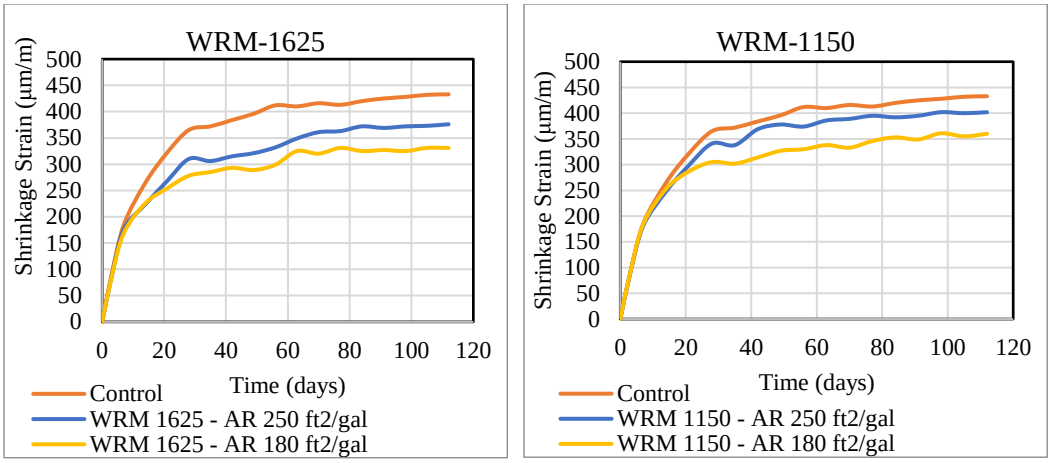

Figure 3-28. Effect of Curing Conditions on Drying Shrinkage

The results showed that the shrinkage potential was influenced by the amount of the curing compound, the elapsed time after the addition of water, and the type of curing compound. Based on Table 3-7, it was found that a direct relationship existed between drying shrinkage, curing compound type, application rate, and β. Better curing methods (such as WRM-1625), or a higher application rate (180 ft^2/gal), resulted in lower drying shrinkage and β.

Table 3-7. Beta vs. Drying Shrinkage in the Preliminary Testing

Curing Methods	Drying Shrinkage (µm/m)	β
WRM-1150 – AR 250 ft^2/gal	402	0.72
WRM-1150 – AR 180 ft^2/gal	360	0.694
WRM-1625 – AR 250 ft^2/gal	376	0.627
WRM-1625 – AR 180 ft^2/gal	331	0.538

3.4.3 Empirical Method for Predictions

To develop the accuracy of the design and meet the project specifications, it is critical not to overlook the impacts of climatic conditions and curing on the concrete

pavement performance. Considering these factors in any project can reduce the deviation from the target performance

3.4.3.1 Ambient Weather Prediction

The combinations of temperature, relative humidity, solar radiation, and wind can change the rate of the water evaporation at the concrete surface during the early-age, which may cause detrimental effects, such as a loss of integrity or delamination [143, 148]. The ACI 308 nomograph was used to characterize the effect of environmental conditions with respect to PE [18]. Figure 3-29 takes into account ambient temperature, relative humidity, concrete temperature, and wind velocity. This nomograph can also be represented by Eq. (3-11):

$$PE = [70^{2.5} - \left(\frac{RH}{100} \times T^{2.5}\right)] \times (1 + 0.4 \times W) \times 0.00001 \quad (3\text{-}11)$$

where

PE = the potential evaporation rate (lb/ft^2/hours),

RH = the ambient relative humidity (%),

T = the ambient temperature (˚F), and

W = the wind velocity (mph)

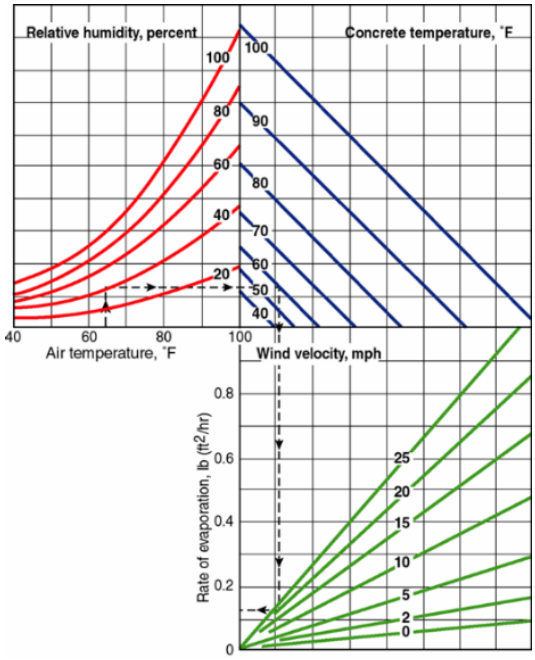

Figure 3-29. PE Nomograph in the ACI 308 Guide

In order to use the reference curves to predict the required application rate of a curing compound under each environmental condition, climatic parameters should be modeled. For this purpose, daily maximum and minimum values of the temperature, relative humidity, and wind speed should be used. These kinds of local climate datasets are available in the archive of global historical weather information. To generate the models, the trigonometric functions were used. Figure 3-30 shows the actual and the predicted data for a field data collection for four days.

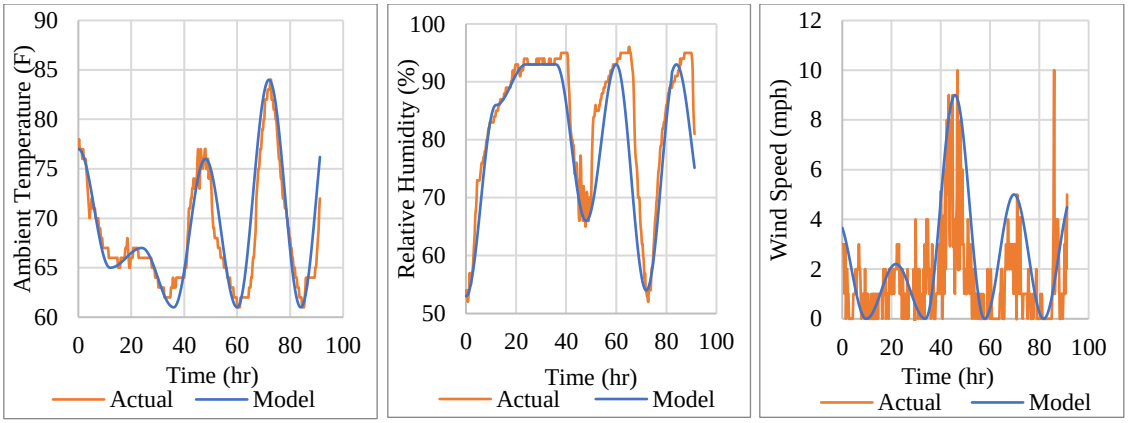

Figure 3-30. Prediction of the Temperature, Relative Humidity, and Wind Speed

3.4.3.2 Curing Effectiveness Laboratory Reference Curves

The preliminary testing data was used to develop a relationship between EI, PE, and the application rate of a given curing compound. The reference curves should provide an empirical method to predict the required application rate under each environmental condition. PE was calculated for the range of conditions that could be created based on those expected in the field. In order to find an appropriate function for this purpose, the suitability of different models was checked with the curve estimation regression statistics in SPSS software [162]. Different curve estimation regression models were checked for each model. The selected parameters were regression coefficients, standard error of the estimate, analysis of variance table, predicted values, residuals, and prediction intervals, as shown in Figure 3-31.

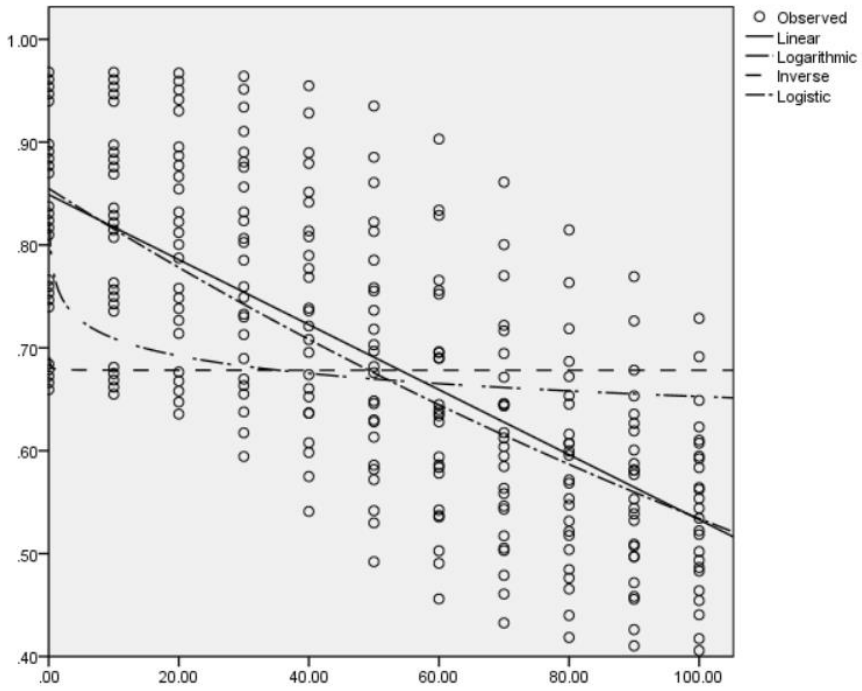

Dependent Variable: E

Equation	Model Summary					Parameter Estimates	
	R Square	F	df1	df2	Sig.	Constant	b1
Linear	.482	254.445	1	273	.000	.849	-.003
Logarithmic	.184	61.408	1	273	.000	.766	-.025
Inverse	.077	22.924	1	273	.000	.678	.001
Logistic	.487	259.172	1	273	.000	1.170	1.005

The independent variable is T.

Figure 3-31. Summary of Curve Estimation Regression Statistics in SPSS

According to the relative goodness-of-fit for these models from the outputs (see Figure 3-31), the logistic model was the best-fit line to the data set. The high R-squared, which provided a reasonable estimate of the strength of the relationship between the model and the response variable, reinforced this choice. Moreover, the higher F value of the overall F-test determined that this relationship was statistically significant.

As the rate of EI changes at different stages, the logistic function or logistic curve was able to model EI versus time. The logistic function is a typical S-shaped curve (sigmoid curve). There are several equations that can generate an inverted S-shaped curve, such as the logistics function in Eq. (3-12). In statistics, the logistic model is usually implemented in the probability models.

$$S(x) = \frac{1}{(1+\exp(-kx))^a} \quad (3\text{-}12)$$

The curing EI can be defined in terms of the AR, PE, and time in the form of Eq. (3-13). The logit function (S-shaped curve) represents a non-linear relationship between EI and elapsed time. The increase in AR, PE, and time would cause EI to decrease.

$$EI(t) = \frac{c}{[1+\exp\left(-t\times\frac{a}{PE}\right)]^b} + \frac{d}{AR} + e \quad (3\text{-}13)$$

where

EI = the effectiveness index for a given curing method,

AR = the application rate (ft^2/gal),

PE = potential evaporation (lb/ft^2/hours),

t = elapsed time (hours), and

a, b, c, d, and *e* = the regression coefficients

In the regression analysis, curve fitting was used to provide the best-fit to the specific curves in the dataset. The regression coefficients for the WRM-1625 curing compound are listed in Table 3-8, which were derived from the SPSS software.

Table 3-8. Regression Coefficients for a Given Curing Compound

Parameter	***a***	***b***	***c***	***d***	***e***
Value	0.0295	146.78	0.157	33.86	0.494

** Note: These Regression Coefficients Are Associated with WRM-1625 Curing Compound*

By knowing PE (ambient conditions) and the desired EI, an appropriate application rate can be determined. The reference curve depends on the curing compound. Figure 3-32 shows the WRM-1625 curing compound, which is a wax-based and white-pigmented compound.

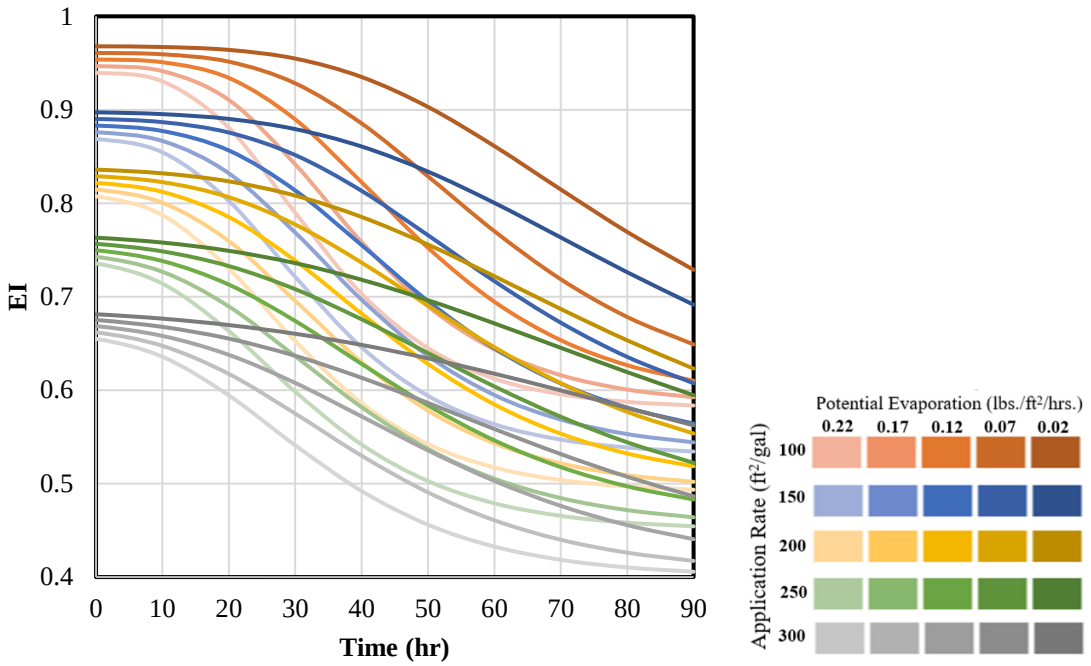

Figure 3-32. Establishing Reference Curves Based on the Preliminary Testing

** Note: These Reference Curves Are Associated with WRM-1625 Curing Compound*

In this reference curve, the expected application rate range to achieve EI between 0.65 and 0.95 was 100 ft^2/gal to 300 ft^2/gal. Using a better curing method (a higher application rate) can keep the relative humidity below the surface (H_f) with fewer changes in its content. Thus, the higher application rates keep EI at a higher range for a longer period. As the curing compound's function is to limit or allow the loss of moisture in the first few hours after placement, the amount of EI is constant due to the bleeding. Depending on the PE, this period can be shorter. In the higher PE values, which represents more severe conditions for curing, EI dropped with a faster rate due to the excessive moisture loss at the early-age.

3.4.3.3 Effect of Curing and Placement Time on the Set Gradient

Moisture evaporates from the exposed surface of concrete, and it makes concrete dry. Greater moisture gradients inside the concrete near the surface are created under severe conditions with higher rates of evaporation. Using a proper curing method can keep the relative humidity below the surface with less changes in its content. The rate of evaporation (J) can be expressed (see Eq. 3-14) by a model suggested by Bazant and Najjar [163] under laboratory conditions (solar effects are not included):

$$J = B\ ln\frac{H_f}{H_a} \tag{3-14}$$

where

B = the surface moisture emissivity (kg/m^2/hr),

H_f = the filtered (on the surface) relative humidity, and

H_a = the ambient relative humidity

The surface moisture emissivity B is a parameter related to the given curing quality and can be formulized at the surface of the pavement with respect to the moisture diffusivity (D^*). The diffusivity governs moisture movement considering the time it takes for it to pass through concrete as Eq. (3-15):

$$\frac{\partial H}{\partial t} = D^* \frac{\partial^2 H}{\partial x^2} + K\frac{\partial T}{\partial t} \tag{3-15}$$

Here, the moisture diffusion is defined according to the thermodynamic equilibrium. A similar expression is used to model the transport of moisture through the interior portions of the slab concrete, but this includes the $\frac{\partial H_s}{\partial t}$ autogenous hydration term and the parameter D as the governing material property. K parameter is the change in relative humidity (H) with dry bulb temperature, and t is time. D can be back-calculated using the data collected from the maturity meter unit as Eq. (3-16):

$$D = \frac{\frac{\partial H}{\partial t}}{\frac{\partial^2 H}{\partial x^2}} \tag{3-16}$$

The curing membrane diffusivity (D^*) can be characterized with respect to the surface moisture emissivity (*B*). *B* factor can readily be found from laboratory weight loss and relative humidity data. This factor serves as a basic material parameter of the curing conditions provided by the curing membrane. Then, the values of *B* over the hardening period are generated, as shown in Eq. (3-17):

$$J = -c.grad(H) \tag{3-17}$$

Thus:

$$B\ ln\frac{H_f}{H_a} = -c(grad(H)) \tag{3-18}$$

where *c* is permeability (kg/m/hr) of the curing membrane:

$$c(grad\ (H)) = c\frac{\Delta H}{\Delta x} = B(Ln(H_a) - \ln(H_f)) \tag{3-19}$$

$$\Delta H = H_f - H_a \tag{3-20}$$

D^* parameter was defined with respect to $\frac{\partial w}{\partial h}$, which was also found from the laboratory weight loss relative humidity testing data. The relative humidity (*H*) data was calculated from the dry bulb (*T*) and dew point (T_{dp}) temperature data using the following expression [143]:

$$H = exp\left[\left(\frac{17.502\ T_{dp}}{240.97+T_{dp}}\right) - \left(\frac{17.502\ T}{240.97+T}\right)\right] \tag{3-21}$$

The changes in the relative humidity due to autogenous hydration ∂H_s were characterized as:

$$\partial H_s = \frac{a+\alpha}{b} \tag{3-22}$$

where *a* and *b* depend on the hydration factors (e.g. w/c and curing temperature), and α is the degree of hydration.

H_f is the unknown parameter that needs to figure the evaporation rate. Based on the previous studies, H_f in the boundary condition formulations was assumed to be equivalent to the ambient relative humidity [164, 165]. However, the curing compound

membrane (type and application rate) may change H_f. Thus, H_f can be defined in accordance with the EI concept, which is a function of the curing treatment method. Based on the Nurse–Saul maturity function, which was discussed Eq. (3-2) to Eq. (3-6), H_f can be written as Eq. (3-23) :

$$t_f = EI \times (t_s - t_a) + t_a \tag{3-23}$$

$$t_{f_i} = EI_i \times \left(t_{s_i} - t_{a_i}\right) + t_{a_i} = \beta_{H_i} \frac{(T_i - T_0)}{T_R - T_0} \times \Delta t + t_{f_{i-1}} = \frac{\frac{(T_i - T_0)}{T_R - T_0} \times \Delta t}{1 + \left(5 - 5 \times H_f\right)} + t_{f_{i-1}} \tag{3-24}$$

$$H_{f_i} = \frac{6}{5} - \frac{\frac{(T_i - T_0)}{T_R - T_0} \times \Delta t}{5[EI_i \times \left(t_{s_i} - t_{a_i}\right) + t_{a_i} - t_{f_{i-1}}]} \tag{3-25}$$

i = number of the time interval (hours),

H_{f_i} = the filtered relative humidity at the i_{th} time interval,

t_{s_i} = the equivalent age of concrete in the sealed chamber at the i_{th} time (hours),

$t_{f_{i-1}}$ = the equivalent age of concrete in the filtered chamber at the ($i_{\text{th}} - 1$) time (hours),

t_{a_i} = the ambient equivalent age of the concrete at the i_{th} time (hours),

EI_i = EI at the i_{th} time interval, and

T_i = the concrete surface temperature at the i_{th} time interval (˚C)

Thus, H_f (i.e., a function of curing practice, EI) can be used in the heat and moisture models at the pavement boundaries to determine the set gradient. Besides the curing method and ambient conditions, the time of placement should be considered as an input into the set gradient determination process. Table 3-9 provides a list of variables and inputs to predict the set gradient using heat and moisture transfer functions.

Table 3-9. Inputs for the Set Determination

Concrete Properties	Climatic Conditions	Curing Conditions
Thermal diffusivity (m^2/day)	Ambient temperature range (˚C)	Placement temperature (˚C)
Hygrothermic coefficient (1/˚C)	Ambient humidity range (%)	Placement time (hr)
Moisture diffusivity (m^2/day)	Wind speed range (m/s)	Curing compound
Stefan-Boltzmann constant ($W/m^2/°K^4$)	Daytime/Nighttime (hr)	Application rate (ft^2/gal)
Surface heat absorptivity		EI
Surface heat emissivity		
Specific heat (Ws/Kg˚C)		
Density (g/cm^3)		

Figure 3-33 displays an example of using H_f to determine the set gradient for different EI values (50%-90%) with the time of placement (4 AM-10 PM). The ambient temperature and relative humidity ranges were 14 ˚C-32 ˚C and 35%-94%, respectively. Figure 3-33 shows that increasing the level of EI (i.e., increasing the quality of the curing method) decreased the set gradient irrespective of the time of placement. The largest positive gradient would be during the daytime as the high ambient temperatures and solar radiation increase the rate of hydration compared to paving in the nighttime. Thus, the optimization of the set gradient is feasible if a proper curing treatment and time of placement are selected. As the set gradient depends on the degree of hydration, the linear temperature gradient is calculated based on the hydration development (in percentage). The further discussions come in Chapter 5.

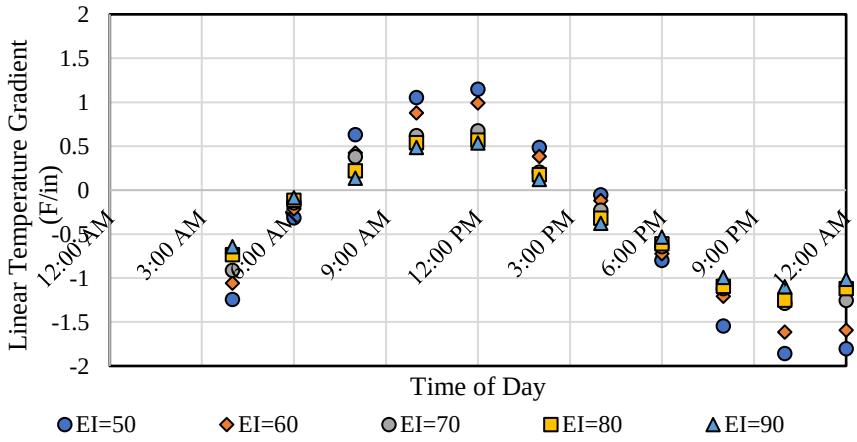

Figure 3-33. Curing Quality and Time of Placement Effects on the Set Gradient

3.5 Summary

This chapter highlighted that the assessment of the quality of curing was undertaken via several test methods in the laboratory. Curing quality was varied by using different application rates to generate different evaporation rates. Moisture loss and abrasion resistance tests were conducted on the surface of cured mortar specimens. Surface-related properties, such as abrasion resistance, surface porosity, and drying shrinkage, were conducted as direct measures of quality. Also, EI (subsequently discussed) and surface DC measurements were taken and applied as indirect measures of effectiveness of the applied curing compounds. Models related to EI and dielectric constant were discussed based on maturity and conductivity, respectively. Laboratory test results subsequently showed that the direct measures had a significant correlation (using the Pearson coefficient of the correlation function) with the indirect methods, EI and DC. Consequently, the mortar mixture characteristics, as well as the curing compound's application rate and the ambient conditions, affected these test results. After the laboratory program data analysis, laboratory reference curves that cover the range of PEs and EIs expected under field conditions were established. The preliminary laboratory testing for the field program was introduced to predetermine the rates and types of curing in the slab testing.

4 FIELD TESTING ON CURING EFFECTIVENESS EVALUATION

This chapter reports test methods from two separate field trials of slab placements to represent different curing conditions and placement times. One set was placed in February (Phase I), and the other was placed in October (Phase II). Figure 4-1 shows the field experiment programs as a flowchart. Several instruments were installed inside the concrete slabs. Each slab was monitored for strain, temperature, relative humidity, displacement, strength gain, and drying shrinkage. One of the key purposes of slab monitoring was to use these data collections in order to assess the quality of curing provided for each slab. Another objective of the slab monitoring was to collect data to assess the slab setting characteristics. The analysis of the collected data mainly focused on early-age slab movements. Results of the setting time, the strain, the corner displacement, the free shrinkage, the EI measurements, the dielectric measurements, the relative humidity profiles, and the thermal gradient profiles are presented in this chapter. These results are used to relate the slab movement to the curing method and time of placement. At the end of this chapter, the use of GPR as a practical approach to assess the curing effectiveness is discussed. A GPR was implemented in three paving projects after the placement of concrete. This section shows how an extensive data set can be done quickly at various places on concrete pavements. The objective is to monitor the consistency of the spraying application and find the non-uniform patterns. In this part, repeatability, dielectric measurements, and uniformity are explained.

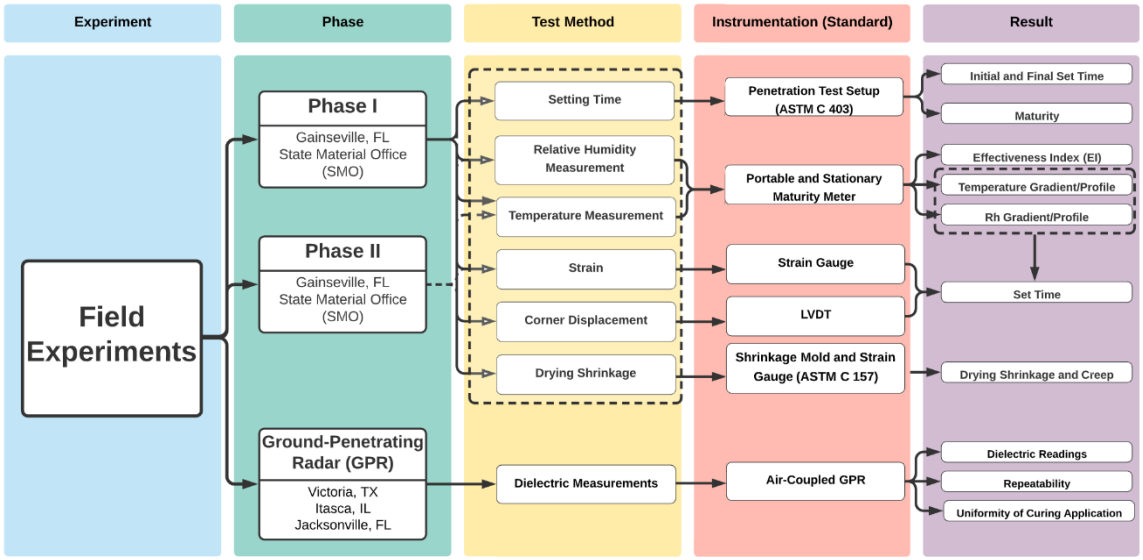

Figure 4-1. Field Experiments Flowchart

4.1 Field Testing and Data Collection Program

Two field investigations were conducted to study the behavior of early-age concrete with respect to variable curing practices and different placement times. The details of these data collection programs are described in the following paragraphs.

4.1.1 Investigation Approach

Different curing compounds with various application rates were used in each phase. Also, several times of placement was considered for the slabs. The details of the curing application and concrete placement are explained through the following sections.

4.1.1.1 Phase I Program

As shown in Figure 4-2, there were four 12×15 ft slabs: three being 10 inches and one being 7 inches thick. In order to create different curing conditions, two curing compound types were selected (WRM-1150 and WRM-1625). Also, two application rates

at different placement times were used to assess the curing method. One slab was left uncured to control the effects of curing practices. A summary of the application rates, curing compounds, and placement times is presented in Table 4-1.

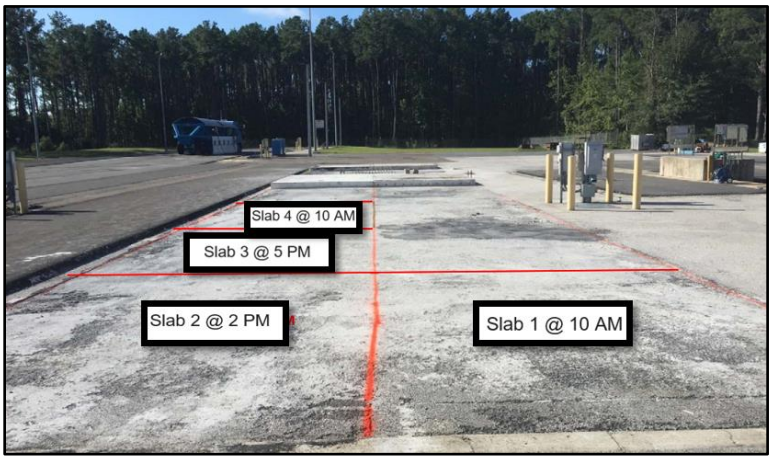

Figure 4-2. Four Test Slab Locations with Time of Placement in Phase I

Table 4-1. Summary of Application Rates and Curing Compounds in Phase I

	Thickness (inch)	Curing Compound	Application Rate (ft^2/gal)	Placement Time
Slab 1	7	WRM-1150*	250	10:00
Slab 2	10	WRM-1625**	250	14:00
Slab 3	10	WRM-1625	180	17:00
Slab 4	10	None	None	10:00

** Non-pigmented and resin-based (hydrocarbon)*
*** White-pigmented and wax-based*

4.1.1.2 Phase II Program

There were three 12×15 ft slabs: two being 10 inches and the other 7 inches thick. These slabs were placed on an asphalt layer at different times, as shown in Figure 4-3. The summary of the curing program is shown in Table 4-2. In each slab, the slump, air

percentages, mix temperatures, and unit weights were measured, as shown in Table 4-3. All slabs were cured with the WRM-1625 compound.

Figure 4-3. Preparing Three Slabs Setups and Instrumentations in Phase II

Table 4-2. Summary of Used Application Rates and Setting Results in Phase II

	Thickness (inch)	Curing Compound	Application Rate (ft^2/gal)	Placement Time
Slab 1	7	WRM-1625	180	10:00
Slab 2	10	WRM-1625	180	13:45
Slab 3	10	WRM-1625	250	17:20

Table 4-3. Summary of Mix Designs Specifications in Phase II

	Slump (inch)	Air (%)	Mix Temperature (˚F)	Unit Weight (lb/ft^3)
Slab 1	2 3/4	2.9	85	35.5
Slab 2	7 3/4	3.1	89	43.7
Slab 3	3 3/4	3	88	34.9

Preliminary laboratory testing for the field program and reference curves were used to determine the rates and types of curing in the slab testing. The target set gradient for Slab 2 in Phase II placement was -10 ˚F, which is the assumed set gradient used in the

Pavement ME software. This number is the nationwide average for the equivalent linear temperature difference from top to bottom of the slab for all climatic regions. Therefore, by considering the probable ambient conditions, the application rate for each compound was established to facilitate the prediction of the set in any given placement [166]. To replicate the effect of weather, the expected values of PE were used. One of the variables was the time of placing. The effects of the placement time on EI, the final set, and the gradients were investigated in the preliminary laboratory testing.

4.1.2 Concrete Slab Placing

The concrete slabs were placed on a structural asphalt concrete course type SP-12.5. The concrete mixture was made with ½ inches nominal maximum size aggregate. The slab concrete was set with wooden forms and braced with 2×4 stakes every 4 ft. along the form boards for support. The stakes kept the top of the forms from bending outward, as shown in Figure 4-4.

Figure 4-4. Wooden Leveling Forms in Concrete Placement

As the concrete was placed, the excess concrete was struck-off along the top of the form boards with a straight and smooth screed board in several passes. Immediately after screeding to remove surface marks and filling in low spots to create a flat and level surface, the concrete was bull-floated. Then, bleed water was formed on top of the concrete surface. As explained in Chapter 2, the curing compounds should be sprayed when the sheen on concrete pavement surface has disappeared. Similar to time and the application rate of the curing compound, the uniformity of the application was important as it was strongly affected by the spraying method. As shown in Figure 4-5, a hand sprayer (consisting of a pump, tank, and pressure regulator) was used to spray the curing compound uniformly. The pressure to apply the curing was determined by the adjustment of the agitator control valve, the pressure regulator, the capacity of the pump, and the pressure loss at the nozzle. To determine the specified application rate (ft^2/gal), the associated amount of curing compound (gal) needed to be uniformly applied to a given surface area (ft^2) consistent with the application rate.

Figure 4-5. Application of the Compound by Using a Hand Spraying Machine

4.1.3 Curing Effectiveness Measurement

The maturity meter unit was installed to measure the temperature and moisture data in the concrete slabs. Soon after the placement of the concrete, measurements were started. This data set was collected to allow for the examination of how EI was tied to the set of the concrete slabs. The relative humidity and temperature data were monitored on all four slabs for the moisture-based maturity computations. Furthermore, data on environmental conditions was collected throughout the entirety of the experiment. After the concrete slab surface operations had been finished, the top portion of the curing plate was placed on the concrete surface with a thin mortar layer on the filtered side of the plate, as shown in Figure 4-6. Once the curing compound was sprayed on the surface of the slab, a bare area was created when the top portion was removed. This part of the curing plate was subsequently fixed on the base plate and put back over the bare spot previously created on the slab surface. The maturity meter unit was then placed on the curing base plate for data collection. Moreover, the dielectric measurement was started after the concrete final setting to extend the curing effectiveness evaluation over a broader area of pavements rather than at a single position.

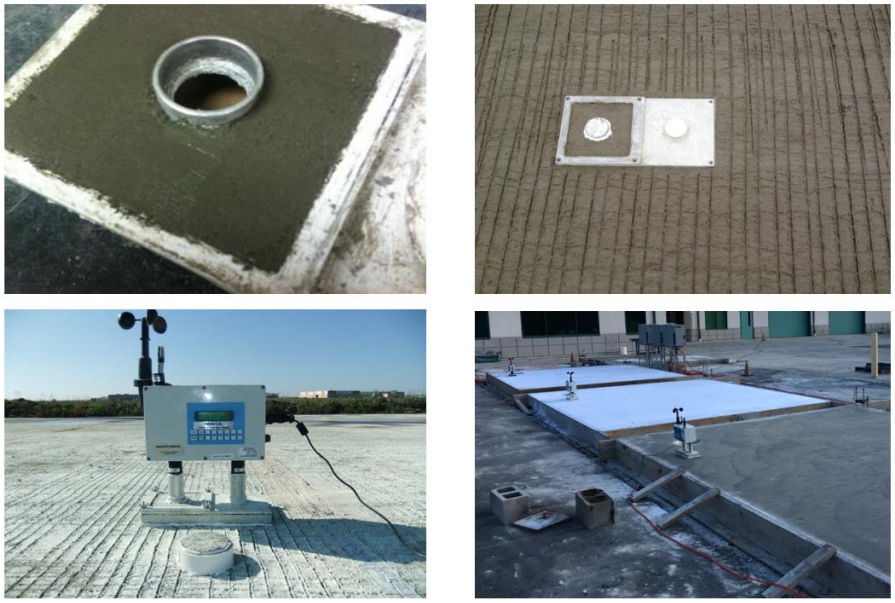

Figure 4-6. Curing Plate Components and Setup of the Maturity Meter Unit

In Phase II, two brass sampling casings were placed in the concrete slab to measure temperature and relative humidity data at specific depths (¼ inches and 3¼ inches). Every casing had several holes at each depth. The first sampling chamber (i.e., ¼ inches depth) was configured to measure the dry bulb and dew point temperatures below the membrane formed by the curing compound. This measurement represented the vapor pressure at the surface of the concrete just below the curing medium. The second sensor was placed deeper in the pavement section (i.e., 3¼ inches depth) to collect the temperature and relative humidity levels closer to a fully sealed condition, as shown in Figure 4-7. Assessment of the effectiveness of a curing compound was conducted based on the comparison between these conditions, i.e., the sealed conditions and the conditions under the curing medium [166, 167].

Figure 4-7. New Approach in Measuring Curing Effectiveness from Slab Surface

As shown in Figure 4-8, a template was used to keep the distance between two casings constant. Additionally, a slide hammer was attached to this template for pushing casings into concrete. This methodology helped place the brass casings in the concrete slabs efficiently. Not only did the brass casing spacing not change, but the casings did not tilt in a downward pivoting movement.

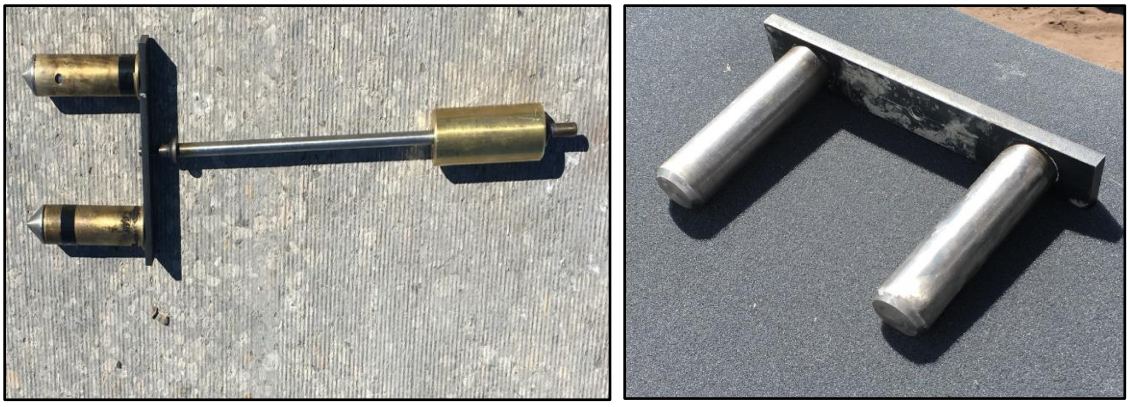

Figure 4-8. The Slide Hammer with Template for Inserting Brass Casings

4.1.4 Dielectric Measurements

The dielectric constant of the concrete slabs was measured by a percometer at specific time interval to indicate the free moisture content on the concrete surface (see Figure 4-9). The value of the dielectric constant was affected directly by the ambient conditions and the curing practice.

Figure 4-9. DC Measurements at the Field Test Program with a Percometer

4.1.5 Data Acquisitions and Sensors

Several instruments and sensors were used on the slabs to collect data about the set behaviors of concrete slabs under different curing conditions. This data set was used to validate the findings from the previous calibration work. Three types of sensors were placed inside the concrete slabs: vibrating wire (VW) strain gauges for the transversal and longitudinal strains in the surface, linear variable differential transformer (LVDT) sensors for vertical displacement of the slabs' corners, and thermocouples for the temperature inside the pavement at different depths. Figure 4-10 shows the schematic drawing of these sensors on the slabs with 7 inches and 10 inches thicknesses in both Phase I and Phase II.

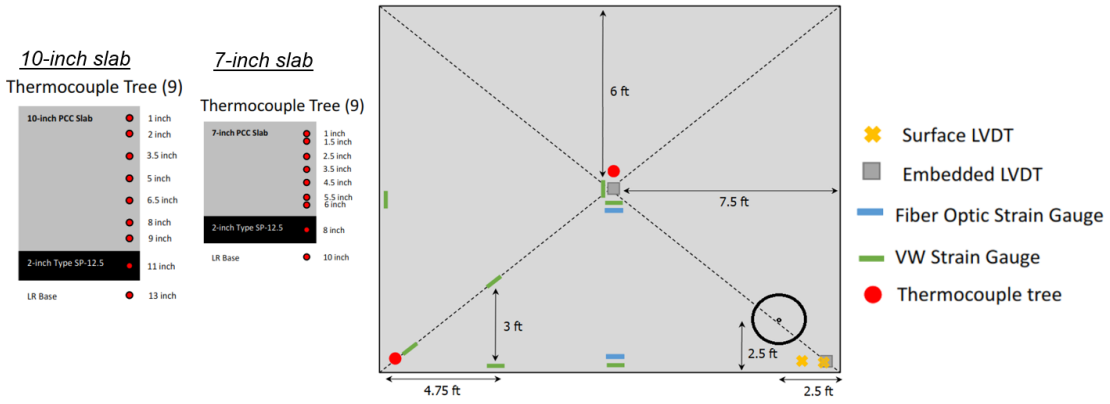

A) Phase I

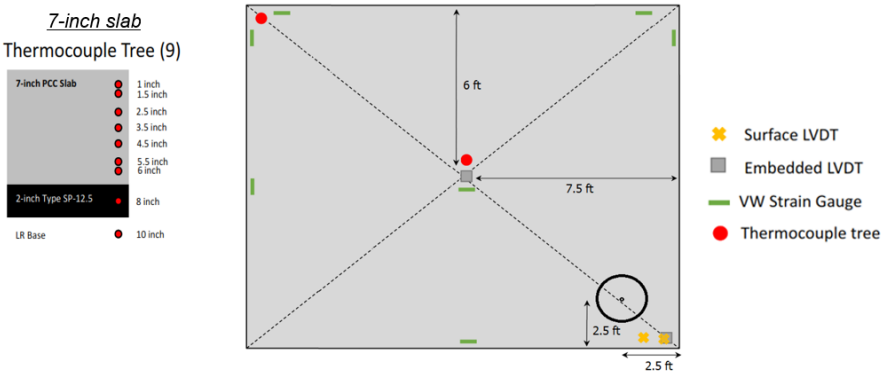

B) Phase II

Figure 4-10. Schematic Drawing of Sensors' Location

The sensors were located in places that would generate the most critical information. For example, strain gauges were placed in the top and bottom of the cross-section, where high strains were anticipated. Two aluminum bars were attached to each strain gauge to ensure that the sensors were anchored adequately in the concrete. Also, LVDTs were placed at corners to provide the slabs shape and movements under daily climatic conditions. The LVDT sensors for measuring vertical displacement were fixed on a metallic stake. The positions of all sensors in Phase I and Phase II are displayed in Figure 4-11.

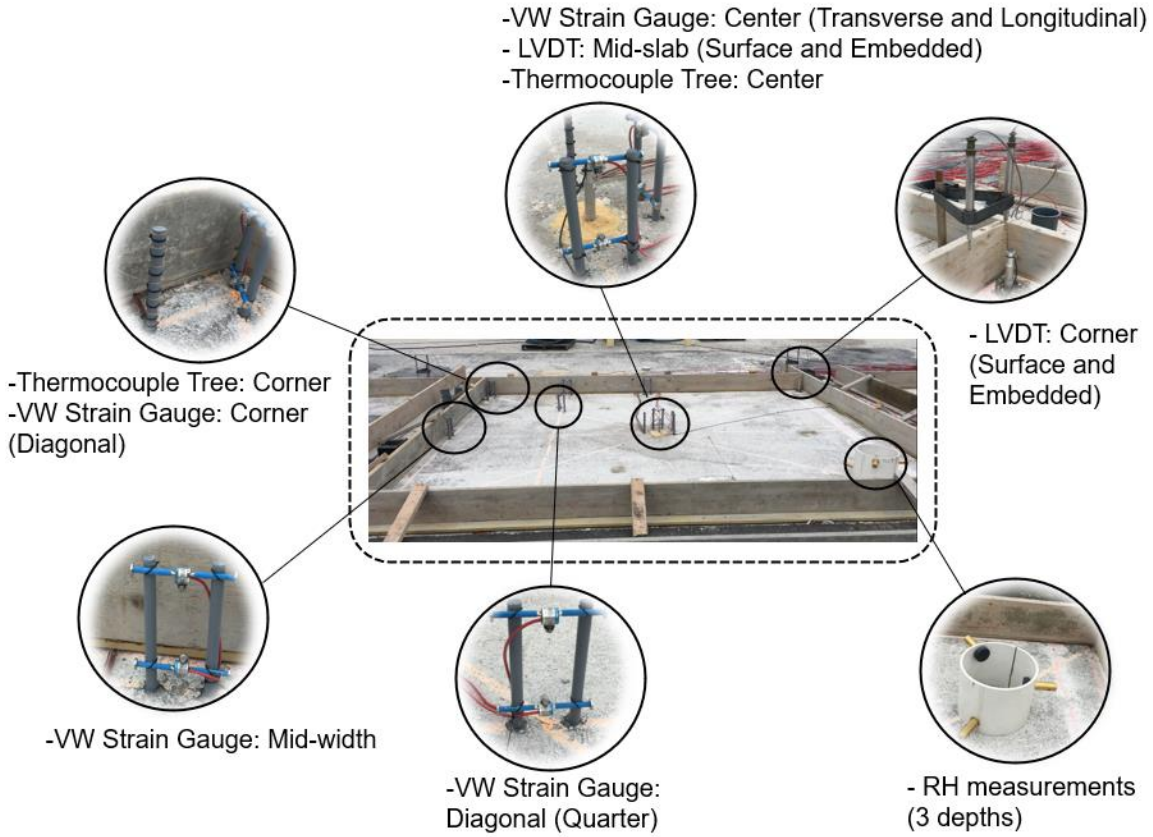

A) Phase I Sensors Layout

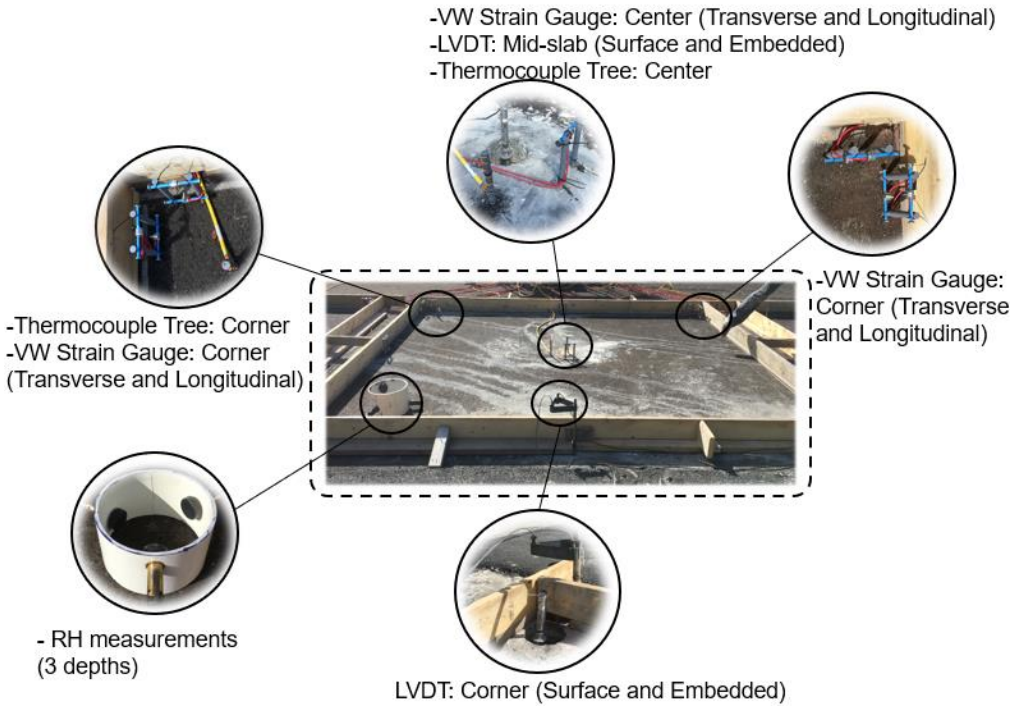

B) Phase II Sensors Layout

Figure 4-11. Position of the Sensors in the Concrete Slabs

4.1.5.1 Strain Gauges

Fourteen strain gauges were placed on the top and bottom of each slab at different locations, such as corners (longitudinal and transversal), mid-slabs (longitudinal and transversal), and the center. The VW strain gauges measured the induced tension in concrete with an electromagnetic coil by measuring the resonant frequency of the vibration. Moreover, the strain gauges had a thermistor in order to offset the effects of the temperature. The list of the VW strain gauges is shown in Table 4-4. Figure 4-12 displays the distance of the strain gauges at the side and corner from the ground base and wooden frame on the sides. All the bottom strain gauges were 2.25 inches away from the base. The distance of top strain gauges was 5.75 inches and 8.75 inches from the bottom of the ground for slabs with a thickness of 7 inches and 10 inches, respectively. Strain gauges

(with a strain limit of 3000 μm/m) were attached to a pair of compressed plastic dowel bars that were anchored into the subgrade prior to the placement of the concrete.

Table 4-4. Strain Gauge Positions and Locations in Each Slab

Name	Sensor	Position	Note
VW0	VW Strain Gauge	Top	Corner (1), longitudinal
VW1		Bottom	
VW2		Top	Corner (1), transverse
VW3		Bottom	
VW4		Top	Corner (2), longitudinal
VW5		Bottom	
VW6		Top	Corner (2), transverse
VW7		Bottom	
VW8		Top	Center, longitudinal
VW9		Bottom	
VW10		Top	Mid-edge, longitudinal
VW11		Bottom	
VW12		Top	Mid-edge, transverse
VW13		Bottom	

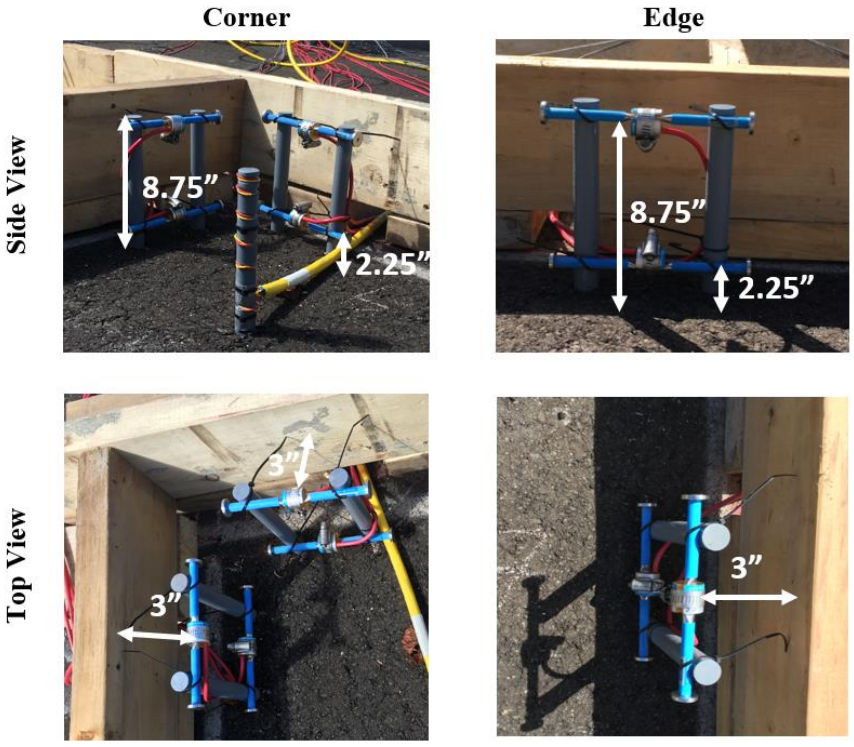

Figure 4-12. The Distance of the Strain Gauges from the Ground and Edges

4.1.5.2 LVDT Sensors

Four LVDTs were used for each slab in order to monitor the slab behavior and configuration, specifically the corner displacement. Table 4-5 lists these sensors with their locations.

Table 4-5. LVDT Sensor Positions and Locations in Each Slab

Name	Sensor	Position	Note
S1	LVDT	Surface	Located in the corner (3 inches edge offset)
S2		Surface	6 inches offset from S1 (corner) LVDT or 9 inches transverse edge offset
EM		Embedded	Mid-slab location
EC		Embedded	Corresponds with S1 location (3inches edge offset)

4.1.5.3 Thermocouple

Thermocouple trees were installed at different positions in order to measure the temperature at various depths of the slabs. The depth from the top surface for each sensor is shown in Figure 4-10. The temperature measurements were conducted at the desired depths by attaching the thermocouple wire ends to plastic dowels at various depths, as shown in Figure 4-13.

Figure 4-13. Thermocouple Tree Along with the Depth of the Concrete Slabs

4.1.6 Concrete Setting

The on-site maturity history and setting of the concrete were monitored right after concrete placement. The initial and final setting of the concrete were defined based on ASTM C 403 [136]. These two terms were measured according to concrete transitions from a fresh state to a hardened state. In this test method, the times required for the mortar to reach specified values of penetration resistance are used to define times of setting. However, the set was a process that occurred over several days. The penetration resistance of the concrete mixture was measured by using multi-sectional needles, as shown in Figure 4-14. The initial and final set times were determined from a plot of penetration resistance versus time. The initial time of the set elapsed after the placement of the mortar portion of the mixture reached a penetration resistance of 500 psi. In contrast, the penetration resistance for the final setting is 4000 psi.

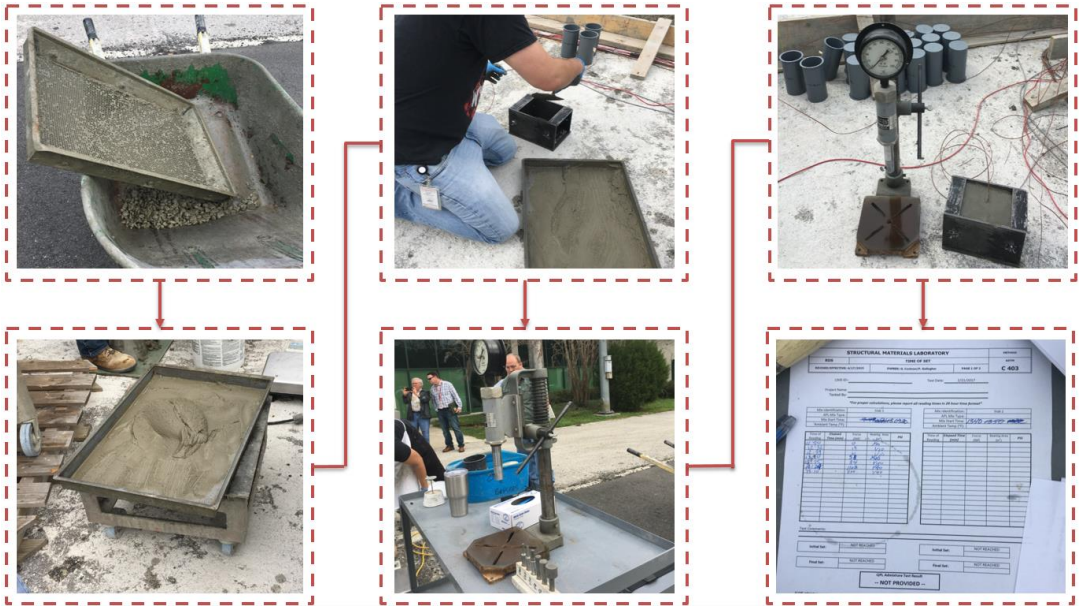

Figure 4-14. The Penetration Test Setup to Measure Initial and Final Setting

4.1.7 Moisture and Temperature Measurements

Dry bulb and dew point temperatures were measured to track the curing process and the formation of gradients in the concrete slabs. A portable maturity unit was used to measure the temperature and relative humidity variations in the concrete at specific depths. The portable maturity unit recorded dew point temperatures based on chilled-mirror technology at 1-minute intervals. As shown in Figure 4-15, three brass casings were placed on a cylindrical mold at specific depths. The measurements were started after the final set of the concrete. With each reading, the lid was removed from the brass casing, and the probe was inserted and kept in the brass casing for at least 20 minutes. After this period, the probe was quickly pulled out, cleaned, and used for the next readings. Prior to the next reading, the gasket of the probe was lubricated.

Figure 4-15. Temperature and Moisture Measurements in Different Depths

4.1.8 Drying Shrinkage

The volumetric changes of concrete due to the loss of capillary water is mostly known as drying shrinkage. The volumetric shrinkage in concrete was created by the

moisture loss as internal strains. These stresses can deform concrete slabs. During and after hardening, concrete was subjected to shrinkage as water was absorbed and not consumed by cement hydration. The amount of shrinkage of a concrete mixture was determined by ASTM C 157 [168]. Shrinkage specimens were prepared in the field and tested to evaluate the effects of adding curing compounds (type and application rate) on the shrinkage rate. The VW strain gauges were used to measure the shrinkage strain (see Figure 4-16). On the first cycle of drying, a portion of drying shrinkage is irrecoverable and indirectly related to the set that occurs in a concrete slab. The model can provide a reasonable prediction of drying shrinkage and creep strains.

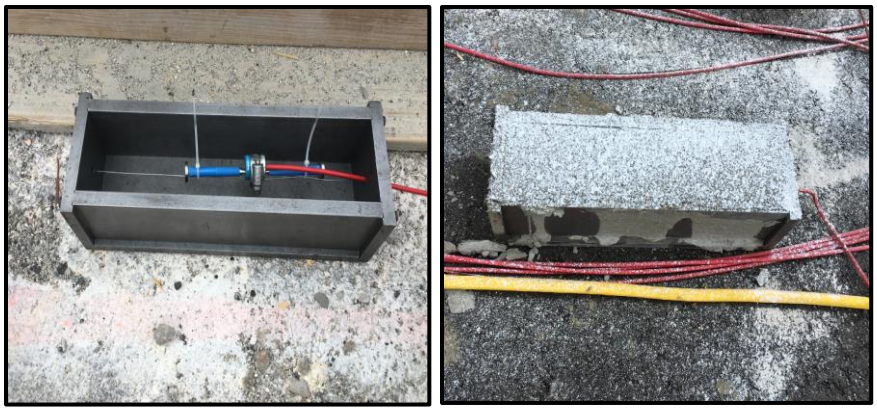

Figure 4-16. A Shrinkage Test Mold with a VW Strain Gauge

4.1.9 Compressive Strength

The compressive strength at the ages of 3, 7, 14, 28, and 56 days old were tested on each slab. For each specific time, three samples were provided and the average strength was reported. All samples were cast from the same concrete batch and were cured with the same curing compound and the applicate rate. As shown in Figure 4-17, all samples were kept adjacent to the slab under the ambient conditions until the test date. Moreover, based on the evolution of compressive strength, the modulus of rupture was calculated

according to the ACI Committee 209 guide [123]. A best-fit regression line fits through data points to interpolate or extrapolate strength (or stiffness) at various ages.

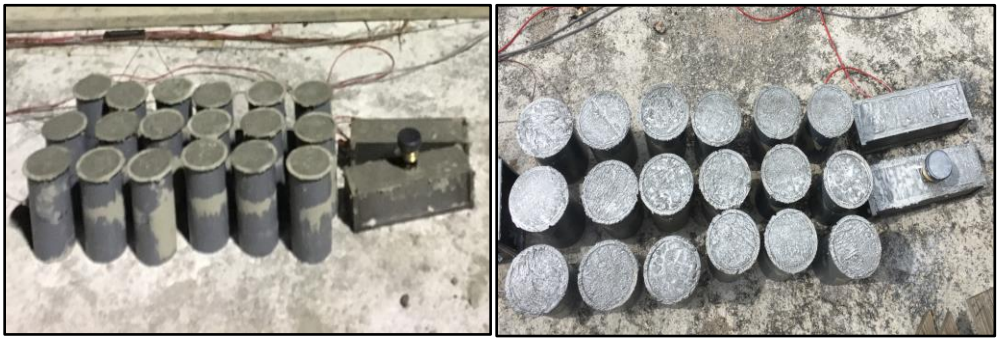

Figure 4-17. Concrete Cylinders for the Compressive Strength Test

4.2 Field Testing Results

Results of the setting time, the free shrinkage, the EI measurements, the relative humidity profiles, the equivalent linear gradient profiles, the induced strains, and the corner displacement are presented in this section. These results were used to relate slab movement to the method of curing and the set gradient of newly constructed concrete slabs.

4.2.1 Phase I Results

To measure the set gradient in Phase I, four slabs were placed and tested in February to study the different curing conditions and placement times. Several instruments and sensors were used on the slabs to collect data and understand the set behavior of concrete slabs under different curing conditions.

4.2.1.1 Setting Time

A penetration specimen was prepared for each slab, and data points were obtained just after concrete placement. Based on the ASTM C 403 [136] procedure, the penetration resistances for the initial setting and final setting were 500 psi and 4000 psi, respectively. The penetration test data and concrete maturity are shown in Figure 4-18. As the concrete setting is a gradual development, any definition of set time can be arbitrary. The time needed for the paste to reach specific values of penetration resistance was measured. This test method depended on different factors, such as w/c ratio, type, and amount of cementitious materials. The results of penetration are listed in Table 4-6. The final setting time for Slab 1 was lower than Slab 2 and Slab 3. Table 4-6 indicates that paving slabs in the morning and at noon increased the concrete temperature due to the rate of hydration and solar radiation. The coincidence of these two factors expedited the hydration reactions. Thus, the final setting time in Slab 1 was much lower compared with the other slabs. The maturity index depended on the measured temperature history of concrete to estimate the hydration process, as shown in Figure 4-19. The initial setting maturity was 226.7 ˚C-hours, and the final setting maturity was 296.9 ˚C-hours for the control (uncured) slab.

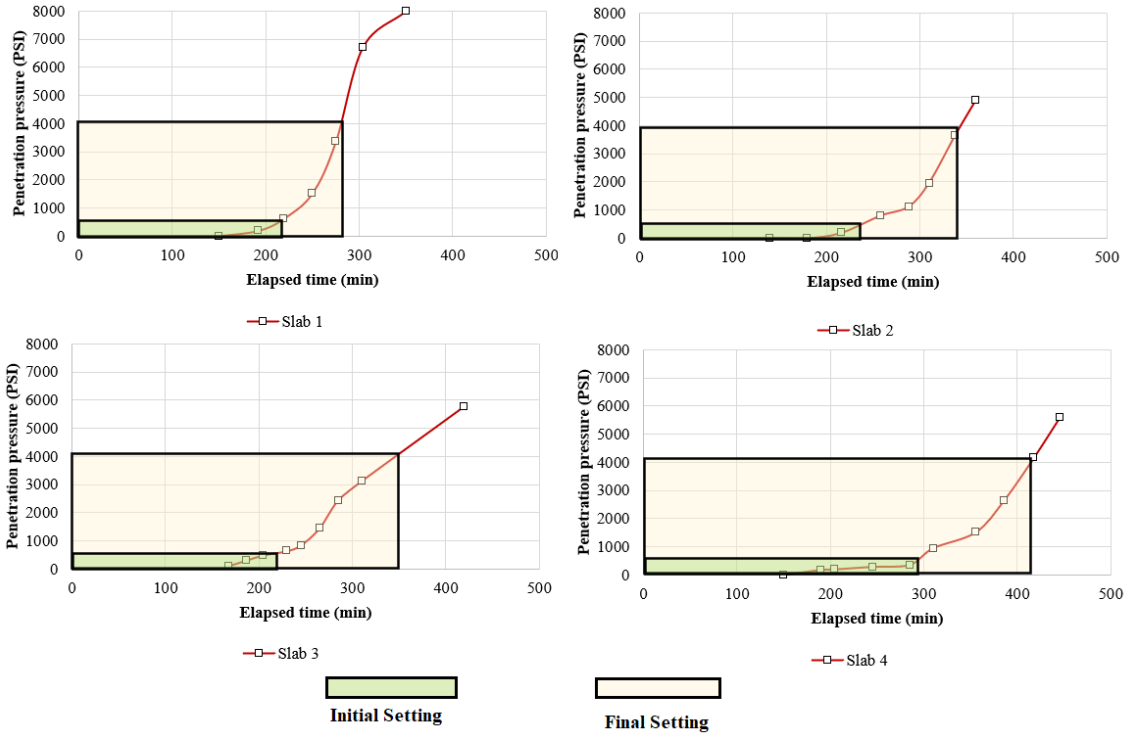

Figure 4-18. Penetration Results for Setting Time (Phase I)

Table 4-6. The Penetration and Concrete Maturity Results (Phase I)

	Time for Initial Set (min)	Time for Final Set (min)	Maturity for Initial Set (˚C-hours)	Maturity for Final Set (˚C-hours)
Slab 1	235	285	186.1	220.3
Slab 2	270	325	160.2	193.4
Slab 3	245	350	167.3	230.1
Slab 4	295	415	226.7	296.9

Generally, in the early age, the initial concrete temperature was the same for all slabs. However, regarding mixtures with different curing conditions, the slab experienced different early-age concrete temperatures. Figure 4-19 shows the concrete temperature from the early hydration of cementitious materials on slabs. For each slab, three cylinders had a thermometer that measured temperature continuously. The shape of the temperature

curves obtained through this test is an indicator of the time of placement. Figure 4-19 indicates that Slab 1, which was placed in the morning, had a higher concrete temperature due to the rate of hydration and solar radiation. However, Slab 2 and Slab 3, which were placed in the afternoon, had a lower temperature at the initial hours.

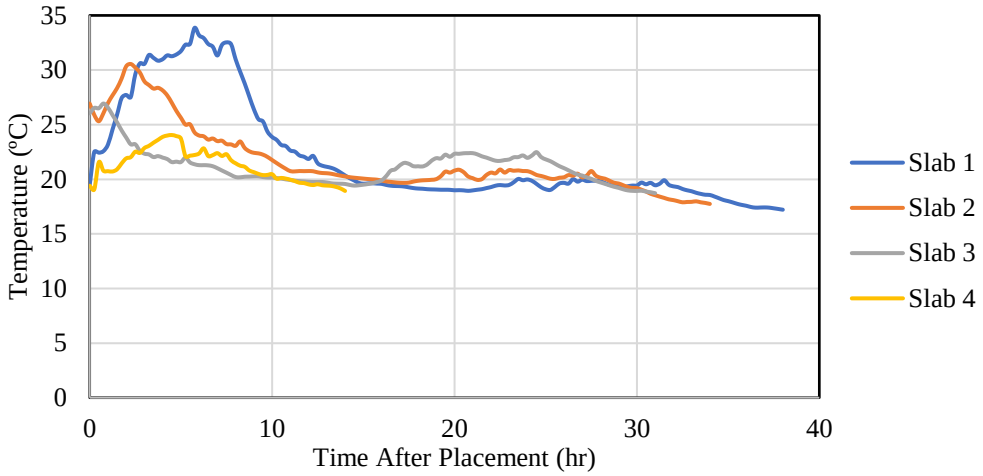

Figure 4-19. Maturity Data After Concrete Placement (Phase I)

4.2.1.2 EI Determinations

EI was calculated using the relative humidity and temperature data collected by the maturity meter system. EI determinations for each slab are shown in Figure 4-20 to Figure 4-23. The higher EI, such as that measured in Slab 2 and Slab 3, showed higher concrete maturity on the filtered side of the plate, which was influenced by the type and the amount of the applied curing compound, and the ambient environment. In Slab 1, WRM-1150 curing compound was sprayed at a 250 ft^2/gal application rate after visible bleeding on the concrete surface had subsided, and sheen had disappeared. The curing compound was non-pigmented, and there was no method to verify the uniformity of the compounds visually. The relative humidity in the sealed and filtered side progressively increased to 90% after approximately 14 hours of monitoring. With the same application

rate, WRM-1625 was used on Slab 2. WRM-1625 had a better performance in keeping EI at a higher level for a longer period. The relative humidity in the filtered side of the plate started to reduce after a given period, which greatly depended on the quality of the curing conditions. The highest application rate, 180 ft^2/gal, was applied on Slab 3. In Slab 3, sealed and filtered relative humidity fluctuated between 90% and 100%, and resulted in a higher EI, 0.77. Slab 4 was cured with no compound and had the lowest EI values. EI remained less than 0.5, and after 72 hours, was 0.44 in Slab 4.

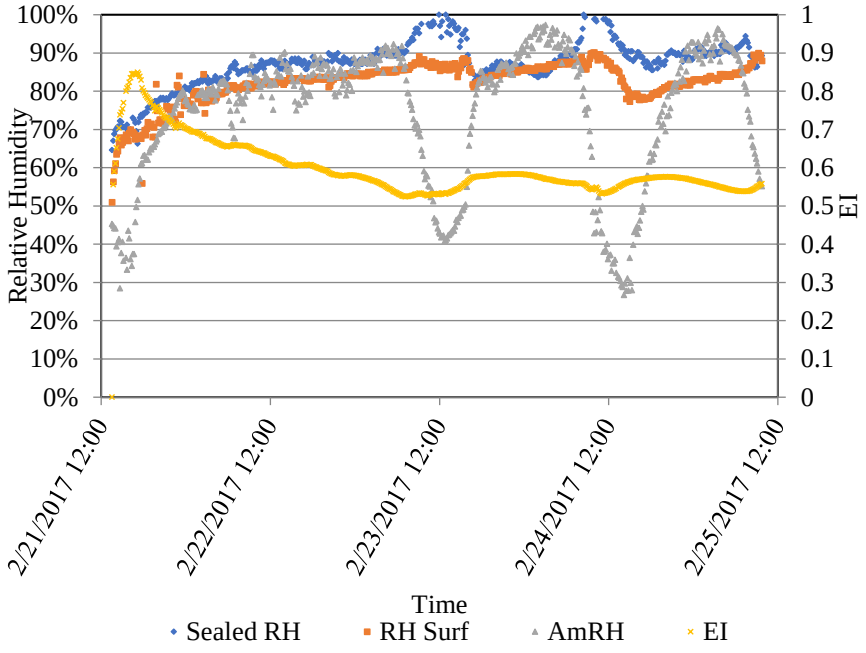

Figure 4-20. EI Determination and Relative Humidity in Slab 1 (Phase I)

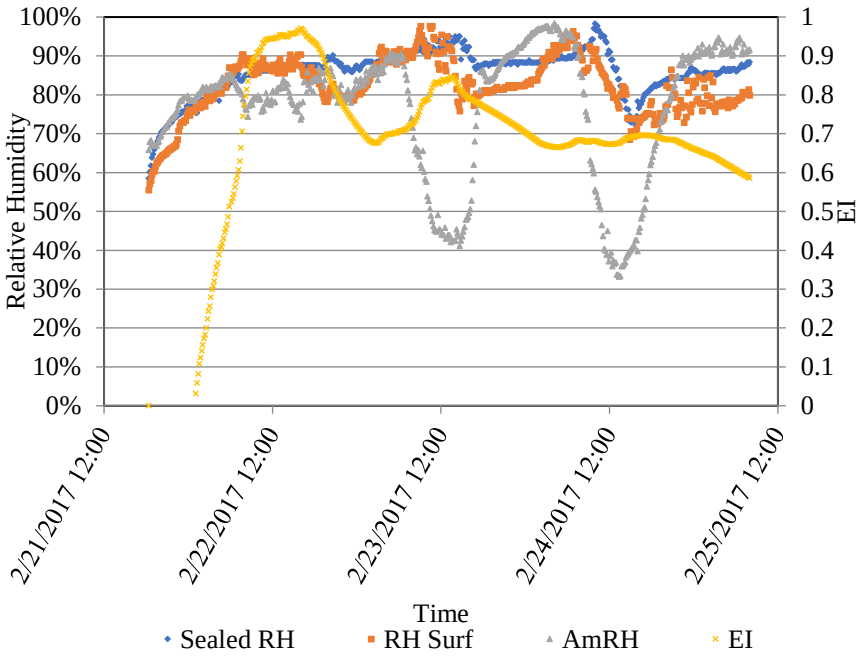

Figure 4-21. EI Determination and Relative Humidity in Slab 2 (Phase I)

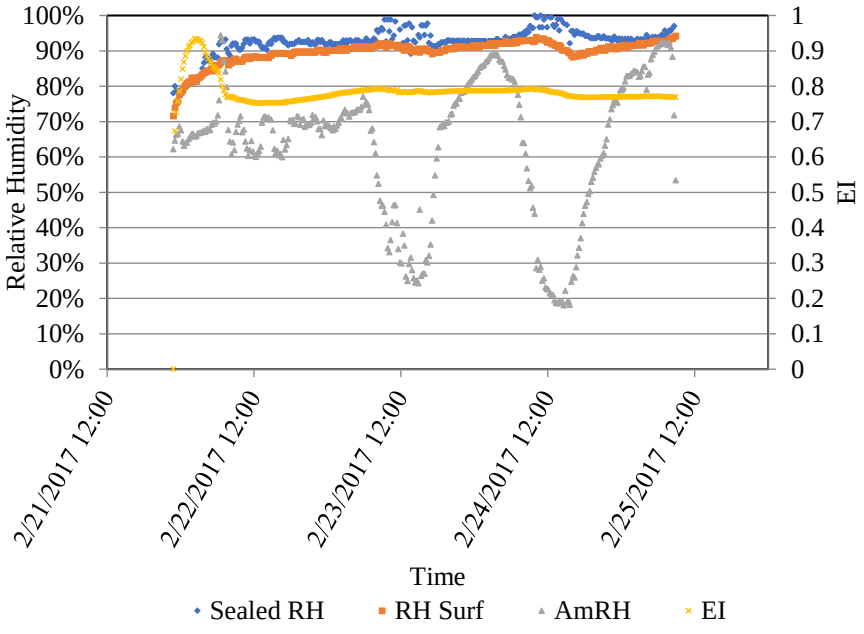

Figure 4-22. EI Determination and Relative Humidity in Slab 3 (Phase I)

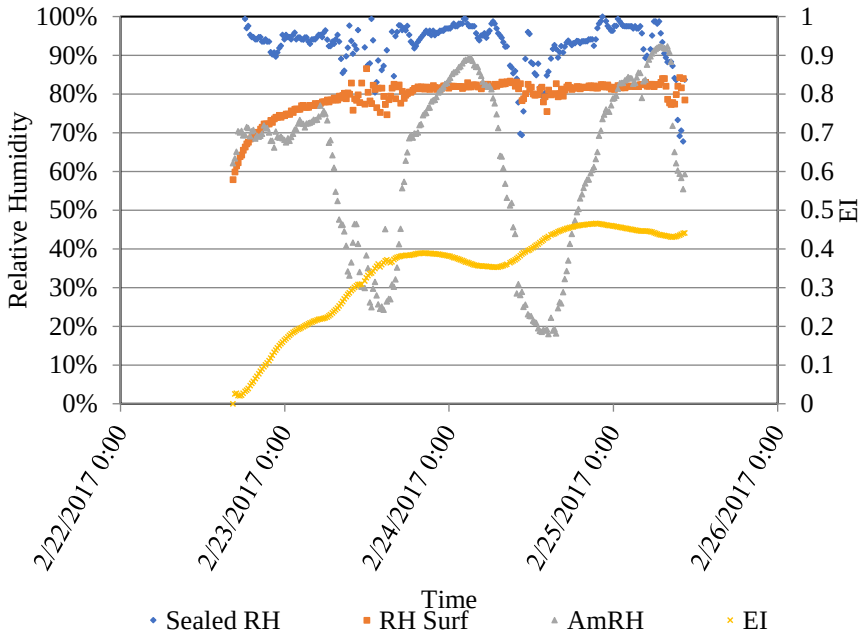

Figure 4-23. EI Determination and Relative Humidity in Slab 4 (Phase I)

4.2.1.3 Dielectric Constant Measurement

DC measurements were used to interpret the curing quality. During bleeding, the moisture content at the concrete surface was high. Thus, greater DC measurements were displayed for the first few hours. After bleeding, DC measurements of all slabs started to decrease. Since Slab 4 was not cured with compound, less unbound free water was available at the concrete surface due to evaporation, and the free water inside of concrete decreased with time for this slab. The DC measurements of both Slab 2 and Slab 3 showed very similar sensitivity. However, the decreasing trends of DC measurements for Slab 1 exhibited a higher decreasing rate of DC measurements compared to Slab 2 and Slab 3. This information differentiated curing quality for different curing conditions. The fitted regression parameters for all slabs are presented in Table 4-7 and Figure 4-24.

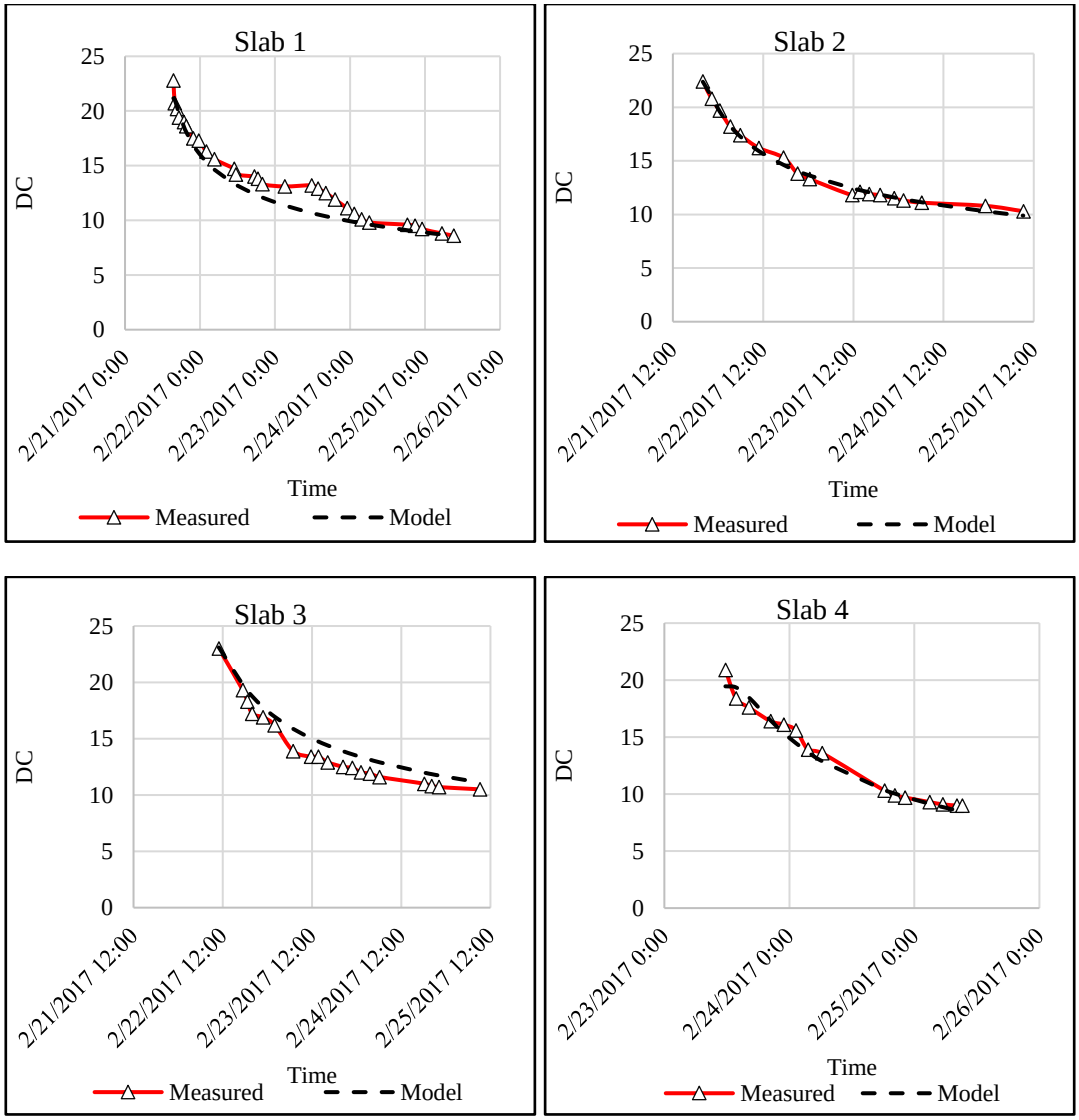

Figure 4-24. Regression Curves for DC Measurements (Phase I)

Table 4-7. Regression Parameters for the Four Test Slabs (Phase I)

Test Section	τ	α	β
Slab 1	21.166	0.049	0.524
Slab 2	22.374	0.041	0.432
Slab 3	23.098	0.036	0.415
Slab 4	19.457	0.052	0.716

Table 4-7 shows a relationship between DC and regression parameters β. The decreasing DC with a lower rate is generally associated with a lower β, representing a higher moisture content. Hence, the utility of β measurements to qualify the curing practice was validated. Figure 4-24 demonstrates that with time, the value of the function converges to a constant value. The decreasing trends of Slab 1 and Slab 2 are very similar during the first 20 hours but diverge afterward. Based on the β parameters shown in Table 4-7, the curing method used for Slab 2 had better quality and moisture retention capability than Slab 1. By comparing the DC values of Slab 3 and Slab 4, a considerable difference was observed between the two trends in the first 8 hours in which dielectric values for Slab 4 showed a higher rate of decrease than that of Slab 3. Referring to Table 4-7, Slab 3 did provide better curing than other slabs considering the fact that using a wax-based curing compound with higher application substantially improved the curing feature compared to the other curing methods.

4.2.1.4 Temperature and Relative Humidity Gradients

Since temperature and moisture gradients inside a concrete slab are non-linear, it is required to convert the non-linear gradients into equivalent linear gradients to facilitate analysis [73]. These equivalent linear gradients represent the differences in temperature and moisture conditions between the top and bottom of the slab. The parameters are determined based on a regression analysis of temperature and moisture profiles. This approach was used to define the linear temperature and humidity gradients through the slab thickness, as suggested by Mohamed and Hansen [102]. This equivalent linear gradient is defined based on Eq. (4-1):

$$\Delta T_{eq} = -\frac{12M^*}{\alpha h^2} \tag{4-1}$$

where,

ΔT_{eq} = equivalent linear temperature gradient (˚C),

h = slab thickness (m),

α = concrete coefficient of thermal expansion (m/m/˚C), and

M^* = bending moment dependent on the temperature (or moisture) distribution expressed as shown in Eq. (4-2)

$$M^* = \int_{-h/2}^{h/2} \varepsilon(z) z dz \quad (4\text{-}2)$$

z = distance from the slab midplane (z is positive downward) (m), and

$\varepsilon(z)$ = strain profile (due to bending) (m/m)

The strain profile was determined by Eq. (4-3):

$$\varepsilon(z) = \alpha(T_z - T_{z,bot}) \quad (4\text{-}3)$$

where

T_Z = current temperature at slab depth z (˚C), and

$T_{Z,\,bot}$ = temperature at slab bottom (˚C)

The equivalent linear temperature gradient was expressed based on the coefficients of a third-order polynomial equation, as shown in Eq. (4-4):

$$T_z = A + Bz + Cz^2 + Dz^3 \quad (4\text{-}4)$$

where

A, B, C, and *D* = regression coefficients

In order to calculate the temperature gradient at a given time, (Eq. 4-5) can be used:

$$\Delta T_{eq} = -12\left(\frac{Bh}{12} + \frac{Dh^3}{80}\right) \quad (4\text{-}5)$$

4.2.1.4.1 Temperature Gradients

Figure 4-25 displays the temperature profiles under the surfaces of Slab 1 at depths 1, 3, and 5 inches, and of Slabs 2-4 at 1, 3, and 8 inches, each of which were measured during the first 80 hours after the concrete placement. Figure 4-25 also shows the impact

of the concrete placement time on the concrete slab temperature at various depths. The temperature profiles of Slab 1 (which was a morning placement) showed a higher maximum temperature compared to Slab 2 and Slab 3, which were afternoon and evening placements. In Slab 1, the peak of heat of hydration started after a few hours from the placement. Thus, this peak coincided with the maximum daily ambient temperature and made the concrete temperature higher than the other slabs. The maturity results (see Figure 4-19) confirm this fact.

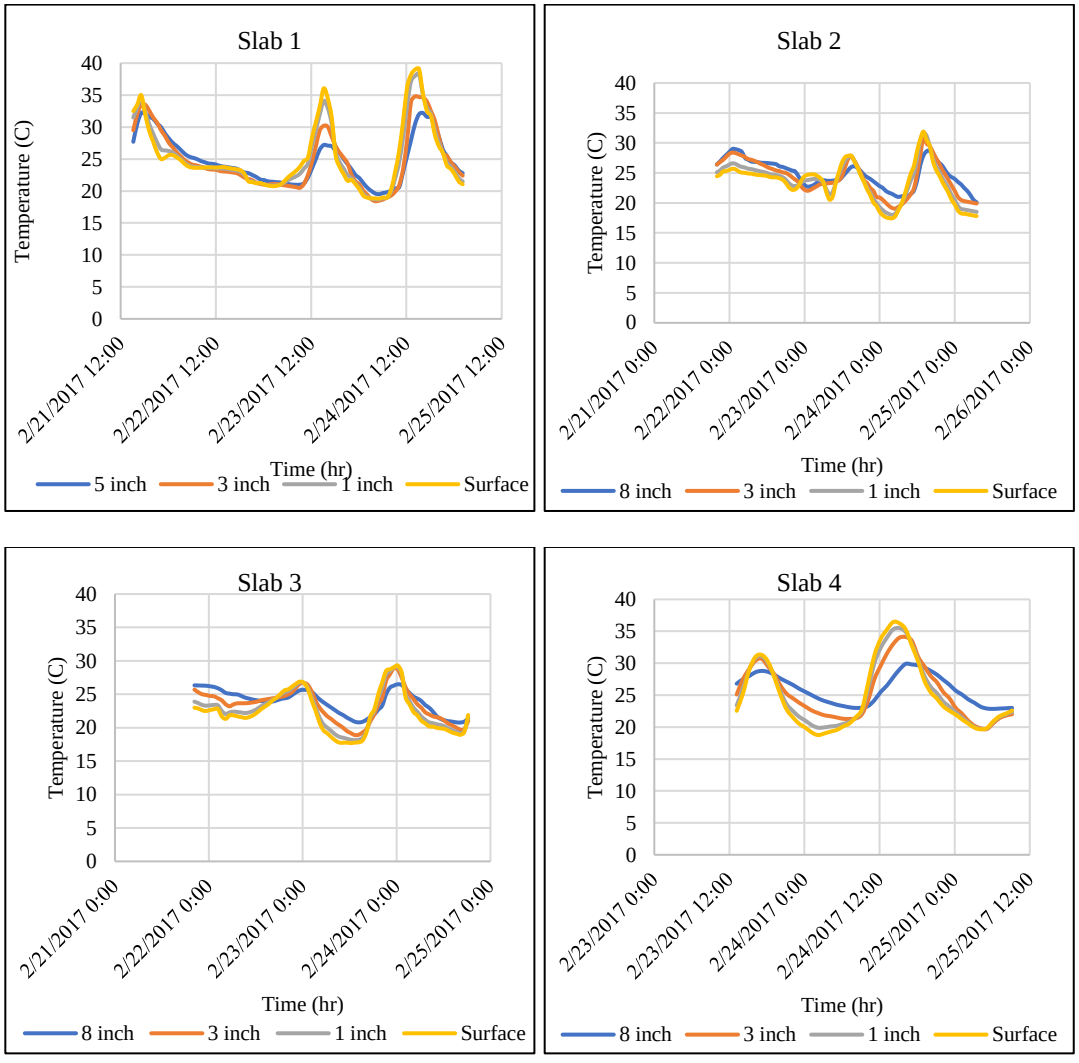

Figure 4-25. Temperature Profiles at Different Depths (Phase I)

The differences in temperature through the pavement provided a better understanding of the distribution profiles, and later the set gradient. There was a temperature differential between the top and the bottom of the slabs. The temperatures at greater depths below the surface were higher than the ambient temperatures at night, and the magnitude of this difference varied with time and depth. The slabs were subjected to larger equivalent linear temperature gradients during the day, in which the bottom of the slab temperature was lower than the surface temperature. Slab temperatures increased in the morning due to solar radiation and dropped later in the evening as the solar energy diminished. The ambient temperature is a factor in specifying the heat of hydration. Generally, hydration at higher ambient temperature happened with a faster rate at early ages but decelerated later on. After the first few days, the absorbed heat dissipated into the air and resulted in lower temperature differences. The equivalent linear temperature gradient between the top and bottom portions of the slab is shown in Figure 4-26. Temperature gradients in concrete slabs caused the slabs to curl either upward or downward. The slabs with better curing practices, such as Slab 2 and Slab 3, had lower temperature gradients. However, Slab 4 had the highest temperature gradient.

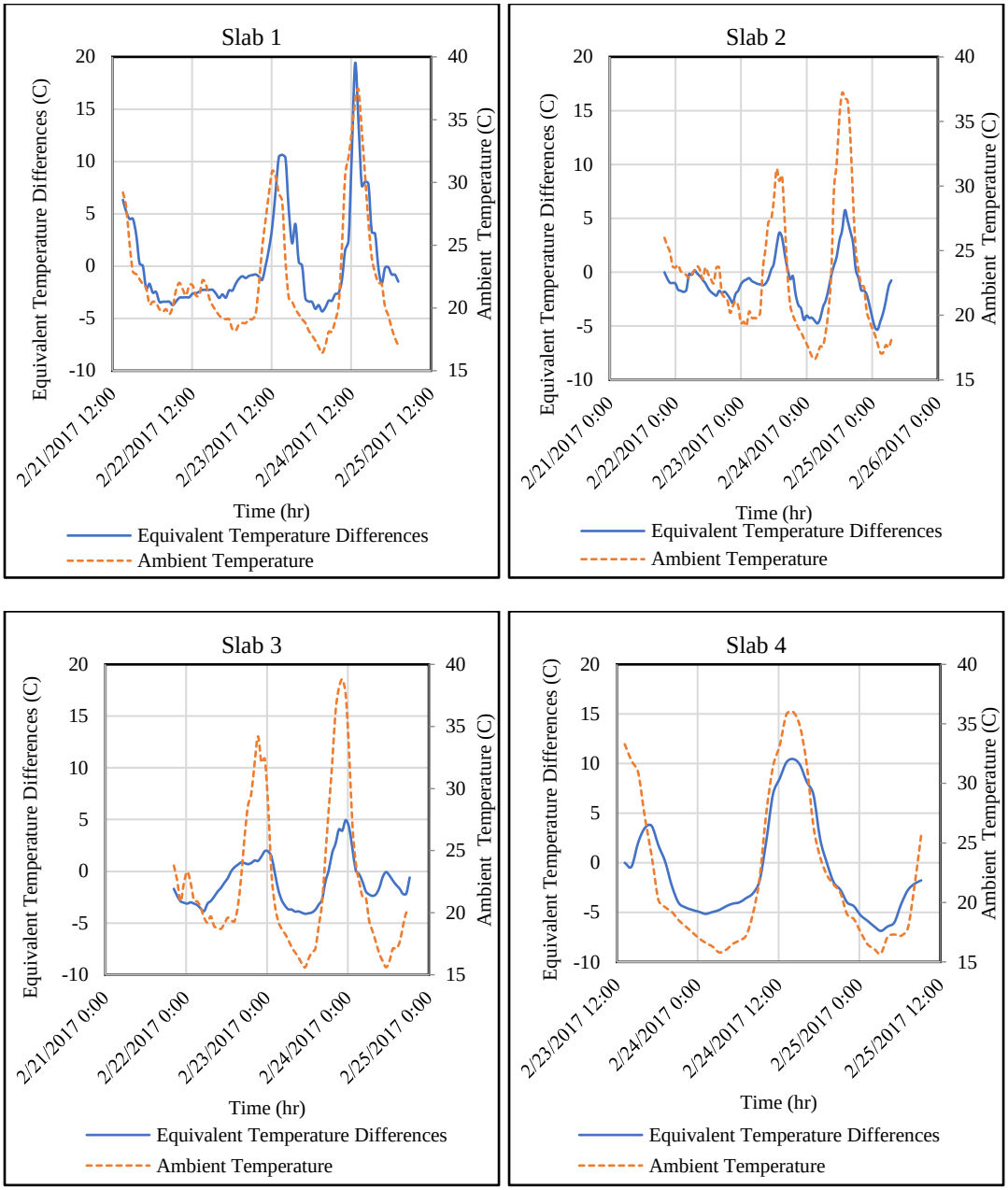

Figure 4-26. Equivalent Linear Temperature Gradient of Slabs (Phase I)

Figure 4-27 to Figure 4-30 show the measured temperatures at various depth of the slabs in the first three days after concrete placement on all slabs. The temperature profiles are displayed in 2-hour increments. In Slab 1, Slab 2, and Slab 3, relatively uniform temperature profiles were observed at the first day after concrete placement. The

reason for this uniform distribution was because of the proper curing treatment. However, Slab 4 showed non-uniform temperature gradients soon after the placement (see Figure 4-30). As shown in Figure 4-27 to Figure 4-30, the maximum temperatures at the surface for each slab were 39.1 ˚C, 28.8 ˚C, 25.8 ˚C, and 35.3 ˚C, respectively. However, the maximum temperatures at the ground for each section were 27.3 ˚C, 24.6 ˚C, 24.3 ˚C, and 27.2 ˚C, respectively.

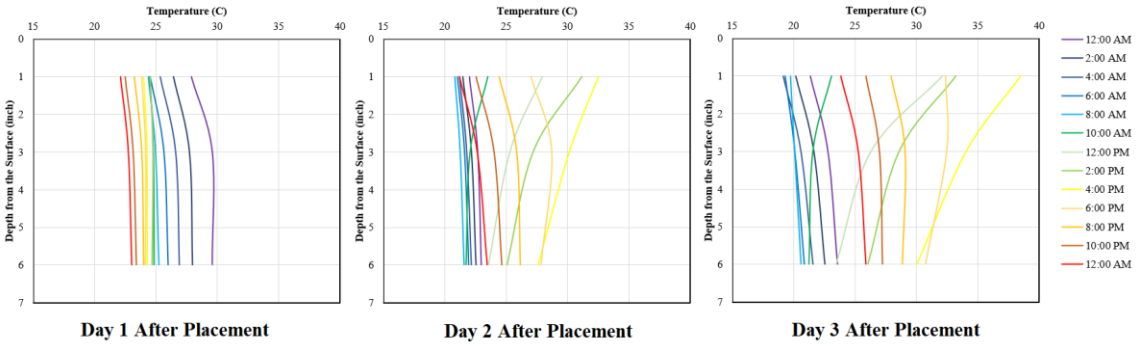

Figure 4-27. Measured Temperature Gradients versus Time for Slab 1 (Phase I)

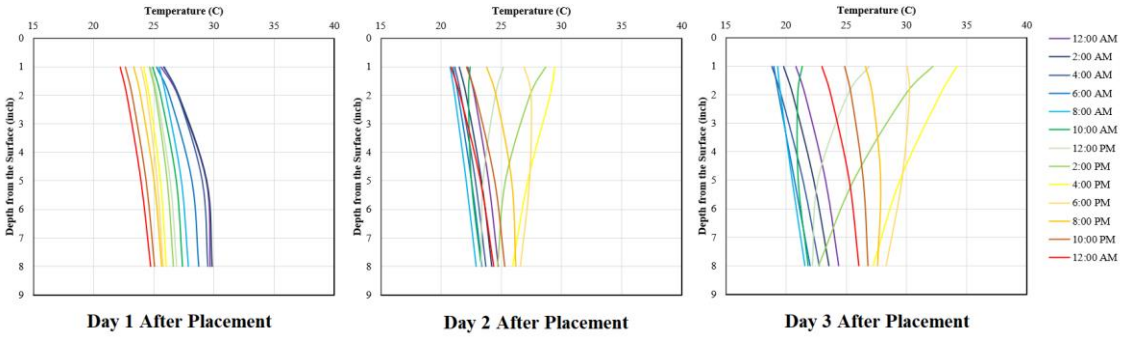

Figure 4-28. Measured Temperature Gradients versus Time for Slab 2 (Phase I)

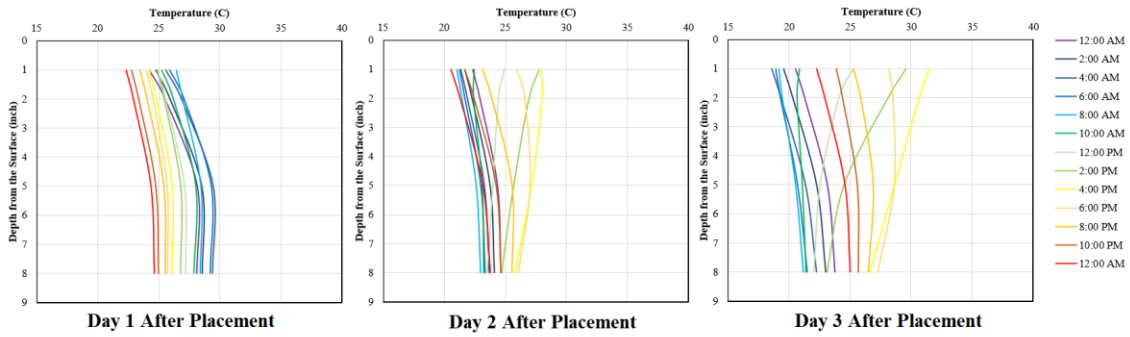

Figure 4-29. Measured Temperature Gradients versus Time for Slab 3 (Phase I)

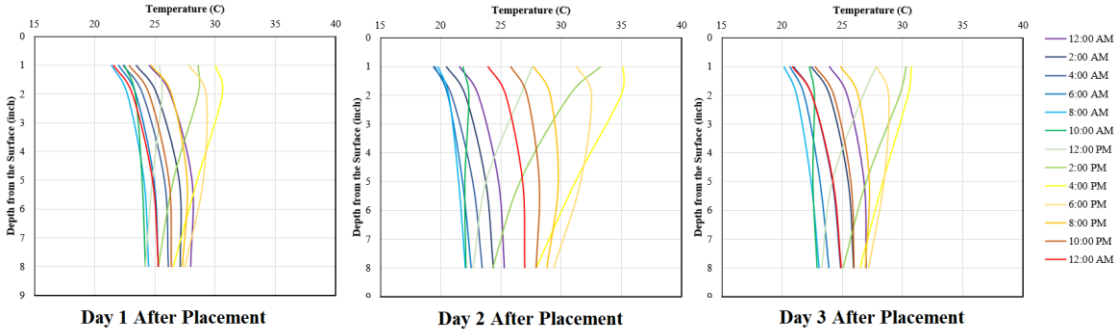

Figure 4-30. Measured Temperatures Gradient versus time for Slab 4

4.2.1.4.2 Relative Humidity Gradients

Figure 4-31 displays the relative humidity profiles under the surfaces of Slab 1 at depths 1, 3, and 5 inches, and of Slabs 2-4 at 1, 3, and 8 inches, each of which were measured during the first 80 hours after the concrete placement.

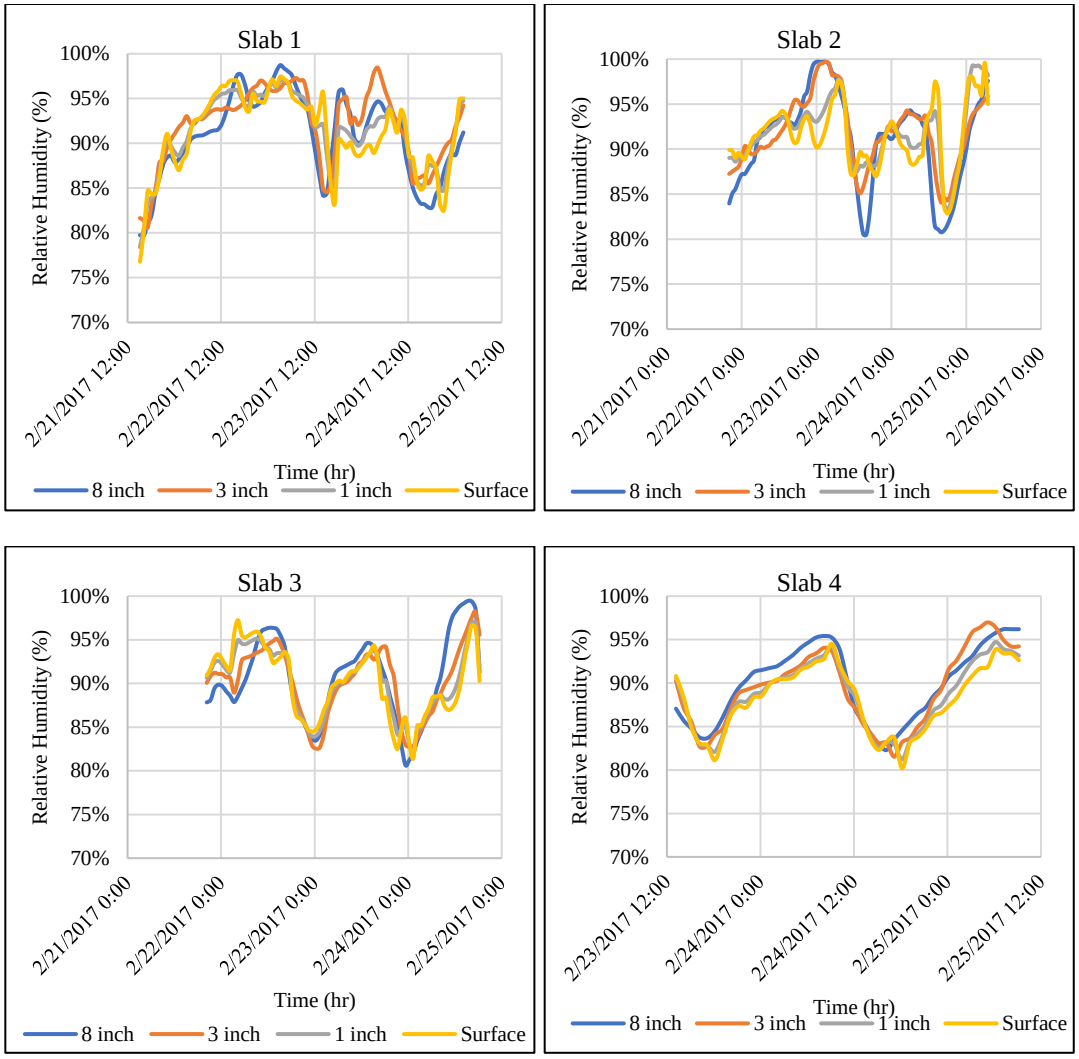

Figure 4-31. Relative Humidity Profiles at Different Depths (Phase I)

As shown in Figure 4-32, the variations of the slabs' relative humidity were different from the temperature trends. The relative humidity near the slab surface was continuously increasing during the initial hours, while the relative humidity at greater depths below the surface remained substantially high. When the concrete setting happened, the relative humidity at different depths of the slab was consistent with the quality of the curing. It was observed that Slab 1 and Slab 4, which were cured with a lower curing quality, tended to have larger moisture gradients.

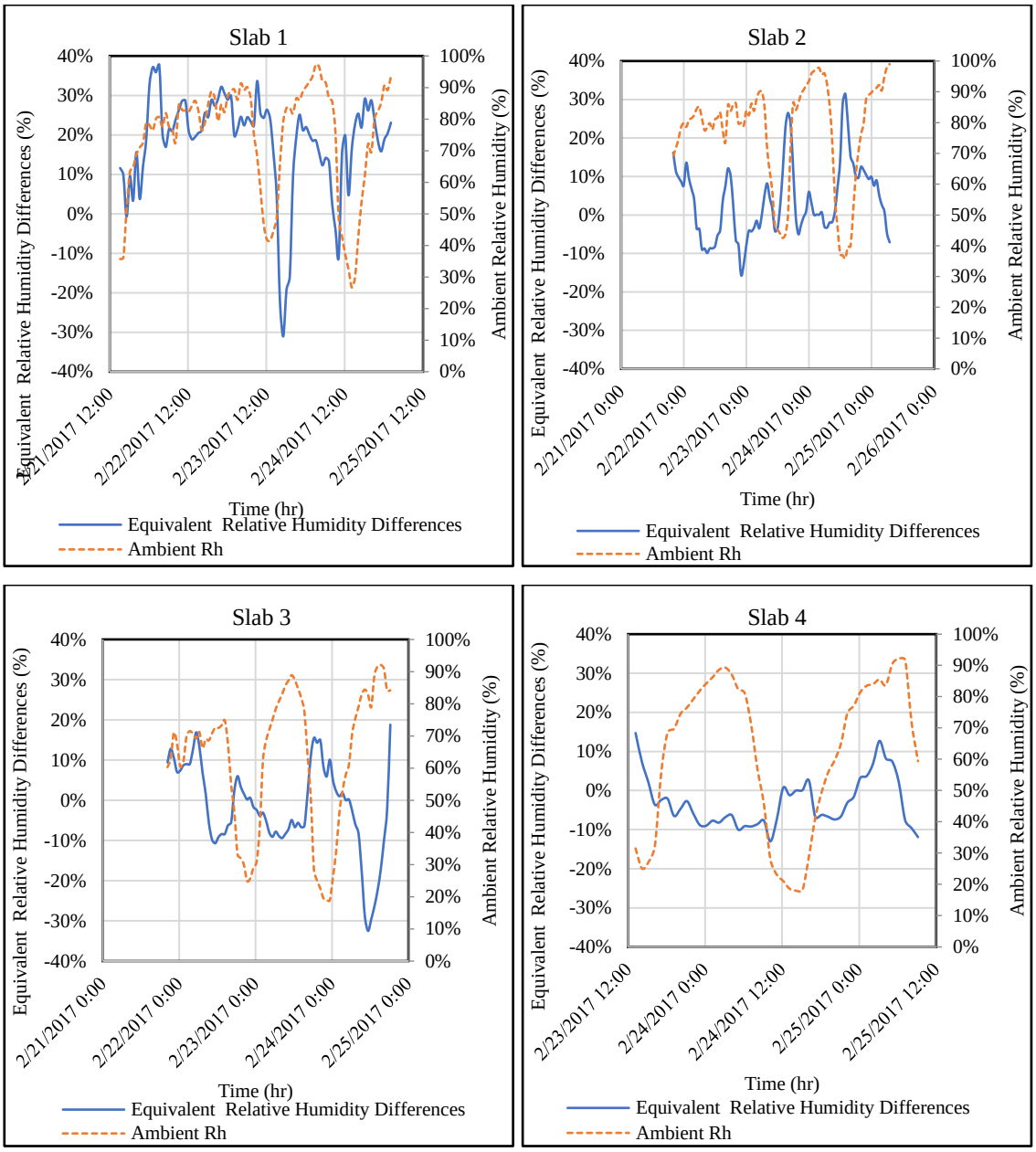

Figure 4-32. Equivalent Linear Relative Humidity Gradient of Slabs (Phase I)

The drying of concrete was due to the moisture movement from the concrete components to the surrounding medium. Thus, the surface and the bottom of concrete were subjected to this kind of drying mechanism. As shown in Figure 4-33, the relative humidity

level on the upper layers was reduced at a higher rate compared to those with the lower layers in slabs. The reason is attributed to the exposure of the top layers to the ambient conditions (the rate of evaporation of moisture from the concrete surface was relatively high). Casting concrete under relatively warm and dry conditions accelerated the hydration rate and the self-desiccation drying.

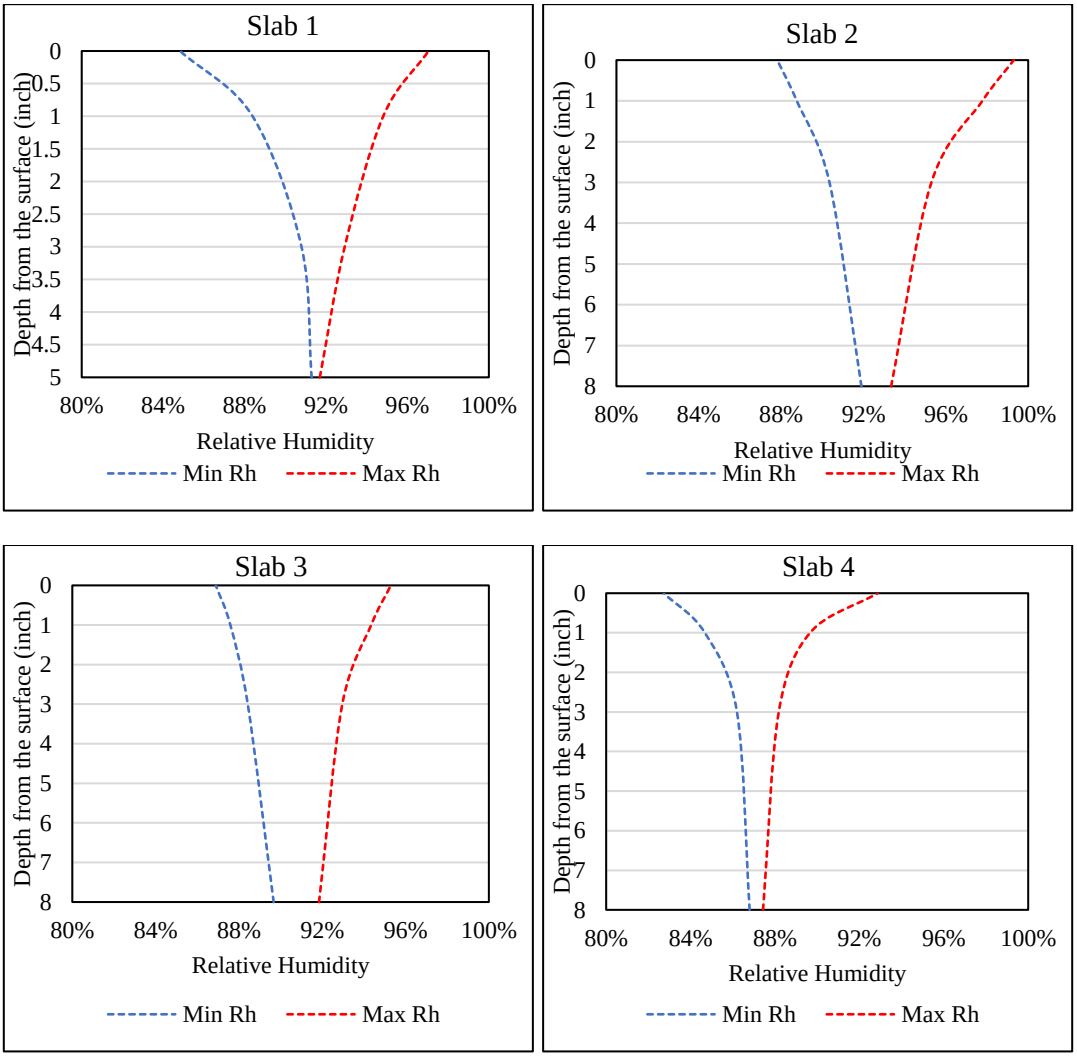

Figure 4-33. Maximum and Min Moisture Profiles in Slabs (Phase I)

4.2.1.5 Computed Strain

Eq. (4-6) was applied to calculate the thermal strains at the concrete slab surface as functions of the temperature values through the slab thickness and the coefficient of thermal expansion.

$$\varepsilon_{Temp\ Grad} = \alpha_c \Delta T_{eq} \quad (4\text{-}6)$$

where

$\varepsilon_{Temp\ Grad}$ = thermal strain due to an equivalent linear temperature gradient through the slab thickness,

α_c = coefficient of thermal expansion of the concrete (m/m/˚C), and

ΔT_{eq} = equivalent linear temperature difference (˚C)

The same procedure is followed to calculate the equivalent linear moisture (i.e., relative humidity) gradient:

$$\varepsilon_{MoistGrad} = -\varepsilon_{\infty} \Delta \left[1 - \left(\frac{RH}{100}\right)^3\right]_{eq} \quad (4\text{-}7)$$

where

$\varepsilon_{MoistGrad}$ = moisture strain due to an equivalent linear moisture gradient through the slab thickness,

ε_{∞} = ultimate shrinkage strain, and

$\Delta \left[1 - \left(\frac{RH}{100}\right)^3\right]_{eq}$ = equivalent linear humidity difference coefficient

The combined net strain of the thermal strain $\varepsilon_{Temp\ Grad}$ and the moisture strain $\varepsilon_{MoistGrad}$ is the equivalent strain ε_{NET}. Thus, the combined net strain consists of equivalent linear temperature and humidity gradients, the coefficient of thermal expansion, and the ultimate shrinkage strain.

$$\varepsilon_{NET} = \varepsilon_{Temp\ Grad} + \varepsilon_{MoistGrad} \quad (4\text{-}8)$$

In reference to the measured strain, Westergaard [169] developed a solution for the stress induced by the temperature variation by assuming that the temperature variation is linear. This solution is commonly used in concrete pavement design for curling analysis. The formula (using the Bradbury solution) for stress at the center of the slab is based on the calculated equivalent linear strain from the strain profile derived from the actual strain readings.

Once the equivalent linear temperature and moisture gradients were computed, the corresponding thermal and shrinkage strains were computed. The net (effective) strain was composed of thermal strain and drying shrinkage strain, as shown in Figure 4-34. Internal strain due to temperature or moisture gradients in concrete caused volumetric changes, such as curling and warping. As displayed in Figure 4-34, the net (effective) strain in Slab 3 was the lowest compared to other slabs. Slab 1 and Slab 4 had higher net strain values. These results were in accordance with the amount of moisture and temperature gradients. Lower temperature and moisture gradients were likely in well-cured concrete slabs (Slab 2 and Slab 3).

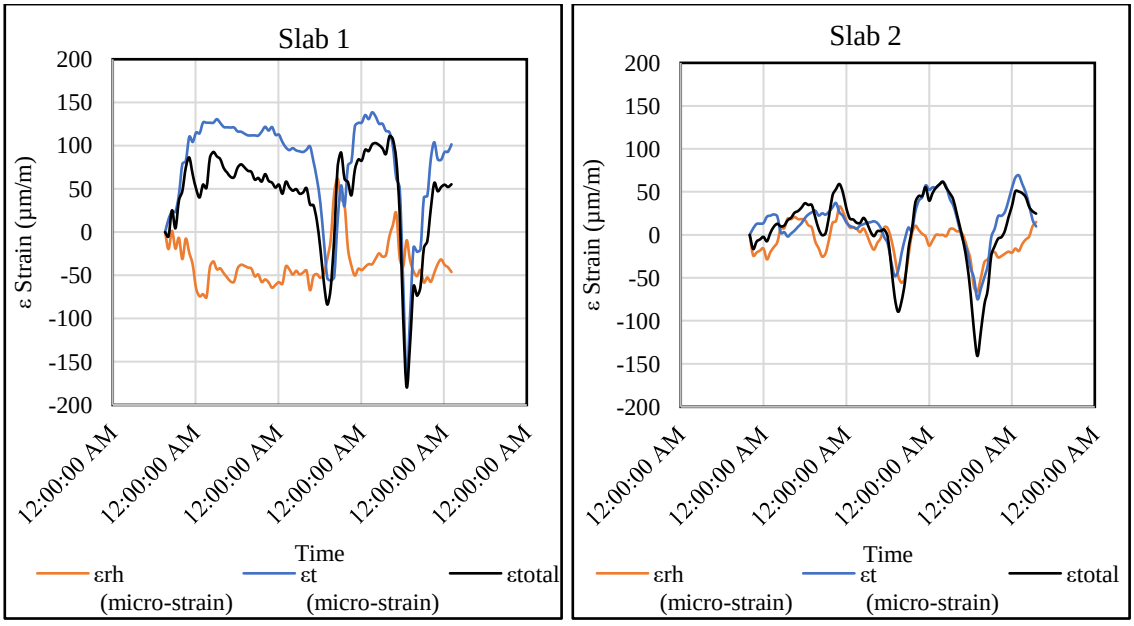

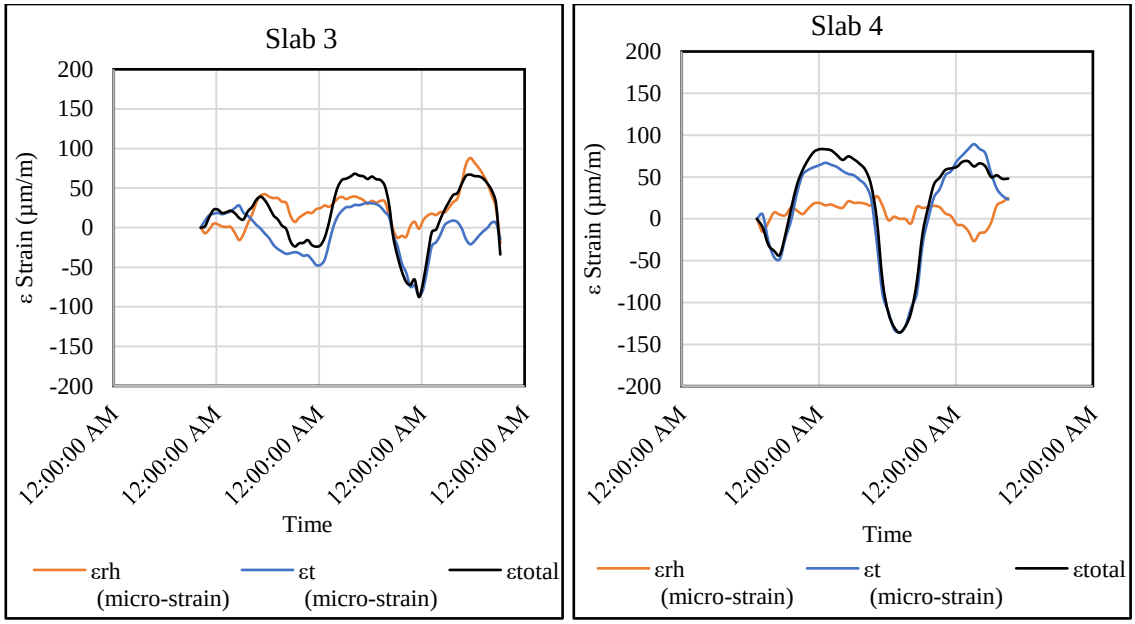

Figure 4-34. Computed Strains Due to Thermal and Moisture Gradients (Phase I)

4.2.1.6 Actual Strain Measurements

As explained in the test method, fourteen strain gauges were placed on the top and bottom of each slab at different locations, such as corners (longitudinal and transversal), mid-slabs (longitudinal and transversal), and center (see Table 4-4 and Figure 4-12). The purpose of these strain gauges was to measure the static strain and its gradient in the transverse and longitudinal directions at different positions. The final set time was regarded as the reference for determining strains. The measured strain gauges at the top and bottom of each slab are shown in Figure 4-35 to Figure 4-38. Both longitudinal and transverse strains over a 7-day period were generally expansive with respect to the initial reference measurements (which were taken roughly at the zero-stress time). The behaviors of the strain fluctuations appeared to be very similar. As expected, the trends of the strain fluctuations were positively related to the trends of the temperature fluctuations, where the concrete strains became expansive as temperature increased and became contractive when the temperature decreased.

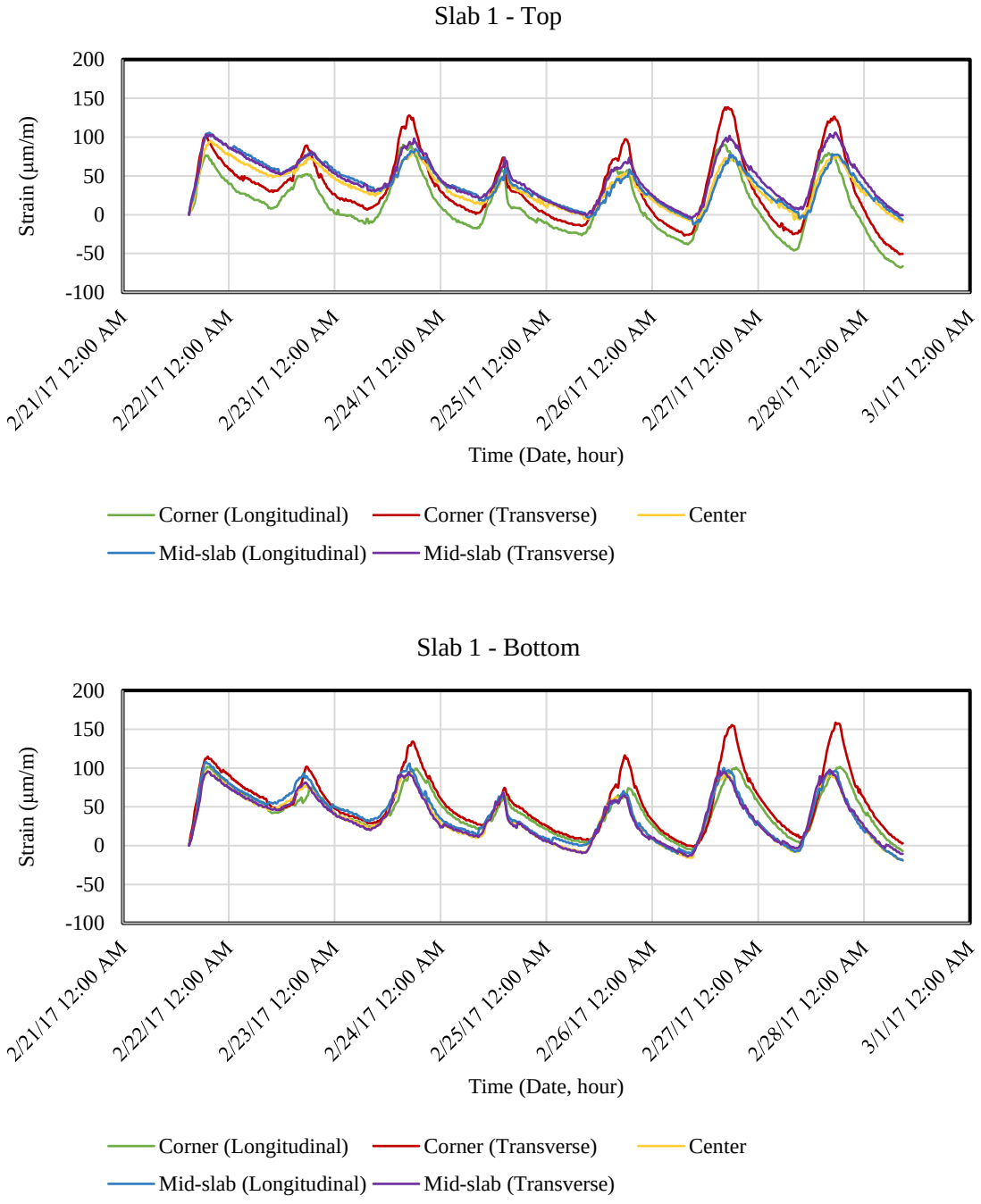

Figure 4-35. Actual Strain Measurements at Slab 1 (Top and Bottom)

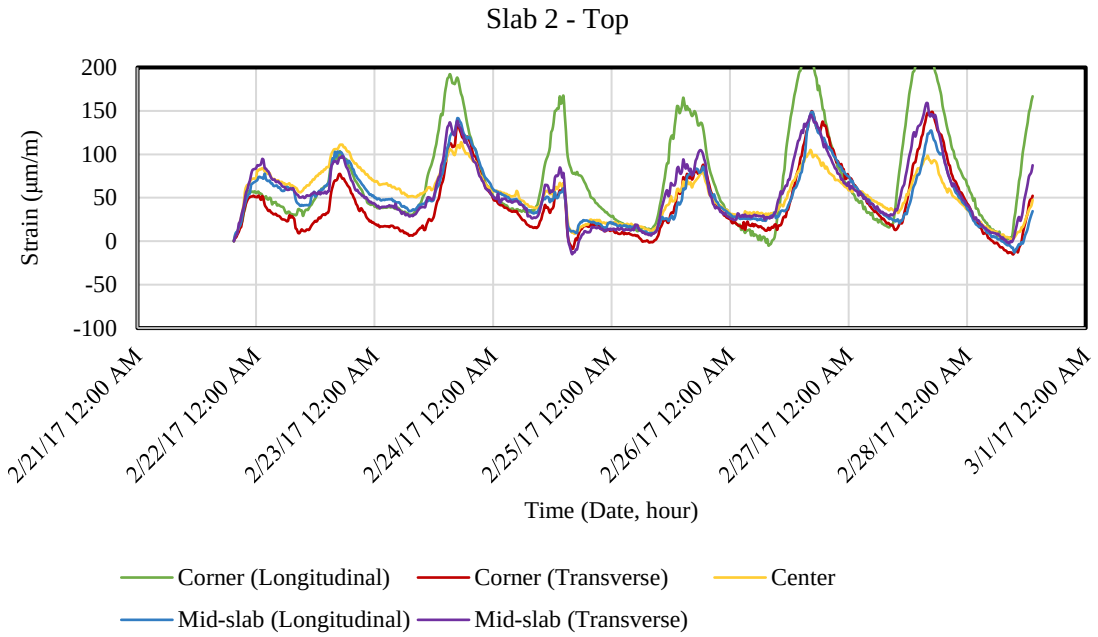

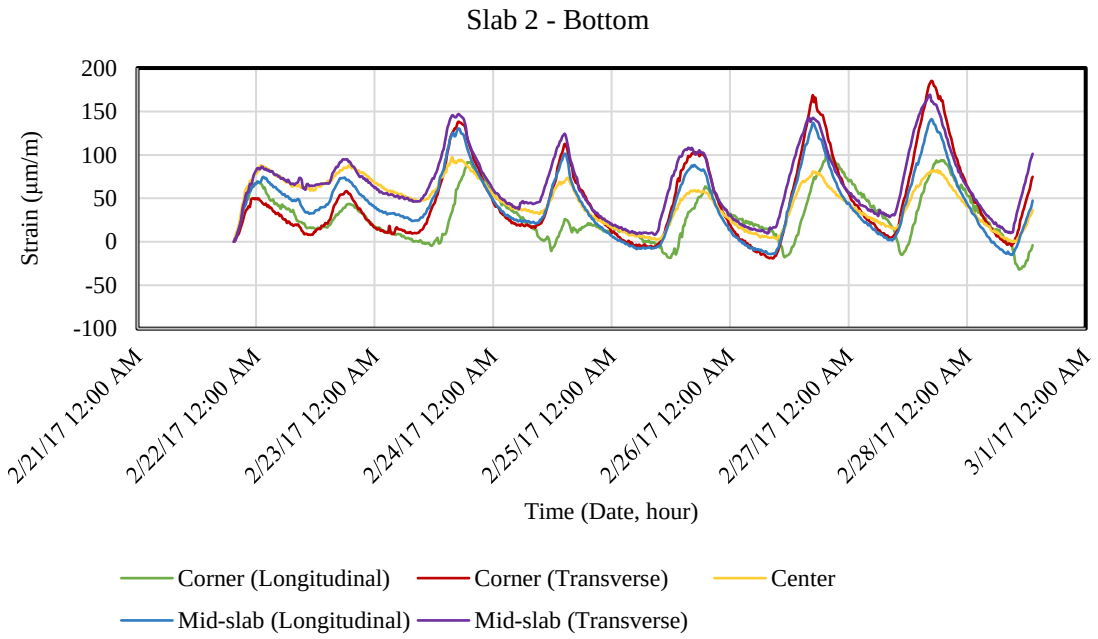

Figure 4-36. Actual Strain Measurements at Slab 2 (Top and Bottom)

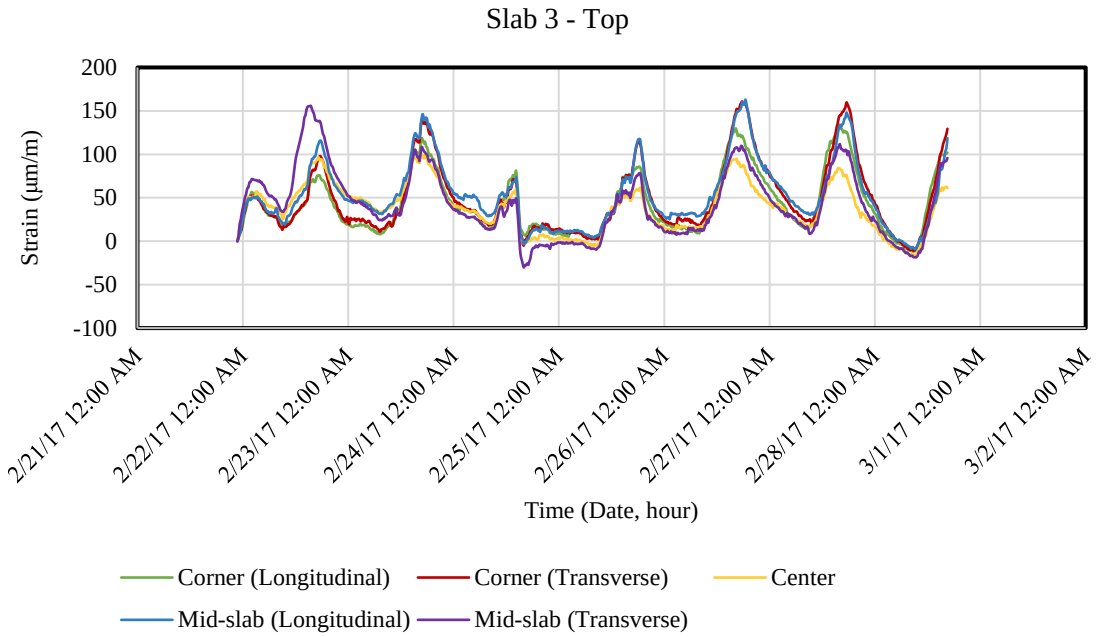

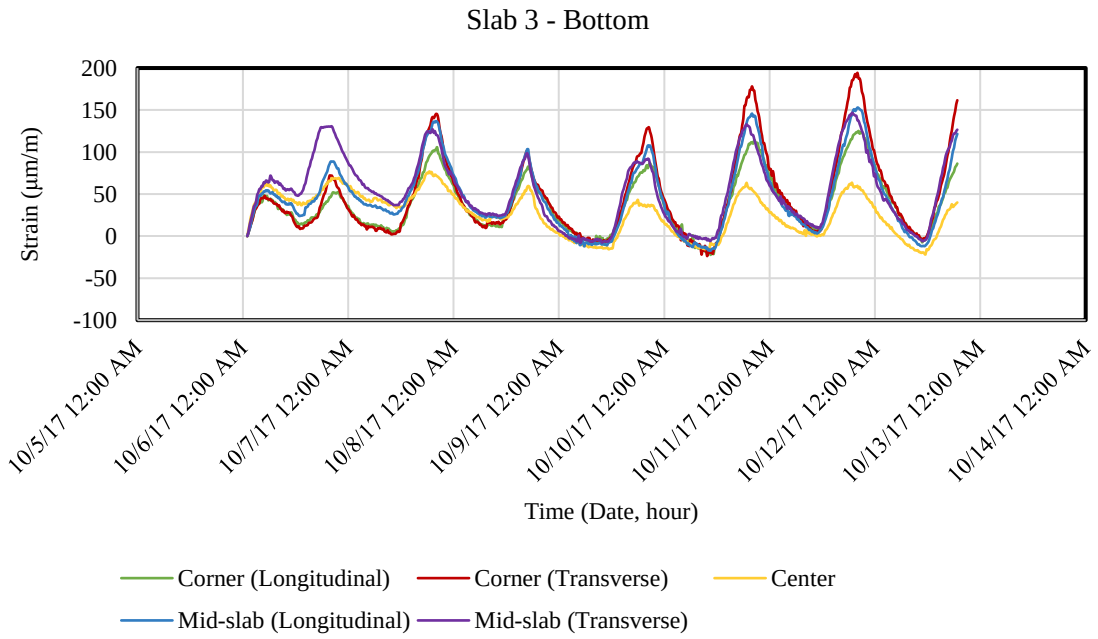

Figure 4-37. Actual Strain Measurements at Slab 3 (Top and Bottom)

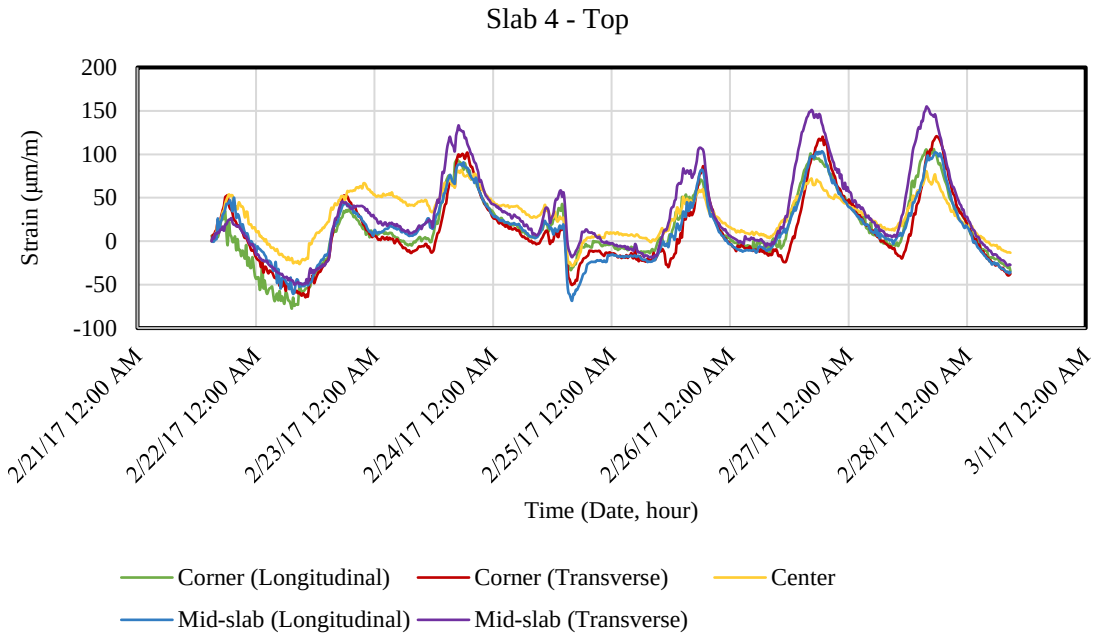

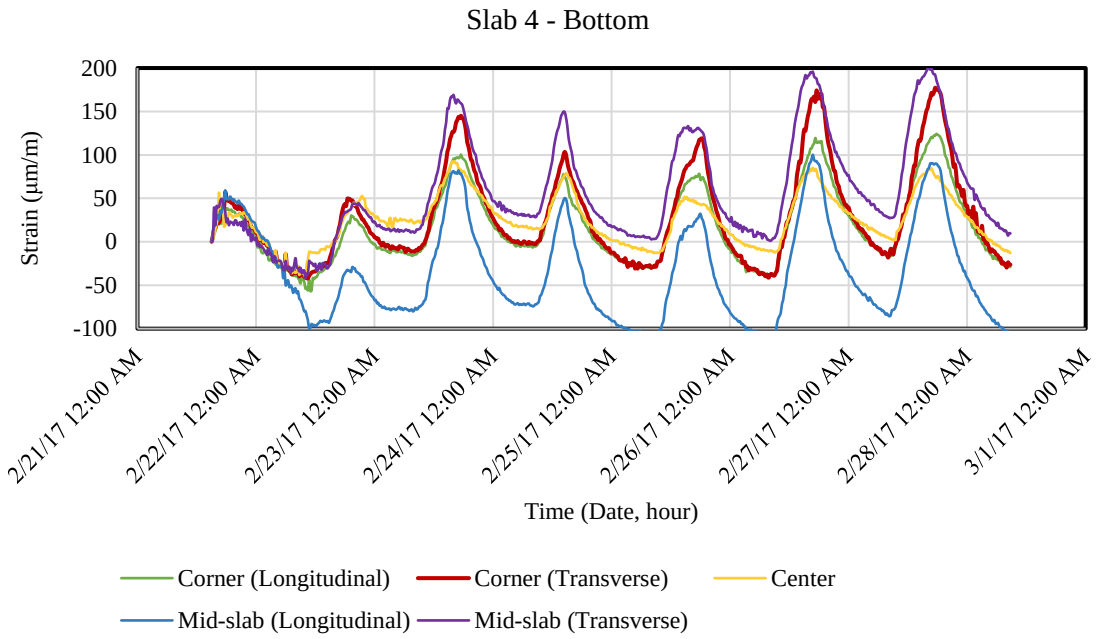

Figure 4-38. Actual Strain Measurements at Slab 4 (Top and Bottom)

There was a trend of higher strains at the top surface compared to the bottom of the slab in all four slabs. The main reason for this difference is attributed to the diurnal temperature gradients in the concrete slabs. From evening to early morning, the temperature on the top surface of the slabs was lower than that at the bottom. Although the slab was deflecting upward during this period, the slab tended to be in contact with the base as long as the curvature did not exceed the pre-compression induced from the dead-weight [170]. Thus, the slab and the base acted as a monolithic section. In this case, the neutral axis was shifted slightly downward, putting the top of the slab at a higher strain compared to the bottom of the slab. This shifting of the neutral axis due to the dead-weight of the slab (caused by the bonding between the slab and base) could be advantageous as the tensile stress at the bottom of the slab was mitigated [171, 172].

4.2.1.7 Drying Shrinkage

Volumetric shrinkage of concrete due to moisture loss was the source of internal strain, contributing to the warping of concrete slabs. During and after hardening, the concrete was subjected to shrinkage as water was evaporated and not consumed by cement hydration. The volumetric change due to the loss of capillary water is known mostly as drying shrinkage. The amount of shrinkage of a concrete mixture was determined by the use of ASTM C 157 test specimens [168]. These specimens were prepared from each slab and tested to evaluate the effects of adding a curing compound on the shrinkage rate. A VW strain gauge was used to measure the modified shrinkage strain procedure for field application via monitoring the relative humidity and temperature directly in the mold. As previously noted, moisture gradients caused permanent shrinkage upon first drying and transitory shrinkage at later ages. The reversible part varied with the daily ambient relative humidity and made daily variations in moisture warping. However, the irreversible shrinkage caused the permanent moisture warping. As shown in Figure 4-39, Slab 1 and Slab 4 had a higher shrinkage compared to the results in Slab 2 and Slab 3. Drying

shrinkage and creep strains were related to the amount of movement and distribution of moisture in a concrete slab.

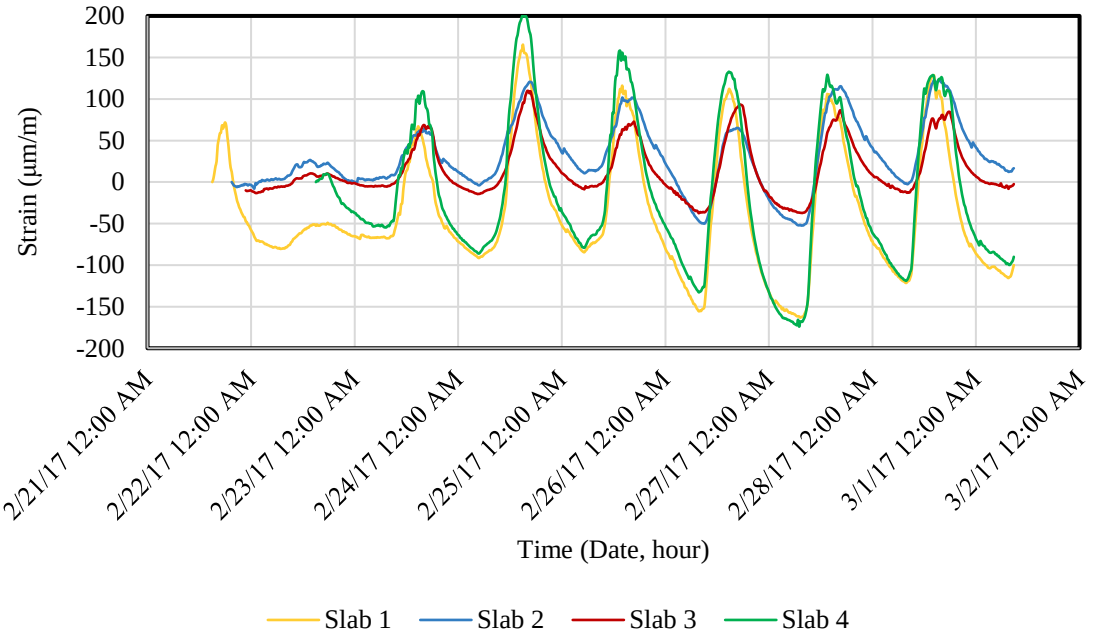

Figure 4-39. The Shrinkage Strains Data from the Four Slabs (Phase I)

4.2.1.8 *Vertical Displacement (Corner Lift-off)*

Figure 4-40 shows the vertical displacements of all four slabs in the first five days after the placement. As explained in the test method, different LVDTs were placed in the concrete to show the behavior and movement of the slabs at the early-age. In this figure, S1 represents the corner LVDT, which was located in the corner (3 inches edge offset). S2 was another LVDT 6 inches offset from S1 (or 9 inches transverse edge offset). Finally, EM is the LVDT that recorded the mid-slab movement. As LVDTs work with voltage, positive delta means that the surface gauge rod is in compression (decrease stroke), and the result is an upward slab movement. The first movement indicates that when the concrete becomes sufficiently stiff to sustain its own dead-weight, the shrinkage strain

exceeds the creep strain and induce the movement of the corner of the slab. Thus, the start point to record the vertical displacement for each slab was the final set time, as determined by ASTM C 403 [136].

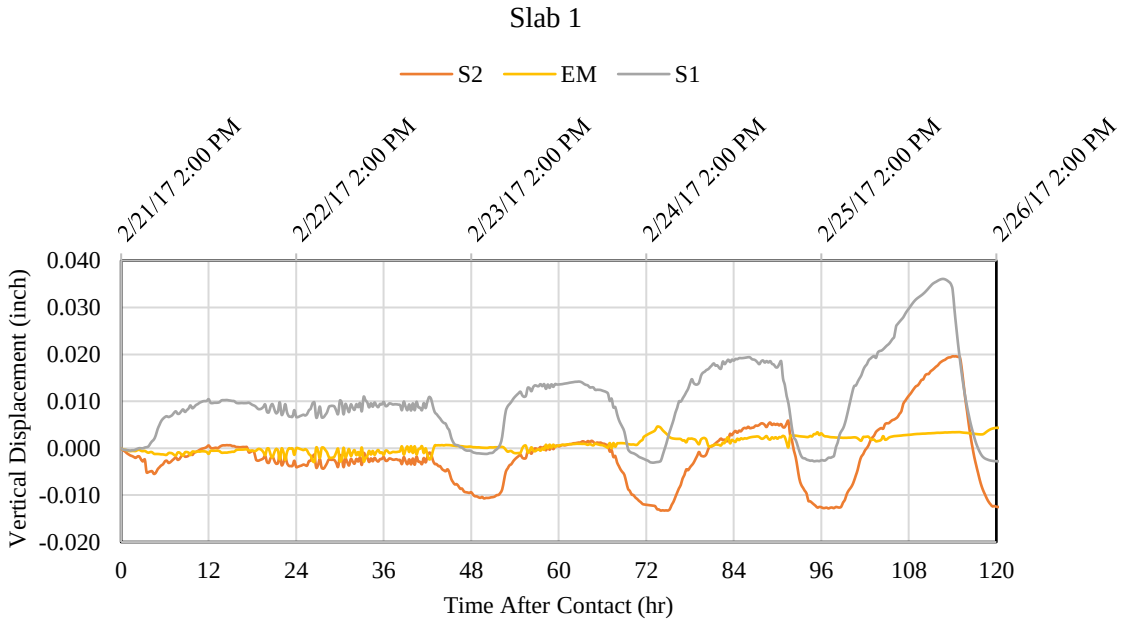

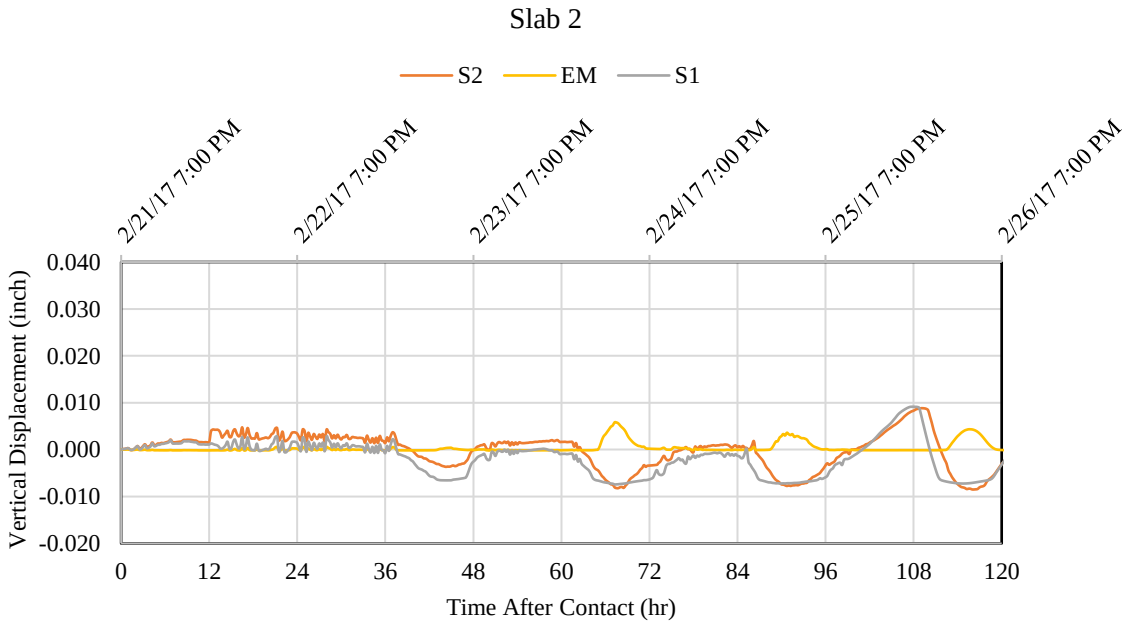

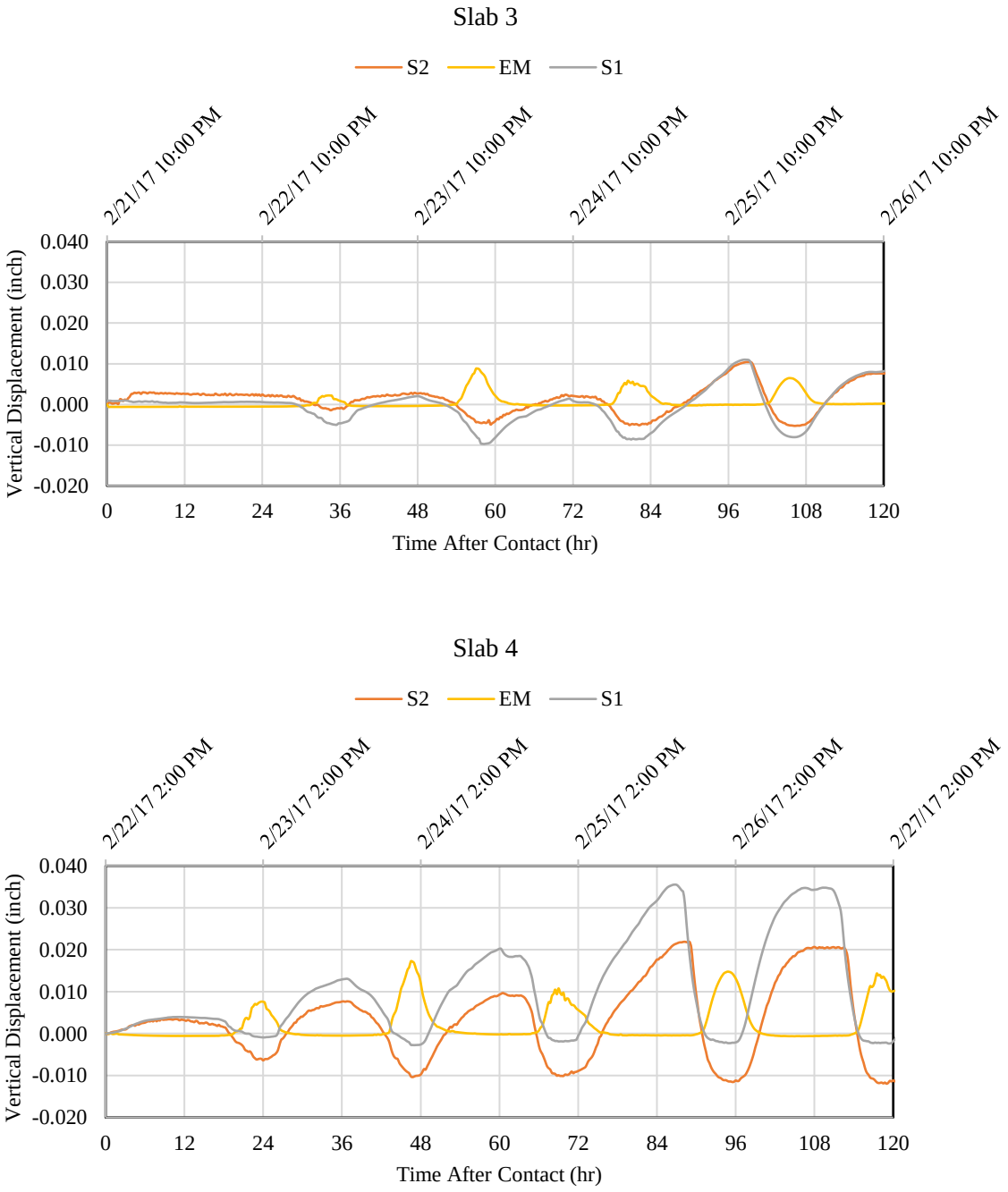

Figure 4-40. Vertical Displacement (Lift-off) of Slabs at Corners (Phase I)

The concrete pavement deformed into a concave configuration when the pavement was subjected to a resultant negative gradient of temperature and moisture through slab thickness. In Figure 4-40, the positive sign means that the corners are moving upward, and the slab configuration is turning into a concave form. As shown in Figure 4-40, the lift-off of Slab 4 was higher than other slabs, and it even reached 0.02 inches of displacement in the first two days and about 0.04 inches after five days. Slabs 2 and 3 were mainly located in the negative region and had a lower dislocation (less than 0.01 inches). The negative sign means slabs tended to have downward curling, which happened afternoon during the maximum daily temperature. Also, Slab 1 showed a relatively high displacement after five days (about 0.04 inches).

In order to show the slab curvature conditions due to varying slab temperature and moisture gradients, slabs' vertical displacements (the difference between corner and mid-slab location) are shown in Figure 4-41. The periods between sunrise and sunset are shown with light and dark colors, which represent day and night, respectively. The positive numbers show upward slab curling, wherein the corners/edges of the slab curl up. The maximum upward curling condition occurred during early morning hours, just before sunrise (at the end of the dark timeframe). In these cases, the bottom of the slab is warmer than the top surface. However, the maximum downward curling condition occurred around noon or in the early afternoon, in which the slab surface was heated by the sun (in the middle of the light timeframe). Under these situations, the top surface of the slab was warmer than the bottom. Slab 4 and Slab 1 had the highest vertical displacement differences. It means that the degree of the upward curling was much higher in these two slabs, which were not cured well. Thus, the curing practices can influence the performance and the built-in curling/warping of the slabs directly.

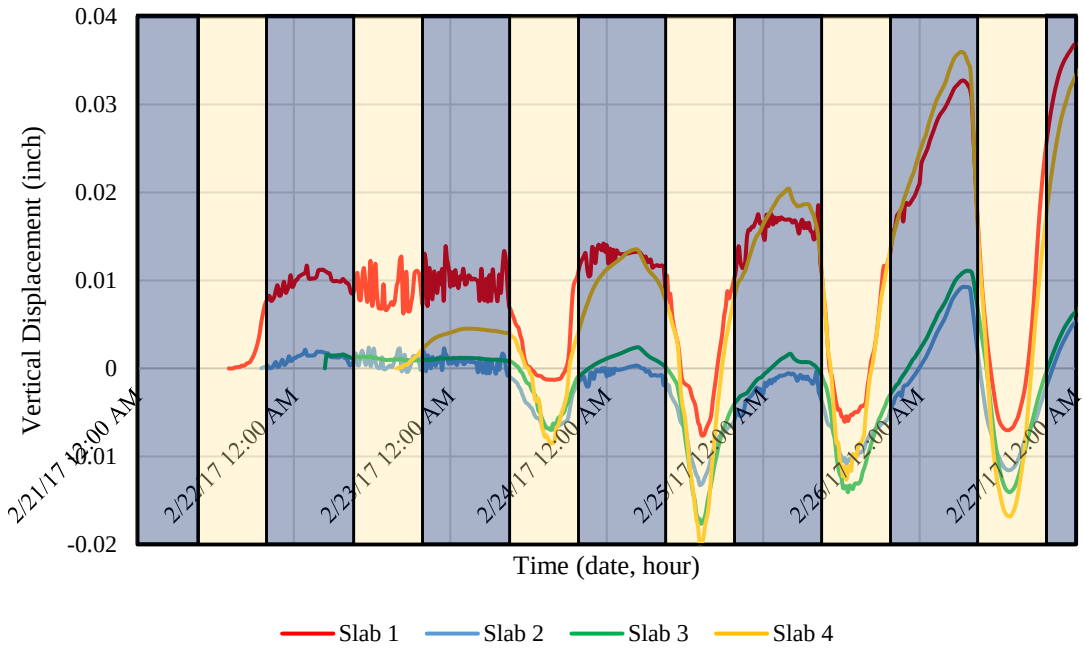

Figure 4-41. Slabs' Vertical Displacement after the Final Set Time

4.2.1.9 Compressive Strength

The compressive strength of 4×8 inches cylinders at the ages of 3, 7, 14, 28, and 56 days old were tested on each slab. For each specific time, three samples were provided, and the average strength was reported. The values of the test results of compressive strength for all the specimens are given in Table 4-8. The compressive results of all samples up to 56 days are shown in Figure 4-42. Cylinders subjected to the better curing method (Slab 2 and Slab 3) showed the highest compressive strengths.

Table 4-8. Cylinder Samples Compressive Strength Results (Phase I)

	Properties	Age														
		3 days			7 days			14 days			28 days			56 days		
		#1	#2	#3	#1	#2	#3	#1	#2	#3	#1	#2	#3	#1	#2	#3
Slab 1	Avg length (in)	8.00	7.90	8.00	7.90	7.90	8.00	7.90	7.70	7.80	8.00	7.90	8.00	7.60	7.60	8.00
	Avg Dia (in)	4.03	4.03	4.03	4.02	4.00	4.03	4.03	4.00	4.03	4.03	4.03	4.00	4.03	4.00	4.03
	Area (in^2)	13.10	13.10	12.60	13.10	12.50	13.40	13.30	13.30	12.50	13.00	12.80	12.70	13.40	13.00	13.10
	f' (psi)	2465	2528	2520	3368	2933	2940	4092	3800	4254	4444	4382	4381	4626	4190	2465
	ρ (lb/ft^3)	140	141	141	139	140	141	140	139	140	140	140	138	139	138	140
	Avg f' (psi)	2504.333			3080.333			4048.667			4402.333			4489		
	Avg ρ (lb/ft^3)	141			140			140			139			138		
Slab 2	Avg length (in)	7.80	7.90	7.60	8.00	8.00	8.00	7.90	8.00	7.90	7.70	7.90	8.00	8.00	7.90	7.80
	Avg Dia (in)	4.03	4.00	4.00	4.05	4.03	4.01	3.98	3.99	4.00	3.99	4.02	4.01	4.03	4.00	4.03
	Area (in^2)	13.40	13.30	13.50	12.60	13.20	13.60	13.60	13.20	12.80	13.30	13.70	13.60	12.70	13.70	13.40
	f' (psi)	2849	2921	2886	3866	3917	3877	4908	4578	4318	4850	4906	4910	5747	5568	2849
	ρ (lb/ft^3)	141	143	142	142	143	139	141	140	141	141	142	141	142	141	144
	Avg f' (psi)	2885.333			3886.667			4601.333			4888.667			5620.333		
	Avg ρ (lb/ft^3)	142			142			141			141			142		
Slab 3	Avg length (in)	8.00	8.00	8.00	8.00	8.00	8.00	7.90	8.00	8.00	7.90	8.00	7.80	8.00	8.00	8.00
	Avg Dia (in)	4.05	4.02	4.02	4.07	4.05	4.03	4.00	4.01	4.00	4.01	4.00	4.03	4.05	4.02	4.05
	Area (in^2)	13.30	13.00	13.40	12.60	13.40	13.20	13.20	13.20	12.90	12.60	13.40	12.80	12.70	12.90	13.30
	f' (psi)	2866	2905	2872	3877	3920	3860	4924	4595	4324	4852	4910	4892	5752	5574	2866
	ρ (lb/ft^3)	143	143	142	141	143	140	141	140	140	141	141	141	142	141	143
	Avg f' (psi)	2881			3885.667			4614.333			4884.667			5627		
	Avg ρ (lb/ft^3)	142			142			140			141			142		
Slab 4	Avg length (in)	8.00	7.90	8.00	8.00	7.60	8.00	8.00	8.00	8.00	7.70	7.70	8.00	7.90	7.70	8.00
	Avg Dia (in)	4.03	4.04	4.03	4.02	4.00	4.02	4.03	4.00	4.03	4.03	4.03	4.00	4.03	4.00	4.03
	Area (in^2)	12.90	12.70	13.00	13.20	13.10	13.20	13.10	13.20	13.00	12.70	13.10	13.30	13.10	13.30	12.90
	f' (psi)	2083	1995	2104	2676	2838	2620	3227	3351	3204	3893	4030	3670	4188	3991	2083
	ρ (lb/ft^3)	140	139	141	140	141	142	140	140	139	140	140	141	140	140	140
	Avg f' (psi)	2060.667			2711.333			3260.667			3864.333			4196.667		
	Avg ρ (lb/ft^3)	140			139			139			140			138		

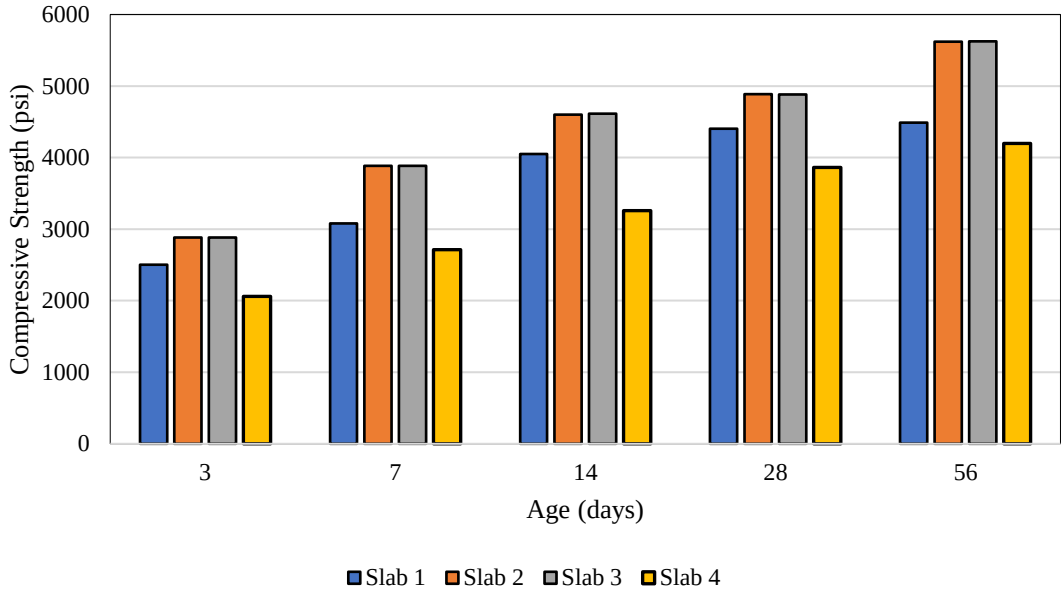

Figure 4-42. Compressive Strength Results of Cylinder Samples (Phase I)

4.2.1.10 Microscopic Analysis (Thin Section)

One of the direct indicators of curing effectiveness was the microstructure characterization of concrete by thin section microscopic analysis. The concrete samples were removed by core testing from each slab at 7 days and were taken to the laboratory for microscopic analysis. The 20-micron thick sample of concrete epoxied to a glass slide were prepared for the examination of the paste microstructure and porosity, as shown in Figure 4-43. The Slab 4 sample had many voids due to the moisture loss during the early ages. However, that use of curing compounds at higher application rates (on Slab 2 and Slab 3) formed a barrier on the concrete surface that led apparently to fewer pore structures and size distributions at or near the surface of the cured concrete (as compared to the sample from Slab 4).

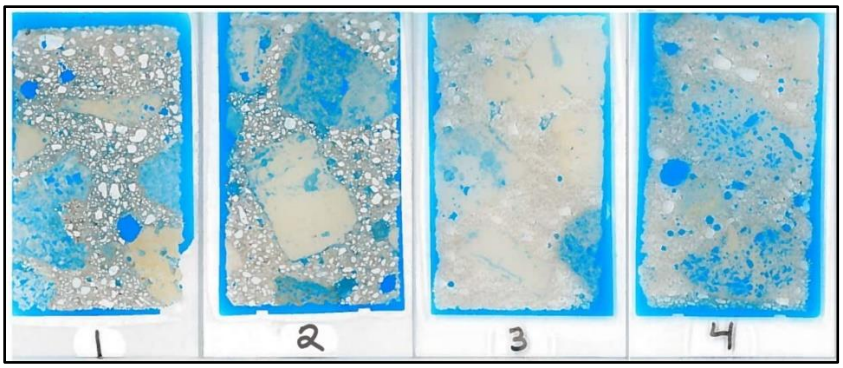

Figure 4-43. Thin Sections from the Cored Specimens of Four Slabs (Phase I)

Thin section images were analyzed with a microscope imaging program that calculated the quantity and concentration of voids based on the measurement of the voids area. In this study, the formation of bleed channels was related to curing effectiveness. These channels were typically irregularly shaped and were created in the paste by bleed water rising to the slab surface passing by aggregate particles or along aggregate boundaries. Slabs 1 to 4 had 2.23%, 1.98%, 1.52% and 4.35% bleed water voids content, respectively.

4.2.1.11 Random Slab Cracking Probability

Cracking will be induced when the restrained stress (the crack driving force, *S*) exceeds the critical level of the tensile strength (the resistance force, *R*) of concrete, i.e., $S \geq R$. The stress is denoted by σ and the strength was denoted by f with an appropriate subscript. The probability of cracking can be modeled assuming that the σ and the f are random variables with a mean and a distribution. Therefore, the probability of cracking P_{cr} can be expressed as shown in Eq. (4-9):

$$P_{cr} = P(Z = \sigma_{cr} - f_t \geq 0) \quad (4\text{-}9)$$

The calculation of P_{cr} can be simplified as shown in Eq. (4-10) by assuming that σ_{cr} and f_t are independent from each other and they follow normal distribution.

$$P_{cr} = \phi\left[\frac{\xi - 1}{\sqrt{COV[f_t]^2 + \xi^2 . COV[\sigma_{cr}]^2}}\right] \quad (4\text{-}10)$$

where,

ϕ = standard normal probability distribution function,

σ_{cr} = cracking stress,

f_t = tensile strength of concrete,

$COV[\sigma_{cr}]$= coefficient of variation of σ_{cr},

$COV[f_t]$= coefficient of variation of f_t,

$$\xi = \frac{\mu_\sigma}{\mu_{f_t}} \quad (4\text{-}11)$$

$\mu_{\sigma_{cr}}$ = expected value of σ_{cr}, and

μ_{f_t} = expected value of f_t

The concept of the probability of failure is demonstrated in Figure 4-44 according to the description given above. The intersection between the stress and the strength distribution represents the area of failure (or the probability of failure), as shown with the red color in Figure 4-44.

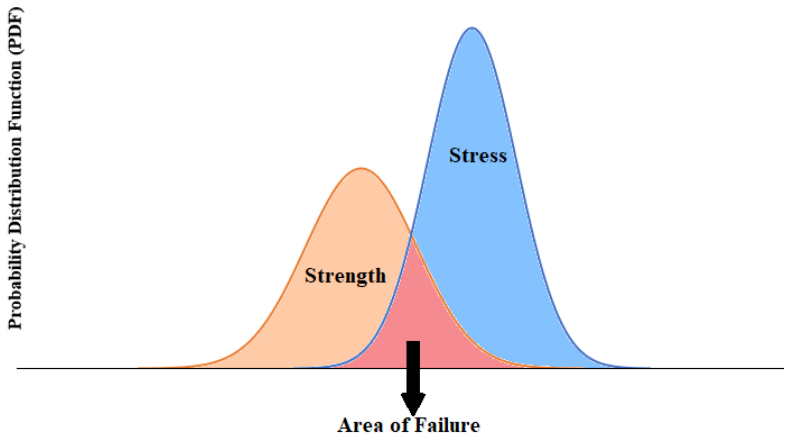

Figure 4-44. Stress and Strength as the Normally Distributed Variables

The cracking probabilities for different placements are shown in Figure 4-45. Using higher application rates or better compounds (Slab 2 and Slab 3) decreased the cracking probability. In Slab 1 and Slab 4, the cracking thresholds had not been met. Moreover, as the set and creep are related, the growth of creep strain in concrete did have impacts on the cracking tendency of concrete. The data determined that a greater random cracking tendency did not result until after the incremental creep strain in the concrete had diminished sufficiently [173]. Cracking in the slabs is inherently random due to the lack of saw cut notches and the fact that the slabs were a typical length, so the potential for cracking is between where the notches would be placed.

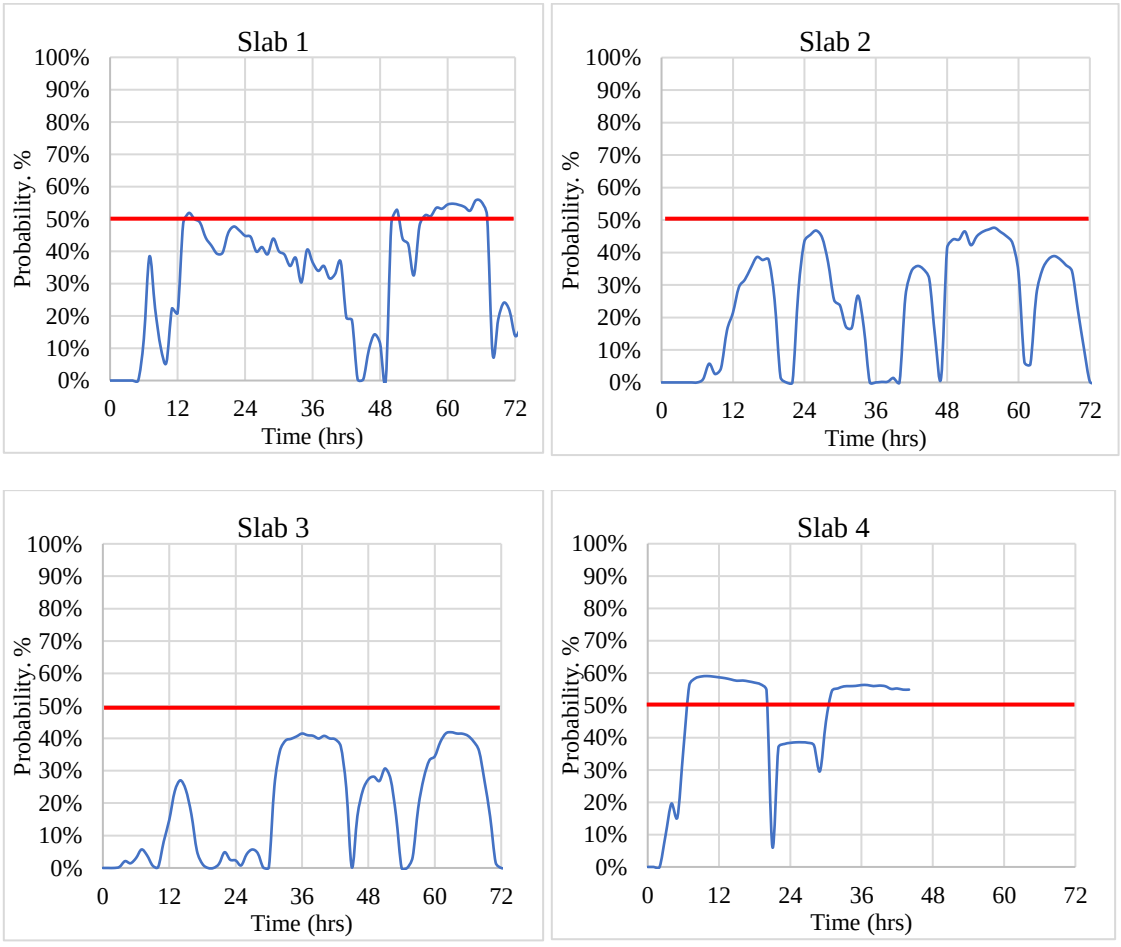

Figure 4-45. Cracking Probabilities for Different Placement Times (Phase I)

4.2.2 Phase II Results

The results of data collection for Phase II with the purposes of achieving the predetermined set gradient in one slab and analyzing the set behavior are presented in the following paragraphs.

4.2.2.1 Setting Time

Results of penetration are shown in Figure 4-46 and Table 4-9. A penetration specimen was prepared for each slab, and data points were obtained just after concrete placement [136].

Table 4-9. The Penetration and Concrete Maturity Results (Phase II)

	Batch Mix Time	Placement		Setting Time (min)		Application Rate (ft^2/gal)
		Start	Finish	Initial	Final	
Slab 1	10/6/2017 10:00	10:45	11:20	245	280	180
Slab 2	10/6/2017 13:45	14:30	15:05	280	335	180
Slab 3	10/6/2017 17:20	17:35	18:10	270	350	250

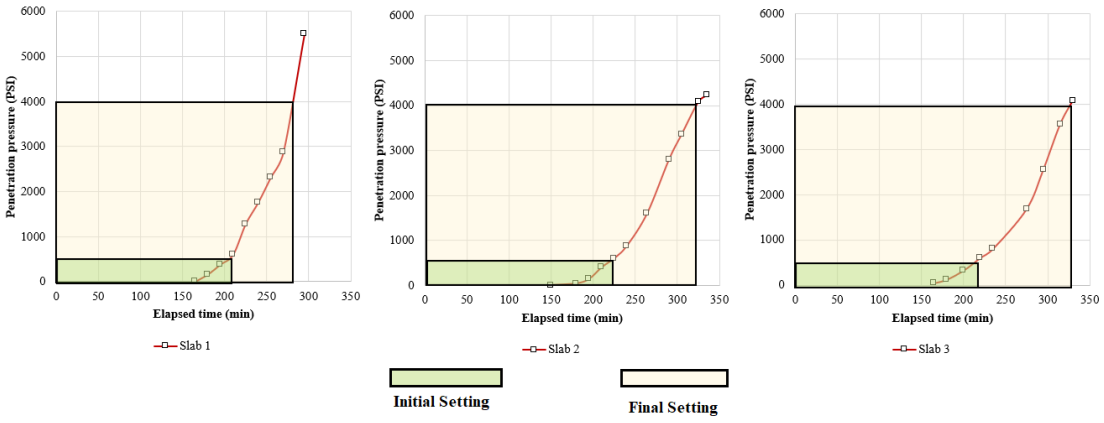

Figure 4-46. Penetration Test Results Based on ACI C 403 (Phase II)

The temperature history of different slabs was used to calculate the maturity index, as shown in Figure 4-47. In order to use data from the set time molds to compare maturity development between slabs, it should be assumed that the concrete for each slab arrives at the site in a similar maturity condition.

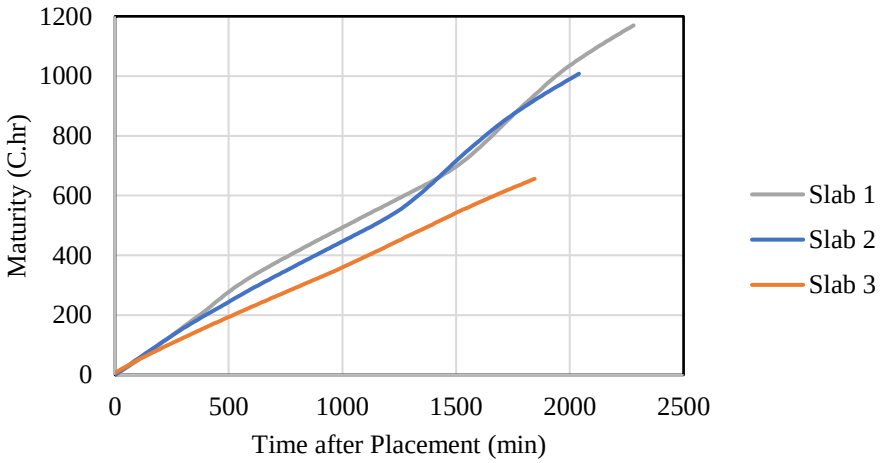

Figure 4-47. Maturity of the Slabs After Placement (Phase II)

Figure 4-48 shows the concrete temperature from the early hydration of cementitious materials on slabs. For each slab, three cylinders had a thermometer that measured temperature continuously. The shape of the temperature curves obtained through this test indicates the effects of time of placement. Figure 4-48 indicates that paving slabs in the morning and at noon increased the concrete temperature due to the rate of hydration. However, mild/cold conditions in the afternoon decreased the rate of the hydration process. Based on the degree of hydration, the built-in gradient can be either positive or negative. Thus, it can impact behavior and configuration of the slabs at the early-age.

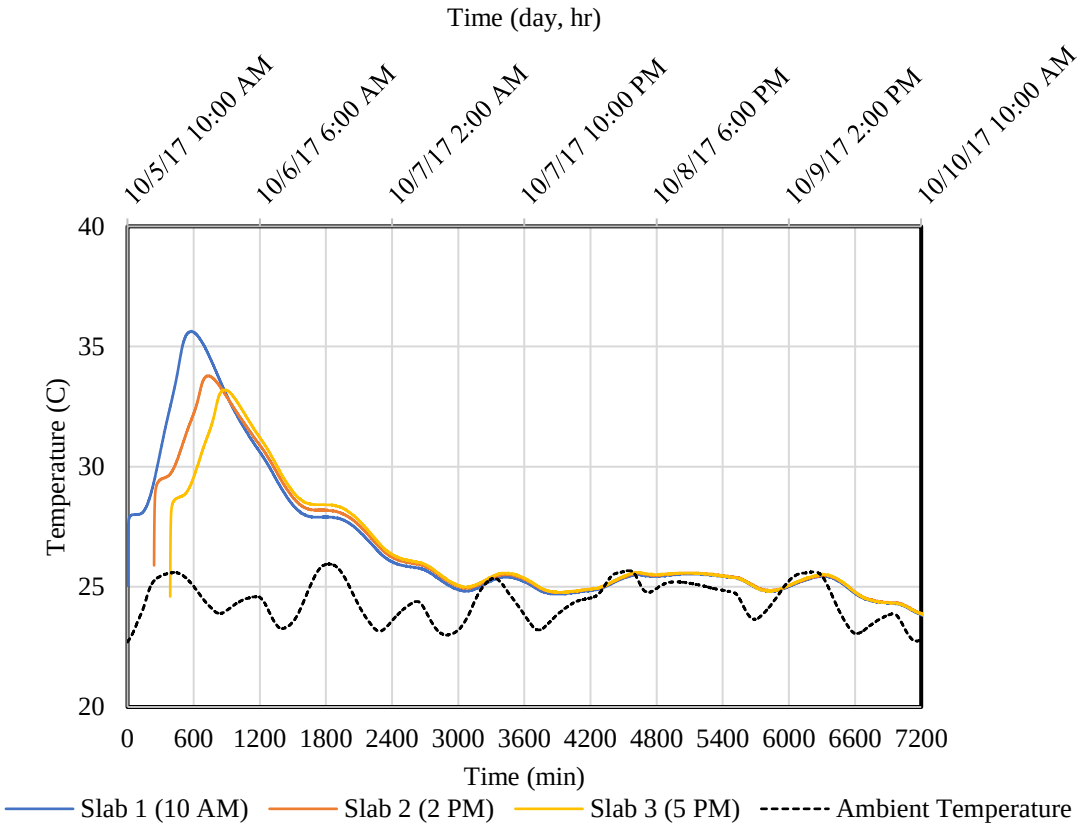

Figure 4-48. Maturity Data After Concrete Placement (Phase I)

4.2.2.2 EI Determinations

The concrete curing evaluation approach (EI) was based on the moisture-modified maturity concept, as shown in Figure 4-49. EI values for afternoon placement (Slab 3) was slightly higher than the morning placements (Slab 1 and Slab 2). Both Slab 2 and Slab 3 were treated with the same curing compound and application rate. Thus, the difference between EI of these two slabs was insignificant. Slab 2 and Slab 3 were placed in the afternoon, which coincided with the peak of daily temperature. The high temperature at the beginning of the data collection caused EI to begin from very low levels to stable in Slab 2 and Slab 3. However, EI in Slab 1 started at 0.5. Finally, the relative humidity in

both sealed and filtered chambers remained at very high levels (more than 90%) most of the time.

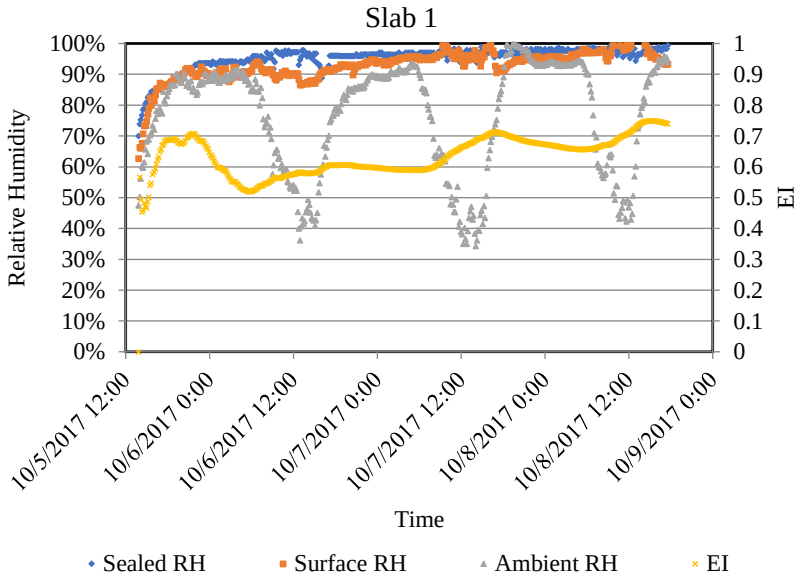

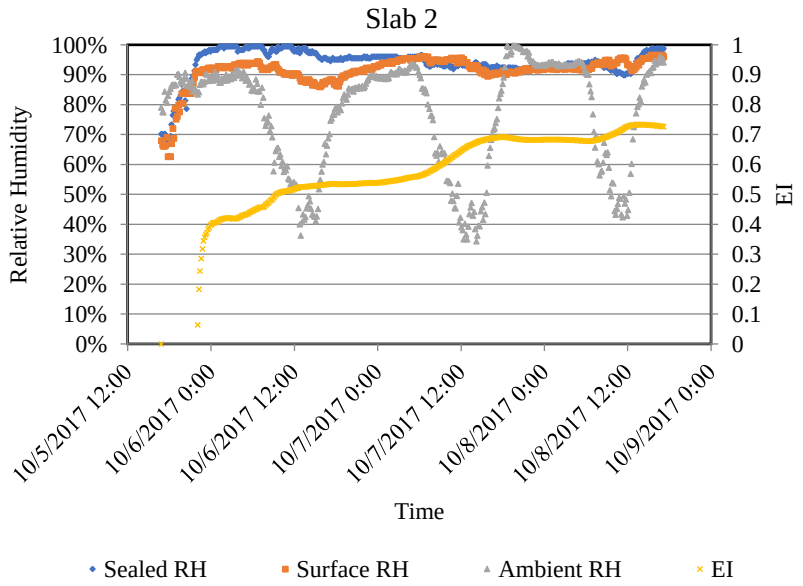

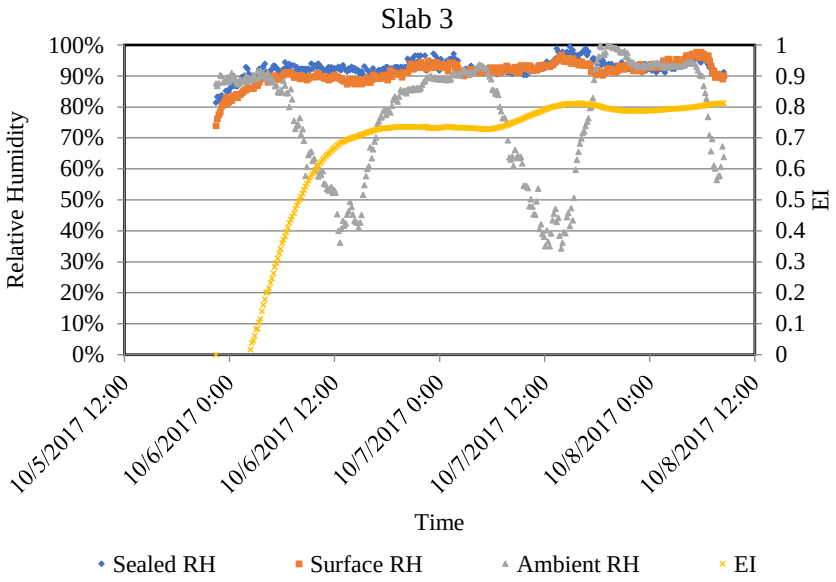

Figure 4-49. EI Determination and Relative Humidity (Phase II)

4.2.2.3 Dielectric Constant Measurements

DC measurements can be used to interpret curing quality. In early-age concrete, when the volumetric moisture content was high, DC measurements were high. However, after a few hours, the DC readings started to decrease due to moisture loss from the water evaporation and the cement hydration, as shown in Figure 4-50. The dielectric trends in all slabs were quite similar; however, the rate of decreasing was different. The beta parameter (from the regression model) in Slab 2 was 0.082, which was higher than Slab 1 and Slab 3 (0.072 and 0.065, respectively).

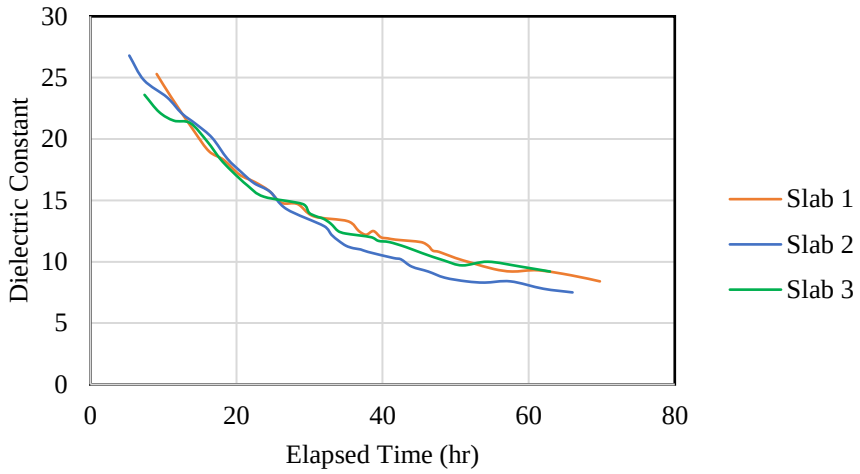

Figure 4-50. Dielectric Constant Measurements (Phase II)

4.2.2.4 Temperature Gradients

Figure 4-51 displays the temperature of three slabs at three depths, which were measured over the first 80 hours after the placement of concrete. The differences in the temperature of concrete pavements help provide a better understanding of the distribution profiles and later the set gradient.

There was a temperature differential between the top and the bottom of the slabs. The layer temperatures were higher than the ambient air temperatures at night, and the magnitude of this difference varied with time and depth. The slabs were subjected to larger temperature gradients during the day, in which slab temperature was lower than the ambient air temperature. Slab temperatures increased in the morning due to solar radiation and dropped later in the evening, as the solar energy diminished. Also, the equivalent linear temperature gradients of the slabs are shown in Figure 4-51. The temperature gradient of Slab 1 was slightly higher than the other slabs.

Furthermore, by comparing Phase I and Phase II constructions, the slab temperature of Phase I was much lower than that of Phase II construction. This difference

was due to the lower ambient temperature in February (Phase I) and the less intensive solar radiation.

Slab 1

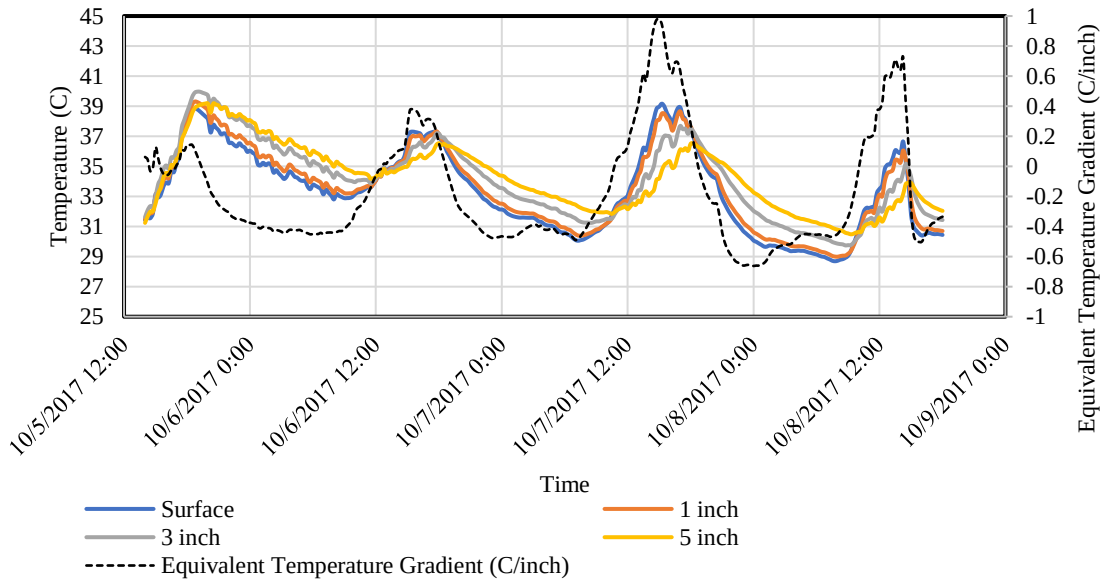

Slab 2

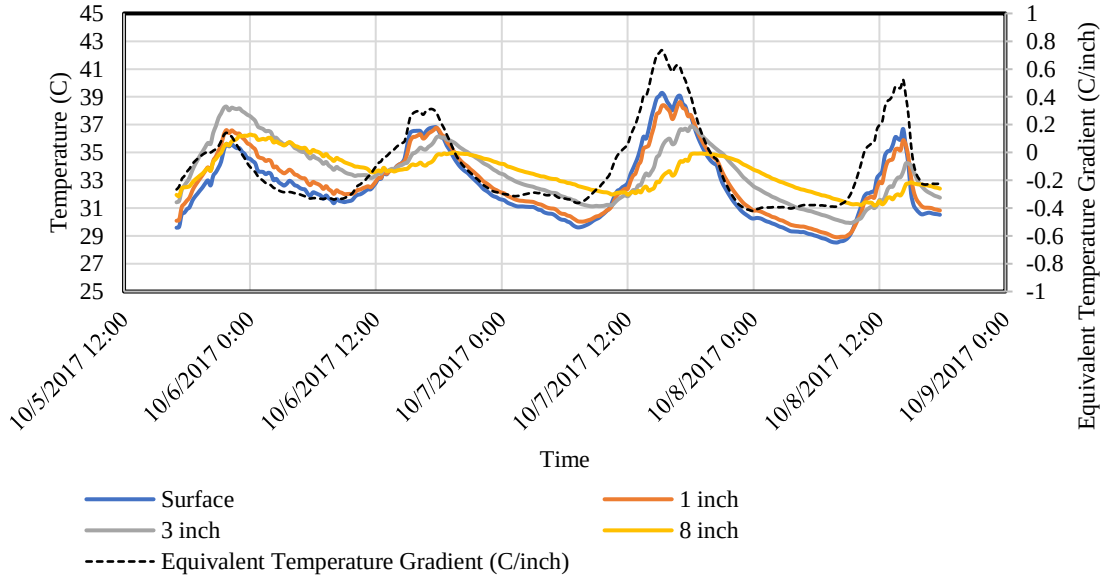

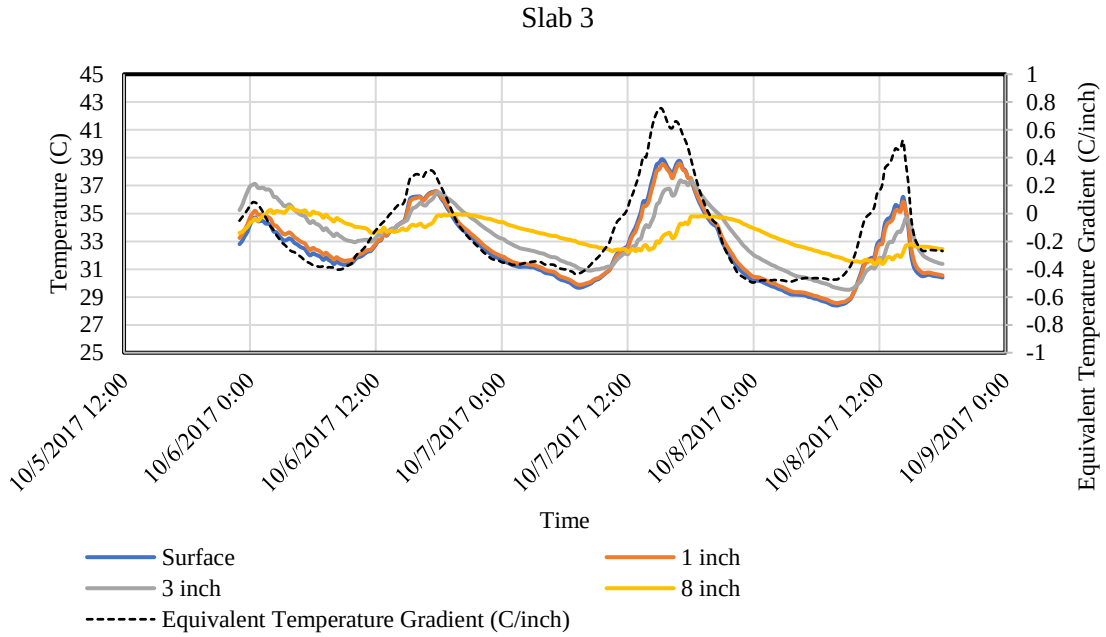

Figure 4-51. Temperature Profiles and Equivalent Gradients (Phase II)

Figure 4-52 to Figure 4-54 display the measured temperatures at various depths of the slab in the first three days after concrete placement on all slabs. The temperature profiles are displayed in 2-hour increments. In all slabs, there were relatively uniform temperature profiles on the first day after the concrete placement.

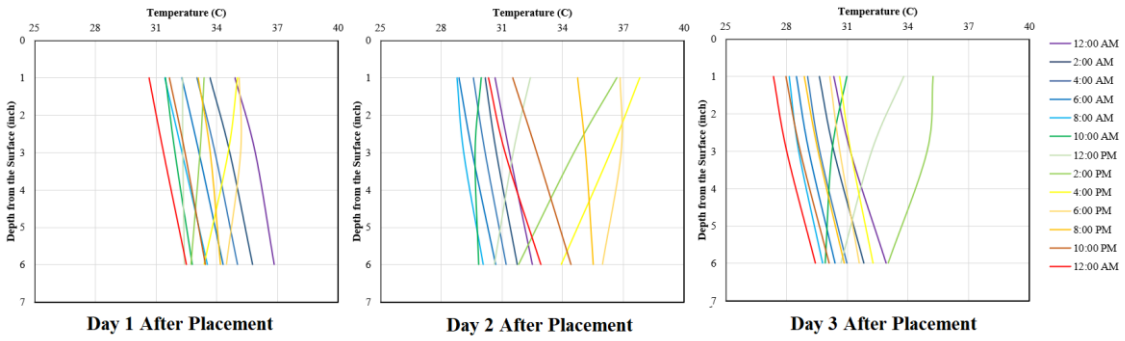

Figure 4-52. Measured Temperature Gradients versus Time for Slab 1 (Phase II)

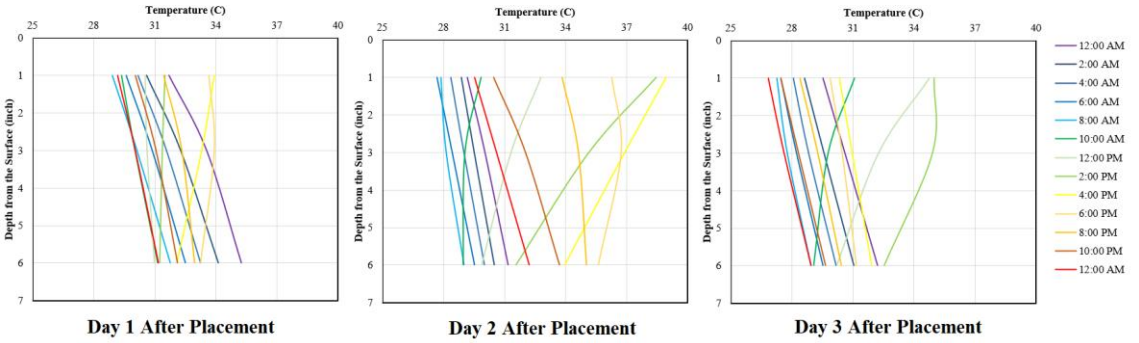

Figure 4-53. Measured Temperature Gradients versus Time for Slab 2 (Phase II)

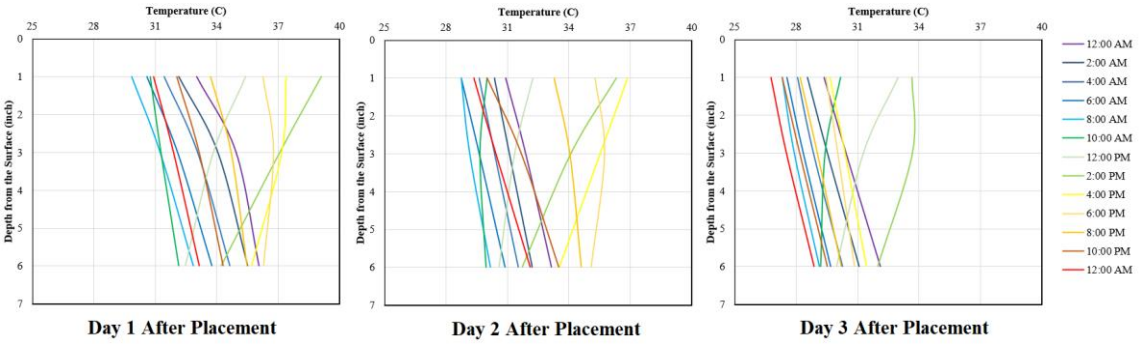

Figure 4-54. Measured Temperature Gradients versus Time for Slab 3 (Phase II)

4.2.2.5 Relative Humidity Gradients

Figure 4-55 displays the relative humidity of three slabs at three depths, which were measured over the first 80 hours after the placement of concrete. the variations of the slabs' relative humidity were different from the temperature trend. The relative humidity near the slab surface was continuously increasing during the first 20 hours after placement. When the concrete set, the relative humidity at different depths of the slab were consistent with the quality of the curing. The gradient of the relative humidity is also shown in Figure 4-55. The highest gradient (with the negative sign) happened in the afternoon, which coincided with the highest temperature during the day. This negative gradient indicated that the relative humidity level on the surface dropped due to water evaporation while the relative humidity at deeper layers remained at a very high value.

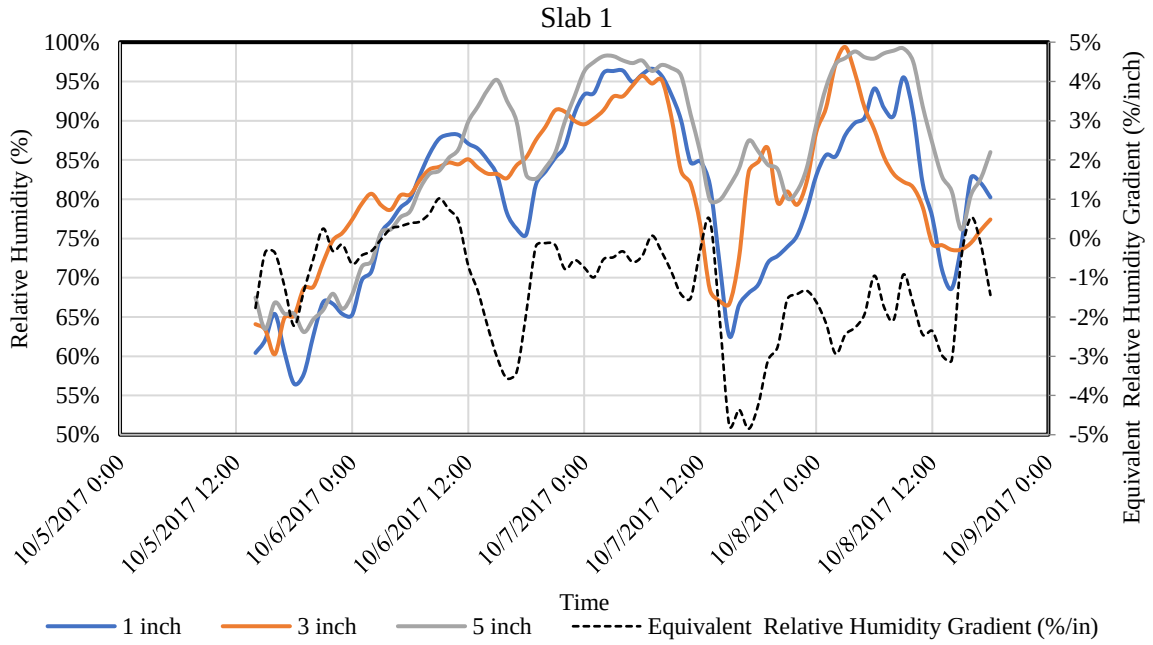
Slab 1
100%
95%
90%
85%
80%
75%
70%
65%
60%
55%
50%
Relative Humidity (%)
5%
4%
3%
2%
1%
0%
-1%
-2%
-3%
-4%
-5%
Equivalent Relative Humidity Gradient (%/inch)
10/5/2017 0:00
10/5/2017 12:00
10/6/2017 0:00
10/6/2017 12:00
10/7/2017 0:00
10/7/2017 12:00
10/8/2017 0:00
10/8/2017 12:00
10/9/2017 0:00
Time
1 inch
3 inch
5 inch
Equivalent Relative Humidity Gradient (%/in)

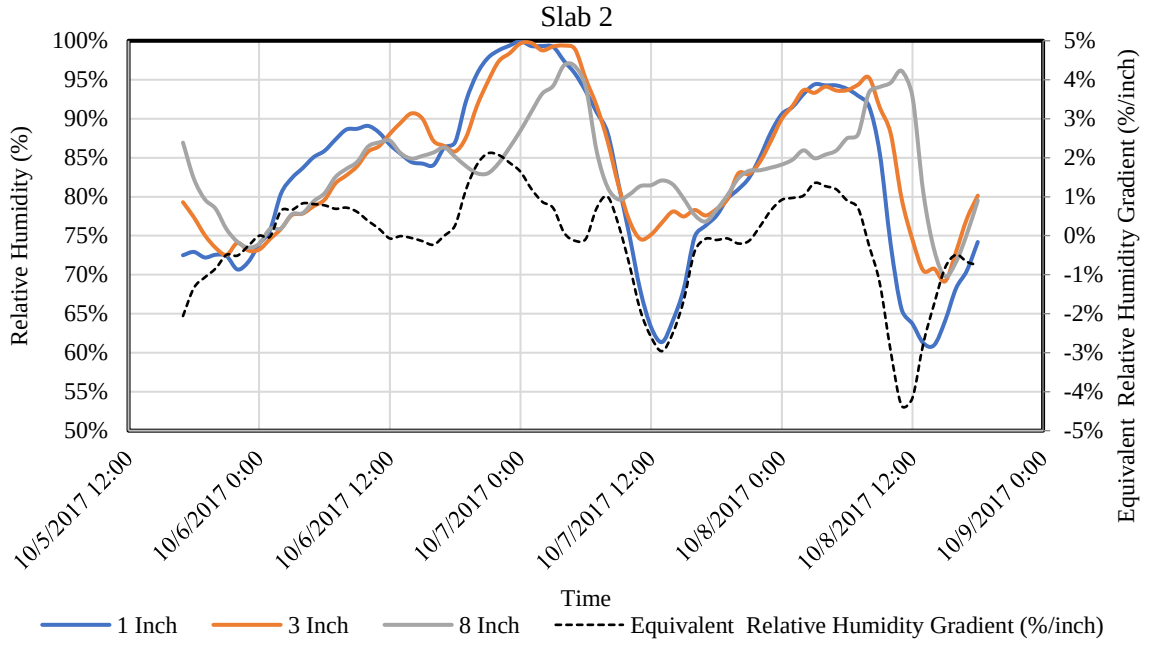
Slab 2
100%
95%
90%
85%
80%
75%
70%
65%
60%
55%
50%
Relative Humidity (%)
5%
4%
3%
2%
1%
0%
-1%
-2%
-3%
-4%
-5%
Equivalent Relative Humidity Gradient (%/inch)
10/5/2017 12:00
10/6/2017 0:00
10/6/2017 12:00
10/7/2017 0:00
10/7/2017 12:00
10/8/2017 0:00
10/8/2017 12:00
10/9/2017 0:00
Time
1 Inch
3 Inch
8 Inch
Equivalent Relative Humidity Gradient (%/inch)

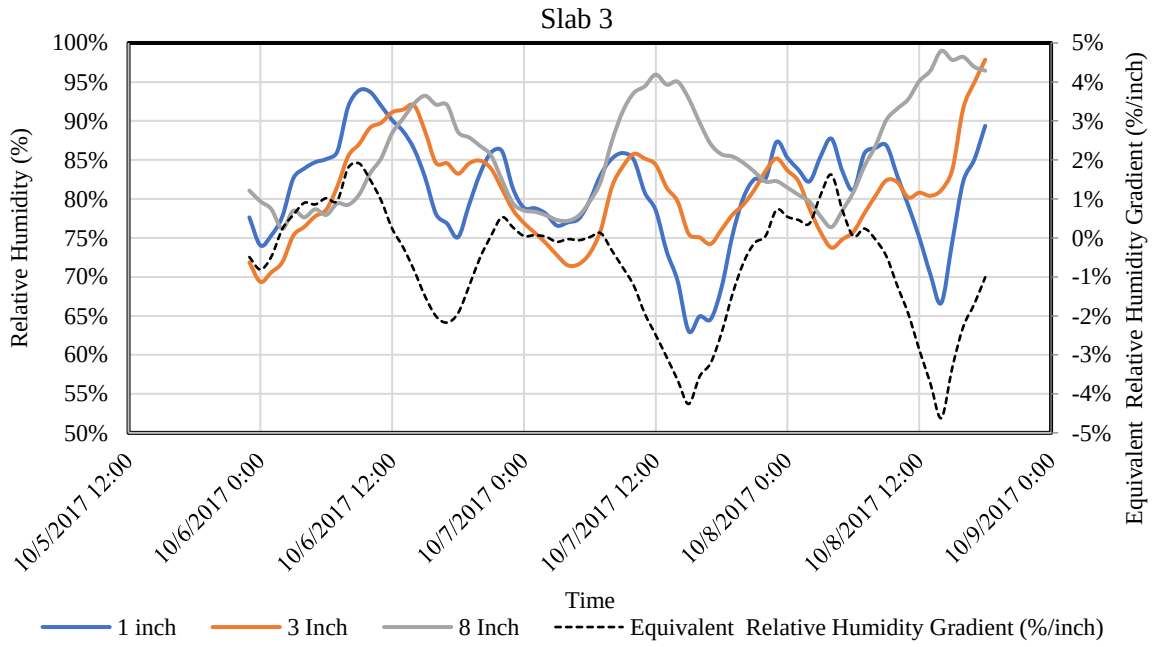

Figure 4-55. Relative Humidity Profiles and Equivalent Gradients (Phase II)

4.2.2.6 Computed Strains

As displayed in Figure 4-56, the net (effective) strain in Slab 3 and Slab 2 was lower than Slab 1. The reason was attributed to the better curing and time of placement. These results were in accordance with the amount of moisture and temperature gradients. Low temperature and moisture gradients were anticipated in well-cured concrete and a lower set. The purpose of strain computation was to calculate the difference between measured strains with theoretical strains, which was associated with the combined thermal and shrinkage strains.

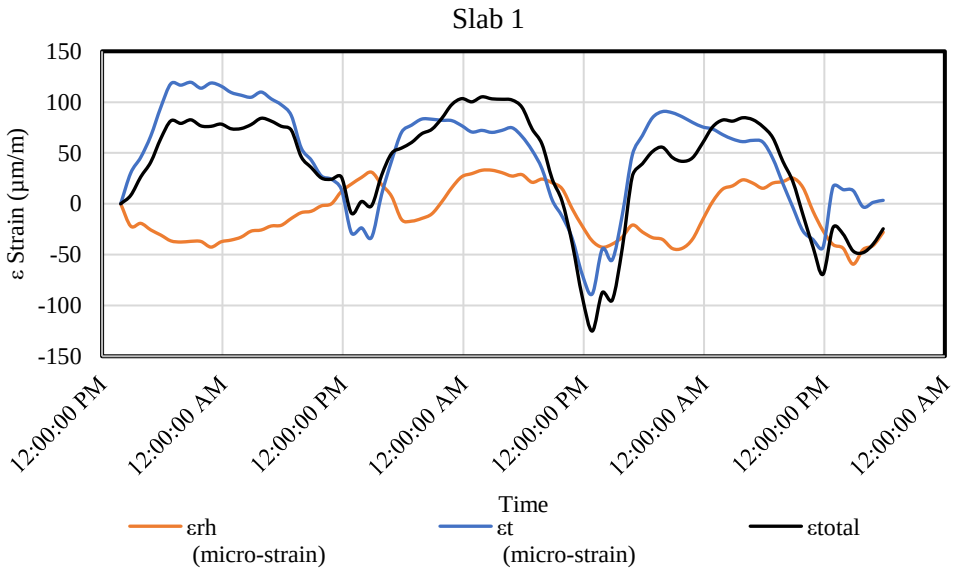
Slab 1
150
100
50
0
-50
-100
-150
ε Strain (μm/m)
12:00:00 PM
12:00:00 AM
12:00:00 PM
12:00:00 AM
12:00:00 PM
12:00:00 AM
12:00:00 PM
12:00:00 AM
Time
εrh (micro-strain)
εt (micro-strain)
εtotal

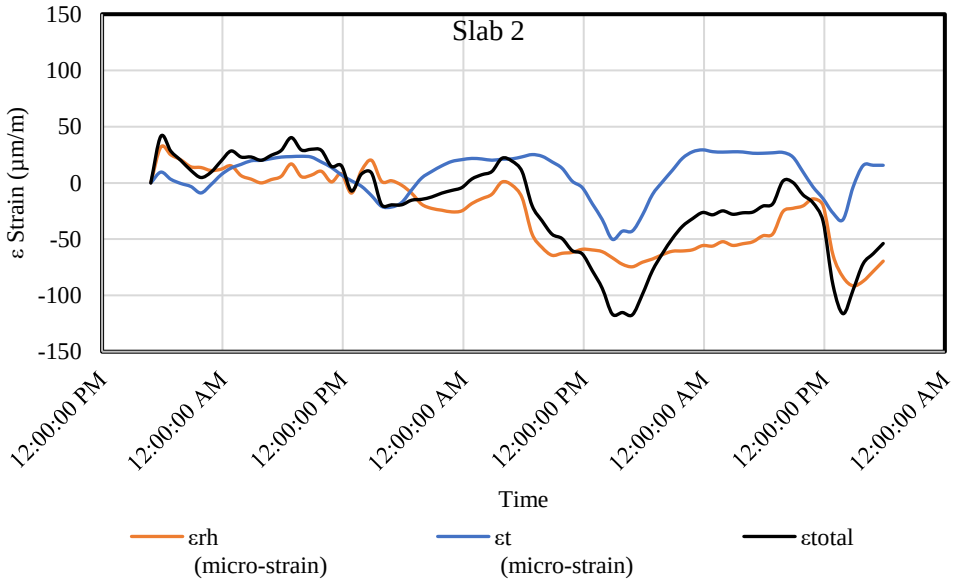
Slab 2
150
100
50
0
-50
-100
-150
ε Strain (μm/m)
12:00:00 PM
12:00:00 AM
12:00:00 PM
12:00:00 AM
12:00:00 PM
12:00:00 AM
12:00:00 PM
12:00:00 AM
Time
εrh (micro-strain)
εt (micro-strain)
εtotal

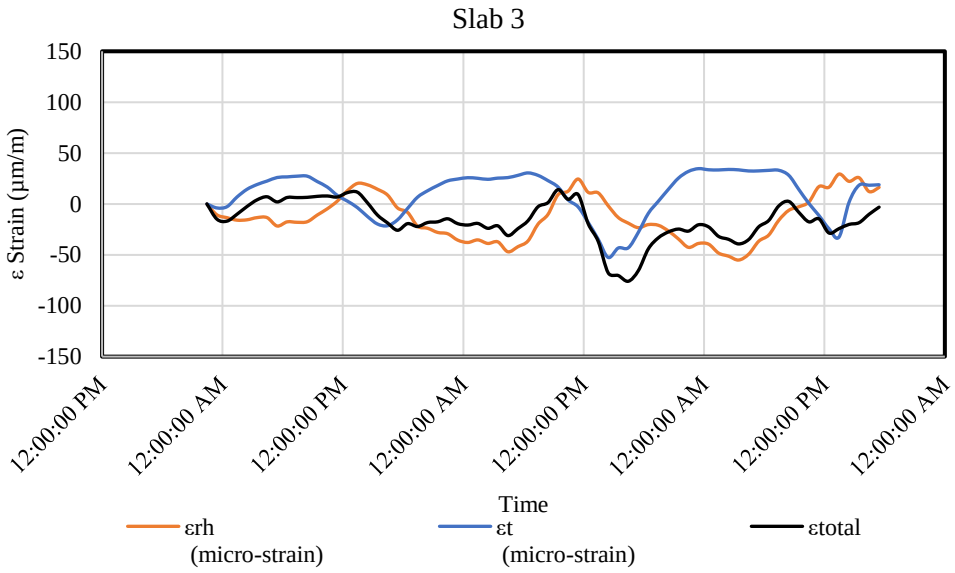

Figure 4-56. Net (Total) Strain Measurements (Phase II)

4.2.2.7 *Actual Strain Measurements*

The measured strain gauges at the top and bottom of each slab are shown in Figure 4-57 to Figure 4-59. Both longitudinal and transverse strains over 7 days were generally expansive with respect to the initial reference measurements (which were taken at the zero-stress time). The trends of the strain fluctuations were positively related to the trends of the temperature fluctuations. The concrete strains increased, and the concrete slab became expansive as temperature increased. On the other hand, the concrete became contractive when the temperature decreased. By dropping the temperature, large compressive strains were induced at the bottom of the slab.

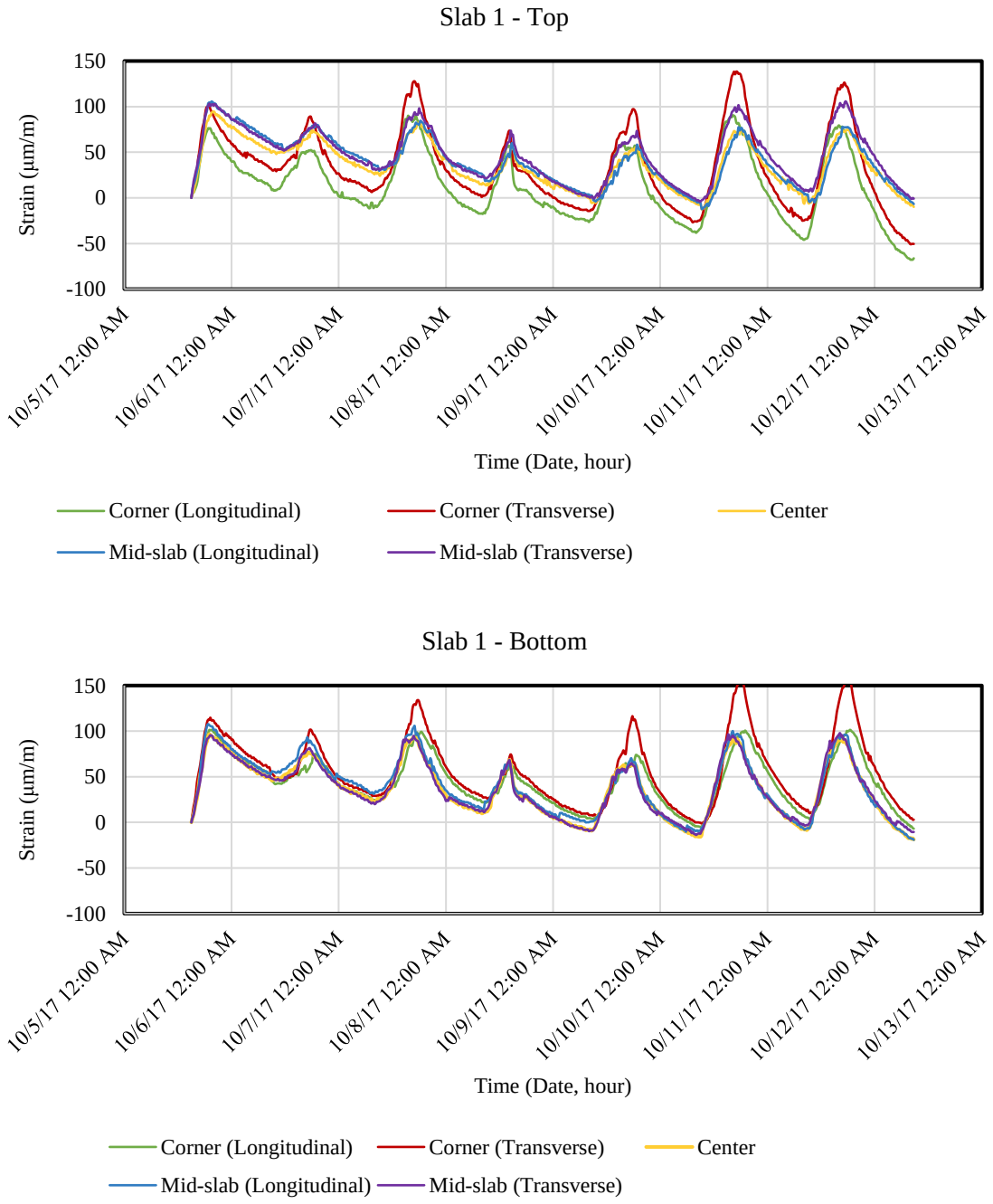

Figure 4-57. Actual Strain Measurements at Slab 1 - Top and Bottom (Phase II)

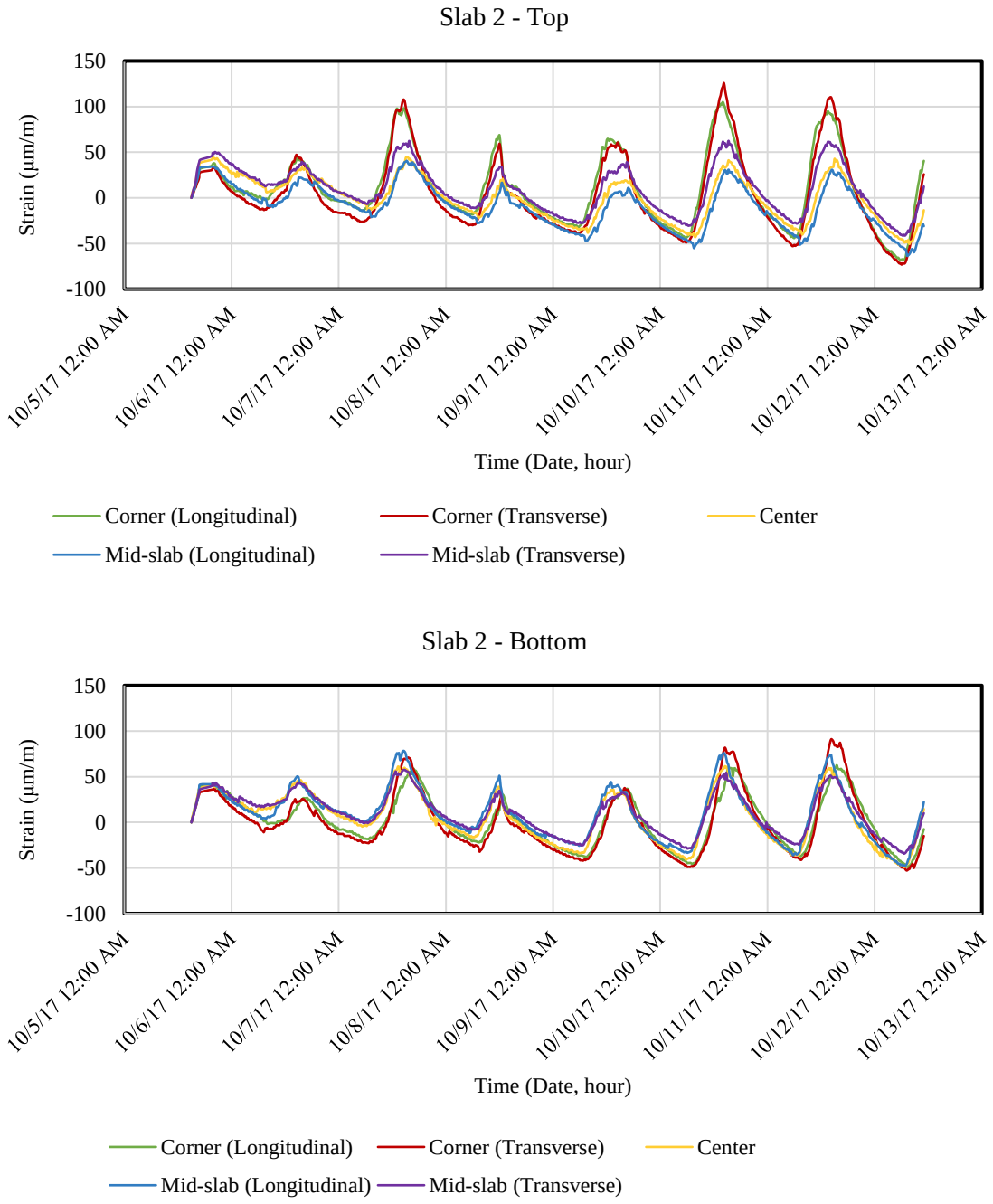

Figure 4-58. Actual Strain Measurements at Slab 2 - Top and Bottom (Phase II)

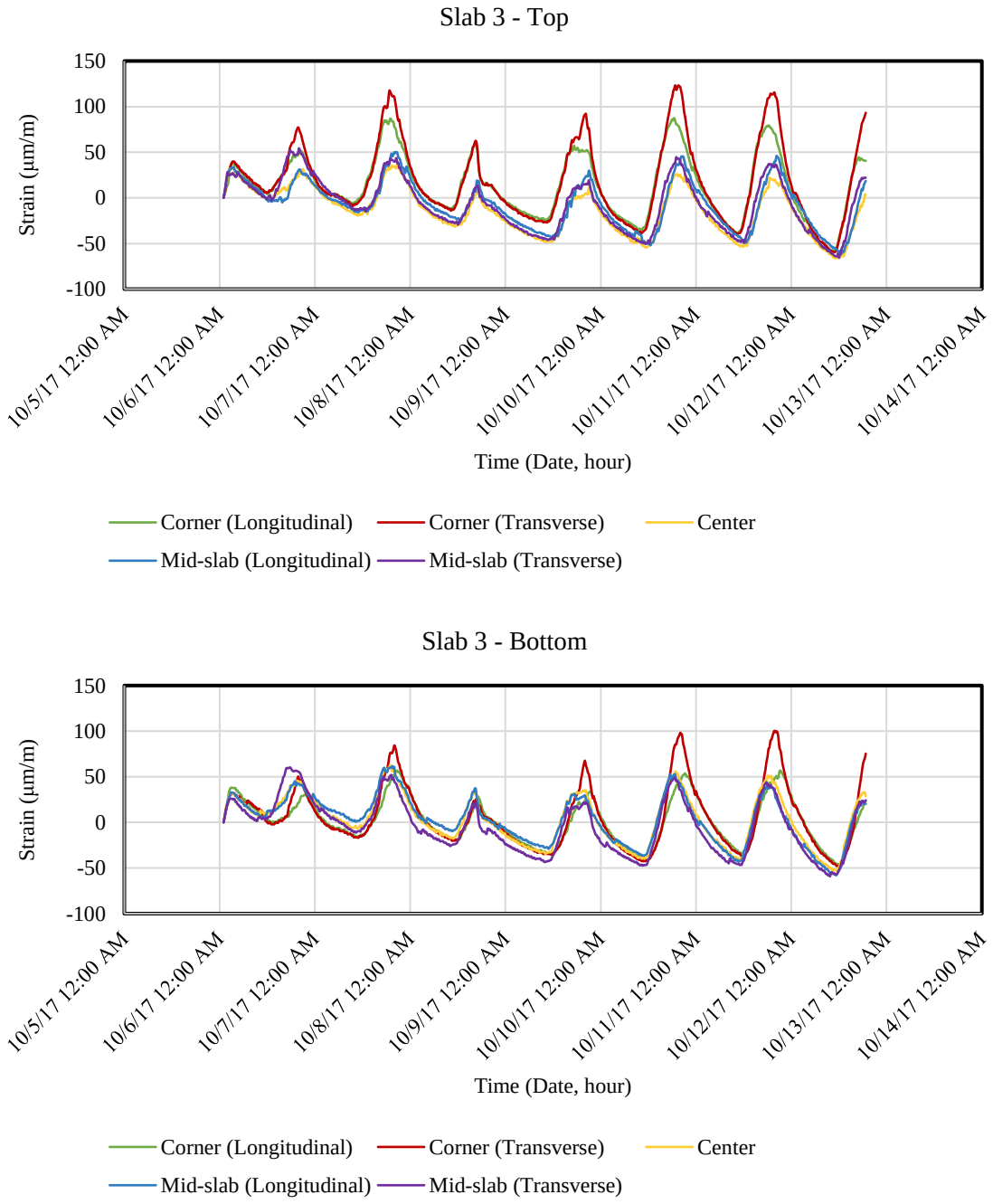

Figure 4-59. Actual Strain Measurements at Slab 3 - Top and Bottom (Phase II)

As previously explained in Phase I, when the slab was bonded to the base, it behaved as a consistent section. Consequently, the neutral axis was shifting down, and the

strain at the top surface was increasing (compared to the bottom). The deflection measurements from the corner and the edge confirmed this upward curling, which caused the loss of friction (bond) between the slab and underlayer base. Moreover, the evaporation of moisture from the exposed slab surface resulted in the drying shrinkage. Thus, the relative humidity of concrete near the top of the slab was low, and at the bottom of the slab was high due to the saturated condition. This moisture difference through the slab depth created non-uniform volume changes and strains.

Figure 4-60 to Figure 4-62 show the temperature and strain in the corner of slabs at both top and bottom of the slab. The left charts in these three figures compare the strain development in the top and the bottom of the slab with the surface temperature. The strain at the top of the slab responded immediately to the temperature changes in the slab. In other words, the highs and lows in the strain pattern were the same as the temperature spike pattern. There was a slight delay between the bottom strain with the temperature spikes. This difference between the top and the bottom of the slab might be because of the restraints caused by the base against the volume changes of the slab. Moreover, the amplitude of strain variations decreased with the distance from the top surface. So, the bottom of the slab showed fewer strain movements.

The right charts in Figure 4-60 to Figure 4-62 show the strain and temperature gradients along with the slab depth. This quantification method was straightforward by measuring the temperatures on the top and bottom surfaces of the slab. However, it is oversimplified due to the non-linearity of the temperature distribution [174]. On the other hand, the measured strain gradients can reflect the slab curling deformation.

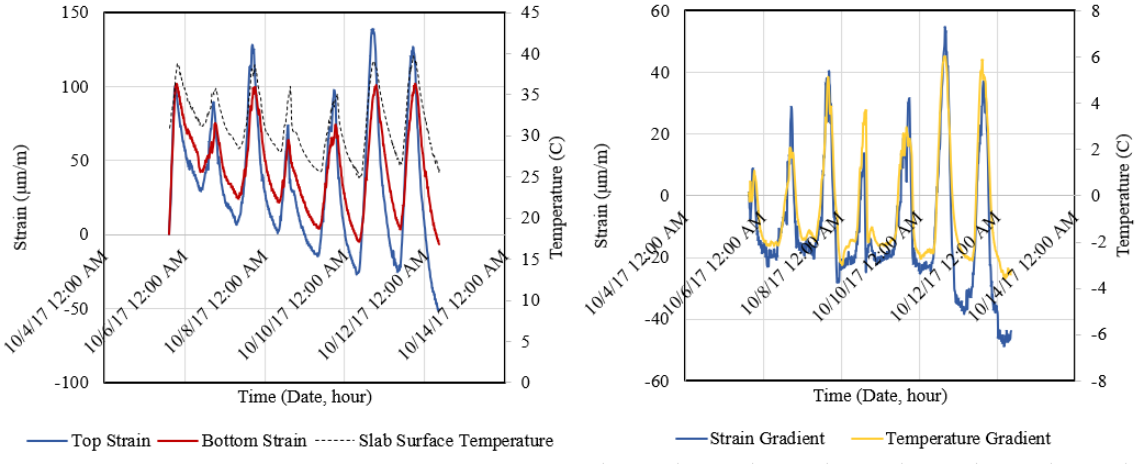

Figure 4-60. Strain and Temperature at Top and Bottom for Slab 1 (Phase II)

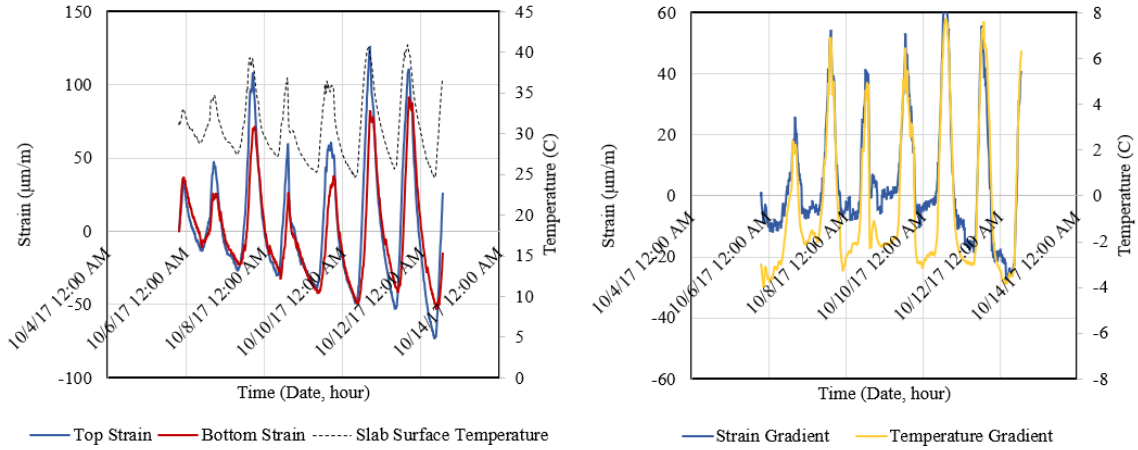

Figure 4-61. Strain and Temperature at Top and Bottom for Slab 2 (Phase II)

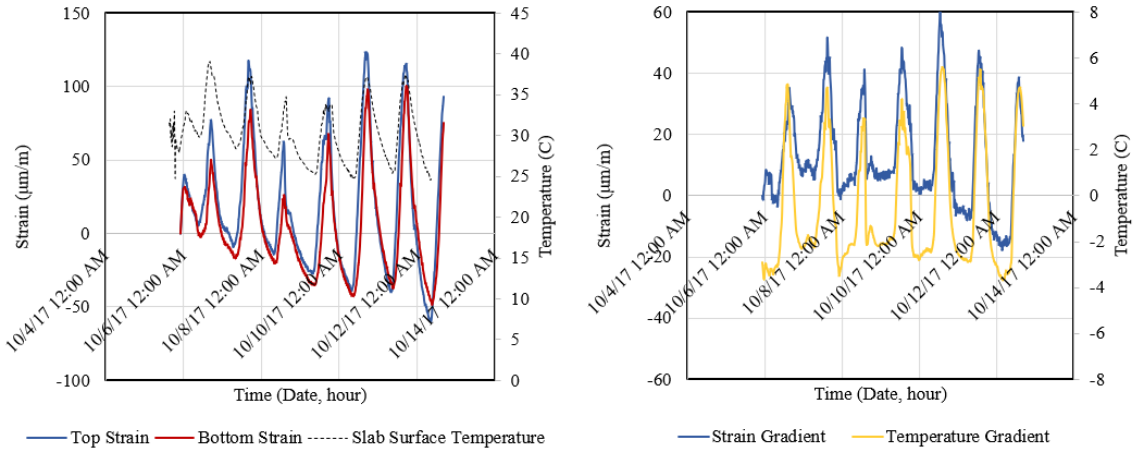

Figure 4-62. Strain and Temperature at Top and Bottom for Slab 3 (Phase II)

In addition, the right side charts in Figure 4-60 to Figure 4-62 indicate that the variations of the strain followed the same pattern as the variations of temperature, but with different magnitudes. The measured strain, which indicated the slab deformation, consisted of both temperature curling and moisture warping. Although the effects of shrinkage at the early have been ignored due to the stability of the relative humidity, the moisture gradient exists in the slab.

An important observation was that the maximum points of the gradients, which happened during the daytime due to the daily peak temperature, were almost identical. However, there was a significant difference in the minimum points. In Figure 4-60, the strain gradient in Slab 1 was in both positive and negative zones (compression and contraction), such as the temperature gradient. However, this gradient in Slab 2 and Slab 3 was almost limited to the compression-only at the first few days. Slab 1 was placed in the morning, and concrete was prone to dry with a higher rate. Thus, this excessive amount of evaporation caused the moisture warping that can be treated as an additional negative strain gradient. This additional negative strain gradient in Slab 2 and Slab 3 was negligible.

4.2.2.8 Drying Shrinkage

Figure 4-63 is a plot of free drying shrinkage versus time based on ASTM C 157 [168]. The length changes that were produced due to the moisture and temperature changes in concrete specimens were measured using strain gauges. The shrinkage amount was almost similar for Slab 2 and Slab 3 in the first 7 days. Slab 1 shrinkage strain was in both contraction and expansion zones. As explained in the former section, the morning placement induced excess stress/strain due to the rapid evaporation of water from the surface of the concrete. The result was the negative strains in Slab 1. However, concrete placement in the afternoon and evening caused less shrinkage in Slab 2 and Slab 3.

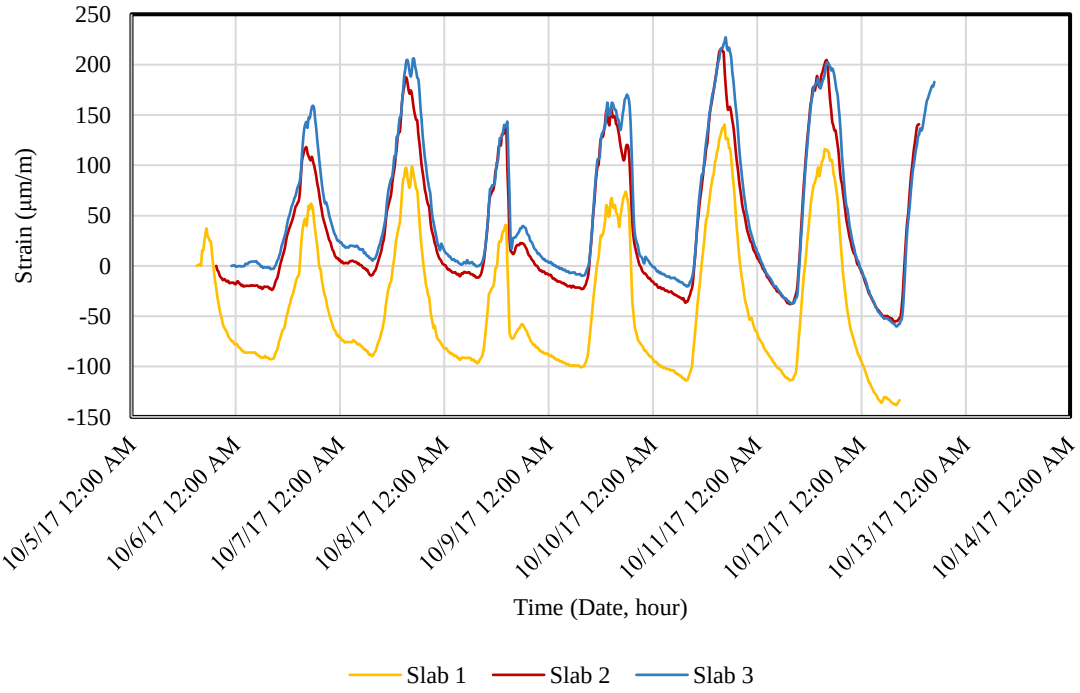

Figure 4-63. The Shrinkage Strains Data from the Four Slabs (Phase II)

4.2.2.9 Vertical Displacement (Corner Lift-off)

Four LVDTs were used for each slab in order to monitor the slab behavior and configuration, specifically the corner displacement. Figure 4-64 shows the vertical

displacements of all four slabs in the first five days after the placement. As explained in the test method, different LVDTs were placed in the concrete to show the behavior and movement of the slabs at the early-age. In this figure, S1 represents the LVDT, which was located in the corner (3 inches edge offset). S2 was another LVDT 6 inches offset from S1 (or 9 inches transverse edge offset). Finally, EM is the LVDT that recorded the mid-slab movement. The amount of corner displacement was limited to 0.01 inches in the first five days.

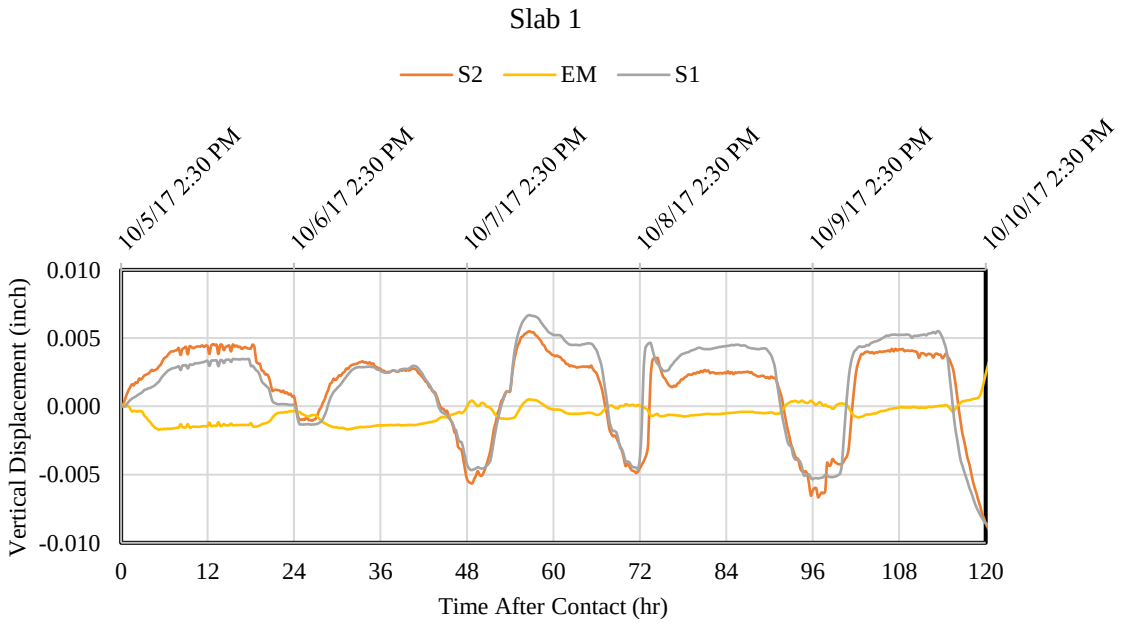

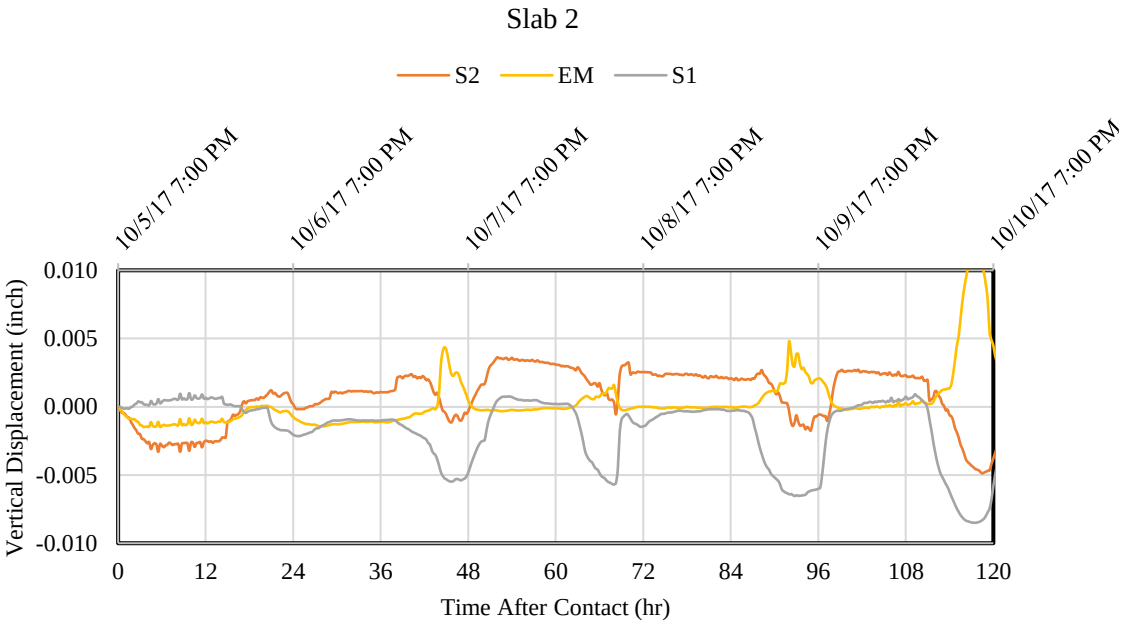

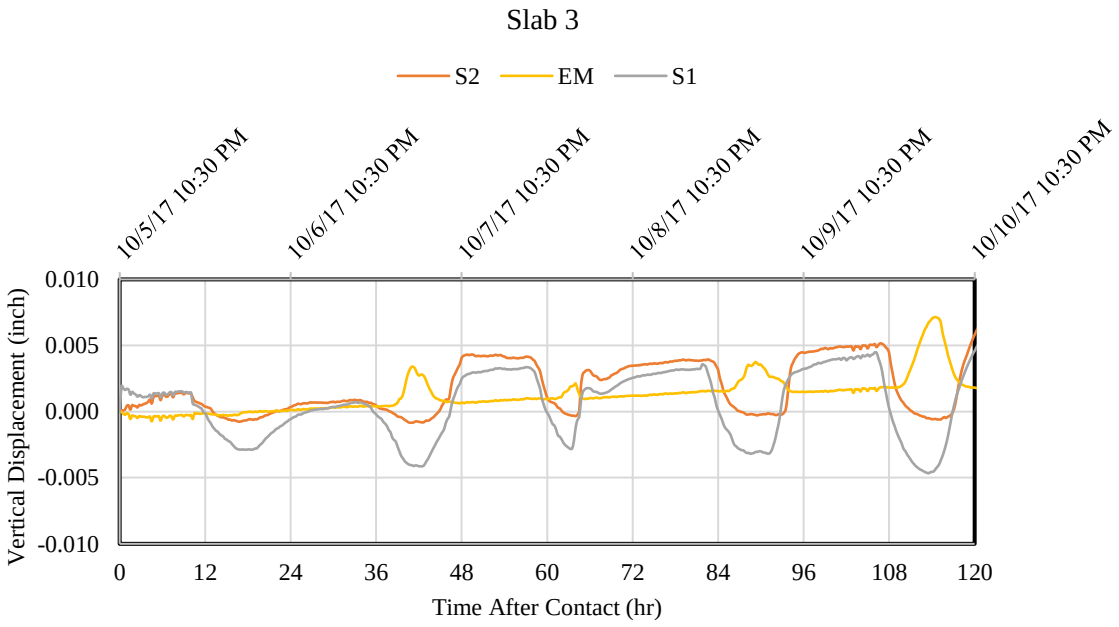

Figure 4-64. Vertical Displacement (Lift-off) of Slabs (Phase II)

The slabs' vertical displacements (the difference between corner and mid-slab location) are shown in Figure 4-65. The daytime and nighttime are shown with light and dark colors, respectively. The positive numbers show upward slab curling. The maximum upward curling condition occurred during early morning hours, just before sunrise (at the end of the dark timeframe). The slab usually is colder on the top surface than the bottom from late at night through mid-morning, resulting in a negative temperature gradient. However, the maximum downward curling condition occurred around noon or in the early afternoon when the slab surface is heated by the sun. Figure 4-65 shows that the behavior of slabs displacements was not identical in the slabs. The built-in gradient was affected by the time of placement. Slab 1 (morning placement) had the highest curling. While Slab 3 (afternoon placement) had milder displacement compare with Slab 1. Slab 3 showed higher downward curling values during the daytime.

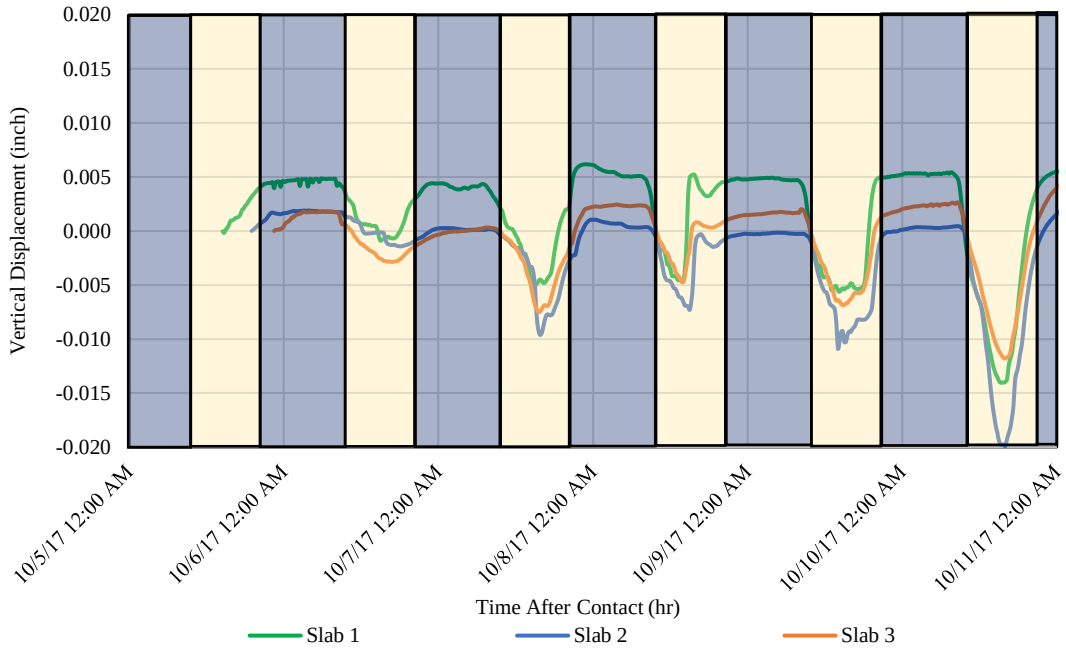

Figure 4-65. Slabs' Vertical Displacement after the Final Set Time

4.2.2.10 Compressive Strength

The compressive strength of 4×8 inches cylinders at the ages of 3, 7, 14, 28, and 56 days old were tested on each slab. For each specific time, three samples were provided, and the average strength was reported. Table 4-10 lists the diameter, height, density (ρ), and compressive strength (f') for each cylinder.

Table 4-10. Cylinder Samples' Compressive Strength Results

	Properties	Age														
		3 days			7 days			14 days			28 days			56 days		
		#1	#2	#3	#1	#2	#3	#1	#2	#3	#1	#2	#3	#1	#2	#3
Slab 1	Avg length (in)	8	8	8	7.60	7.55	7.55	7.75	7.65	7.75	7.8	7.75	7.75	7.65	7.65	7.7
	Avg Dia (in)	4	4	4	4.00	4.01	4.00	4.02	4.01	4.02	4.02	4.02	4.01	4.02	4.02	4.02
	Area (in^2)	13	13	13	12.57	12.63	12.57	12.69	12.63	12.69	12.69	12.69	12.63	12.69	12.69	12.69
	f' (psi)	2873	2895	2878	3865	3920	3867	4918	4584	4328	4867	4898	4885	5770	5592	5539
	ρ (lb/ft^3)	142	142	142	140.9	142.1	143.8	140.4	140.2	140	140.7	141.1	141.1	141	140.6	140.9
	Avg f' (psi)	2880			3880			4610			4880			5630		
	Avg ρ (lb/ft^3)	142			142			140			141			141		
Slab 2	Avg length (in)	7.65	7.65	7.55	7.5	7.35	7.3	7.7	7.7	7.65	7.65	7.45	7.5	7.8	7.65	7.55
	Avg Dia (in)	4.01	4.02	4.01	4	4.01	4	4.01	4.01	4.01	4.01	4.01	4.01	4.01	4.01	4.01
	Area (in^2)	12.63	12.69	12.63	12.57	12.63	12.57	12.63	12.63	12.63	12.63	12.63	12.63	12.63	12.63	12.63
	f' (psi)	2099	2009	2097	2667	2851	2621	3221	3364	3212	3911	4031	3684	4191	3992	4425
	ρ (lb/ft^3)	139.7	139	140.6	139.9	140.5	141.6	140	139.3	139	139.5	139.8	140.1	139.4	139.9	139.4
	Avg f' (psi)	2070			2710			3270			3880			4200		
	Avg ρ (lb/ft^3)	139			140			140			140			140		
Slab 3	Avg length (in)	8	8	8	7.75	7.7	7.75	7.7	7.75	7.65	7.7	7.65	7.65	7.7	7.65	7.7
	Avg Dia (in)	4	4	4	4	4.01	4.01	4.01	4	4.01	4.01	4.01	4.01	4.01	4.02	4.02
	Area (in^2)	13	13	13	12.57	12.63	12.63	12.63	12.57	12.63	12.63	12.63	12.63	12.63	12.69	12.69
	f' (psi)	2462	2539	2538	3350	2931	2950	4110	3816	4273	4452	4366	4370	4615	4204	4664
	ρ (lb/ft^3)	140	140	141	138.9	139.7	140.2	139.8	138.7	139	139.5	139.7	137.9	138.9	137.4	139.2
	Avg f' (psi)	2510			3080			4070			4400			4490		
	Avg ρ (lb/ft^3)	140			139			139			140			138		

Figure 4-66 displays the average compressive strength for slabs at different ages. These results were used to model the modulus of rupture (or the cracking moment) using methods discussed in ACI Committee 209 [123].

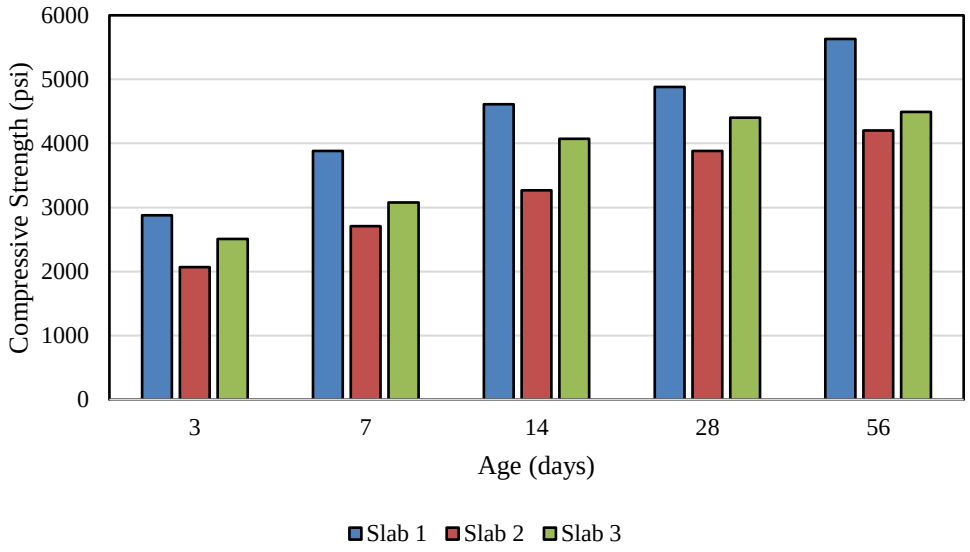

Figure 4-66. Compressive Strength Results of Cylinder Samples

4.3 Using GPR in the Field Data Collection

Dielectric measurements with a percometer were relatively consistent and had a good relationship with the moisture retention capability of the different curing kinds. However, the application of percometer in the field tests was still limited because the data collection should be manually done at each location on concrete pavements. This type of data collection prevented the research team from getting an extensive data set done quickly at different places. Thus, using GPR as a practical approach assessed the curing effectiveness faster with better data acquisition. The field data was collected in a series of

paving projects in Victoria, TX; Itasca, IL; and Jacksonville, FL. GPR was the core instrument in these field studies. The primary purpose was to measure DC by using GPR at the surface of concrete pavements and monitor the curing quality. Then, the utility of DC measurements to qualify curing performances was proven by statistical analysis.

Figure 4-67. Using GPR on Newly Placed Concrete Pavements

Before the data collection, the software was calibrated in air and against a metal plate to ensure uniformity in the results (the metal plate reflects 100% of the incident energy). The software pre-installed in the computer can quickly calculate the DC for the surface concrete spatially as the cart is moved over the pavement surface. GPR operated by transmitting electromagnetic pulses into a pavement structure. This method results in an accurate determination of DC. The DC values depend on arrival time and amplitude. The reflected pulses, referred to as the radar waveform, display DC and thicknesses of the layers within the pavement, as shown in Figure 4-68.

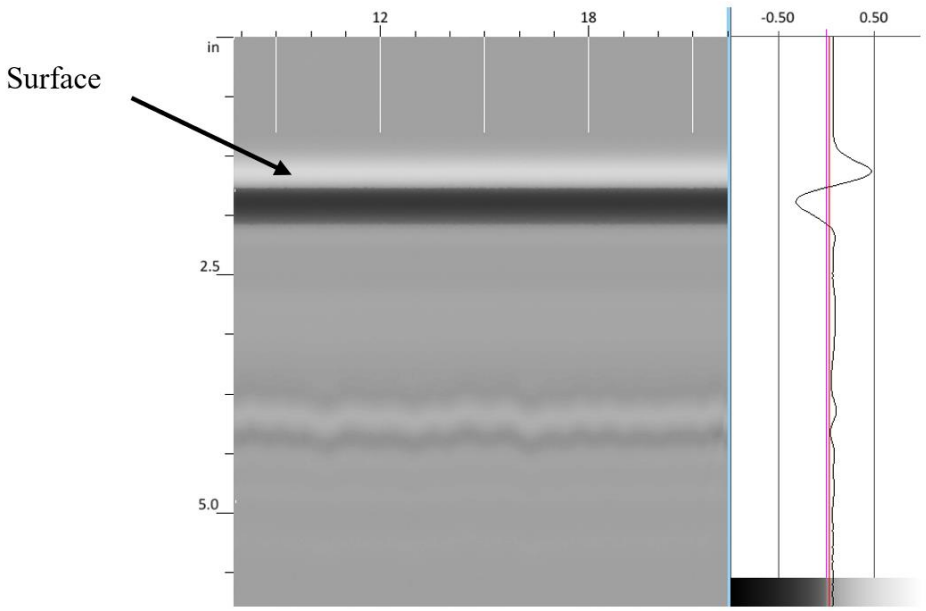

Figure 4-68. Linescan and Oscilloscope of the Signal Reflections

Figure 4-68 is a grayscale frame, which displays the cross-sectional view of the pavement. The reflection polarity provided important information. The transmit pulse had a certain polarity, peak, and color. The white and black colors determine the greater pulse reflections and higher DC, while the grey color implies low reflections and DC. The first straight horizontal bands on top of the frame in Figure 4-68 is a combination of the transmit pulse in air and concrete surface reflection. The surface is located at the first white peak within, as shown in Figure 4-68. Also, the amplitude variations on the bottom of the frame indicate changes in moisture. On the right side of Figure 4-68, the oscilloscope is displayed.

In order to obtain the dielectric constant from the dispersion of GPR waves, the permittivity and geometry of waveguides were considered. The DC values of the pavement layers were determined by comparing the amplitude of a reflected signal from the surface to the amplitude of a signal reflected from a metal plate. Nevertheless, only upper layers of the pavement are investigated, and being multi-layered with different compositions might lead to errors due to interference of surface reflected and direct

(transmitter to receiver) waves [84, 85]. The most common technique for assessing the first DC layer, $\varepsilon_{r,1}$, is based on the reflection amplitude from the pavement surface, based on Eq. (4-12) [175]:

$$\varepsilon_{r,1} = \left(\frac{1+\left(\frac{A_0}{A_p}\right)}{1-\left(\frac{A_0}{A_p}\right)} \right)^2 \tag{4-12}$$

where $\varepsilon_{r,1}$ is DC of the first layer, A_0 is the amplitude of surface reflection, and A_p is the amplitude of the GPR wave, which can be obtained by calibration with a metal plate [83, 176]. Typically, the range of signal frequencies of GPR is within 400 MHz to 2 GHz for investigations. The depth of penetration is noticeable where the signal fluctuates. The higher frequency yields to better resolution but a lower penetration depth [86]. In this study, the standard frequency for most GPR antennas was used, i.e., 1.6 GHz [177]. As the purpose was to work in contact with or proximity to the surface of the concrete (moisture variation detection on the surface), this frequency was suitable for these data collections. For each pulse, the travel time of the reflected signal was recorded to be within 4.52 ns (nanoseconds), which depended on the depth of the interface and the moisture content in concrete. Also, the GPR data collections were performed with a speed of 8 km/h, and DC was measured every 1 cm, as long as the wheels were rolling.

4.3.1 Repeatability

The data collected during the paving of the Victoria, TX; Itasca, IL; and Jacksonville, FL was from test sections, which were 37 m, 160 m, and 57 m long, respectively. Figure 4-69 indicates that it is possible to achieve a high degree of repeatability of the collected data. The data was collected three times after the application of the curing compound. The positioning of the GPR device was important during the repetition of the data collection process. The data showed that the relative standard deviation of the three repetitions at each location was low. In order to show the variation

statistically, the coefficient of variation (CV) was used, which is the ratio of standard deviation/mean. The average CV for three repetitions in Victoria, TX; Itasca, IL; and Jacksonville, FL data collections was 0.68, 0.94, and 0.85, respectively. The Itasca's CV was slightly higher than 1, which indicated a relatively high variation. However, Victoria and Jacksonville data collections showed relatively low magnitudes that reflected acceptable repeatability of the data collection procedure. The GPR device was calibrated each time before data was taken to ensure the accuracy of the data.

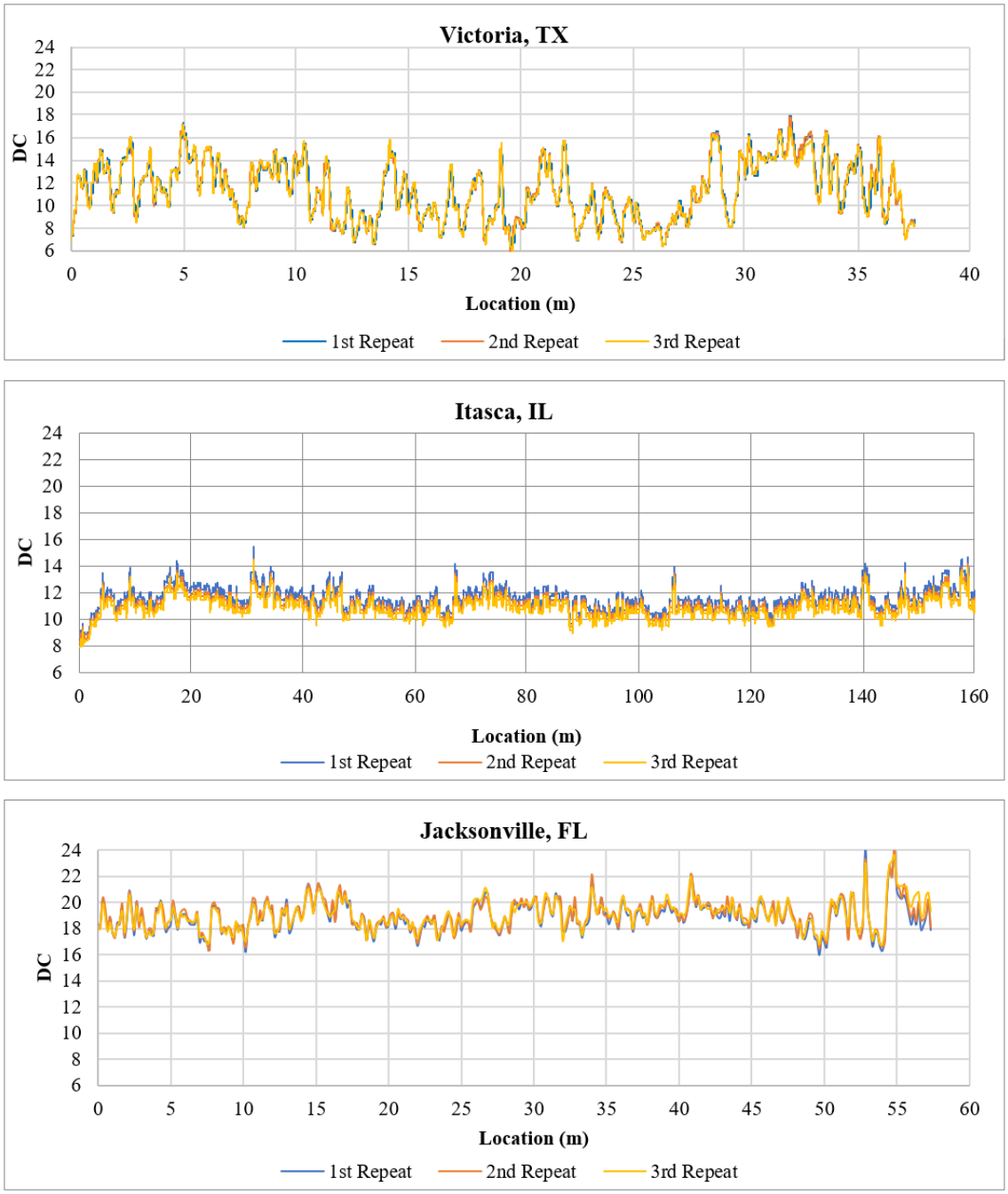

Figure 4-69. Data Collection Repeatability from Three Measurement Rounds

4.3.2 Curing Effectiveness Measurements

The curing method affects the concrete hydration by governing the evaporation of the available moisture [178]. As curing depends on the moisture, the effectiveness of a curing practice can be correlated to the volumetric change of concrete water [179]. Therefore, changes in the dielectric values with time for early-age concrete was correlated with the capability of maintaining moisture in concrete. In these field experiments, the evaluation was conducted in terms of the dielectric measurements. The volumetric change rate of available concrete surface moisture reflected the performance of the curing practice; a lower rate of reduction of the free moisture represented a superior curing practice in retaining water inside concrete [38].

Initially, the moisture content at the concrete surface was very high, so the DC measurements were correspondingly high as well. Gradually, DC measurements began to decrease over a 72-hour period. Figure 4-70 shows the effect of time on the DC measurements along the pavement section. The later readings were taken a few hours later than the initial reading at the same locations. The shapes of the amplitude of the data sets were almost the same, whereas the magnitudes of the earlier readings were higher compared to those of the later readings. This phenomenon is the key for understanding and evaluating the curing effectiveness. In the meantime, since more free moisture is held at the surface, the DC measurements are expected to stay at a higher level for a more extended period compared with those of uncured concrete.

Additionally, Figure 4-70 demonstrates the material variation and time effects on the DC measurements as well as the repeatability of the data collection. The material changes come from the inhomogeneity of the concrete (non-uniform distribution in the aggregates, air voids, and moisture) and the curing compound application. Localized moisture or greater amounts of curing application can cause bumps (due to high DC of water), and the presence of air voids can lead to those drops in the DC trend (due to low DC of air).

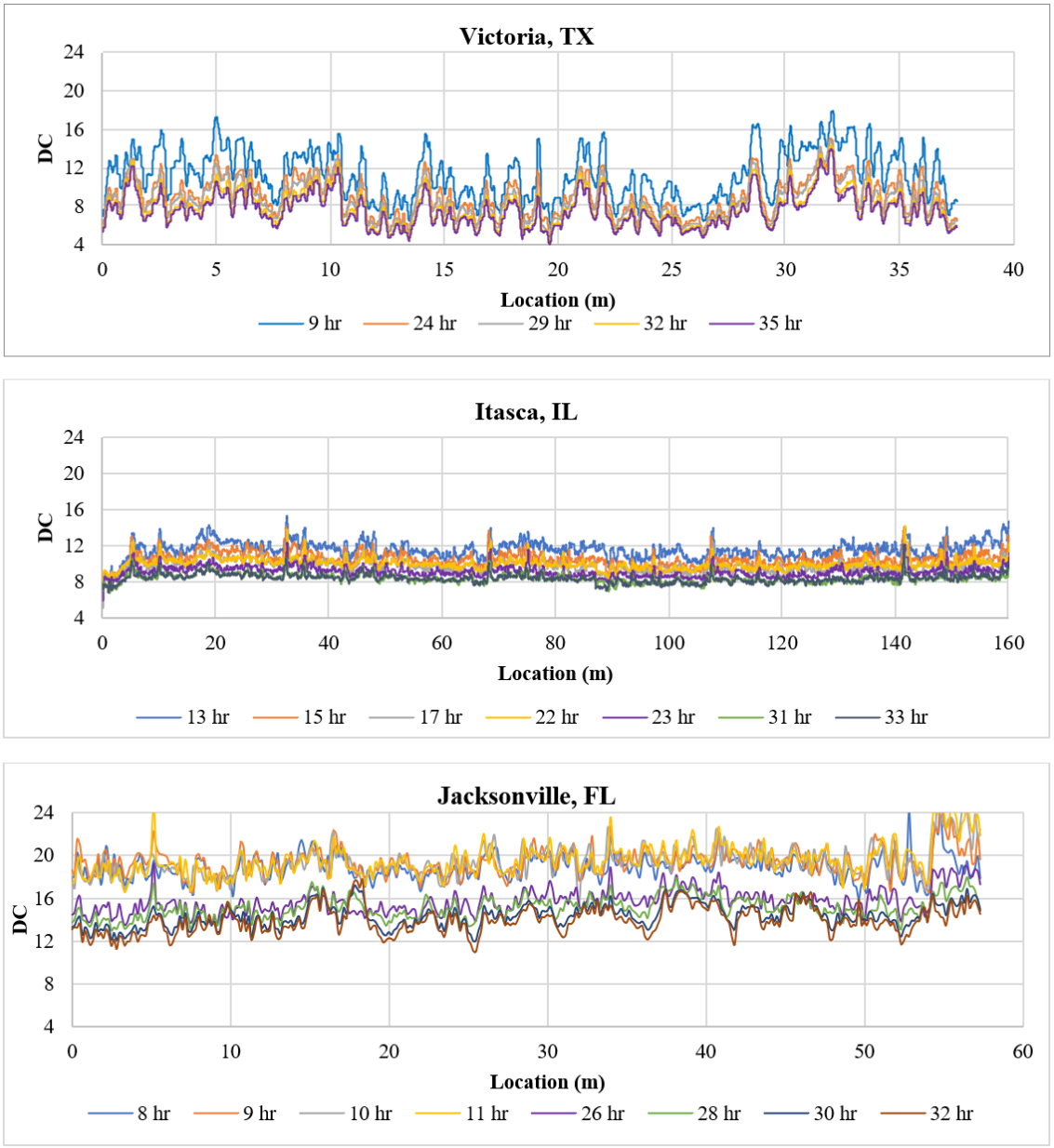

Figure 4-70. GPR Data Interpretation the Effect of Time

As shown in Figure 4-71, DC dropped very rapidly for all the sections within the first 20 hours after curing was applied. The fitted regression parameters are presented in Table 4-11. The regression parameter beta for all three slabs were relatively low compared to the previous research experiments. Victoria's beta was slightly higher than the other

test results. The reason was attributed to the high temperature of the project site during the summer placement. However, the Jacksonville's beta was marginally lower than the Victoria and Itasca data collections due to the higher ambient relative humidity.

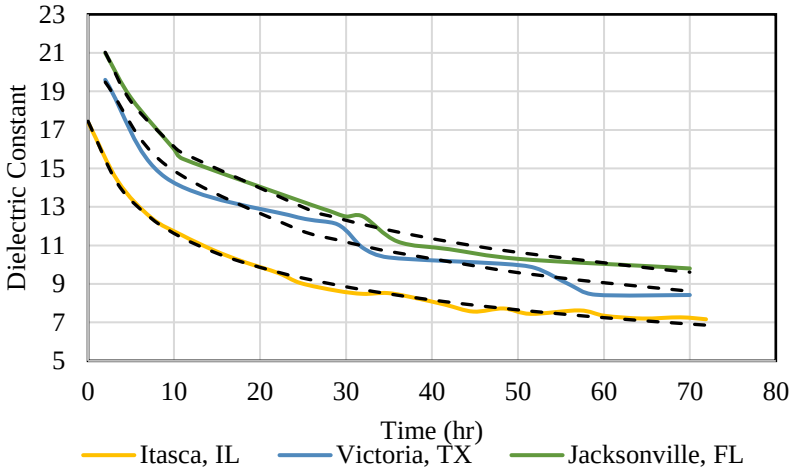

Figure 4-71. DC Measurements for Three Construction Sites

Table 4-11. Regression Parameters for the DC Measurements

Field Data Collection	τ	α	β
Victoria, TX	21.7	0.079	0.46
Itasca, IL	17.4	0.069	0.40
Jacksonville, FL	23.6	0.062	0.39

4.3.3 Uniformity

The purpose of this task was to monitor the consistency of the spraying application and find the non-uniform pattern in spraying outcomes. Figure 4-72 shows pictures from spraying operations in test sections and identifies the curing was over-sprayed in the sections where hand spraying was used. The result was creating a thicker white banded area compared to the other locations. In addition, there were multiple areas

with no curing compound on it. The lack of sufficient amounts of curing compounds may cause excess water evaporation and drying shrinkage.

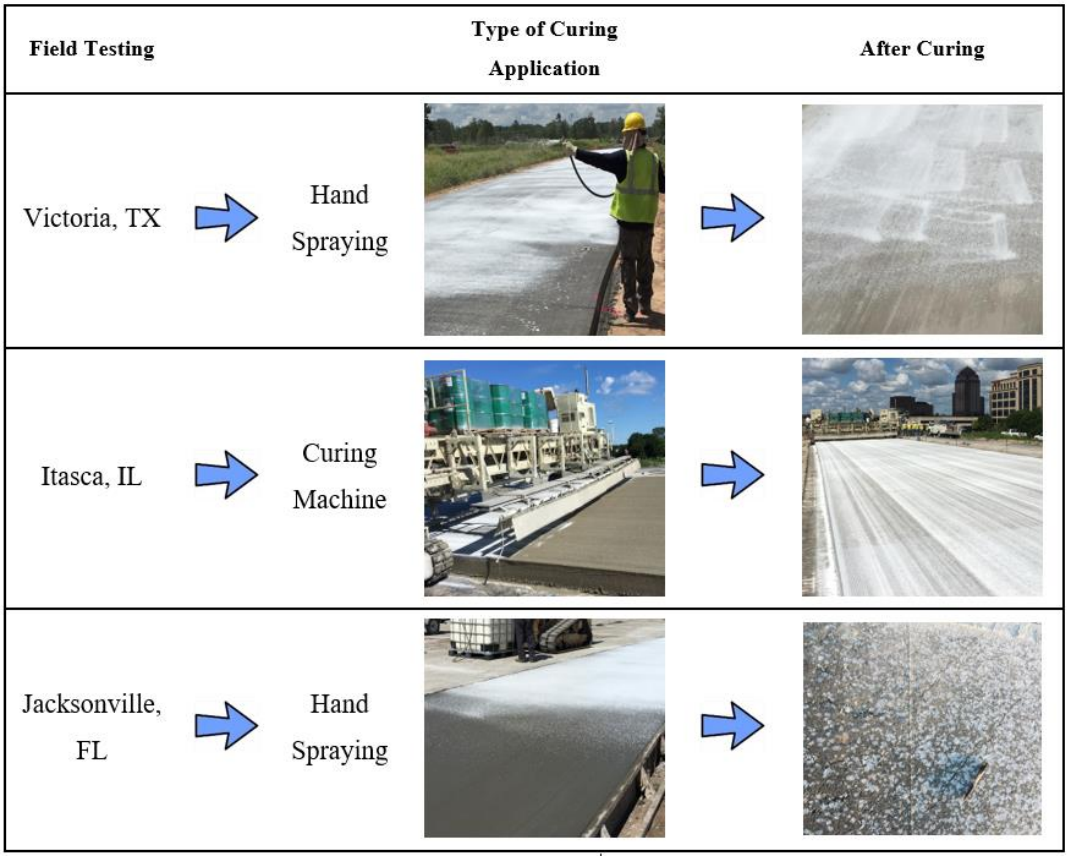

Figure 4-72. Uniformity of Curing Application on Field Slab Placements

The application of the curing compound introduced extra moisture to the surface of concrete. Therefore, it temporarily increased DC of the cured area depending on the application rate of the sprayed curing compound. As the free moisture evaporated and time elapsed, the dielectric slowly dropped down to a lower level. However, if the curing was sprayed at a very high application rate in one spot, it took much longer before DC started to decrease at that specific spot. The DC results correctly showed this phenomenon. Thus, GPR was beneficial to detect the uniformity of the curing application. Also, GPR

reinforced the importance of having a thicker curing compound layer (i.e., higher application rate) in terms of maintaining a favorable humid curing environment at the surface of concrete pavements.

4.3.3.1 PWL Concept in the Uniformity Monitoring

GPR scans are typically collected in the longitudinal direction of the slab. The results provide dielectric profiles versus the length of the pavement. By running GPR several times in the first hours, the dielectric constant at different locations can be tracked. Due to the surface moisture evaporation, various values for dielectric constant would be collected for a single position over time in different GPR collection sessions. In terms of quality control, excessive variation in the DC reading can be minimized based on employing the PWL concept to limit deviation in curing quality. This concept should still apply despite the change in dielectric constant with time. Using the PWL concepts involves statistical analysis of the dielectric data to determine the total estimated percent of the DC deviation that is within specification limits.

The PWL specifications are intended to specify the statistical probability of conformance to material properties and construction details. PWL is defined as the percentage of data above the lower specification limit, beneath the upper specification limit, or between these two limits. The upper and lower quality limits should be defined to check how much data is out of the acceptable range.

PWL is calculated by using the sample average ($\bar{x}$) and sample standard deviation (Sn) of the number (n) of readings. Moreover, the specification tolerance limits are defined with two levels: L for lower tolerance and U for upper tolerance. Based on these two parameters, the respective quality indexes are defined as QL for lower quality and QU for upper quality. In any project, the contractor can meet the specified acceptance criteria by using a proper curing practice. For curing purposes, the quality levels can be defined based on dielectric and measured with GPR.

The first step is to define lower (L) tolerance and upper (U) tolerance limits. The QL and QU are computed as $QL = \frac{\bar{x}-L}{Sn}$ and $QU = \frac{U-\bar{x}}{Sn}$, respectively. Then, the PWL is determined by the use of Eq. (4-13):

$$PWL = (P_L + P_U) - 100 \quad (4\text{-}13)$$

where P_L is the percent within the lower specification limit, and P_U is the percent within the upper specification limit. Based on the relationship between the dielectric changes and other material properties, the upper and lower limits can be defined—for example, the higher DC loss corresponded with a lower application rate.

4.3.3.1.1 Acceptable and Rejectable Quality Levels

As a part of developing the PWL concept, quality specifications can be defined based on the acceptable quality level (AQL) and the rejectable quality level (RQL). AQL is defined as the minimum quality level of a work to be considered entirely acceptable, and RQL is the maximum level of actual quality at which construction can be considered unacceptable (rejectable) [180]. Both threshold limits only apply for PWL quality index analysis.

The proper levels of AQL and RQL can be challenging to set accurately. Although it is not feasible to have all results meet specifications (PWL=100), a small number of poor results should be allowed because of the inevitable variabilities in any production process [181, 182]. Thus, AQL should be some value less than 100 PWL. Moreover, AQL must also be set at a value equal to the maximum amount of defective material present within the pavement that will not substantially degrade overall road quality, which is 90-95 PWL [182]. RQL is commonly set much lower than AQL because it represents a PWL below which the pavement is under acceptable range. Typical values of RQL range 30-60 PWL.

Many researchers recommend AQL be set at a PWL of 90% and RQL at 50% for pavements, whereas the FAA has set RQL at 55% [183]. As PWL concept is based on

mean and standard deviation, the standardized variable transformation can be used along with the AQL and the RQL, to be related to the total area (or probability) under the standard normal distribution, which is equal to 100% [93].

One of the main advantages of the PWL concept is that construction test data follows a normal distribution and that appropriate standard deviations are developed from this normally distributed data [184, 185]. Although researchers found evidences of non-normality with some of the data, the levels and types of non-normality did not influence the PWL results negatively [96]. Non-normality may happen when PWL data is deviated from normality due to multimodality (more than one mode or peak), skewness (asymmetry of the distribution), and kurtosis (flatness of the distribution).

Instead of using histograms and making normal probability plots to check the normality of a distribution, Anderson-Darling (A-D) normality test was conducted that shows whether or not a dataset comes from a normal distribution.

There are two hypotheses for the Anderson-Darling test for the normal distribution: the null hypothesis is that the data is normally distributed; the alternative hypothesis is that the data is non-normal. The p-value for the Anderson-Darling test was used to show whether the test is significant. If the p-value is low (e.g., <=0.05), the data do not follow the normal distribution. The Anderson-Darling statistic uses the cumulative distribution function (CDF), as shown in Eq. (4-14) [186]:

$$AD = -N - \frac{1}{N}\sum_{i=1}^{N}(2i-1)\left(\ln\left(F(Y_i)\right) + \ln\left(1 - F(Y_{N+1-i})\right)\right) \quad (4\text{-}14)$$

where N is the population size, $F(Y_i)$ is the CDF, and i is the i^{th} sample when the data is sorted in ascending order. Finally, the p-value was calculated for the normal distribution [187]. Depends on the AD value, there are four different expressions to define the p-value. Figure 4-73a shows the frequency of the actual distribution (the visual shape of the dataset) and the normalized distribution (based on the sample mean and standard deviation). The data set is a distribution of the dielectric constant standard deviation, which resembles a skewed (chi-square) distribution. In the variance distribution, the median variance and the average variance are not similar. Usually, the average variance is greater than the median variance [184]. However, the actual dataset was a good fit for a normal distribution. In

order to prove this normality, the Anderson-Darling statistic test was used to calculate the normal probability, as shown in Figure 4-73b.

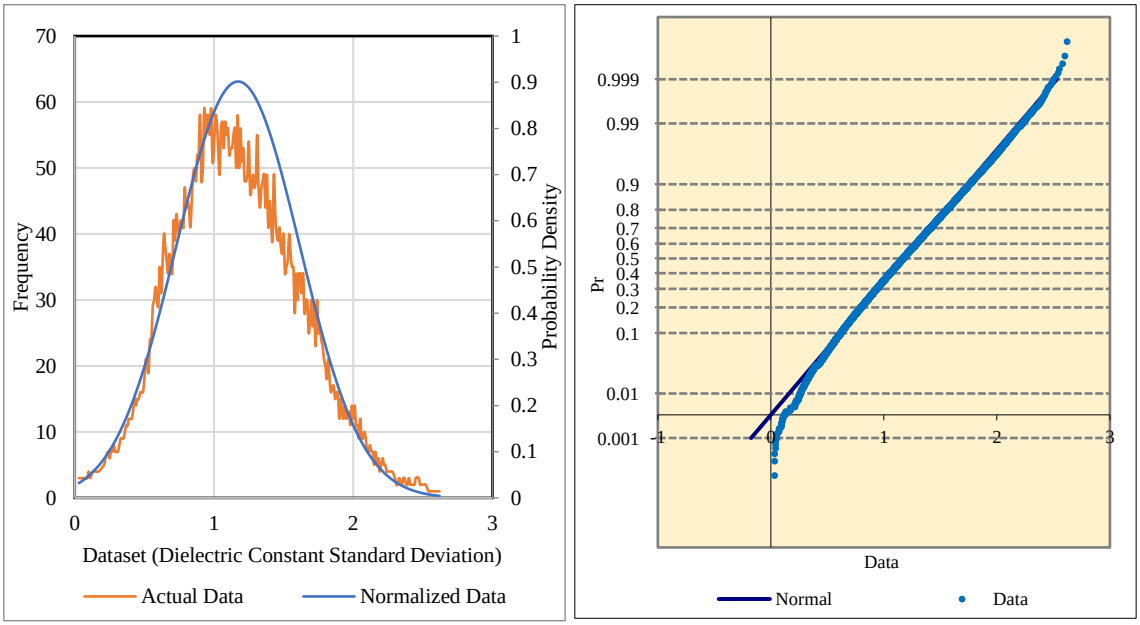

Figure 4-73. Normal Distribution and the Normal Probability Plot for the Dataset

The calculated p-value was 0.0851, which was higher than 0.05. Then, the null hypothesis that the data is from a normal distribution is accepted. The normal probability plot in Figure 4-73b confirms this finding as the points should fall in a relatively straight line.

4.3.3.1.2 Quality Specification Concepts

The curing compound's function is to limit or allow the loss of moisture in the first few hours after placement. The standard deviation of measured dielectric constant values for a single location represents, to some extent, the curing effectiveness at that location. In other words, checking the standard deviation of several DC measurements of a single location is an indication of the magnitude of change the dielectric is undergoing. Figure 4-74 displays the standard deviation plots from the initial data collection carried out in Jacksonville, FL experiment. As free surface moisture evaporated, the dielectric

value decreased over time. Also, as shown in Figure 4-74, the later readings demonstrated a higher level of standard variation (red line represents the average of standard deviation at that point in time). However, any spike in the standard deviation trends indicates a lack of uniformity in the curing application. This abnormality implies that a relatively high standard deviation value for any location can be considered as insufficient curing. For example, in the Jacksonville field test, approximately between 50-60 m from the beginning point of paving were susceptible to poor curing due to spikes in standard deviation graphs.

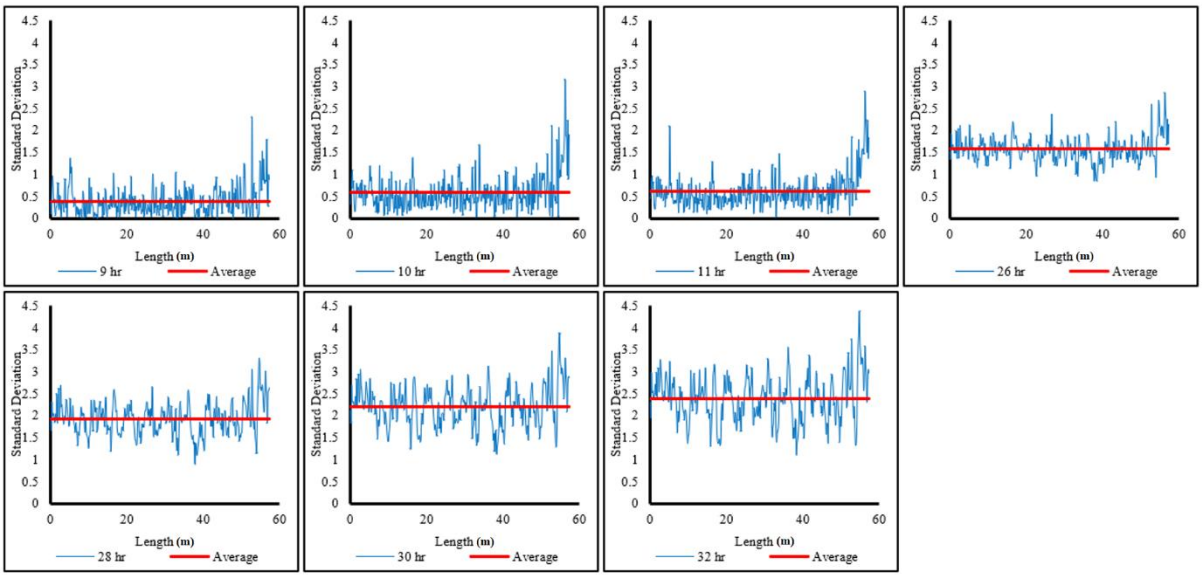

Figure 4-74. Standard Deviation of All Data Collections from the Beginning

For example, to analyze the curing quality for an entire pavement section (57 m), the standard deviation of two data collections 3 hours apart is shown in Figure 4-75. Differences in this plot show a non-uniformity in the spraying, i.e., curing did not work consistently on each part of the pavement. The average standard deviation in this plot is 0.37. Furthermore, if it is assumed that the acceptable standard deviation is 1.0, then there are twelve spots with a higher standard deviation that should be checked. In this case, another round of spraying would be recommended. This method can help to locate those regions that require a re-application of the curing compound. In order to establish and

determine the quality limits at different times after concrete placement, the PWL concept is used.

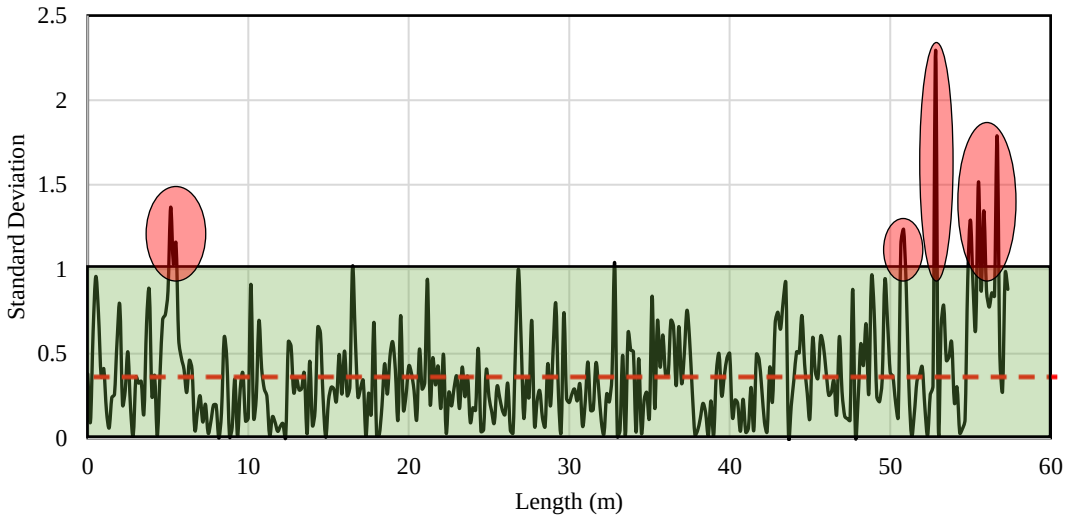

Figure 4-75. Example of Standard Deviation on the Same Trace

**Note: Between Two Data Collections Separated by 3 Hours*

The higher the deviation of this plot, the worse the curing uniformity. As long as the standard deviation is higher than an acceptable level, it indicates that the curing quality on those spots needs more attention regarding the high variance among different data collections. The advantage of this method is that limits can be specified based on the curing situation, environmental conditions, and quality level based on the contracts' specifications. The proposed method involves the establishment of quality control and/or acceptance testing limits for given project conditions. The limits will likely pertain to the timing, location, and project conditions. A reasonable level of process control variability for quality construction should be established for the PWL parameters. The acceptance levels take into account both the average (mean, μ) value of the acceptance parameter and the variability (standard deviation, σ) of the evaluation parameter.

As explained in the above paragraphs, there is no lower tolerance limit because all standard deviations are above zero, and lower values are preferred. The surface area under the normal distribution plot at Z (similar to PWL) can be found in the standard normal probability tables. For example, at Z=1.28, the surface area under the standard normal distribution is 0.90 (equal to 90 PWL). It means that there is a 90% probability that pavement construction work is less than or equal to upper specification tolerance. The quality index depends on the sample sizes (i.e., as the sample size increases, the Q value approaches the Z value).

The FAA has adopted a uniform standard quality level for acceptance that assumes design parameters can vary one standard deviation (1σ) on either side of the mean (μ) [188]. As shown in Figure 4-76, the area under a normal distribution, one standard deviation on one side of the mean, is 34.1% of the total area. Thus, the total acceptable area is 84.13%. The quality level was able to be determined by the contractor's data or historical data. When PWL is below the acceptable zone, the curing process should be repeated at those locations.

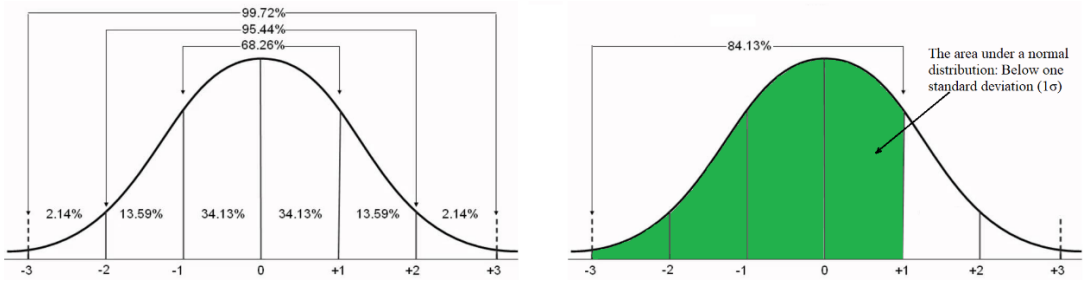

Figure 4-76. The Normal Distribution Curve with the Acceptable Limit

**Note: One Standard Deviation (1σ) above the Mean (μ)*

As discussed previously, quality level goals are set based on AQL and RQL. The contractor's assumptions are closely related to the AQL, which means the RQL can be expressed in terms of the AQL as shown in Eq. (4-15) [189]:

$$RQL=AQL - area\ 1\sigma\ on\ either\ side\ \mu = AQL-34.1\% \quad (4\text{-}15)$$

Many agencies, such as FAA, have approved 90 PWL as the AQL, which means that the RQL can be accepted at (90-34.1)=55.9 PWL and still meet the designer's specifications. By setting AQL at 90 PWL, the specifications imply that 10% of unsatisfactory results are the maximum amount that will not substantially degrade overall road quality. At the AQL, production quality should meet 90% of the design requirements, and 10% of the work can be considered defective. At the RQL, 55% of the work needs to meet the design requirements, and 45% of the work can be considered defective from a design viewpoint. Below the RQL, a large portion of the designer's intent is likely not being met, and the work is rejected [189].

4.3.3.2 Checking the Application Uniformity

Specification boundaries should be set according to engineering assessment and statistical analysis to determine an acceptable range around the target value. The AQL and RQL were assumed 90% and 55%, respectively. The standard normal values associated with AQL and RQL were determined (Z=0.125 and Z=1.28) on each case and timeframe. Figure 4-77 shows all three data collections with their AQL and RQL levels on each timeframe. As shown in Figure 4-77, the total area can be divided into three regions. Green zone implies acceptance with no inspection is needed. The assumption is that there is no defection in spraying uniformity. If the quality level is between AQL and RQL (yellow zone), then it is considered as an acceptance, and defective spots are less likely. Even Though defects in spraying applications would degrade overall concrete pavement performance, they will not reduce the quality to a point where the pavement has no value. The red zone shows the actual quality at which curing uniformity can be considered. In Figure 4-77, the spikes in the red zone represent the poor quality in the spraying pattern and non-uniform application. Thus, the advantage of using this concept is to find these locations and respray them to compensate for the lower quality of cure.

Victoria, TX

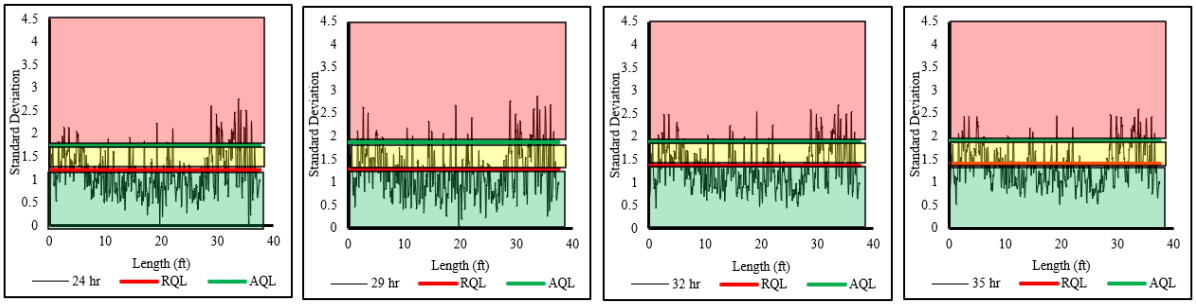

Itasca, IL

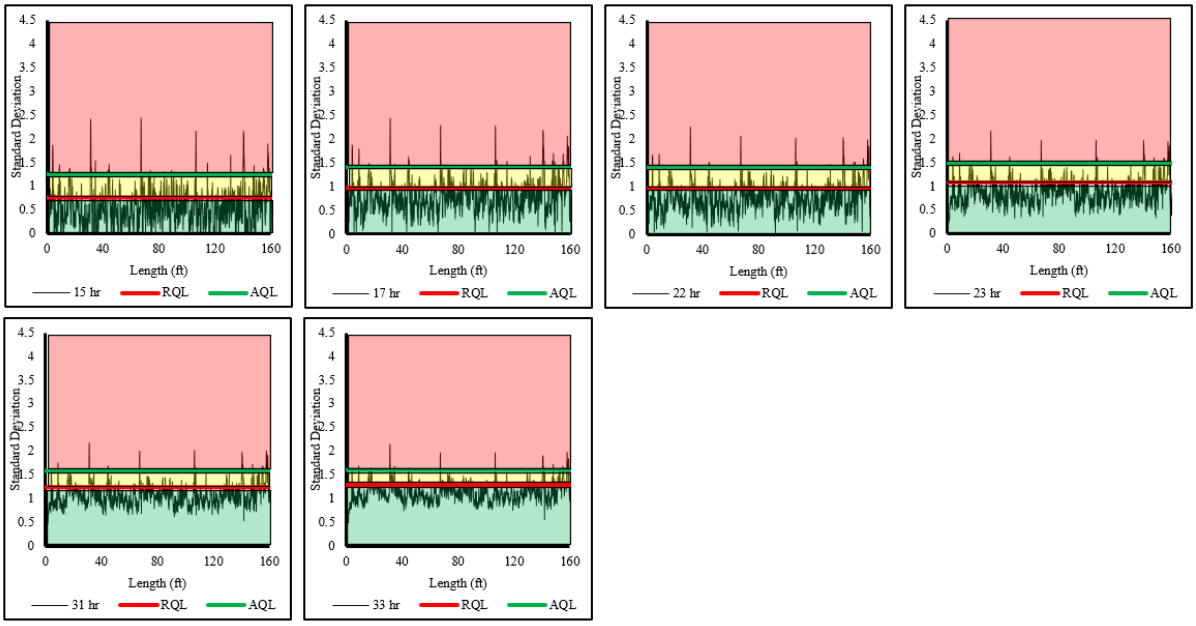

Jacksonville, FL

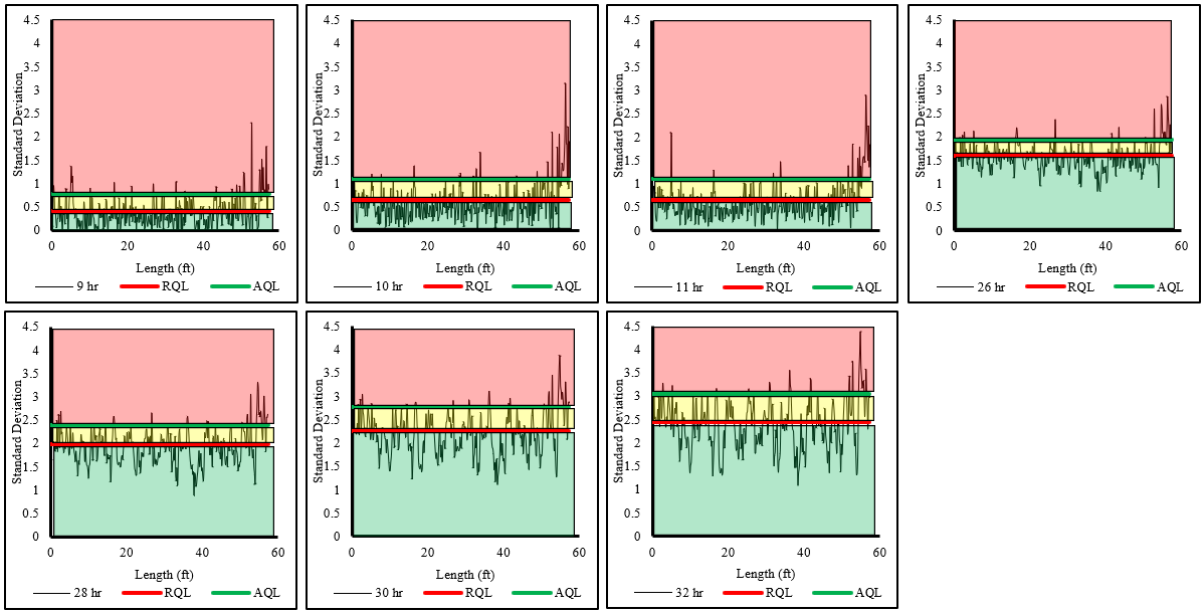

Figure 4-77. AQL and RQL Levels to Determine the Non-uniform Spots in Curing

Each set of collected data indicated that the green zone became wider over time. It means that there would be fewer spikes (i.e., susceptible spots) in later ages. This fact confirmed that the regression analysis: the dielectric constant changes were not significant after the first 12 hours. In other words, the first few hours were the most critical timeframe to fix the possible problems in the curing applications. Otherwise, the likely preservation could be too late to compensate for the deficiencies in curing compound spraying.

One of the most important findings was the effects of the spraying pattern on the uniformity and performance of curing. The Itasca, IL data collection was performed with a curing machine. Figure 4-77 shows that there were only a few spots with non-uniform spraying patterns. Moreover, these spots were just a single location that could have been fixed with minimal effort. However, red zones in both Jacksonville, FL and Victoria, TX, which were hand-sprayed, indicated several areas that needed attention. Thus, a broader area needed another round of spraying due to non-uniform patterns in spraying applications. For example, Figure 4-78 shows data collections at Jacksonville, FL. The dielectric constant, the standard deviation, and the AQL limit are shown in this plot.

Furthermore, the visual photographs of this section are superposed on the spatial DC data. The uniform curing application can be observed at the beginning and the middle of the road. However, there are some non-uniformities, which were indicated by red circles around the spikes higher than the AQL limit. One of the most important findings was the effects of the spraying pattern on the uniformity and performance of curing. Thus, a broader area needed another round of spraying due to non-uniform patterns in spraying applications.

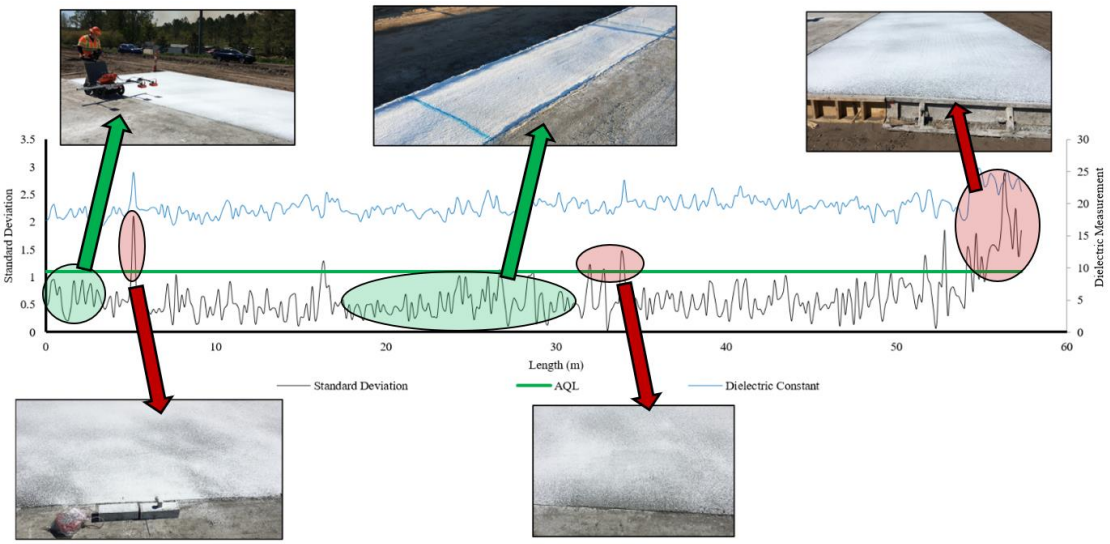

Figure 4-78. Superposing DC Data with the Visual Photographs of the Sections

4.4 Summary

This chapter highlighted all the field data collection programs from two separate field trials to represent different combinations of curing conditions, placement times, and ambient conditions. Several instruments were installed inside the concrete slabs. Each slab was monitored for strain, temperature, relative humidity, displacement, strength gain, and drying shrinkage. In these experiments, each slab was monitored up to seven days after placement. Data was collected in order to assess the quality of curing. The primary purpose

of the slab monitoring in Phase I was to collect data to assess the slab setting characteristics. Whereas the key purpose of Phase II was to achieve the predetermined set gradient. Early-age behavior of concrete slabs were discussed to relate slab movement to the method of curing. Additionally, using GPR as a practical approach to assess the curing effectiveness and uniformity was discussed. GPR was the main equipment in those field studies.

5 METHODOLOGY, MODELING, AND APPLICATION

The set gradient or the built-in gradient of the slab was accounted for in the analysis according to the discussion presented in Chapter 4. The set gradient has been termed the built-in temperature gradient, or perhaps the zero-stress temperature gradient if the warp strain is expressed in terms of temperature strain. In this chapter, the temperature and moisture differences between the top and the bottom of the pavement were calculated at corners to obtain the theoretical strains. Then, the results are compared with the measured strains from the corner's displacement in order to compute the set gradient. Although Pavement ME has a -10 ˚F temperature difference built into its computation of equivalent slab gradient, this number is highly dependent on the project conditions. Then, calibration of performance for design purposes is discussed to address the effect of climate. Finally, the probabilistic models are used to evaluate the relationship between the target set gradient and the environmental effects and curing practices.

5.1 The Set Analysis

As previously noted, upon first drying, the induced shrinkage strain is not entirely recoverable; some of it is permanent. The surface of a PCC pavement dries out, and the moisture level below remains at a relatively high level. The induced moisture gradient causes an upward warping of the slab that occurs along the edges and corners. The amount of permanent strain depends on many factors, such as curing and PCC mix design. As part of the drying shrinkage in PCC is irreversible, the remaining reversible portion varies with the ambient relative humidity.

The amount of the residual or set permanent curling/warping built into the test slabs is represented by the difference between the theoretical (calculated) and the

measured (actual) gradients. Based on the measured LVDT displacement of the slab's corner, the induced strains were calculated. The medium-thick plate theory was used to represent slab lift-off at the corner. Once the strain profiles in the slabs are obtained, the slab stresses can be calculated using the Bradbury solution. Finally, the equivalent set gradient can be expressed in terms of temperature. The models and calculations are explained in the following sections.

5.1.1 Corner Displacement

Consistent with curling, a concrete slab deforms into a concave configuration when the pavement is subjected to a resultant negative gradient of temperature and moisture through the thickness. If a negative combined equivalent linear temperature and moisture gradients are high enough, the interfacial tensile strength may be exceeded, and the slab edge or corner may separate from the underlying base. It is useful to model the slab curling and warping behavior to assess the set gradient in concrete slabs relative to interfacial separation.

Westergaard's solution is one-dimensional along the center of the slab. The medium-thick plate theory provides the basis for the 2D solution based on boundary conditions representing slab lift-off at the corner. Figure 5-1 presents a concrete slab, which is resting on a subgrade and is subjected to curling and warping. The coordinate system of the slab is also shown in Figure 5-1. The solution of the displacement *w* due to curling and warping was assumed to be of the general form shown in Eq. (5-1):

$$w = (A_1 cosx + A_2 sinx)(B_1 cosycoshy + B_2 sinysinhy)e^{-x} \quad (5\text{-}1)$$

where

w = slab corner displacement,

$A_1, A_2, B_1,$ and B_2 = coefficients,

X = distance along the X-axis,

x = dimensionless distance= $\frac{X}{\ell}$,

Y = distance along the Y-axis, and

y = dimensionless distance= $\frac{Y}{\ell}$

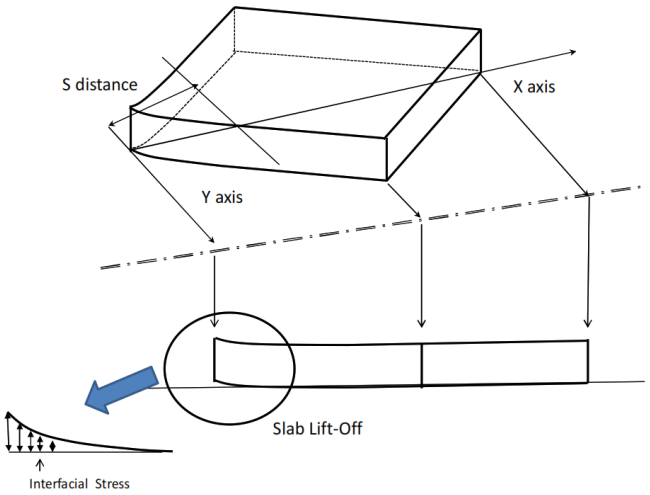

Figure 5-1. Corner Lift-off Displacement due to Curling and Warping

This form of the equation was chosen in order to include the effects of the boundary conditions on the lift-off displacement. Letting the bending moment and the shear force in the X-direction be denoted as M_x and V_x, respectively, per unit width of the cross-section and using the medium-plate theory, the moment at the slab corner, i.e., at (0, 0), can be expressed as:

$$M_x = D\left\{\frac{\partial^2 w}{\partial x^2} + v\frac{\partial^2 w}{\partial y^2} + \frac{\varepsilon(1+\mu)}{h}\right\} = 0 \qquad (5\text{-}2)$$

where

ε = the effective strain,

D = flexural rigidity of slab = $\frac{Eh^3}{12(1-v^2)}$, and

h = the slab thickness (m)

assuming that the slab corner detaches itself from the base due to curling and warping. In that case, this form of equation allows the separation distance of the slab along the *X*-direction be denoted as *S*, i.e., the slab is in contact with the base at a distance *S* from the corner along the *X*-axis. The bending moment at the point of contact, i.e. (*S*, 0), in the *X*-direction can be given as shown in Eq. (5-3):

$$M_x = D\left\{\frac{\partial^2 w}{\partial x^2} + v\frac{\partial^2 w}{\partial y^2} + \frac{\varepsilon(1+v)}{h}\right\} = -\frac{1}{6}S^2 h\rho \tag{5-3}$$

where ρ is the density of concrete. Because the slab has not separated from the underlying base at a distance *X*=*S*, the deflection at that point will still be zero. Hence, the deflection at the point of contact can be written as Eq. (5-4):

$$(A_1 coss + A_2 sins)B_1 e^{-s} = 0 \tag{5-4}$$

where $s = S/\ell$ and other variables were denoted before.

Using the medium-thick plate theory, the equation for shear force can also be written for the given curling-warping lift-off displacement problem. The shear force along the *X*-axis denoted as V_x at the corner of the slab, i.e., at (0, 0), is zero and can be expressed as Eq. (5-5):

$$V_x = D\left\{\frac{\partial^3 w}{\partial x^3} + \mu\frac{\partial^3 w}{\partial x \partial y^2}\right\} = 0 \tag{5-5}$$

Once the slab corner deflects upward from the ground, the shear force at the point of lift-off along the *X*-axis, i.e., at *X*=*S* and *Y=0*, is equal to the dead-weight portion of the slab that has separated itself from the underlying base. The shear force along the *X*-axis at the point of contact can be given as Eq. (5-6):

$$V_x = D\left\{\frac{\partial^3 w}{\partial x^3} + \mu\frac{\partial^3 w}{\partial x \partial y^2}\right\} = -\frac{1}{2}Sh\rho \tag{5-6}$$

Substituting the expression for deflection *w* and after simplifying these equations, the end expressions are given as Eq. (5-7):

$$\{A_1(cos\ s - \sin s + A_2(sin\ s + \cos s)\}B_1 + \{(A_2 - A_1)cos\ s - (A_2 + A_1)\sin s\}B_2 = -\frac{Sh\rho l^3 e^s}{4D} \tag{5-7}$$

For a given curling and warping situation, material properties (i.e., μ, ρ, k, $E(t)$), and slab dimensions (i.e., length, width, and thickness) are known beforehand. In the abovementioned system of equations, there are five unknowns, A_1, A_2, B_1, B_2, and S, that need to be solved. Since there are five equations as well as five unknowns, the system of equations can be solved for a given net (effective) strain (ε_{NET}). The strain calculated from the displacement was considered as the field-measured strain (discusses in APPENDIX). The corresponding vertical displacement w and the delamination or separation distance S can then be obtained for the given curling and warping conditions.

5.1.2 One-Dimensional Stress

Westergaard [190] suggested expressions for the state of stresses and displacements in concrete slabs based on the gradients inside of them. In the concrete slab deflection and stress analysis due to curling, the temperature distribution through the thickness of the slab was assumed to be linear. The interior stress for an infinite slab is (5-8):

$$\Delta\varepsilon_{u(WES)} = \frac{\alpha_t \Delta_t}{(1-v)} \tag{5-8}$$

where $\Delta\varepsilon_{u(WES)}$ is the strain element because of the temperature changes in the concrete slab, α_t is the concrete coefficient of thermal expansion, v is Poisson's ratio of concrete, and Δ_t is the temperature differences between the top and the bottom of the concrete slabs. Strain values (ε_x) due to the temperature were calculated based on the Westergaard's analysis [191] (maximum at strain happens at x = 0):

$$\varepsilon_x = \frac{1}{E}\left(\sigma_x - v\sigma_y\right) - \alpha(\Delta_t) \tag{5-9}$$

$$\sigma_x = \sigma_0\left[1 - \left(\frac{2cos\lambda cosh\lambda}{sin2\lambda + sinh2\lambda}\right)[(tan\lambda + tanh\lambda)]\right] \tag{5-10}$$

where

ε_x = the longitudinal strain,

σ_x = the longitudinal stress,

σ_y = the transverse stress = $\sigma_0 + v(\sigma_x - \sigma_0)$,

σ_0 = the maximum tensile stress due to temperature gradients = $\frac{E\alpha_t.\Delta T}{2(1-v)}$,

E = modulus of elasticity of concrete,

λ = constant = $\frac{b}{\sqrt{8}\ell}$,

ℓ = the radius of relative stiffness = $\sqrt[4]{\frac{Eh^3}{12(1-v^2)k}}$,

h = the slab thickness,

k = the modulus of the subgrade reaction,

b = the slab width, and

α_t = concrete coefficient of thermal expansion

In this study, σ_0 was considered as the maximum curling stresses, which was induced by the equivalent linear temperature gradient.

5.1.3 The Set Calculation

The early-age data (i.e., strain and temperature) was studied to determine the built-in gradients in the concrete slabs. Slabs deform when the combined equivalent linear gradients in the slabs fall below the amount locked (after creep has taken place) into the slab at the time of construction (the zero-stress gradient). In these cases, the slabs curl upward and cause tensile stress at the top of the slab. The amount of the set or permanent curling/warping built into the test slabs was represented by the difference between the theoretical and the measured strains. The ε_{set} is the difference between the theoretical and measured strains (see Eq. 5-11):

$$\varepsilon_{set} = \varepsilon_{measured} - \varepsilon_{theoretical} \quad (5\text{-}11)$$

The negative equivalent linear gradient permanently built into the slabs can be expressed in terms of the stress ratio (r). The stress associated with ε_{set} is reported with

respect to a ratio between the flexural stress due to load and the flexural strength of concrete as:

$$r_{set} = \frac{\sigma}{MOR} \tag{5-12}$$

where σ is the equivalent stress level derived from the set strain determination, and MOR is the modulus of rupture of the concrete. Based on the evolution of strength, MOR is modeled based on Eq. (5-13), which is similar to the form of the equation describing the evolution of compressive strength provided by ACI Committee 209 [123]. A best-fit regression line is fit through data points to interpolate or extrapolate strength (or stiffness) at various ages.

$$f_r(t) = \left(\frac{t}{a+b\times t}\right) \times f_{r28} \tag{5-13}$$

t = age of concrete (days),

f_r = MOR at age t (MPa),

f_{r28} = MOR at age of 28 days (MPa), and

a, b = fitting parameters

The setting of the concrete was characterized in this manner to facilitate correlation to pavement performances, such as the equivalent temperature difference. It will be shown subsequently that a zero-stress or built-in permanent gradient depends on curing quality. The set calculations in both Phase I and Phase II are discussed in the following paragraphs. In addition, the process of the set determination (summarized in a tabular format) for a single slab is explained in APPENDIX as an example.

5.1.3.1 Phase I

The difference between the measured and theoretical strain, including the irrecoverable strain, is reflective of the curing quality, as shown in Figure 5-2. The difference in Slab 3 between theoretical and actual strain measurements was lower than

other slabs. Thus, the amount of irreversible strain in this slab was less than the other slabs. However, the significant difference between the measured and theoretical strains indicates that the residual strains on Slab 1 and Slab 4 were considerable.

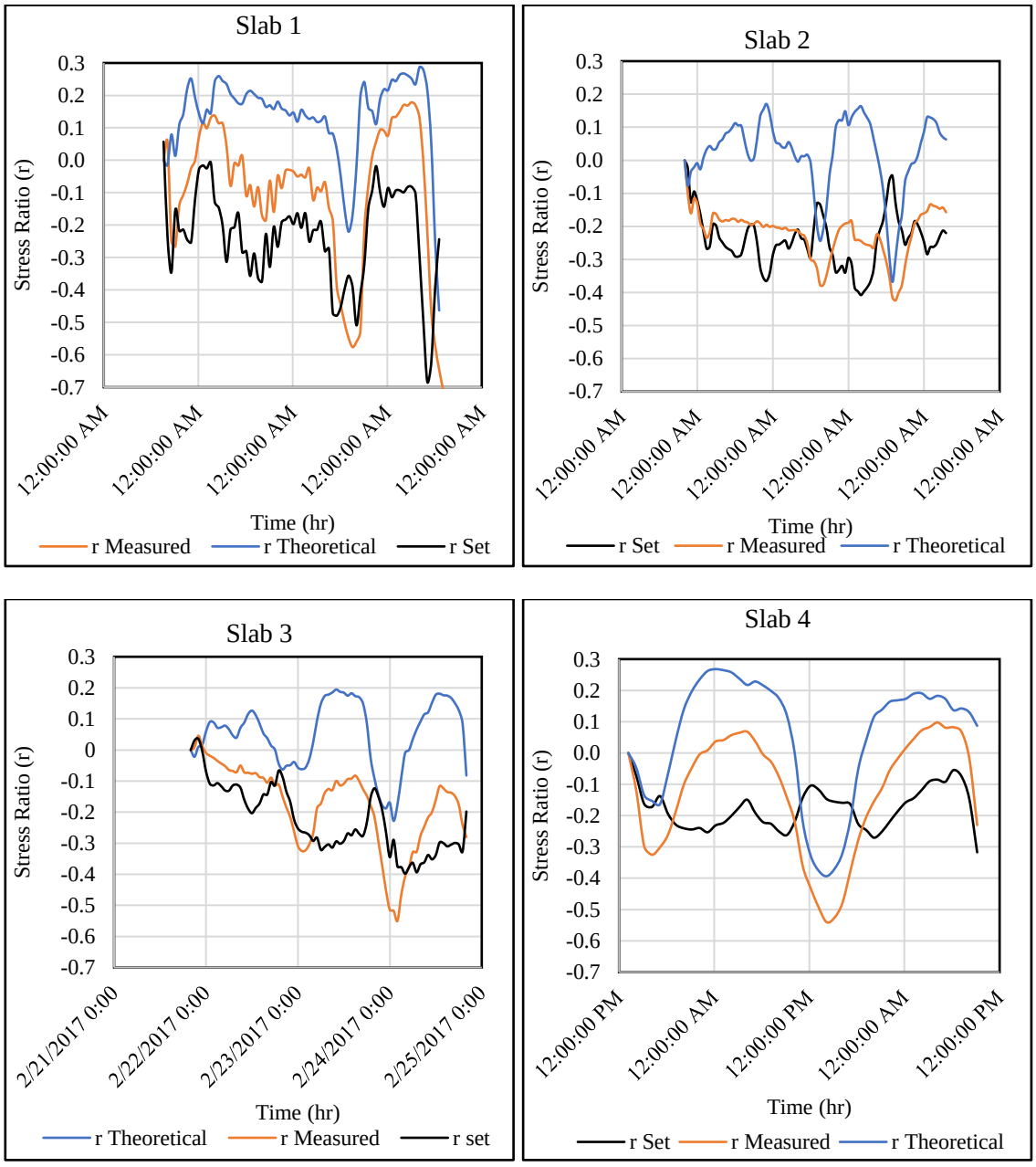

Figure 5-2. Theoretical and Measured Stress Ratio Profiles and r_{set} (Phase I)

The considerable irreversible strain is attributed to large temperate and moisture gradients. The process of calculating r_{set} gradient for Slab 3 is explained with tables and figures in ten steps in APPENDIX.

5.1.3.2 Phase II

The difference between the measured and theoretical strain, including the irrecoverable strain, is shown in Figure 5-3. The difference in Slab 3 between theoretical and actual strain measurements was lower than other slabs. The amount of irreversible strain in Slab 3 was not as much as Slab 1. However, the significant difference between the measured and theoretical strains indicates that the residual strains on Slabs 1 and 2 were considerable. This outcome was attributed to large temperate and moisture gradients.

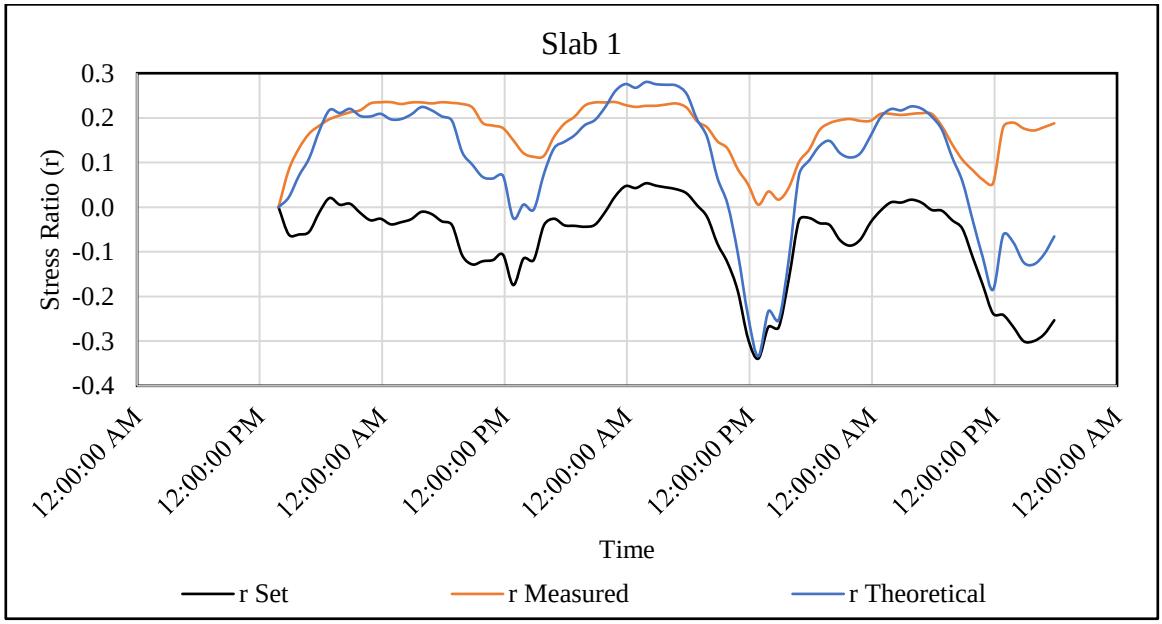

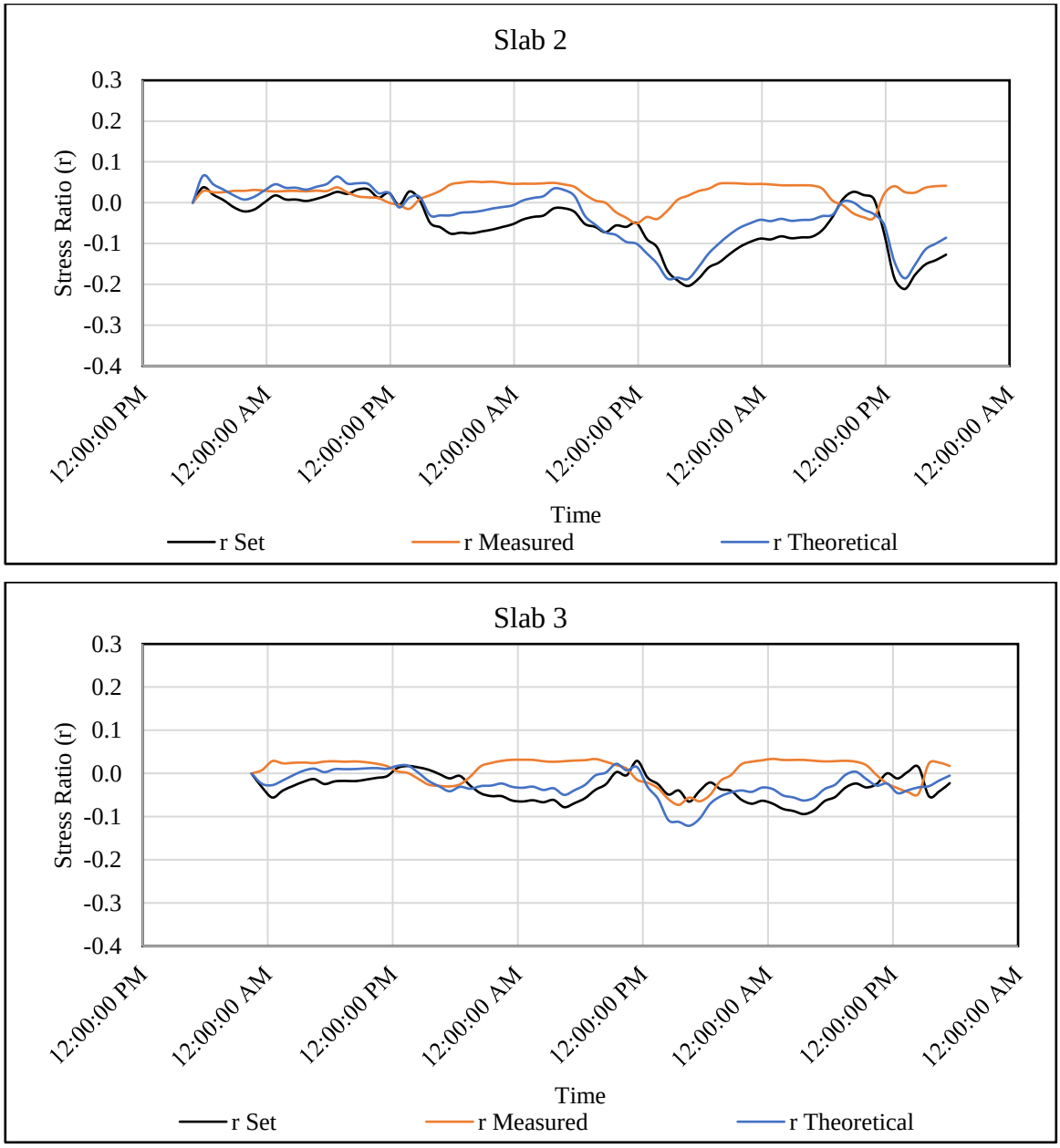

Figure 5-3. Theoretical and Measured Stress Ratio Profiles and r_{set} (Phase II)

5.2 Interpretation and Findings

Calibration of performance for design purposes should inherently address the effect of climate on fatigue cracking of concrete slabs. Even though the interaction of the

climate with performance is complex, curing effectiveness affects slab support and ultimately affects the critical slab stresses and cracking. Not only do diurnal moisture and temperature gradients through the slab affect the slab cracking, they also affect the permanent built-in curling and warping that occurs during construction.

The key factors associated with the performance of curing compounds in terms of EI were addressed in this investigation. EI should be useful when choosing the most appropriate application rate for a given curing compound. In

Table 5-1, a summary of four slabs in Phase I is presented. The value of EI, weighted over the history of EI, is listed.

Table 5-1. The Set Gradient and Equivalent Temperature Gradient (Phase I)

	Curing Compound	Application Rate (ft^2/gal)	Time of Placement	r_{set}	Equivalent Set Gradient Temperature (F/in)	Total Equivalent Temperature Difference at Set (F)	EI
Slab 1	WRM-1150	250	10:00	-0.190	-2.44	-16.8	0.081
Slab 2	WRM-1625	250	14:00	-0.113	-1.10	-10.8	0.115
Slab 3	WRM-1625	180	17:00	-0.075	-0.67	-6.4	0.076
Slab 4	None	None	10:00	-0.162	-1.87	-18.2	0.075

The direct relationship between EI and set for testing slabs under different curing conditions are shown in Figure 5-4. A higher EI is generally associated with a lower set, which represents a lower irreversible shrinkage. EI is a function of PE and AR. Therefore, in a particular set (either low or high state), the distribution of EI (material-driven and weather-driven) should be considered.

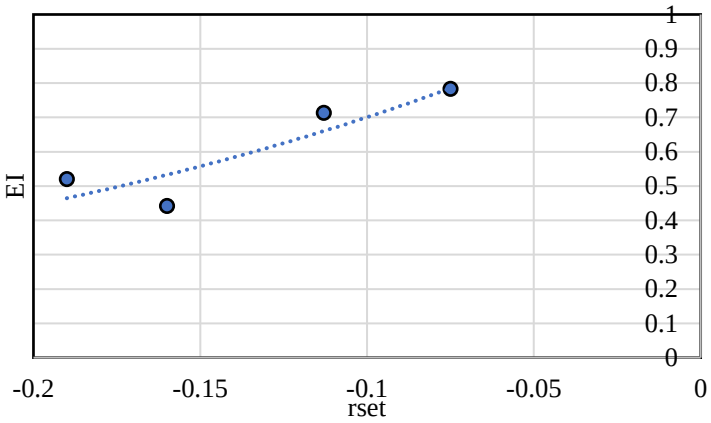

Figure 5-4. EI vs. Set Gradient in Slabs (Phase I)

One of the purposes of Phase II was to achieve a -10 ˚F temperature difference in Slab 2. The temperature difference in Slab 2 (2 PM placement) was close to -10 ˚F (-10.1 ˚F). Phase II results are shown in Table 5-2. Although Slab 1 and Slab 2 were treated with the similar curing compound and application rate (WRM-1625 and 180 ft^2/gal, respectively), the total built-in temperature gradient was not identical. The reason was that the built-in temperature gradient is primarily affected by the weather conditions during the setting process. The largest negative built-in curling was observed for Slab 1, which was placed in the morning. In this case, the slab's displacement reached its maximum amount due to the solar radiation and heat of hydration at about the same time. Thus, a relative high positive temperature gradient was formed when the slab hardened. Afternoon and evening constructions of Slab 2 and Slab 3 induced a milder temperature gradient at the final set.

Table 5-2. The Set Gradient and Equivalent Temperature Gradient (Phase II)

	Curing Compound	Application Rate (ft^2/gal)	Time of Placement	r_{set}	Equivalent Set Gradient Temperature (F/in)	Total Equivalent Temperature Difference at Set (F)	EI
Slab 1	WRM-1625	180	10:45	-0.158	-1.71	-12.1	0.740
Slab 2	WRM-1625	180	14:30	-0.121	-1.13	-10.1	0.726
Slab 3	WRM-1625	250	17:35	-0.096	-0.82	-8.0	0.812

In addition, a higher built-in gradient was observed in Phase II compared with Phase I in the similar treatment and time of placement. By comparing the slabs in both phases, the higher built-in temperature gradients in the October construction (Phase II) compared to the February construction (Phase I). Thus, not only the time of placement on the day, but also the construction season of the year significantly influences the built-in temperature gradient.

As the summary of set gradient results, there were four variables in the field testing: PE, application rate, curing compound type, and time of placement. Based on the similarities and dissimilarities among the slabs in both Phase I and Phase II, some conclusions can be drawn. In the same PE for both phases, Slab 1 and Slab 2 were treated with the same curing compound and the same application rate. However, the amount of the set gradient was significantly different due to the various time of placement. Another case is Slab 3 in each phase, which had the same time of placement and the same curing compound. In this situation, changing the application rate has changed the set gradient. In Phase II, Slab 2 and Slab 3 were placed on the same day with the same curing compound. Even though a higher application rate was used in Slab 2 (which was placed at 2 pm), the set gradient was higher than Slab 3. Thus, the application rate did not improve the set gradient independently. In other words, all variables should be considered together. Finally, all the slab in Phase II were treated with the same curing compound under the same climate. The highest negative built-in was observed in Slab 1, which was placed in the morning. Choosing the right time under each condition would help to control the gradient. Therefore, the magnitude of the permanent curl/warp can deviate significantly from -10 °F even in the similar pavement sections.

5.3 Set Gradient Framework

The amount of the residual or set permanent curl/warp built into the concrete accounts for the creep effect. This creep includes the irrecoverable strain and is reflective of the curing quality. Figure 5-5 is a framework that shows the development of the residual, or set permanent curl/warp, which is gradually built into a concrete slab; it is indirectly represented by the difference between the theoretical and the measured displacement. Since the magnitude of permanent curl/warp (which can be estimated from the slab measurements) diminishes with time, it also reflects the effects of creep.

The set in the concrete slab develops over time as does the amount of permanent, non-recoverable strain; only a portion of the non-recoverable strain, however, contributes to the built-in or warping set. The values for the set coefficient (Ψ) (i.e., strength/elastic modulus), drying shrinkage strain, and creep strain as conceptually illustrated are shown in Figure 5-5 up to 72 hours after placement. There is less creep strain at any point in time after the final setting to 72 hours. Creep, as a time-dependent deformation, is relatively high at the early ages. Creep mostly evolves with curling/warping behavior and tends to negate the tensile stresses. As shown in Figure 5-5, the creep strain seems to diminish after a few days from construction of the slab [3].

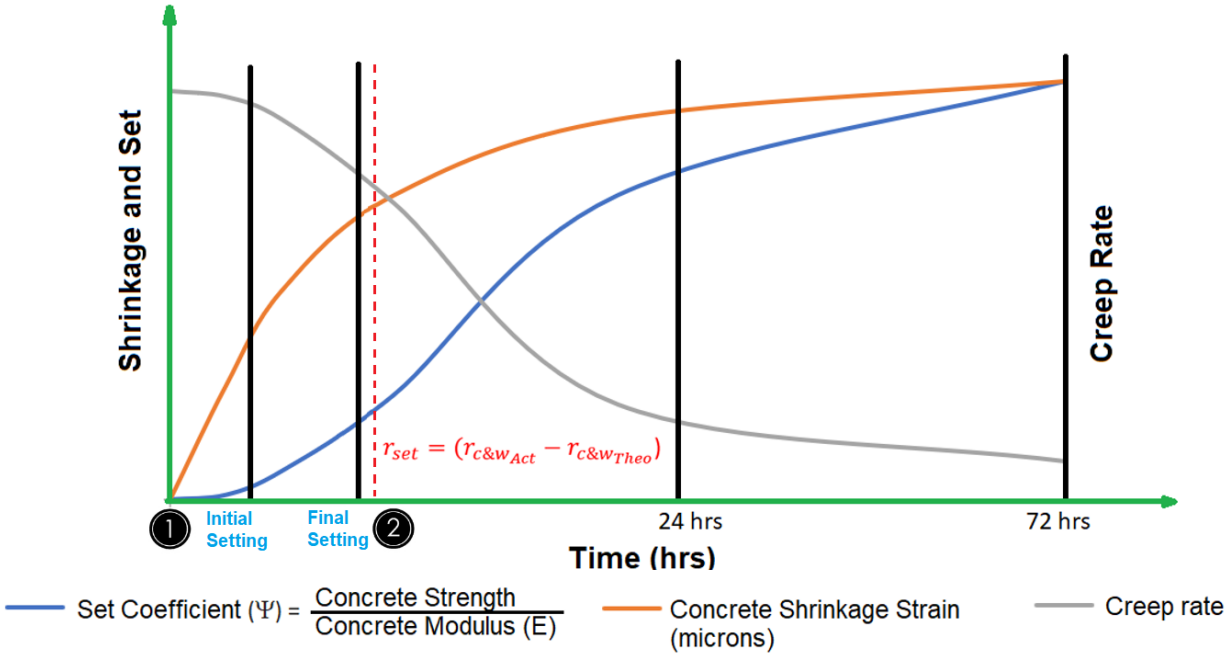

Figure 5-5. Framework for Built-in Set Parameter Estimation

Figure 5-5 also shows the initial and final setting of concrete as defined by ASTM C 403 [136]. These setting states occur as concrete has a transition from a fresh state to a hardened state. The zero-stress is the moment that concrete transfers from a plastic state to a solid state, which is shortly after the final set time (Point 2). During the period from Point 1 to Point 2, no stresses can be developed. As shown in Figure 5-5, creep strain due to the dead-weight of the concrete will subside about 72 hours after placement. After that, shrinkage is mostly recoverable. If plastic shrinkage occurs, it does so before the initial set, as defined by ASTM 403 [136]. It is likely that a combination of plastic shrinkage and irrecoverable shrinkage develops between the initial and final set stages. The irrecoverable shrinkage (due to the forming of new bonds) and creep strain occurs after the final set but before 72 hours. The irreversible shrinkage contributes to the permanent moisture warping, while the reversible shrinkage coincides with seasonal variation in slab moisture and daily variations in temperature.

5.4 Calibration Analysis

As discussed earlier, an effective negative temperature gradient can be permanently set in the slabs, in terms of the stress ratio (*r)*, as shown in Figure 5-6. The setting of the concrete was characterized in this manner to facilitate a correlation with the pavement performance, such as the equivalent temperature difference. A "zero-stress" or "built-in" permanent gradient depends on curing quality, but the upper illustration in Figure 5-6 pertains to the assessment of the set gradient from a calibration analysis of slab cracking perspective. The magnitude of the set gradient is estimated from the calibration of JPCP cracking and is expressed relative to a gradient of -10 ˚F as defaulted in the Pavement ME software. As previously noted, the residual or set permanent curling/warping built into the test slabs is represented by the difference between the theoretical and measured strains.

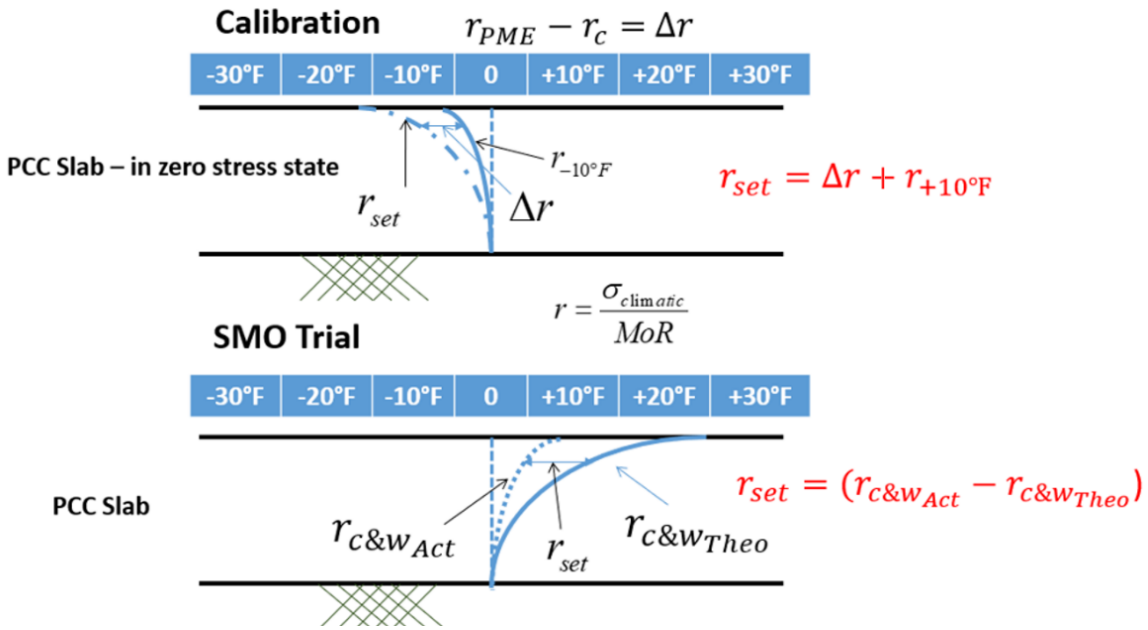

Figure 5-6. The Permanent Built-in Curling and Warping During Construction

The set gradient was extracted from the difference between the stress ratio related to the theoretical gradient and the stress ratio related to the measured gradient. The set gradient was also previously extracted from the analysis of slab cracking data by examining the difference between the calibrated stress ratio ($r_c = \left\{\frac{\log(N_{f_c})}{C_1}\right\}^{-\frac{1}{C_2}}$) as a function of the actual loads to failure (N_{f_c} – determined at 10% slab cracking level as the terminal cracking value) and a theoretically-based stress ratio ($r_{PME} = \left\{\frac{\log(\frac{N_i}{D_{PME}})}{C_1}\right\}^{-\frac{1}{C_2}}$) as a function of the load count (N_i) and damage (D_{PME}) generated by the Pavement ME software associated with bottom-up cracking. This difference is curling and warping related and is related to r_{set} in Eq. (5-18):

$$r_{set} = \Delta r + r_{-10\,°\mathrm{F}} \tag{5-18}$$

with respect to the Pavement ME software. The parameter $r_{-10\,°F}$ is the set gradient defaulted in Pavement ME and is applied to both bottom-up and top-down cracking determinations as was the r_{PME} parameter.

The total transverse cracking in JPCP (in terms of %cracked slabs) is acquired by combining the percentages of predicted bottom-up and top-down slab cracking and subtracting the probability that both appear in the same slab [15]. Figure 5-7 shows detailed calculations of how the loads of failure and level of cracking are determined. As previously noted, the threshold cracking for the design was set at 10% and, although the analysis of the performance data is not shown here, the comparability can be seen in the field performance.

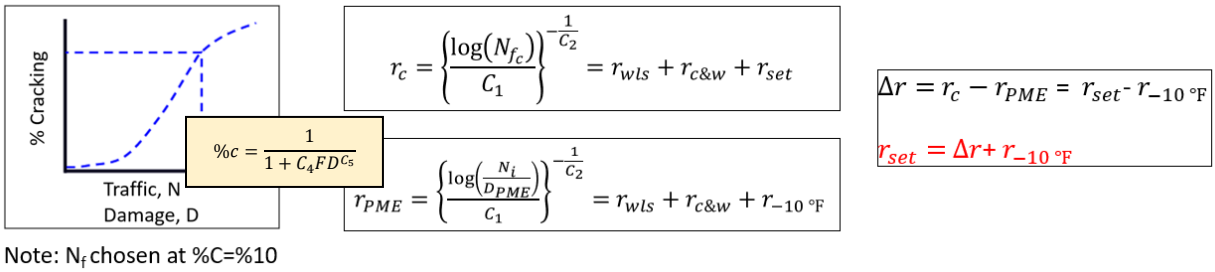

Figure 5-7. The Calculation of C_4 and C_5 Based on Load Damage in Pavement ME

Based on the regional calibration, the transverse cracking of concrete slabs initiates at the concrete surface and propagates downward (top-down cracking) [192]. The intensity depends on slab length, support and ambient conditions, and material properties. In top-down cracking, pavement often is exposed to excessive negative temperature gradients that cause fatigue damages on the surface. This gradient ultimately causes transverse cracks on the surface of concrete pavement. Slabs with high negative temperature and moisture gradients have a high tensile stress at the top near the middle of the critical longitudinal edge [193, 194]. The top-down stresses become critical in the presence of a considerable permanent upward curling/warping [192].

Parameters C_4 and C_5 are calibration constants to adjust cracking damage trends to improve goodness-of-fit with field data. The accumulated damage due to loading is fatigue damages (FD), which considering all critical factors for JPCP transverse cracking, can be defined as follows

$$FD = \sum \frac{n_i}{N_i} = \frac{N}{N_f} \tag{5-19}$$

where i accounts for changes in PCC, age, axle type, load level, traffic path, and temperature.

n_i and N_i are the applied and allowable number of load applications at different conditions, respectively. N_f is the ultimate number of loads to failure, which is determined using the following field calibrated fatigue model (Eq. 5-20):

$$Log(N_f) = C_1\left(\frac{1}{r}\right)^{C_2} + 0.4371; r = r_L + r_e + r_{set} \quad (5\text{-}20)$$

Although it is not elaborated, it is inferred through the correlation of distress level that the parameter N_f is also an alternative candidate for calibration through curve fitting for the C_1 and C_2 (fatigue damage calibration) coefficients. The parameter r is the stress ratio and is equal to the stress in the slab (σ) divided by the slab strength or the MOR. Also, r_e and r_L are stress ratios based on environmentally (climatic gradients) induced stress and wheel load stress, respectively. Climatic gradients are a combination of the temperature and moisture effects being different at the top of the slab, from those at the bottom and are believed to have a significant effect on the performance of the pavement. Eq (5-19) and Eq (5-20) can be simplified as:

$$\frac{\partial FD}{\partial r} = N\frac{\partial\left(\frac{1}{N_f}\right)}{\partial r} = N\frac{\partial}{\partial r}\left(10^{-(C_1+C_2 r)}\right) = -ln(10)\, C_2 FD \quad (5\text{-}21)$$

$$\Delta FD = -ln(10)\, C_2 FD r_{set} \sim 4 \cdot FD \quad (5\text{-}22)$$

Referring to the cracking model encompassed within the Pavement ME software (see Figure 5-7), the focus of a calibration effort is to determine the appropriate values of C_4 and C_5:

$$\%c = \frac{1}{1+C_4 FD^{C_5}} \quad (5\text{-}23)$$

which relates loads of failure and level of cracking. The threshold cracking for the design was set at 10%, the comparability can be seen in the field performance as well. Prior to the determination of C_4 and C_5 based on analysis of performance (i.e. ($\%c$) – damage (FD)) data, it is advantageous to transform the cracking model into load application terms as well as convert into a linear form mathematically as:

$$\%c = \frac{1}{\left[1+C_4 FD^{C_5}\right]} = \left[1 + C_4 N^{C_5} N_f^{-C_5}\right]^{-1} \quad (5\text{-}24)$$

$$\left[\frac{1}{\%c} - 1\right] N_f^{C_5} = C_4 N^{C_5}$$

$$Ln\left\{\left[\frac{1}{\%c}-1\right]\right\}+C_5Ln\{N_f\}=Ln(C_4)+C_5Ln(N)$$

$$Ln\left\{\left[\frac{1}{\%c}-1\right]\right\}=Ln(C_4)+C_5\left\{Ln(N)-Ln\{N_f\}\right\}=Ln(C_4)+C_5\{Ln(FD)\}$$

$$Ln\left\{\left[\frac{1}{\%c}-1\right]\right\}=Ln(C_4)-C_5Ln\{N_f\}+C_5\{Ln(N)\}$$

where the FD data can be generated from Pavement ME software runs for the specific site input. Thus, in the linear form ($y=b+mx$), the constituents are as shown in Table 5-3:

Table 5-3. Converting the Performance Cracking Model into Linear Form

Elements	Equations
y	$Ln\left\{\left[\frac{1}{\%C}-1\right]\right\}$
x	$Ln(N)$
m	C_5
b	$Ln(C_4)-mLn\{N_f\}$

In order to compare the percent cracking and damages of different conditions, performance data from eight sections included in the long-term pavement performance (LTPP) database with respect to FD were chosen to show the process of calibration. The cracking percentage (i.e., a mix of bottom-up and top-down cracking sites) was calculated using Eq. (5-23). Figure 5-8 demonstrates the predicted *c%* versus total FD. The fatigue cracking damage was run for each site over its life where cracking data were available. Also, the nationally calibrated cracking model is shown in this figure with a black dashed line.

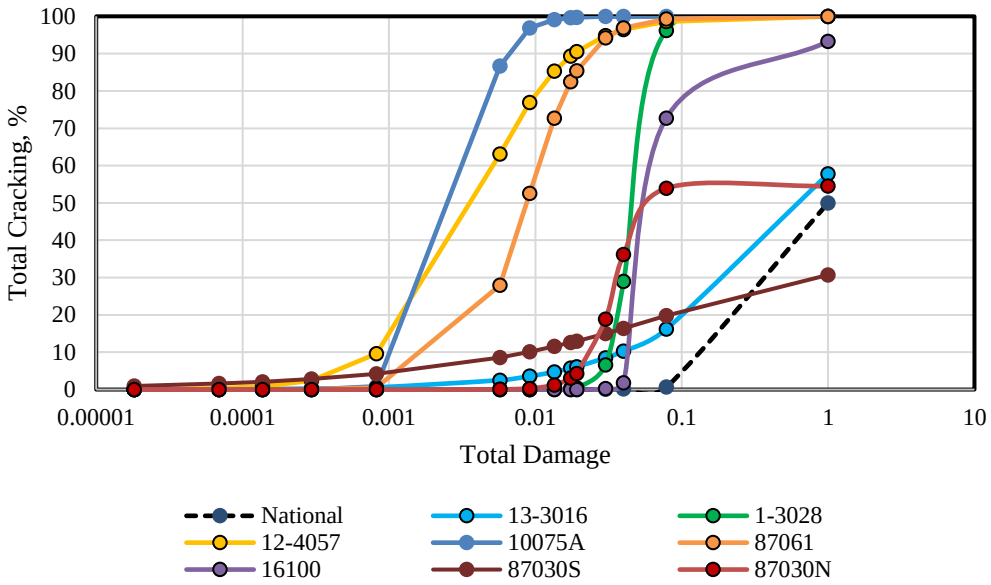

Figure 5-8. Cracking Model Shown with the Field Data from Eight Sites

A best-fit S-shaped curve was fit to the data by using calibration coefficient C_4 and C_5. The calibration coefficients for these eight sections and the national calibrated model are shown in Table 5-4.

Table 5-4. Calibration Coefficients for Different Sections and National

	National	**13-3016**	**1-3028**	**12-4057**	**10075A**	**87061**	**16100**	**87030S**	**87030N**
C_4	1	0.7302	0.0000	0.0004	0.0000	0.0000	0.0723	17.1964	13.46374
C_5	-1.68	-0.7697	-6.1367	-1.4277	-3.3838	-2.2517	-3.7489	-0.5192	-0.6038

Figure 5-9 summarizes the computation of the set stress ratio for the calibration slabs correlated to the calibration coefficients C_4 and C_5. As expected, the choice of the coefficients varies with r_{set}. The computations of the design conditions using these correlations for the selection of the coefficients indicate greater performance and lower

design thicknesses with increasing values of r_{set}. Since the set of the slab can be controlled, there is justification for including the default Pavement ME set and calibration C_4 and C_5 coefficient values in the correlation (values circled in red).

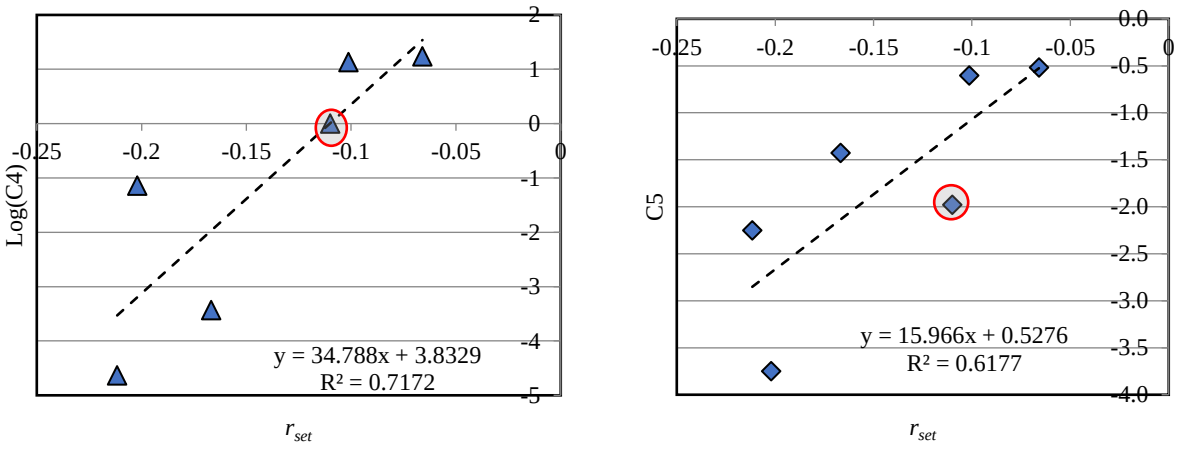

Figure 5-9. Correlation to C_4 and C_5 for Eight Calibration Sites

The blue points came from the field performance data, and the point in the red circle is the Pavement ME national calibration. In these figures, the Pavement ME conditions fit in this plot and serve as validation of the approach. It is well accepted that the set gradient will vary with climatic and material factors that affect how the concrete sets during the hardening process.

Analysis of the amount of heat and moisture movement that occurs during the setting of the concrete is a basis to anticipate the development of the set as it occurs throughout a paving operation.

$$\frac{\partial Ln\left(\frac{1}{\%c}-1\right)}{\partial FD} = \frac{1}{\left(\frac{1}{\%c}-1\right)}\frac{\partial\left(\frac{1}{\%c}-1\right)}{\partial FD} = C_5\frac{\partial(LnFD)}{\partial FD} = \frac{C_5}{FD} \tag{5-25}$$

$$\rightarrow \frac{\partial\left(\frac{1}{\%c}-1\right)}{\partial FD} = \left(\frac{1}{\%c}-1\right)\cdot\frac{C_5}{FD}$$

$$\rightarrow \frac{\partial FD}{\partial r}\cdot\frac{\partial\left(\frac{1}{\%c}-1\right)}{\partial FD} = -ln(10)\,C_2 FD\cdot\left(\frac{1}{\%c}-1\right)\cdot\frac{C_5}{FD} = -ln(10)\,C_2\left(\frac{1}{\%c}-1\right)C_5$$

$$\rightarrow \frac{\partial(\%c)}{\partial r} = -ln(10)\, C_2 \left(\frac{1}{\%c} - 1\right) C_5$$

$$\rightarrow \Delta\%c = -ln(10)\, C_2 \left(\frac{1}{\%c} - 1\right) C_5 \cdot r_{set}$$

Calibration for fatigue cracking is done with performance data that consists of cracking percentage (*%c*) and traffic load information. The linear form of the *%c* equation or model is used to analyze *%c* – traffic (*%c*-N_e) data, which is used to determine the N_f parameter for a given site. Whether the *%c* data is analyzed in terms of the damage (*FD*) or the traffic (N_e), the form of the trend line is the same. Due to this feature, the *%c*-N_e and *%c*-*FD* models share the same value of C_5 with the only difference between the C_4 values being the $e^{C_5 Ln\{N_f\}}$ term, as noted above. In addition to the determination of the C_4 and C_5 values, obtaining the corresponding set gradient values expressed in terms of the stress ratio is another part of the calibration process. Given the amount of damage, the percent of cracking (*%c*) depends upon the set on each slab. Table 5-5 shows the initial cracking damages associated with the set in both Phase I and Phase II. According to Eq. (5-25), the cracking percentage is directly related to the total damage. Also, the higher set gradient corresponds to the higher percentage of cracking.

Table 5-5. Percentage of Cracking, Damage and r_{set}

	Slab	%Cracking (*%c*)	Damage (*FD*)	r_{set}
Phase I	Slab 1	12.12%	0.290	-0.190
	Slab 2	9.48%	0.272	-0.113
	Slab 3	7.21%	0.244	-0.075
	Slab 4	18.41%	0.331	-0.162
Phase II	Slab 1	15.01%	0.308	-0.158
	Slab 2	13.21%	0.293	-0.121
	Slab 3	10.42%	0.266	-0.096

By improving both environmental and loading models, as well as the consideration of the built-in curling and warping in fatigue damage calculations, the fatigue cracking in concrete pavements can be better predicted.

5.5 Dependence of Creep on Set

The early-age impacts of creep on the set gradients in concrete slabs is quite complicated because of the fluctuating stress [10]. The total deformation should not be divided into shrinkage and creep elements due to the complexity of its behavior [195]. Although the total deformation is a well-defined concept and separated into two components of creep and shrinkage, both of them are complex phenomena. Under typical conditions, concrete slabs at early ages are almost water saturated right after placement. As the surface is subjected to various levels of exposure, water evaporates from the exposed surface until equilibrium with the adjacent environment is reached. In the test program, the shrinkage strain was measured in accordance with the ASTM C 157 [168]. A strain gauge was used to measure the free shrinkage strain for each slab, which is an internal volumetric strain caused by moisture loss. Relative humidity was measured within another specimen to establish the relationship between the moisture content and shrinkage strain.

Activation energy can be calculated by using mortar cube specimens (2-inch sides) based on ASTM C 1074 [196]. In order to calculate the initial activation energy in the lab, a mortar mixture was prepared with the same cementitious material contents and the same w/c that was used for the slabs in the field. Mortar cube specimens were treated (based on the four slabs curing practice) and kept in temperature-controlled (12, 25, and 35 °C) water baths a day after. The compressive strength tests performed at 3, 7, 14, and 28 days were conducted on the samples. Three specimens were considered at each age and the average strength was reported. The strength versus age was analyzed to calculate the relationship between the strength development rate (*k*-value) and the curing temperature. Thus, Eq. (5-14) should be optimized for the strength-age estimation at each curing temperature:

$$S = S_u \frac{k(t-t_o)}{1+k(t-t_o)} \tag{5-14}$$

where

S = the average compressive strength at the age of t (MPa),

t = the testing age (day),

S_u = limiting strength (MPa),

t_o = age when strength development is assumed to begin (day), and

k = the rate constant (1/day)

The activation energy for creep is assumed to be a function of the magnitude of the strength of the concrete. The compressive strength of a standard cylinder (4×8 inches) was tested at 1, 3, 7, and 14 days after placement to calculate hydration degree and maturity. The best-fit values of the factors were computed using regression analysis. Figure 5-10A shows how the compressive strength value for each temperature was calculated by interceptions of best-fit lines of the reciprocal of strength against the reciprocal of age [197]. The activation energy was computed by the best-fit straight-line slope of the natural logarithm of reciprocal of age against the reciprocal of the curing temperature (see Figure 5-10 B). The rate of change in Figure 5-10 B was the magnitude of activation energy divided by the gas constant (8.314 J/mol/˚K). In this test, E_a value was 3828 K. As using curing compounds with different application rates may change the activation energy, specimens according to treatment practice were made and cured. Table 5-6 shows the activation energy for each specimen.

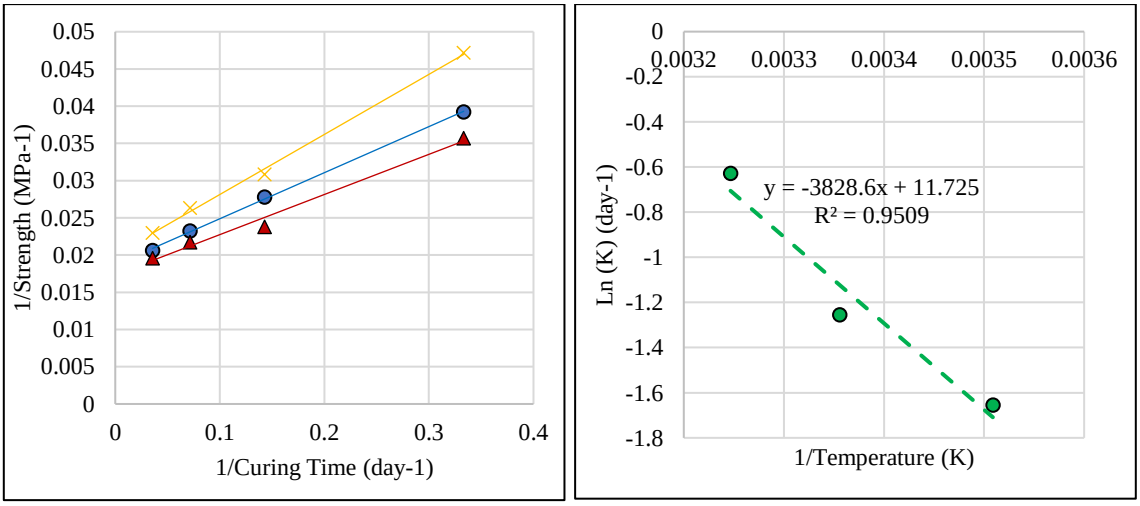

A) Reciprocal of Strength vs. Reciprocal of Age; B) Logarithm of Reciprocal of Rate Constant vs. Reciprocal of Curing Temperature.

Figure 5-10. Activation Energy Graphs

EI, which was defined in accordance with concrete maturity concepts, is a convenient way to delineate the differences in curing conditions [83, 143]. This index is a function of the equivalent age of concrete, which is sensitive to different curing conditions and is based on the Arrhenius concept. Thus, EI was associated with the activation energy as well. Laboratory testing was conducted to evaluate the effectiveness of a given curing compound with respect to its application rate. Table 5-6 shows the resulting EI values for each method of curing. A clear trend is evident between EI and E_a determined for the method of curing. Determination of activation energy in this manner is an effective way to quantify the effect of materials during the curing process.

Table 5-6. Activation Energy for Different Curing Practices

Sample	Curing Compound	Application Rate in (ft^2/gal)	Activation Energy (E_a)	EI
1	WRM-1150*	250	4026	0.69
2	WRM-1625**	250	4211	0.72
3	WRM-1625	180	4354	0.75
4	None	None	3828	0.61

** Non-pigmented and resin-based (hydrocarbon)*
*** White-pigmented and wax-based*

Pre-instrumented sections of the test slabs consisted of four gauges that were isolated from the slab concrete via coring and placed in the slab; coring operations were conducted the day following the placement of the concrete. These strain gauges were oriented with the longitudinal axis of the slab. The lead wire for each gauge was routed underneath the slab to protect it during the coring of the strain gauge. Furthermore, the gauges were placed transversely in the mid-slab region to facilitate the measurement of the longitudinal strain of the slab. The instrument installations are shown in Figure 5-11; the coring was undertaken at the locations indicated in this figure.

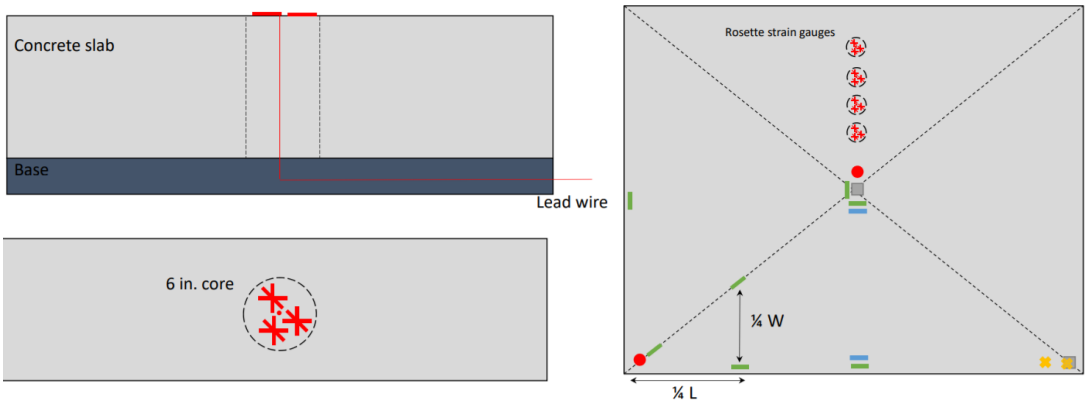

Figure 5-11. Rosette Strain Gauges Instrumentations for Cored Samples

Gauges were installed on the top (1 inch from the surface and 6 inches from the base) and were embedded in the bottom (5 inches from the surface, 2 inches from the base) in Slab 1. Strain within the cored area is shown in Figure 5-12 with a black line. Figure 5-12 shows that the creep process was taking place, although the initial strains were not captured. The amount of the residual or set permanent curling/warping from Figure 5-12 built into the concrete was represented by the amount of creep strain. This creep included the irrecoverable strain and was reflective of the curing quality.

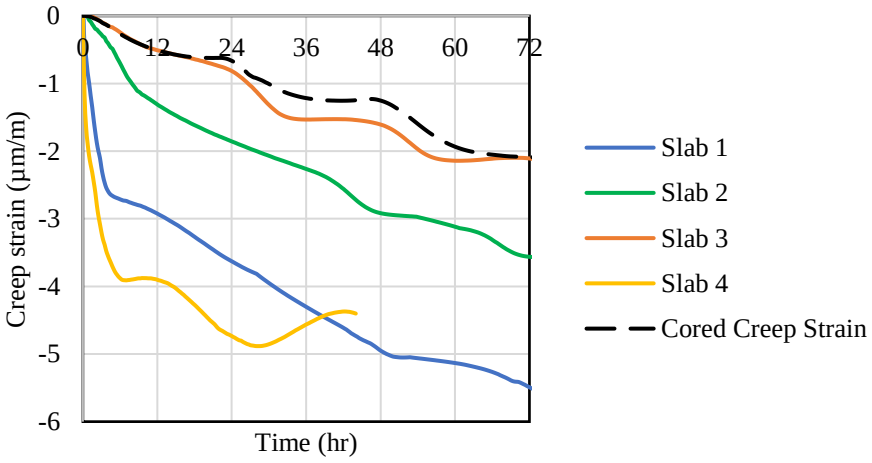

Figure 5-12. Creep Strains in the Cored Specimen and Slabs (Phase I)

The relaxation occurred following coring of the concrete around the strain gauges. The creep strain in the test slabs, which was the time-dependent deformation, primarily occurred once the slabs were able to sustain tensile and compressive stress, such as when slab lift-off occurred. Strain computations were undertaken to assess the possible on-set of creep strain over time. As explained, the differences between the measured and calculated strains in each test slab were the basis of the set strain determinations as affected by the curing conditions. Slab 1 and Slab 4, which experienced greater built-in gradients, also had a greater amount of early-age creep. The amount of creep strain in Slab 2 and Slab 3 was much less than Slab 1 and Slab 4 in longer ages. The measured creep strain of the cored sample was much less compared to the computed Slab 1 creep strain. The creep strain affected the magnitude of r_{set} subsequently discussed.

Creep behavior is typically described in terms of compliance (J), which represents stress-dependent strain as a function of the time of loading (t) and the equivalent age of the concrete (t_0). The average compliance $J(t, t_0)$ that represents the effective stress-dependent strain by unit stress is shown in Figure 5-13. The average compliance (J) versus time was not similar among the slabs. The early-age drying creep results showed that compliance followed the same pattern. The compliance in Slab 3 was the lowest and gradually increased with a low rate. Slab 4 compliance increased with a higher speed. The same behavior was observed in the creep strain results.

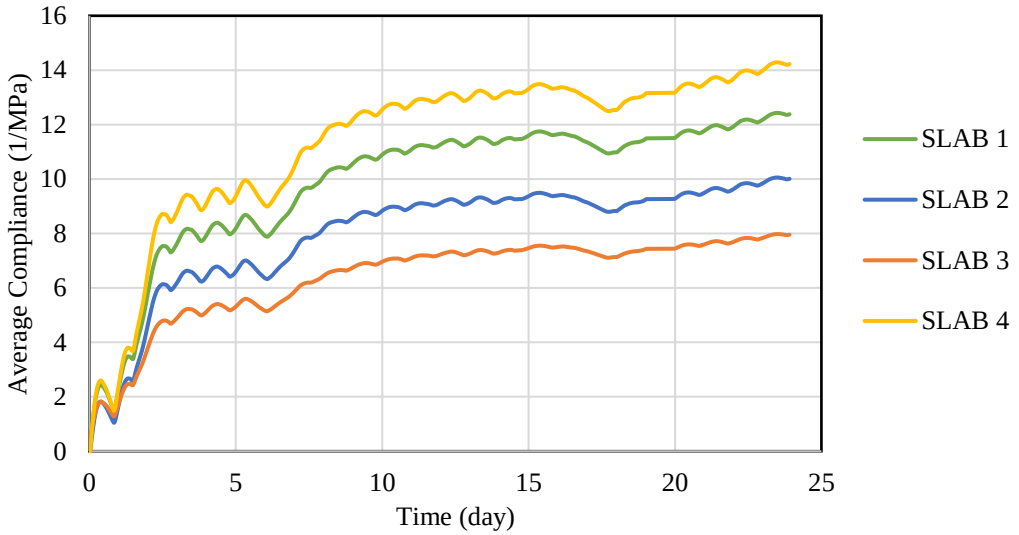

Figure 5-13. Predicted Creep Based on ACI 209 Model (Phase I)

5.6 Specification Development

One aspect of this study was to investigate the behavior of early-age concrete pavement and its relationship to longer-term cracking performance. The slab set gradient and quality can be highly variable even in the same project, and a combination of climatic factors and curing methods at the time of concrete placement can lead to low or high permanent curl/warp. By considering the probable ambient conditions (wind, humidity, and temperature), the application rate can be quantified to facilitate analysis to predict the set in a given placement. Since temperature and relative humidity gradients inside the concrete slabs are non-linear, it is required to transform these non-linear gradients into equivalent linear gradients to facilitate curling/warping analysis. The equivalent gradient represents the differences between the top and bottom of the slab.

The probabilistic models were used to evaluate the relationship between the target set gradient and the environmental effects and curing practices. To qualify the range of curing combinations expected on the construction of the test slabs, the set gradient target

was defined in two levels. The specification to achieve a low and high set was determined at a 70% probability. According to the target set, the distribution of AR was adjusted. EI was a convenient way to delineate the differences in the curing method and quality. The key factors associated with the performance of curing compounds were used in the preparation of the curing table. EI was used to choose the most appropriate application rate for a given curing compound under different conditions.

5.6.1 Important Factors in the Set Gradient Prediction

It is well accepted that the set gradient will vary with climatic and material factors that affect how the concrete sets during the hardening process. Analysis of the amount of heat and moisture transport that occurs during the setting of the concrete is a basis to anticipate the development of the set.

5.6.1.1 Climatic Effects

Climatic conditions can affect the temperature and moisture distribution inside a concrete slab. Based on the updated weather history data from the weather station (National Climatic Data Center), the maximum and the minimum ambient temperature and relative humidity were reported for each day (in this example, Gainesville, FL is selected). In order to simplify the weather record, the average daily ambient temperature and relative humidity are presented in Figure 5-14. The temperature and humidity profiles helped to characterize the ambient conditions. The highest temperature occurs in the afternoon, and the relative humidity follows an inversed trend of the ambient temperature.

To quantify the effects of weather on the set, PE is useful to account for the effects of ambient temperature, relative humidity, concrete temperature, and wind velocity on a year-round basis. The ACI 308 nomograph was used to describe the effect of weather with respect to PE. Figure 5-15 takes into account ambient temperature, relative humidity, and wind velocity.

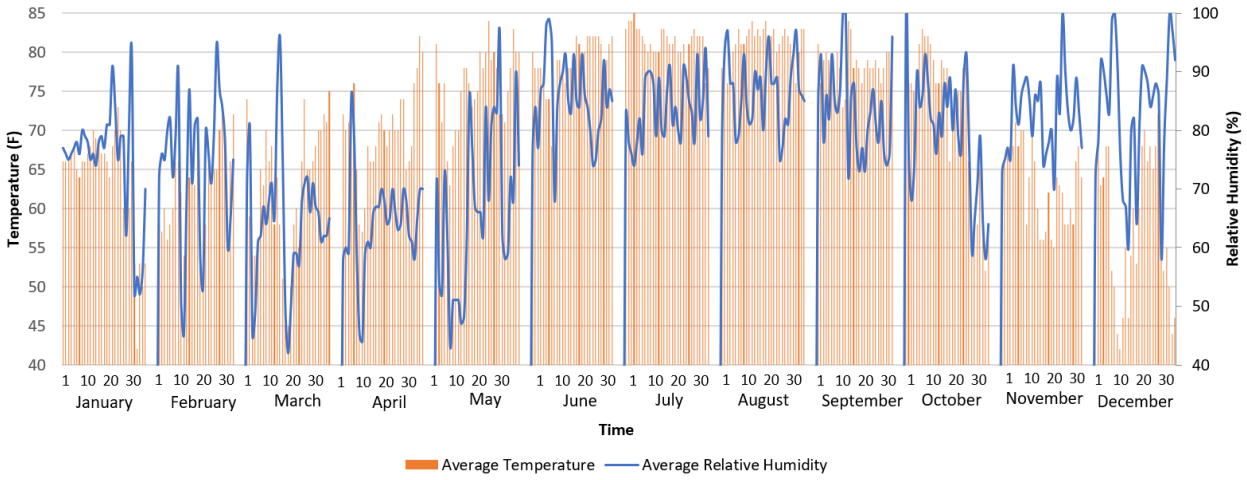

Figure 5-14. Year-Round Temperature and Relative Humidity at Gainesville, FL

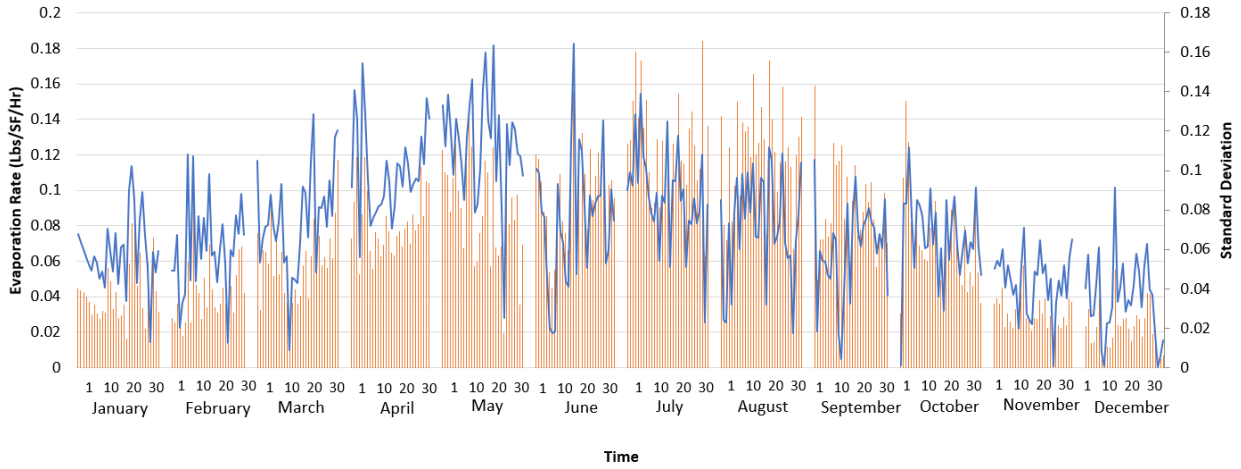

Figure 5-15. Year-Round PE at Gainesville, FL

As shown in Figure 5-15, the average temperature on summer days is higher compared with other months of the year. The standard deviation is displayed on the secondary axis in Figure 5-15. The standard deviation lower than 0.2 indicated a relatively low variation. For the months with a higher PE (Spring and Summer), the hourly data

points were spread out over a wider range of values due to the temperature and relative humidity differences.

The values of the analysis of variance (ANOVA) were studied, which indicated whether the PE differences between days and nights are significant, especially in warmer days of the year. Based on a defined level of 0.05, when the significance factor of PE is less than or equal to 0.05, a significant difference exists between PE average with the maximum and the minimum PE each day. Otherwise, PEs with the significance factor greater than 0.05 have a negligible difference from the average PE [198]. Table 5-7 shows that the concrete placement on the hot days is tightly dependent to the hour of the day. In other words, placing concrete in colder days of the year (Fall and Winter) would not change PE substantially compared to the mean value. However, PE differences in the hot days of the year are high. The established climatic database for each region can be evaluated statistically.

Table 5-7. Analysis of Variance (ANOVA) for PE in Different Months

		Jan	Feb	Mar	Apr	May	Jun	Jul	Aug	Sep	Oct	Nov	Dec
Mean		0.042	0.042	0.056	0.080	0.092	0.099	0.126	0.120	0.090	0.072	0.030	0.022
Std Dev		0.059	0.061	0.072	0.099	0.114	0.076	0.090	0.071	0.060	0.067	0.043	0.036
Sig.*	Min PE	0.472	0.258	0.106	0.042	0.091	0.000	0.000	0.000	0.011	0.024	0.089	0.547
	Max PE	0.892	0.672	0.067	0.004	0.000	0.000	0.000	0.064	0.108	0.316	0.741	0.955

* *Note: The mean difference is significant at the 0.05 level.*

5.6.1.2 Thermal Conductivity and Moisture Diffusivity

The thermal conductivity and moisture diffusivity in concrete are governed by the state of concrete temperature, relative humidity, and degree of hydration. Temperature and relative humidity were back-calculated based on the thermal conductivity and moisture diffusivity. Figure 5-16 shows concrete thermal conductivity (K) and moisture diffusivity (D) for a sample as a function of the degree of hydration. As concrete matures, both conductivity and diffusivity become lower over time. By using adjusted K and D, the

temperature and moisture distribution can be predicted according to the prevailing climate conditions (PE).

The purpose of this section is to determine the set gradient for any concrete pavement. Based on the previous studies [10, 11], the built-in temperature gradient corresponds to the temperature gradient in the slab at the time of the zero-stress state. According to literature, the zero-stress temperature happens in the concrete slabs when the range of degree of hydration is 36-47%. Then, the numerical temperature and moisture models were employed for performing the analysis. Thus, using the average value of 0.42 as the key degree of hydration should be acceptable.

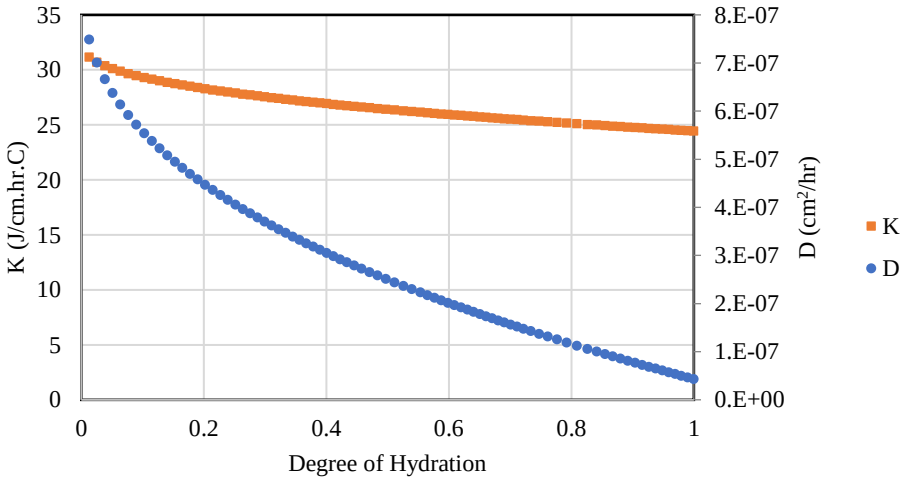

Figure 5-16. Hydration's Effect on K & D (T=20ºC and RH=0.9)

5.6.1.3 Time of Construction

Time of construction, i.e., month, day, and hour, can be considered in the design process. The connection of the predicted built-in temperature gradient to the time of placement can change the design, performance, and the curing program. For instance, the slab placement in hot weather (such as summer or around noon) will cause a relatively high positive built-in temperature gradient lock into the slab. On the other hand, cooler

weather (winter or nighttime) can induce a relatively small or even negative built-in temperature gradient.

The effects of time of placement on the set gradient were previously investigated and very helpful in establishing relationships that define how weather conditions and the method of curing affect the set gradient. The test data indicated that a relationship exists between EI and AR under different curing conditions, as shown in Figure 5-17. Higher quality is generally more readily achieved with placements at or towards the end of the paving day. The relationships pertaining to the first 72 hours after placement.

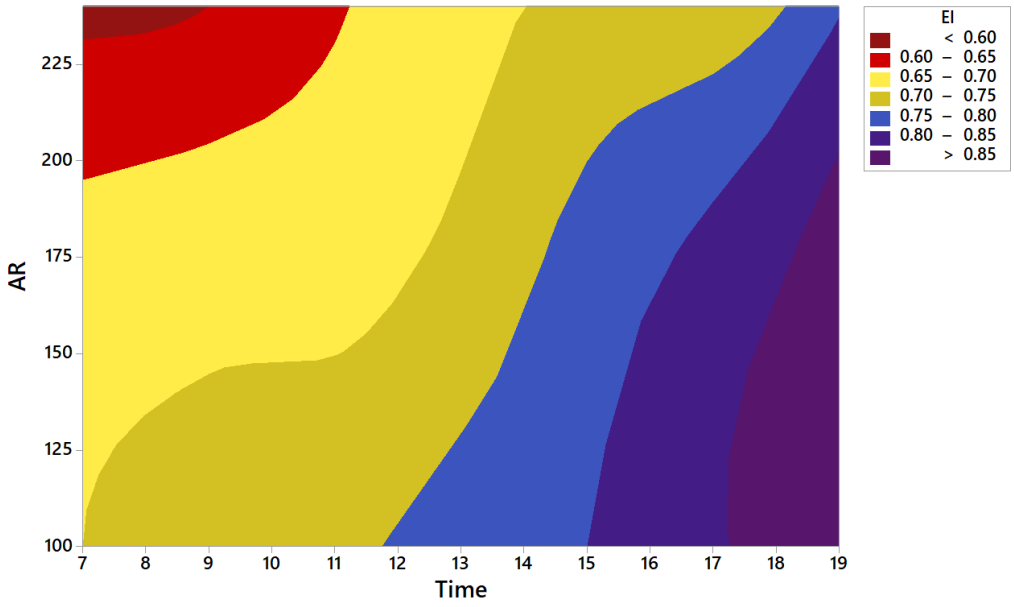

Figure 5-17. Effects of the Application Rate and Time of Placement on EI

5.6.2 Dependence of EI on Application Rate and Environmental Conditions

EI shows the quality of the curing and can be correlated with the long-term behavior of concrete slabs. The required EI can be selected to meet the minimum requirements. EI is a function that depends on AR and PE. Therefore, in a certain set (either low or high state), the distribution of EI (material-driven and weather-driven) should be considered.

As shown in Figure 3-32, by using the same application rate, EI was decreased by increasing PE values. AR affected this trend significantly in higher PEs. Eq. (3-12) presented the EI relationship with PE, AR, and time in WRM-1625 curing compound. As shown in Figure 5-18, the distribution is represented by probability density (%f) and accumulative (%F) functions, both of which were used to define the ranges of EI. As EI depended on PE and AR, in a constant PE, different distributions can be plotted for various AR values.

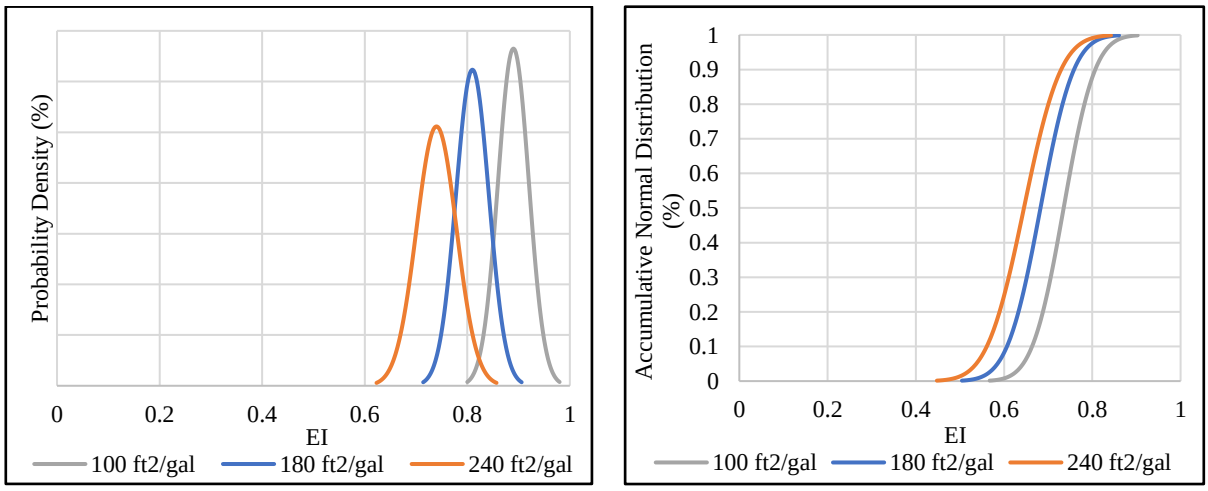

Figure 5-18. EI Distributions for Different Application Rates in a Constant PE

Figure 5-19 displays the normal distribution of EI for different PE conditions in a constant AR. Higher PE values resulted in lower EIs with higher standard deviations. Using lower application rates, such as 240 ft^2/gal, shifted the data trend to the left side of the graph and increased the variances. Figure 5-19 shows how the data was spread out.

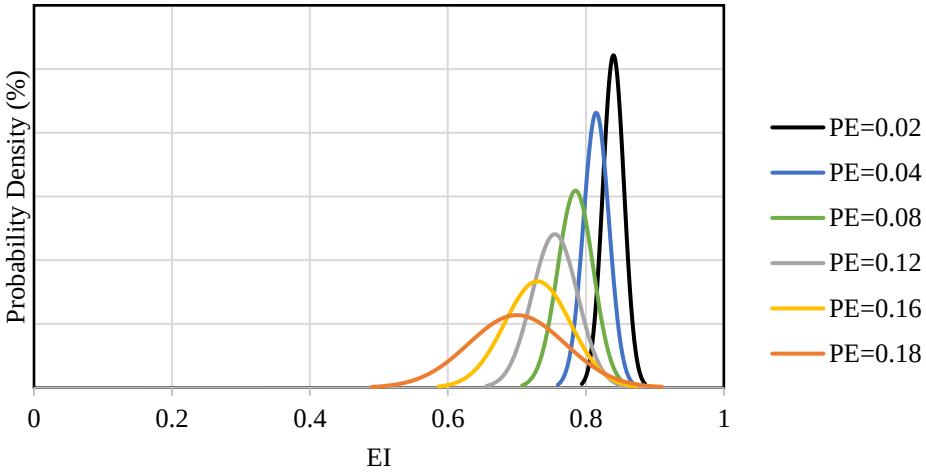

A) AR=100 ft^2/gal

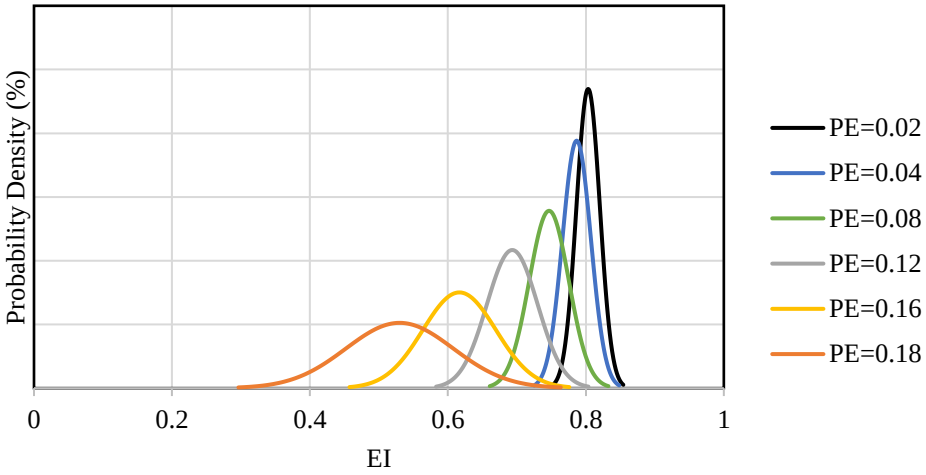

B) AR=180 ft^2/gal

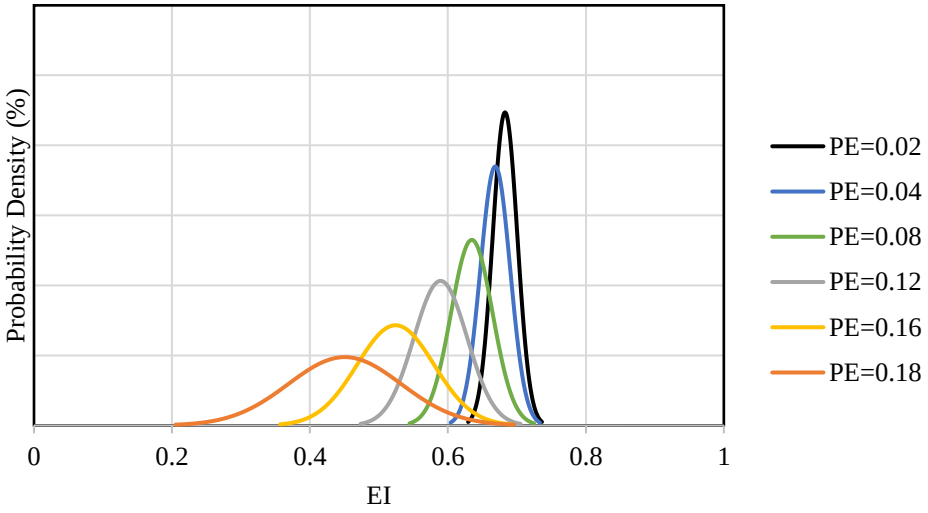

C) AR=240 ft^2/gal

Figure 5-19. EI Distributions for Different PE Values in A Constant AR

Assessment of the previously collected test data indicated that curing effectiveness could affect the final set gradient. Different levels of curing effectiveness and different application rates at different placement times were used to facilitate the assessment of the sensitivity of the set to a change in the curing method.

5.6.3 Dependence of Set Gradient on Application Rate and Climatic Conditions

The set gradient depends on PE and the application rate. By defining two levels (low and high) for the set gradient, the required application rate can be calculated with a 70% confidence level. According to the target set, the normal distribution curves will change. For instance, in the low set case (lower than 0.5), the weather-driven EI distribution would be to the left of the AR-driven EI distribution, and in the case of the high set (more than 1.5), it would be reversed. Moreover, the mean and variance will change as well. The objective of this process was to determine a set gradient target (either

low or high) and predict the required AR by considering the ambient curing conditions (PE).

Based on the weather conditions and the month of the placement, PE is determined from the weather data. It is important to know how much curing compound should be used to achieve a low set with 70% probability and more. The EI normal distribution curves can be used. Figure 5-20 shows the PE=0.04 and AR=100 ft^2/gal distributions in one graph. Each curve has a particular shape, as its distribution is specific. In order to make sure to estimate the required AR to achieve the set target correctly, the differences between these PE and AR distribution graphs should not be significant. In other words, the chosen AR should give a high set gradient 70% of the time. AR that will yield an EI that exceeds the minimum EI (EI for a given PE at the target gradient) 70% of the time. Figure 5-20 shows an example of choosing 100 ft^2/gal for PE=0.04. The overlap area is not too much, and the AR distribution can shift to the left side by using less compound. In this case, the first guess (100 ft^2/gal) exceeds the required specifications (overdesign). This fact can be proven by doing the *t*-distribution test as well. Therefore, the iteration with a lower AR should be repeated.

If it is acceptable to presume that two different populations have similar standard deviation, an alternative procedure (i.e., the pooled *t*) can be implemented instead of the two-sample *t* procedure. As just one standard deviation is considered, the test will follow one *t*-distribution with n_1+n_2-2 freedom degrees [199].

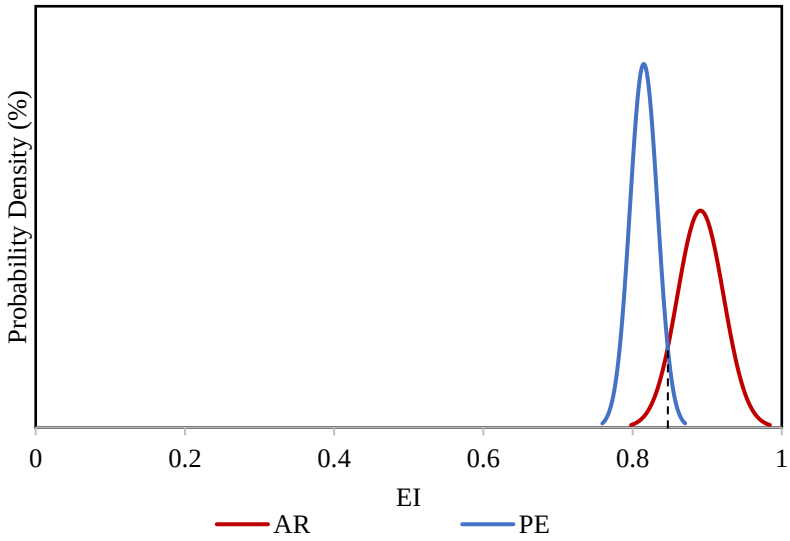

Figure 5-20. EI Normal Distributions for PE=0.04 and AR=100 ft^2/gal (Low Set)

In a given PE (based on the temperature, relative humidity, and wind velocity), the value of AR is associated with either a high or low set condition placement. The first step was to determine the variance and the mean in the EI normal distributions for both AR and PE. The purpose was to find a certain AR in which the average EI from PE was significantly different from the average EI-AR normal distribution. The significance level was assumed to be 70%. Then, the null and alternative hypothesis should be formulated [200]:

$$H_0: \mu B - \mu H = 0 \quad (5\text{-}15)$$

$$H_1: \mu B - \mu H \neq 0 \quad (5\text{-}16)$$

The mean and variance for PE and AR distributions were calculated.

$$\bar{x}_p = 0.815 \; and \; {s^2}_p = 0.000342$$

$$\bar{x}_A = 0.891 \; and \; {s^2}_A = 0.000961$$

Using this information, the pooled estimate of the population variance can be calculated:

$$s^2 = \frac{(n_p-1)s^2{}_p+(n_A-1)s^2{}_A}{n_p+n_A-2} \quad (5\text{-}17)$$

Although the user can calculate the test statistic, the critical *t*-statistics at a 70% confidence level (the alternative hypothesis was two-tailed) should be calculated. Using a statistics table, the user can calculate the 0.30 critical values for a *t*-distribution with 60 degrees of freedom to be −1.045 and 1.045. Now the user can calculate the test statistic:

$$t = \frac{0.891-0.815}{0.0255\sqrt{\frac{1}{31}+\frac{1}{31}}} = \frac{0.076}{0.006483} = 11.72$$

Thus, the null was rejected, and there was a significant difference between PE and AR distributions with 70% confidence. Since the test statistic did not lie within the critical region, the null rejection was failed. It means that there was a significant difference between the two population means at 70% confidence.

The needed AR can be obtained from the backward calculation. By considering the 0.30 critical value, the $t<1.045$ conditions should be satisfied. Therefore, the mean value for EI distribution for AR was 0.811. In this case, the overlap area between PE and AR was much higher compared to the first iteration, as shown in Figure 5-21. The equivalent AR for EI=0.811 is 172.45 ft^2/gal. This process should be repeated for each PE ranges at different time placements (in both low and high set gradient targets).

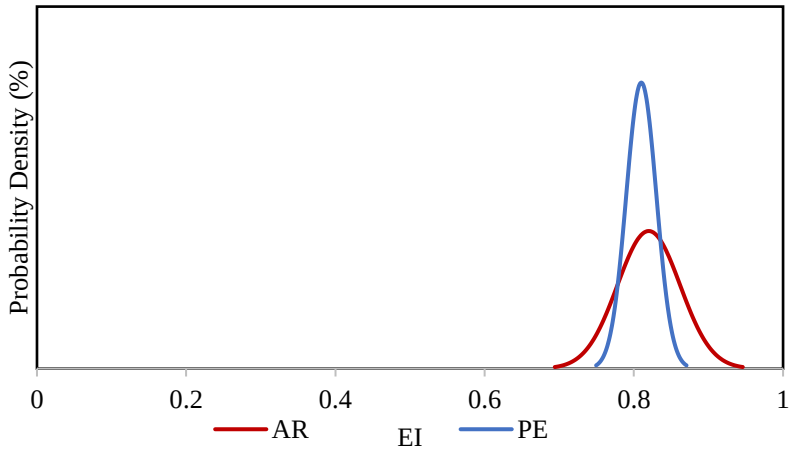

Figure 5-21. EI Normal Distributions for PE=0.04 and AR=172.4 ft^2/gal (Low Set)

This process in the high set gradient targets is the same; however, the location of PE and AR normal distributions might be different compared to the low set. In other words, the weather-driven EI distribution would be to the right side of the AR-driven EI distribution, as shown in Figure 5-22.

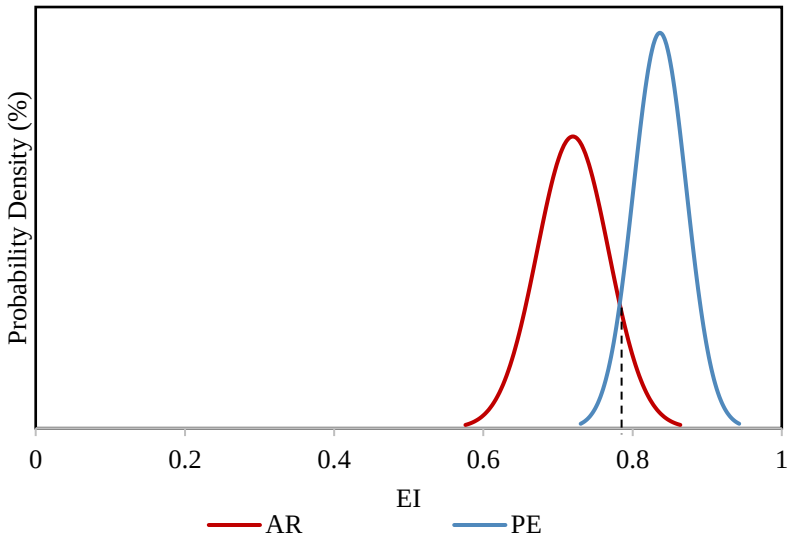

Figure 5-22. EI Normal Distributions for PE=0.16 and AR=180 ft^2/gal (High Set)

5.6.4 Specified Application Rate

Different levels of effectiveness and different application rates at different placement times were used to facilitate the assessment of the sensitivity of the set to a change in the curing method. In developing the application rates, a minimum probability of 70% was used to achieve the target set values as previously indicated. By using the normal distribution of the set gradient, the application rate was determined for different placement times (7 AM-10 AM, 10 AM-3 PM, 3 PM-7 PM, 7 PM-10 PM, 10 PM-3 AM, and 3 AM-7 AM). In the development of the application rates, two compounds were used, WRM-1150 and WRM-1625. The ambient conditions, along with different curing applications, were the critical factors in creating the range of the application rates. Table 5-8 provides the application rate for each curing compound for a specific range of ambient environmental conditions at the time of slab placement.

Table 5-8. Required Application Rate for Low and High Set Conditions

PE	Set	WRM-1150						WRM-1625					
		7 AM-10 AM	10 AM-3 PM	3 PM-7 PM	7 PM-10 PM	10 PM-3 AM	3 AM-7 AM	7 AM-10 AM	10 AM-3 PM	3 PM-7 PM	7 PM-10 PM	10 PM-3 AM	3 AM-7 AM
0.02-0.04	LOW	157.5	135.1	153.2	169.9	173.6	178.8	194.1	163.4	196.1	203.1	209.2	215.8
	HIGH	220.9	191.1	215.2	238	244.7	247.8	270.1	230.4	274.7	284.6	293.8	301.2
0.04-0.06	LOW	148	130.3	141.7	154.2	164.8	172.5	183.6	157.1	181.2	188.2	198.5	207.1
	HIGH	201.2	176.4	194.1	210.6	223.4	231.5	247.6	212.5	246.3	254.8	267.2	280.1
0.06-0.08	LOW	147.9	129.2	136.5	147	159.9	166.5	176.6	152.9	174.3	175.8	187.9	198.2
	HIGH	183.8	169	179	191.4	208.9	213.6	226.2	199.4	228.8	230.5	245.1	258.6
0.08-0.10	LOW	142.5	128.4	132.5	143.6	153.8	166.2	174.9	155.3	167.2	172.4	185.6	196.4
	HIGH	177.4	163.2	168.4	180.3	196.8	208.1	217.6	194.1	210.6	217.8	234	246.8
0.10-0.12	LOW	139.1	127.6	129.1	140.2	149.7	165.4	169.2	155.2	160.4	168.7	180.6	190.9
	HIGH	168.2	155.9	156.4	169	181.5	190.3	207.5	188.9	194.9	203.7	219.1	231.1
0.12-0.14	LOW	133.7	124.9	123.7	132.6	139.4	158.1	164.5	153.9	153.3	162.8	171.2	182
	HIGH	158.9	145.7	144	153.5	161.7	179.6	196.3	178.2	177.7	188.3	196.8	210.5
0.14-0.16	LOW	126.3	111	119.9	127	127.1	141.8	159.3	144.4	148.4	152.2	165.1	179.2
	HIGH	145	122.8	134	142.1	149.3	158.2	180.3	159.2	164.2	169.4	180.1	196.2
0.16-0.18	LOW	115.1	100.6	109.2	112.2	115.1	132.4	149.2	137.1	141	146.7	155.2	164.5
	HIGH	127.4	107.7	117.6	120.5	129.8	143.5	167.4	145.9	151	156	163.2	175.8
0.18-0.20	LOW	110.2	96.8	103	106.9	114	124.9	137.6	124.9	134	136.9	144.6	149.2
	HIGH	123.3	106.6	114.2	117.8	125	136.9	159	138.2	147.7	152.2	159.8	162.7

5.6.5 Probabilistic Model for Structural Failure (Cracking Probabilities)

As explained in Chapter 3, cracking is induced when restrained stress exceeds the critical level of tensile strength. The probability of cracking can be modeled, assuming that the stress and the strength are the random variables with a mean and a distribution. In the distribution diagram, the intersection between the stress and the strength distribution represents the area of failure (or the probability of failure). Therefore, by using Eq. (4-10), the probability of cracking can be assessed. In the probability failure of concrete calculation, the weather impacts (PE), material properties, structural inputs, and the curing practices should be considered.

The coefficient of variations of stress and strength were assumed to be 0.25 and 0.15, respectively. Also, the thickness values of the slab were assumed 7 and 10 inches. Figure 5-23 shows the predicted probability (percent cracking) for a paving operation with PE=0.10 on a slab that is 12 ft long and 7 inches thick. The defined set gradient is in a high state.

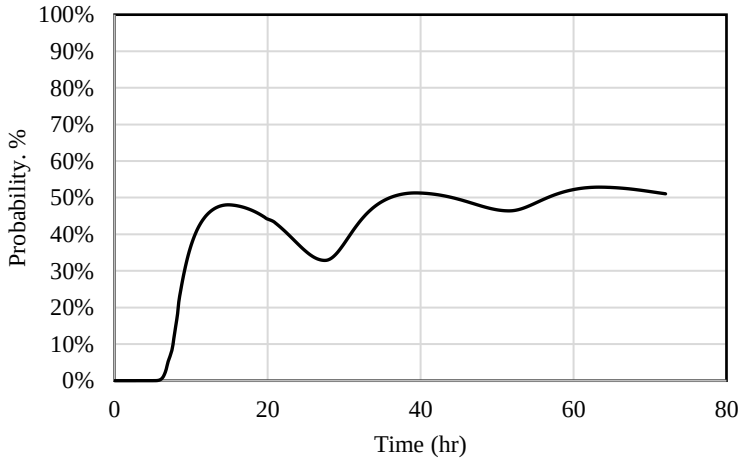

Figure 5-23. Probability of Cracking Calculation for a Certain Set Gradient

(PE=0.10|High Set Gradient|7 inches Thickness|12 ft Length)

The slab thickness and depth are the most important structural inputs in random cracking. Cracking occurs after concrete hardens and continues depending on the slab thickness, length, and the ambient conditions (PE). The probability of cracking within a 72-hour period following paving varies according to the set gradient. In Figure 5-24, the probabilities of cracking are depicted in different PE (0.05, 0.10, 0.15, and 0.20) values. Each graph considers the low and high set states, separately.

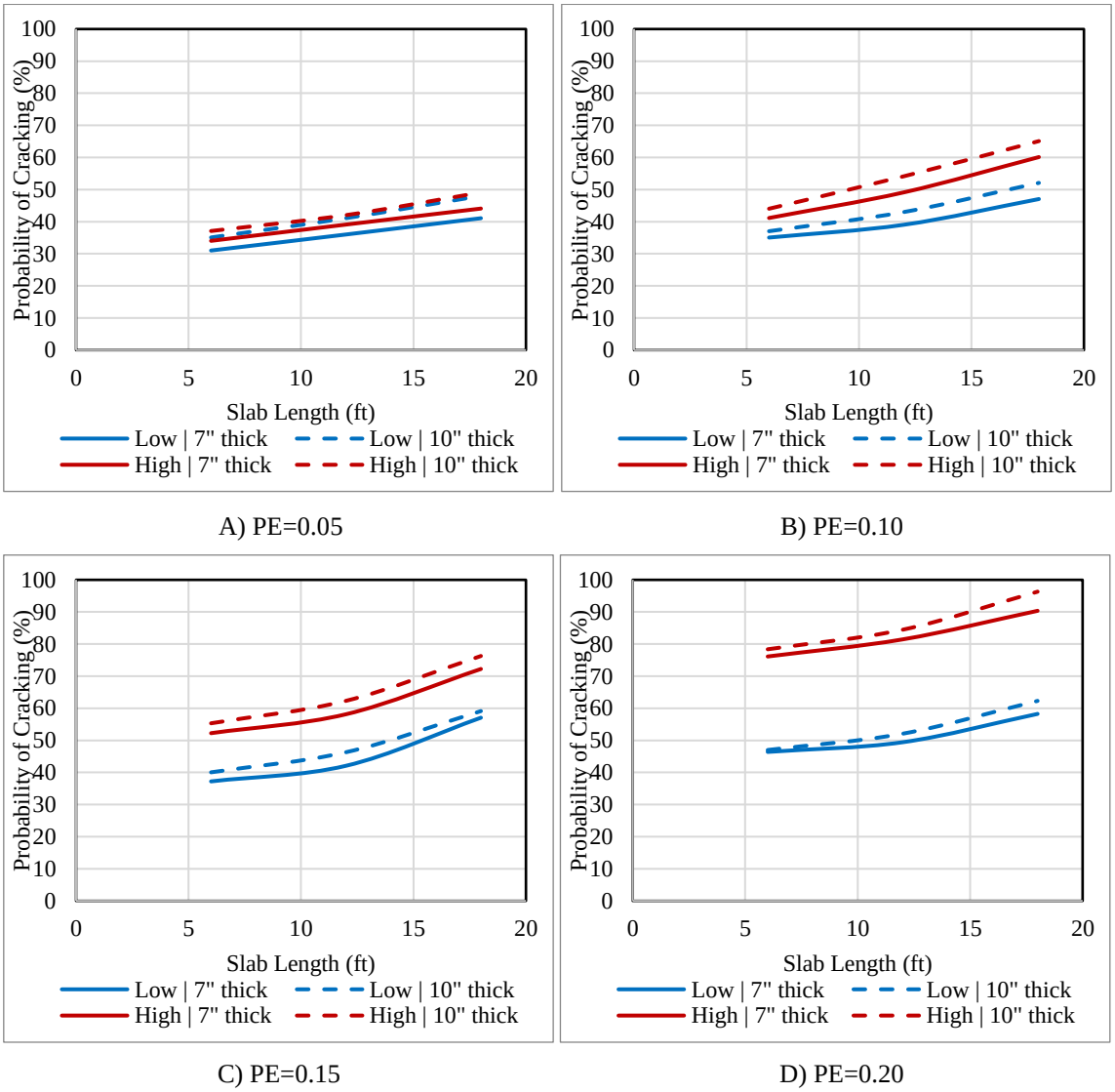

A) PE=0.05 B) PE=0.10

C) PE=0.15 D) PE=0.20

Figure 5-24. Cracking Probability with Environmental Conditions and Slab Length

5.7 Summary

In this chapter, the calculation of the set gradient of the slabs in both phases was discussed. The set gradient also was expressed in terms of the temperature gradient. The process of calculating r_{set} gradient for slabs was explained with tables and figures, and the curing quality was compared with the amount of the set gradient. The key factors associated with the performance of curing compounds in terms of EI were addressed in this investigation. Then, calibration of performance for design purposes was discussed to address the effect of climate on fatigue cracking of concrete slabs. Also, the dependence of creep and set was studied. In this part, creep was defined as a thermally activated process based on the activation energy. The influence of age and moisture content on this creep mechanism was taken into consideration. Finally, the probabilistic models were used to evaluate the relationship between the target set gradient and the environmental effects and curing practices. The key factors associated with the performance of curing compounds were used in the preparation of the curing table. EI was used to choose the most appropriate application rate for a given curing compound under different conditions.

6 CONCLUSIONS

This study consisted of several laboratory and field experiments in order to characterize the effects of climatic boundary conditions on the curing performance and the set gradient of early-age concrete. The following conclusions are drawn based on the results and discussions presented in this dissertation:

To evaluate curing performance in the laboratory, direct and indirect indicators were introduced. Direct test methods measured moisture loss, surface abrasion resistance, surface porosity, and drying shrinkage. However, indirect indicators evaluated the curing effectiveness indirectly.

- In curing with a higher application rate, significant moisture loss was prevented. The low moisture loss was achieved by limiting water transmission.
- The higher wind speed increased the moisture loss amount. The rate of evaporation depends directly on wind velocity. As ASTM C 156 did not cover the ambient conditions, this standard is not an appropriate method for testing the curing quality under the field conditions.
- In the abrasion resistance test, the weight loss of the treated samples with a higher application rate was lower than the untreated samples because of high strength.
- In the water sorptivity measurement, exposure to wind resulted in a substantial increase of WSI, which was considered as a poor curing quality.
- The interconnected capillary pores and bleed channels were related to curing quality. Better curing resulted in a lower percentage of capillary pores at the surface.

- The higher application rate prevented moisture loss and mitigated the adverse effects of shrinkage. Also, the drying shrinkage was increased by elevating the wind speed level.
- EI (based on the concrete maturity concept) was sensitive to climatic conditions and the quality of curing practices. A higher EI indicated a higher concrete moisture-modified maturity on the filtered side.
- The changes in DC indicated the changes in free moisture content. Controlling the rate of changes was an indicator of the curing effectiveness at different application rates under different conditions. The better the curing practice (the higher application rates), the longer it took for DC to drop to lower levels.
- The correlation between EI and moisture dependent factors, such as moisture loss, sorptivity, shrinkage, and DC was relatively high.

EI has a wide range of usages, including in the laboratory and the field of construction. EI is a practical means to address the impact of field ambient conditions. The preliminary testing data was used to develop a relationship between EI, PE, and the application rate of a given curing compound. The reference curves provided an empirical method to predict the required application rate of a curing compound for each environmental condition. As the values of EI are evaluated over designated periods, the quality of a given curing compound can be monitored on a real-time basis. A contractor will be enabled to quantify the needed amount of curing compound that should be applied on the concrete slab based on ambient conditions to meet minimum requirements.

A comprehensive concrete curing evaluation was conducted based on two separate field trials of slab placements. Different combinations of curing conditions and placement times were tested in these field trials. The fundamental purposes of slab monitoring were to use data collections in order to evaluate the quality of curing and assess the slab setting characteristics.

- Paving slabs during the daytime increased the concrete temperature due to the rate of hydration and solar radiation. The coincidence of these factors expedited the hydration reactions and decreased the setting time. The rate of hydration affected the built-in gradient and behavior of the slabs at the early-age.
- The temperatures of concrete slabs at greater depths below the surface were higher than the ambient temperatures at night, and the magnitude of this difference varied with time and depth. The slabs were subjected to larger temperature gradients during the day, in which the bottom of the slab temperature was lower than the surface temperature. The slabs with better curing practices had lower temperature gradients.
- The temperature profiles were relatively uniform at the first day after concrete placement. The reason for this uniform distribution was because of the proper curing treatment.
- The relative humidity near the slab surface was continuously increasing during the initial hours, while the relative humidity at greater depths below the surface remained substantially high. When the concrete setting happened, the relative humidity at different depths of the slab was consistent with the quality of the curing. The slabs with a lower curing quality tended to have larger moisture gradients.
- Moisture gradients caused permanent shrinkage upon first drying and transitory shrinkage at later ages. The reversible part varied with the daily ambient relative humidity. However, the irreversible shrinkage caused permanent warping.
- Internal strain changes due to temperature or moisture gradients in concrete triggered curling and warping. The trends of the strain fluctuations were highly related to the trends of the temperature fluctuations. The strain at the top responded immediately to the temperature changes in the slab. The strain differences between the top and the bottom of the slab might be because of the restraints caused by the base against the volume changes of the slab.
- The concrete strains became expansive as temperature increased and became contractive when the temperature decreased. The strain can be controlled due to the better curing and time of placement.

- The concrete pavement was deformed into a concave configuration when the pavement is subjected to a resultant negative gradient through slab thickness. The maximum upward curling condition occurred at the early morning (mainly right before sunrise). In this case, the bottom of the slab is warmer than the top surface. Although the slab was deflecting upward during this period, the slab tended to be in contact with the base when the curvature did not exceed the pre-compression induced from the dead-weight. On the other hand, the maximum downward curl occurred in early afternoon, in which the slab surface was heated by the sun. Under these situations, the top surface of the slab was warmer than the bottom. The curing practices influenced the performance and the built-in curling/warping of the slabs directly.

In terms of the stress ratio (r), an effective negative temperature gradient can be permanently set in the slabs. The setting of the concrete was characterized in this manner to facilitate a correlation with the pavement performance. The amount of the residual or set permanent curling/warping built into the test slabs was represented by the difference between the theoretical (calculated) and the measured (actual) gradients. The large irreversible strain was attributed to large temperate and moisture gradients.

- The built-in temperature gradient was mainly influenced by the weather conditions during setting. The largest negative built-in curling was observed in the morning placements. In this case, a large positive temperature gradient was formed when the slab hardened. Afternoon constructions induced a milder temperature gradient at the final set. The built-in temperature gradient was significantly influenced by the time placement of the day and the construction season of the year.
- The difference between the measured and theoretical strain, including the irrecoverable strain, reflected the curing quality. Lower temperature/moisture gradients and a lower set were anticipated in well-cured concrete. Also, a higher EI was generally associated with a lower set. Different levels of effectiveness and

different application rates at different placement times were used to facilitate the assessment of the sensitivity of the set to a change in the curing method.

The set gradient varied with the climatic changes. Even though the interaction of the climate with performance was complex, curing quality affected slab stresses and cracking. Calibration of performance for design purposes should inherently address the effect of climate on fatigue cracking of concrete slabs. Not only did diurnal moisture and temperature gradients through the slab affect the slab cracking, but also affected the permanent built-in curling and warping that occurred during construction.

- The magnitude of the set gradient was estimated from the calibration of JPCP cracking and was expressed relative to a gradient of -10 ˚F as defaulted in the Pavement ME software.
- Referring to the fatigue cracking damage model encompassed within the Pavement ME software, the focus of a calibration effort was to determine the appropriate values of calibration coefficient C_4 and C_5 to improve goodness-of-fit with field data. The choice of the coefficients varied with r_{set}. The computations of the design conditions using these correlations for the selection of the coefficients indicated greater performance and lower design thicknesses with increasing values of r_{set}. Since the set of the slab can be controlled, there is considerable evidence for including the default Pavement ME set and calibration C_4 and C_5 coefficient values in the correlation.

Dielectric measurements were taken at the surface of concrete pavements using GPR during the field investigations. GPR data was typically collected in the longitudinal direction of the slab. Due to the surface moisture evaporation, various values for the dielectric constant were collected over time in different GPR data collection sessions.

- The GPR system was used to collect an extensive dataset for the evaluation of the curing effectiveness over the entire concrete slab within a brief period of time.

- It was possible to achieve a high degree of repeatability of the data collection.
- The GPR system was useful to suggest the uniformity based on the DC variances and statistical analysis. One of the most important findings of GPR surveys was the effects of spraying pattern on the uniformity and performance of curing. By using the PWL concept, spikes in the standard deviation trends were detected and interpreted as a sign of non-uniformity spots in the curing application.
- The GPR system was helpful in identifying the effects of varying curing application rates and timing of a given curing compound for a new project with known climatic conditions.

APPENDIX A

This chapter describes the process of the r_{set} determination (also summarized in a tabular format). The process of mathematical calculating of the set gradient is discussed with tables and figures in ten steps. Actual ambient temperature and moisture are collected in the field. The equivalent linear temperature and moisture gradients (third-order polynomial equation) are used to characterize the temperature and moisture profiles for a single slab. Based on the measured LVDT displacement of the slab's corner, the induced stress and strain are calculated. To calculate the set, r_{set} is determined based on the net difference in stress. Finally, the equivalent set gradient can be expressed in terms of temperature. Thus, negative equivalent linear temperature gradients are permanently built into the slabs in terms of the stress ratio.

6.1 Step #1 Actual Ambient Temperature and Relative Humidity

The ambient temperature and relative humidity. The set gradient occurs due to environmental effects during the first days after placement on temperature and moisture profile variations within the slab that coincide with a fully supported slab configuration.

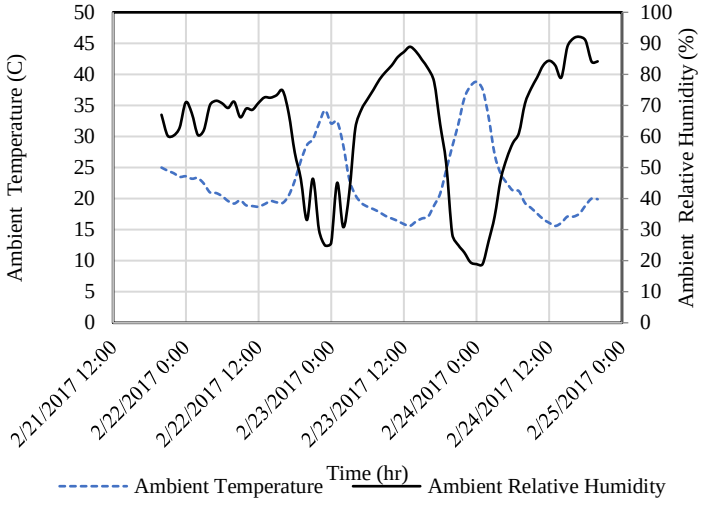

Real Time	Elapsed Time	AmbT	AmRH
2/21/2017 19:59	0.00	25.00	67
2/21/2017 20:09	0.2	24.50	67.7
2/21/2017 20:18	0.5	24.10	64.4
2/21/2017 20:28	0.8	23.50	62.4
2/21/2017 20:38	1.0	23.60	60.3
2/21/2017 20:48	1.3	23.20	61.9
2/21/2017 20:58	1.5	23.30	64.5
2/21/2017 21:08	1.8	22.40	61.6
2/21/2017 21:18	2.0	21.00	60.3
2/21/2017 21:28	2.3	20.90	60
2/21/2017 21:37	2.5	20.40	61.1
2/21/2017 21:47	2.8	19.60	61.7
2/21/2017 21:57	3.0	19.20	62.9
2/21/2017 22:07	3.3	19.70	69.7
2/21/2017 22:17	3.5	18.90	71.2
2/21/2017 22:27	3.8	18.80	71.4
2/21/2017 22:37	4.0	18.70	71
2/21/2017 22:46	4.3	19.10	71.2
2/21/2017 22:56	4.5	19.60	70.7
2/21/2017 23:06	4.8	19.40	70.5
2/21/2017 23:16	5.0	19.30	67.5

Figure A-1. The Ambient Temperature and Relative Humidity

6.2 Step #2 Characterize the Temperature and Relative Humidity Profiles

Actual ambient temperature and moisture data were collected in the field. The equivalent linear temperature and moisture gradients (fitted by third-order polynomial equations versus time) are used to characterize the temperature and moisture profiles for Slab 3.

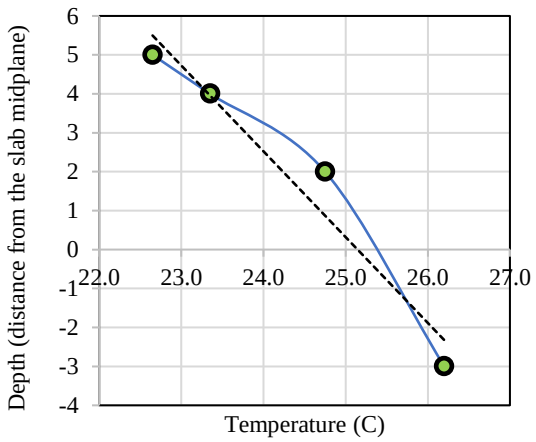

8 inch	3 inch	1 inch	Surface	D	C	B	A	ΔT
26.2	24.8	23.4	22.7	0.0073	-0.0805	-0.4218	25.857	3.1

Figure A-2. The Equivalent Linear Temperature Gradient

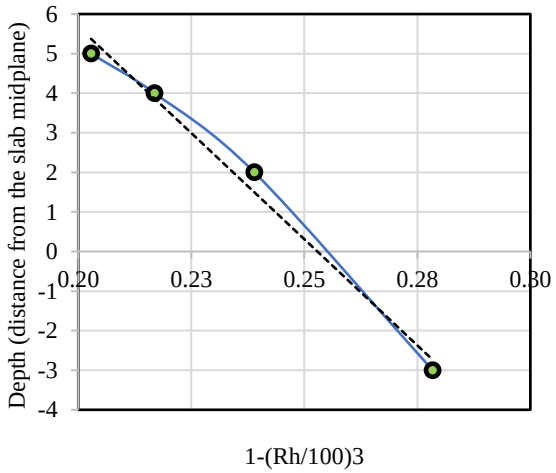

8 inch	3 inch	1 inch	Surface	D	C	B	A	Δ(1-rh3)
0.90	0.91	0.92	0.93	0.0001	-0.0013	-0.0089	0.2668	0.074

Figure 0-3. The Equivalent Linear Relative Humidity Gradient

6.3 Step #3 Plot Equivalent Temperature and Relative Humidity Differences

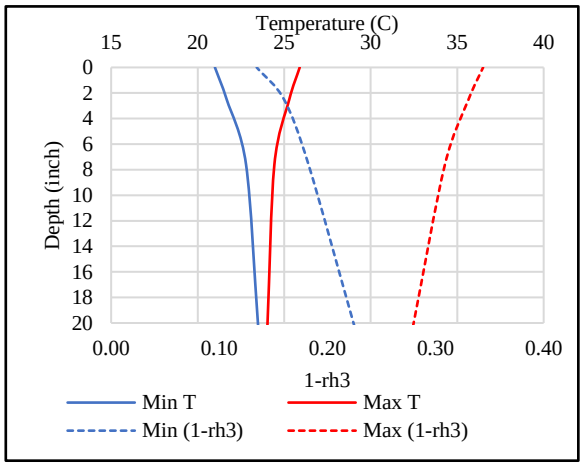

Temperature

Real Time	Elapsed Time	8 inch	3 inch	1 inch	Surface
2/21/2017 19:59	0	26.4	26.2	24.4	23.5
2/21/2017 20:59	1	26.4	25.9	24.2	23.4
2/21/2017 21:59	2	26.3	25.7	23.9	23.0
2/21/2017 22:59	3	26.3	25.3	23.7	22.9
2/21/2017 23:59	4	26.3	25.0	23.4	22.6
2/22/2017 0:59	5	26.3	24.9	23.3	22.5
2/22/2017 1:59	6	26.2	24.8	23.4	22.7

Relative Humidity

Real Time	Elapsed Time	8 inch	3 inch	1 inch	Surface	8 inch	3 inch	1 inch	Surface
2/21/2017 19:59	0	0.86	0.89	0.89	0.89	0.36	0.29	0.30	0.30
2/21/2017 20:59	1	0.87	0.90	0.90	0.90	0.33	0.28	0.28	0.28
2/21/2017 21:59	2	0.88	0.90	0.91	0.91	0.32	0.27	0.26	0.25
2/21/2017 22:59	3	0.88	0.91	0.91	0.92	0.32	0.25	0.24	0.23
2/21/2017 23:59	4	0.89	0.91	0.92	0.93	0.28	0.24	0.21	0.20
2/22/2017 0:59	5	0.90	0.91	0.93	0.93	0.27	0.24	0.21	0.19
2/22/2017 1:59	6	0.90	0.91	0.92	0.93	0.28	0.24	0.22	0.20

Figure A-4. The Equivalent Linear Temperature Profiles vs. Depth

The coefficients of the fitting equation for a given time were calculated for both temperature and relative humidity. Then, the equivalent temperature and relative humidity were obtained.

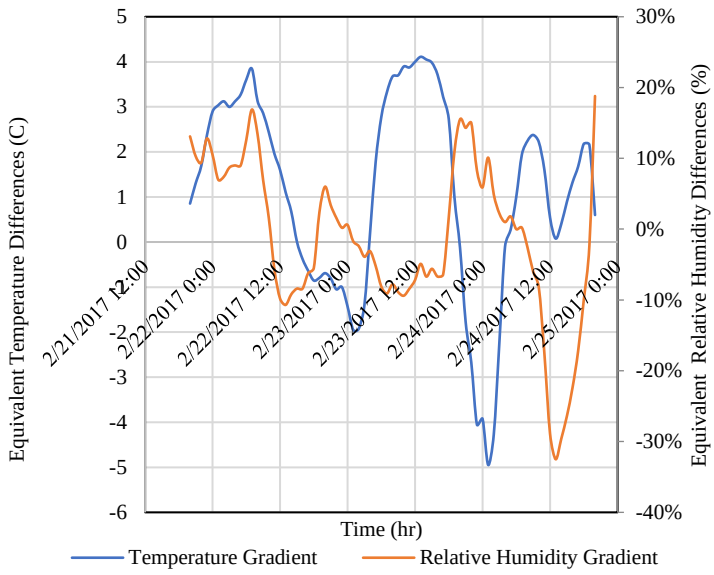

Real Time	Elapsed Time	ΔT/in	Δrh/in
2/21/2017 19:59	0	-0.0854	0.0131
2/21/2017 20:59	1	-0.1303	0.0103
2/21/2017 21:59	2	-0.1691	0.0094
2/21/2017 22:59	3	-0.2368	0.0128
2/21/2017 23:59	4	-0.2896	0.0105
2/22/2017 0:59	5	-0.3034	0.0070
2/22/2017 1:59	6	-0.3123	0.0074
2/22/2017 2:59	7	-0.2998	0.0087
2/22/2017 3:59	8	-0.3123	0.0090
2/22/2017 4:59	9	-0.3272	0.0090
2/22/2017 5:59	10	-0.3603	0.0126
2/22/2017 6:59	11	-0.3845	0.0169
2/22/2017 7:59	12	-0.3129	0.0134
2/22/2017 8:59	13	-0.2859	0.0069
2/22/2017 9:59	14	-0.2437	0.0016
2/22/2017 10:59	15	-0.1959	-0.0057
2/22/2017 11:59	16	-0.1602	-0.0098
2/22/2017 12:59	17	-0.1102	-0.0107
2/22/2017 13:59	18	-0.0674	-0.0092
2/22/2017 14:59	19	-0.0009	-0.0084
2/22/2017 15:59	20	0.0377	-0.0084
2/22/2017 16:59	21	0.0638	-0.0062
2/22/2017 17:59	22	0.0855	-0.0055
2/22/2017 18:59	23	0.0795	0.0024
2/22/2017 19:59	24	0.0691	0.0060

Figure A-5. The Equivalent Temperature and Relative Humidity Differences

6.4 Step #4 Equivalent Strains

The equivalent linear temperature and moisture gradients induce strains, which trigger curling and warping.

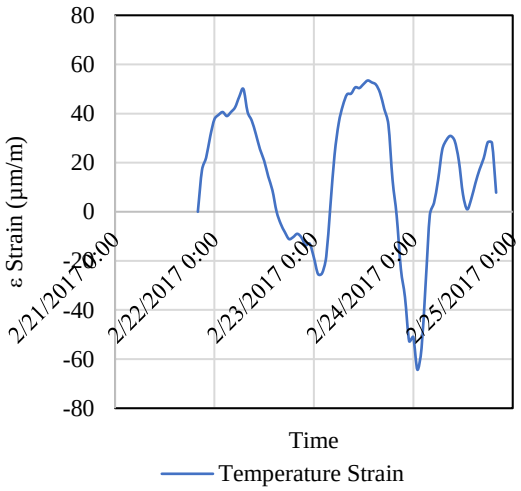

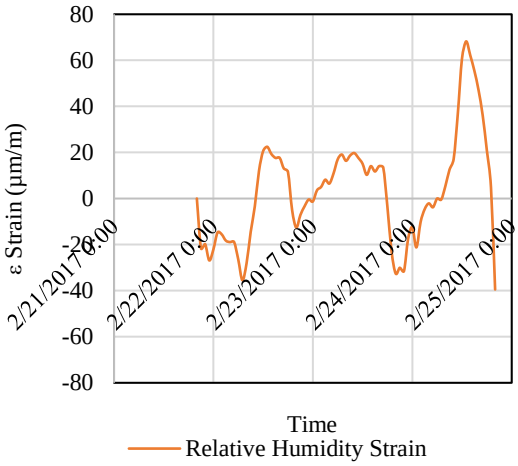

$$\varepsilon_{Temp\ Grad} = \alpha_c \Delta T_{eq}$$

$$\varepsilon_{MoistGrad} = -\varepsilon_\infty \Delta \left[1 - \left(\frac{RH}{100}\right)^3\right]_{eq}$$

Real Time	Elapsed Time	εt (micro-strain)	εrh (micro-strain)
2/21/2017 19:59	0	0.000	0.000
2/21/2017 20:59	1	16.939	-21.630
2/21/2017 21:59	2	21.983	-19.740
2/21/2017 22:59	3	30.784	-26.880
2/21/2017 23:59	4	37.648	-22.050
2/22/2017 0:59	5	39.442	-14.700
2/22/2017 1:59	6	40.599	-15.540
2/22/2017 2:59	7	38.974	-18.270
2/22/2017 3:59	8	40.599	-18.900
2/22/2017 4:59	9	42.536	-18.900
2/22/2017 5:59	10	46.839	-26.460
2/22/2017 6:59	11	49.985	-35.490
2/22/2017 7:59	12	40.677	-28.140
2/22/2017 8:59	13	37.167	-14.490
2/22/2017 9:59	14	31.681	-3.360
2/22/2017 10:59	15	25.467	11.970
2/22/2017 11:59	16	20.826	20.580
2/22/2017 12:59	17	14.326	22.470
2/22/2017 13:59	18	8.762	19.320
2/22/2017 14:59	19	0.117	17.640
2/22/2017 15:59	20	-4.901	17.640
2/22/2017 16:59	21	-8.294	13.020
2/22/2017 17:59	22	-11.115	11.550
2/22/2017 18:59	23	-10.335	-5.040
2/22/2017 19:59	24	-8.983	-12.600

Figure A-6. The Induced Strains from Temperature and Relative Humidity

6.5 Step #5 Calculated Net (Total) Strains

The net strain, $\varepsilon_{NET(total)}$, is then determined by superposing the temperature strain, $\varepsilon_{Temp\ Grad}$ and the moisture strain $\varepsilon_{MoistGrad}$.

$$\varepsilon_{NET(total)} = \varepsilon_{Temp\ Grad} + \varepsilon_{MoistGrad}$$

The effective strain is composed of thermal strain and drying shrinkage strain. Internal strain changes due to thermal or moisture change in concrete is a volumetric effect.

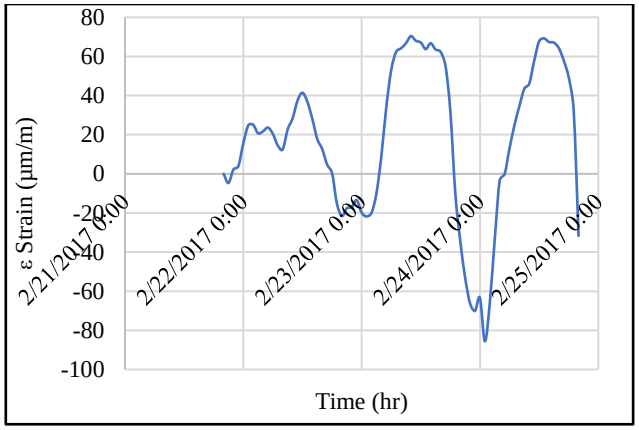

Real Time	Elapsed Time	εt (micro-strain)	εrh (micro-strain)	εtotal
2/21/2017 19:59	0	0.000	0.000	0.000
2/21/2017 20:59	1	16.939	-21.630	-4.691
2/21/2017 21:59	2	21.983	-19.740	2.243
2/21/2017 22:59	3	30.784	-26.880	3.904
2/21/2017 23:59	4	37.648	-22.050	15.598
2/22/2017 0:59	5	39.442	-14.700	24.742
2/22/2017 1:59	6	40.599	-15.540	25.059
2/22/2017 2:59	7	38.974	-18.270	20.704
2/22/2017 3:59	8	40.599	-18.900	21.699
2/22/2017 4:59	9	42.536	-18.900	23.636
2/22/2017 5:59	10	46.839	-26.460	20.379
2/22/2017 6:59	11	49.985	-35.490	14.495
2/22/2017 7:59	12	40.677	-28.140	12.537
2/22/2017 8:59	13	37.167	-14.490	22.677
2/22/2017 9:59	14	31.681	-3.360	28.321
2/22/2017 10:59	15	25.467	11.970	37.437
2/22/2017 11:59	16	20.826	20.580	41.406
2/22/2017 12:59	17	14.326	22.470	36.796
2/22/2017 13:59	18	8.762	19.320	28.082
2/22/2017 14:59	19	0.117	17.640	17.757
2/22/2017 15:59	20	-4.901	17.640	12.739
2/22/2017 16:59	21	-8.294	13.020	4.726
2/22/2017 17:59	22	-11.115	11.550	0.435
2/22/2017 18:59	23	-10.335	-5.040	-15.375
2/22/2017 19:59	24	-8.983	-12.600	-21.583

Figure A-7. The Calculated Net Strains

6.6 Step #6 Theoretical Equivalent Stresses

Once the strain profiles in the slabs were obtained, the slab stresses were readily calculated using the Bradbury solution. This solution is widely used today in rigid pavement design for curling stress analysis based on the assumption that the temperature variation is linear. The formula for the stress is based on the calculated equivalent linear strain determined from the strain profile.

$$\sigma_{c\&w} = \frac{E.\varepsilon_{NET(total)}}{2}\left(\frac{C_1+\nu C_2}{1+\upsilon^2}\right) = \frac{E.(\varepsilon_{Temp\ Grad} + \varepsilon_{MoistGrad})}{2}\left(\frac{C_1+\nu C_2}{1+\upsilon^2}\right)$$

C = Bradbury Coefficient (at the slab center)
$= 1 - (2cos\lambda cosh\lambda/(sin2\lambda + sinh2\lambda))[(tan\lambda + tanh\lambda)cos\ y/\sqrt{2}\ell\ cosh\ y/\sqrt{2}\ell + (tan\lambda - tanh\lambda)sin\ y/\sqrt{2}\ell\ sinh\ y/\sqrt{2}\ell]$; at slab center at y = 0 and C=. $1 - (2cos\lambda cosh\lambda/(sin2\lambda + sinh2\lambda))[(tan\lambda + tanh\lambda)]$

λ $= \frac{b}{\sqrt{8}\ell}$; $\ell = \sqrt[4]{\frac{Eh^3}{12(1-\nu^2)k}}$; $E = 57{,}000\sqrt{f_c'}$; $f_c' = \left(\frac{MoR}{7.5}\right)^2$

C = Bradbury Coefficient (at the slab edge, C_1 and C_2)
$= 1 - \sqrt{2}sin\left(\frac{y}{\sqrt{2}\ell} + \frac{\pi}{4}\right)e^{-\frac{y}{\sqrt{2}\ell}} = 1 - C'$

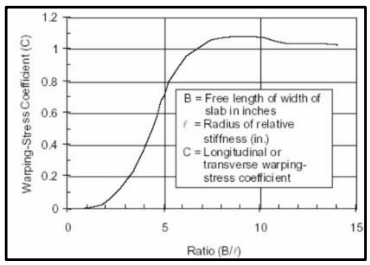

ℓ	λ	sin()	cos()	tan()	tan()	ℓ/(sqrt(2)*ℓ	cos	sin	C	C-center	L/ℓ
23.83	2.6703	103.510	-12.932	0.481	-1.500	0.712	0.957	0.506	0.963	1.060	7.55
27.16	2.3435	53.255	-7.339	-0.044	-2.008	0.625	0.975	0.390	0.886	0.994	6.63
28.88	2.2033	40.032	-5.418	-0.389	-2.340	0.588	0.980	0.345	0.839	0.947	6.23
30.01	2.1204	33.834	-4.416	-0.661	-2.604	0.565	0.983	0.319	0.807	0.914	6.00
30.83	2.0640	30.182	-3.789	-0.892	-2.829	0.550	0.985	0.303	0.782	0.888	5.84

Figure A-8. Bradbury Solution for Calculating the Theoretical Equivalent Stresses

6.7 Step #7 Summarized Measured LVDT Displacement of Slab's Corner

The induced stress can be determined based on slab corner deformations measured by the LVDT. The concrete slab deformed into a concave configuration when the slab was subjected to a resultant negative gradient of temperature and moisture through the slab thickness.

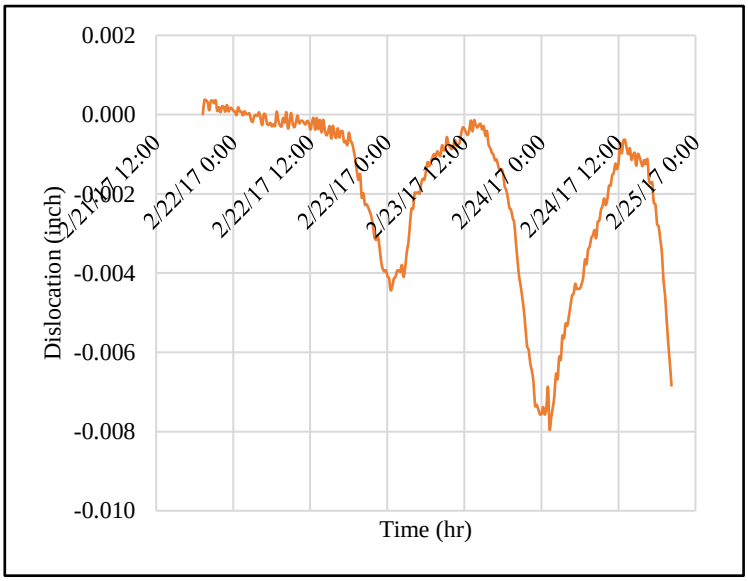

Real Time	Deflection (in)
2/21/2017 19:16	0.00001103
2/21/2017 19:31	0.00037125
2/21/2017 19:46	0.00036427
2/21/2017 20:01	0.00030839
2/21/2017 20:16	0.00011131
2/21/2017 20:31	0.00034531
2/21/2017 20:46	0.00035329
2/21/2017 21:01	0.00028843
2/21/2017 21:16	0.00036078
2/21/2017 21:31	0.00009285
2/21/2017 21:46	0.00018815
2/21/2017 22:01	0.00006042
2/21/2017 22:16	0.00020910
2/21/2017 22:31	0.00019364
2/21/2017 22:46	0.00007389
2/21/2017 23:01	0.00024103
2/21/2017 23:16	0.00008287
2/21/2017 23:31	0.00016819
2/21/2017 23:46	0.00015921
2/22/2017 0:01	0.00009784
2/22/2017 0:16	0.00007838

Figure A-9. Measured LVDT Displacement of Slab's Corner

6.8 Step #8 Induced Stresses due to Measured Surface Deformation

Similar to the permanent curling and warping, concrete slab deforms into a concave shape when subject to a periodic negative temperature gradient along the depth. If the net negative gradient is high enough, the slab edge or corner may break the interfacial bond and separate from the underlying base. The medium-thick plate theory provides the basis for the 2D solution based on boundary conditions representing slab lift-

off at the corner. This form was chosen based on its capability to represent the effect of the boundary conditions on the lift-off displacement. The equations to calculate the bending moment and displacement for different boundary conditions can be written in Table A-1:

Table A-1. The Boundary Conditions Equation Set for the Lift-off Displacement

No.	Boundary Conditions	Equations
1	M_x @ (0,0)	$M_x = D\left\{\frac{\partial^2 w}{\partial x^2} + v\frac{\partial^2 w}{\partial y^2} + \frac{\varepsilon(1+\mu)}{h}\right\} = 0$
2	M_x @ $(s,0)$	$M_x = D\left\{\frac{\partial^2 w}{\partial x^2} + v\frac{\partial^2 w}{\partial y^2} + \frac{\varepsilon(1+\nu)}{h}\right\} = -\frac{1}{6}S^2 h\rho$
3	w @ $(s,0)$	$(A_1 coss + A_2 sins)B_1 e^{-s} = 0$
4	V_x @ (0,0)	$V_x = D\left\{\frac{\partial^3 w}{\partial x^3} + \mu\frac{\partial^3 w}{\partial x \partial y^2}\right\} = 0$
5	V_x @ $(s,0)$	$V_x = D\left\{\frac{\partial^3 w}{\partial x^3} + \mu\frac{\partial^3 w}{\partial x \partial y^2}\right\} = -\frac{1}{2}Sh\rho$

Substituting the expression for deflection *w in Mx and Vx*. Then, *five unknowns (A1, A2, B1, B2,* and *S*) will be determined in a given total strain. After some additional algebra, one can further derive the stress in the slab based on the calculated total strain:

$$A_2 B_1 - \upsilon A_1 B_2 - \frac{\varepsilon_{total}(1+\nu)l^2}{2h} = 0$$

$$\varepsilon_{total} = \frac{(A_2 B_1 - \upsilon A_1 B_2) \times 2h}{(1+\nu)l^2}$$

$$* \; w(0,0) = A_1 \times B_1 \qquad **(A_1 + A_2)B_1 - (A_1 - A_2)B_2 = 0$$

$$\varepsilon_{total} = \frac{(\frac{A_2}{A_1} - \upsilon A_1 \frac{(A_1 + A_2)}{(A_1 - A_2)}) \times 2hw}{(1+\nu)l^2}$$

$$\varepsilon = \frac{2\sigma}{E}(\frac{1+\nu^2}{C1 + \nu C2})$$

$$\sigma = \frac{E\left(\frac{A_2}{A_1} - \upsilon A_1 \frac{(A_1+A_2)}{(A_1-A_2)}\right) \times 2hw}{(1+\nu)l^2} \times \frac{C1+\nu C2}{(1+\nu^2)}$$

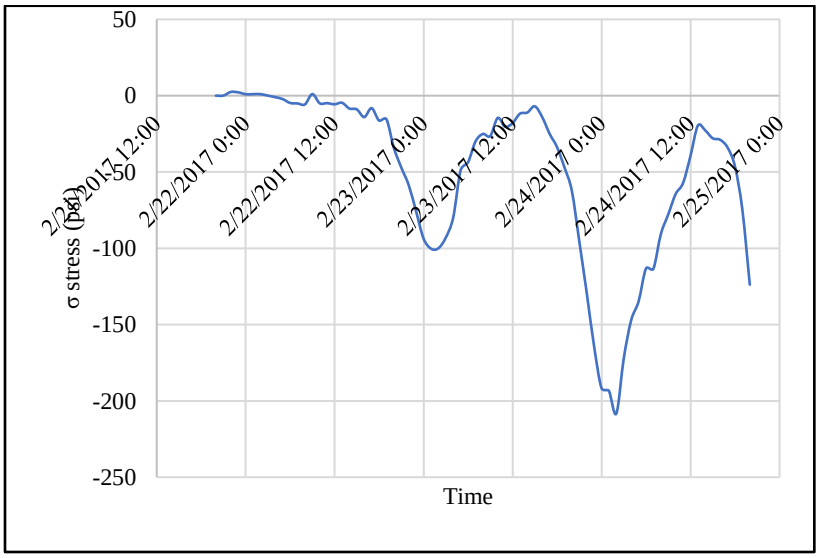

Figure A-10. Induced Stresses due to Measured Surface Deformation at Corners

6.9 Step #9 r_{set} Calculation

An effective way to present the equivalent linear gradient that is permanently built into the slabs is in terms of the stress ratio *r*.

$$r = \frac{\sigma}{MOR}$$

where σ (can be either $\sigma_{measured}$ or $\sigma_{Theoretical}$) is the equivalent stress level derived from the set strain determination and MOR is the modulus of rupture of the concrete.

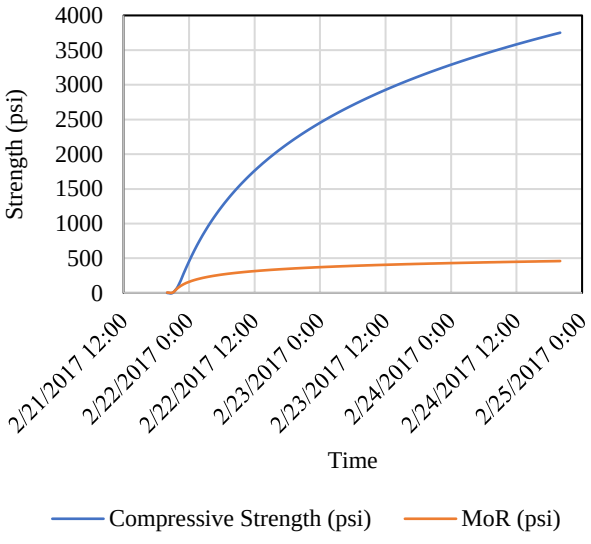

Real Time	Elasped time (hrs)	Age, day	Str Ratio	MR, psi	Epcc, psi	fc'	k1	Um
2/21/2017 19:59	0.0	0.00	0.01	6	44632	1	7032	14.06
2/21/2017 20:59	1.0	0.04	0.01	6	44632	1	7032	14.06
2/21/2017 21:59	2.0	0.08	0.13	74	567610	97	89431	178.86
2/21/2017 22:59	3.0	0.13	0.21	125	956911	276	150768	301.54
2/21/2017 23:59	4.0	0.17	0.27	159	1224731	452	192965	385.93
2/22/2017 0:59	5.0	0.21	0.32	186	1427671	614	224939	449.88
2/22/2017 1:59	6.0	0.25	0.36	207	1590373	762	250574	501.15
2/22/2017 2:59	7.0	0.29	0.39	225	1725753	897	271904	543.81
2/22/2017 3:59	8.0	0.33	0.41	240	1841407	1021	290126	580.25
2/22/2017 4:59	9.0	0.38	0.44	253	1942176	1136	306003	612.01
2/22/2017 5:59	10.0	0.42	0.46	264	2031327	1243	320049	640.10
2/22/2017 6:59	11.0	0.46	0.47	275	2111169	1342	332629	665.26
2/22/2017 7:59	12.0	0.50	0.49	284	2183391	1436	344008	688.02
2/22/2017 8:59	13.0	0.54	0.50	293	2249266	1524	354387	708.77
2/22/2017 9:59	14.0	0.58	0.52	301	2309776	1607	363921	727.84
2/22/2017 10:59	15.0	0.63	0.53	308	2365694	1686	372731	745.46
2/22/2017 11:59	16.0	0.67	0.54	315	2417639	1761	380916	761.83
2/22/2017 12:59	17.0	0.71	0.55	321	2466114	1832	388553	777.11
2/22/2017 13:59	18.0	0.75	0.56	327	2511535	1900	395710	791.42
2/22/2017 14:59	19.0	0.79	0.57	332	2554246	1965	402439	804.88
2/22/2017 15:59	20.0	0.83	0.58	338	2594538	2028	408787	817.57
2/22/2017 16:59	21.0	0.88	0.59	343	2632659	2088	414793	829.59
2/22/2017 17:59	22.0	0.92	0.60	347	2668819	2145	420491	840.98
2/22/2017 18:59	23.0	0.96	0.61	352	2703201	2201	425908	851.82
2/22/2017 19:59	24.0	1.00	0.61	356	2735964	2255	431070	862.14

Figure 0-11. Calculating Concrete Strength and MOR

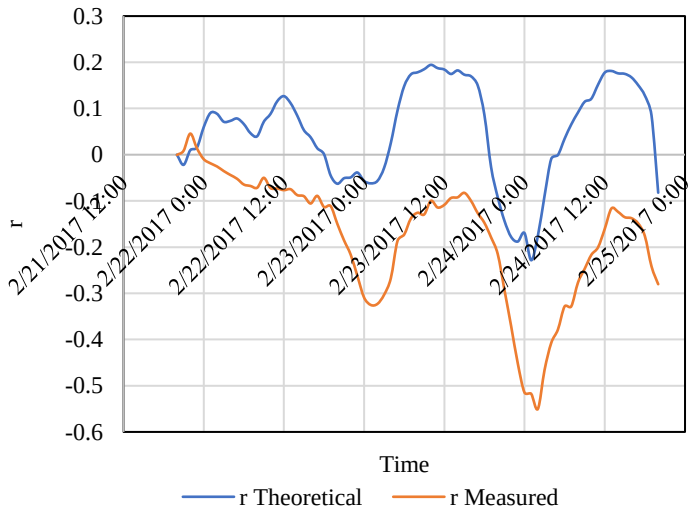

Real Time	Elapsed Time	r Theoretical	r Measured
2/21/2017 19:59	0	0.000	0.000
2/21/2017 20:59	1	-0.022	0.009
2/21/2017 21:59	2	0.010	0.046
2/21/2017 22:59	3	0.016	0.014
2/21/2017 23:59	4	0.059	-0.009
2/22/2017 0:59	5	0.090	-0.018
2/22/2017 1:59	6	0.089	-0.025
2/22/2017 2:59	7	0.071	-0.035
2/22/2017 3:59	8	0.073	-0.044
2/22/2017 4:59	9	0.078	-0.052
2/22/2017 5:59	10	0.067	-0.064
2/22/2017 6:59	11	0.047	-0.068
2/22/2017 7:59	12	0.040	-0.072
2/22/2017 8:59	13	0.071	-0.050
2/22/2017 9:59	14	0.088	-0.072
2/22/2017 10:59	15	0.116	-0.073
2/22/2017 11:59	16	0.127	-0.077
2/22/2017 12:59	17	0.112	-0.075
2/22/2017 13:59	18	0.085	-0.087
2/22/2017 14:59	19	0.053	-0.090
2/22/2017 15:59	20	0.038	-0.106
2/22/2017 16:59	21	0.014	-0.089
2/22/2017 17:59	22	0.001	-0.113
2/22/2017 18:59	23	-0.045	-0.111
2/22/2017 19:59	24	-0.063	-0.150

Figure A-12. Calculating *r* for Both $\sigma_{measured}$ and $\sigma_{theoretical}$

The set stress ratio, r_{set}, is defined based on the net difference in slab stresses. Then, the r_{set} is based on the net difference in stress.

$$r_{set} = (r_{measured} - r_{Theoretical})$$

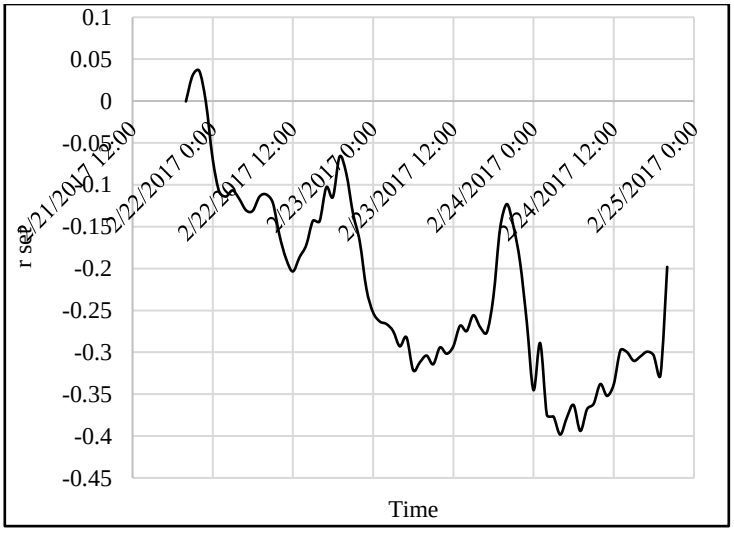

Real Time	Elapsed Time	r Theoretical	r Measured	r set
2/21/2017 19:59	0	0.000	0.000	0.000
2/21/2017 20:59	1	-0.022	0.009	0.030
2/21/2017 21:59	2	0.010	0.046	0.036
2/21/2017 22:59	3	0.016	0.014	-0.002
2/21/2017 23:59	4	0.059	-0.009	-0.069
2/22/2017 0:59	5	0.090	-0.018	-0.109
2/22/2017 1:59	6	0.089	-0.025	-0.114
2/22/2017 2:59	7	0.071	-0.035	-0.107
2/22/2017 3:59	8	0.073	-0.044	-0.117
2/22/2017 4:59	9	0.078	-0.052	-0.130
2/22/2017 5:59	10	0.067	-0.064	-0.131
2/22/2017 6:59	11	0.047	-0.068	-0.114
2/22/2017 7:59	12	0.040	-0.072	-0.111
2/22/2017 8:59	13	0.071	-0.050	-0.121
2/22/2017 9:59	14	0.088	-0.072	-0.160
2/22/2017 10:59	15	0.116	-0.073	-0.189
2/22/2017 11:59	16	0.127	-0.077	-0.203
2/22/2017 12:59	17	0.112	-0.075	-0.186
2/22/2017 13:59	18	0.085	-0.087	-0.172
2/22/2017 14:59	19	0.053	-0.090	-0.143
2/22/2017 15:59	20	0.038	-0.106	-0.144
2/22/2017 16:59	21	0.014	-0.089	-0.103
2/22/2017 17:59	22	0.001	-0.113	-0.114
2/22/2017 18:59	23	-0.045	-0.111	-0.066
2/22/2017 19:59	24	-0.063	-0.150	-0.087

Figure A-13. Calculating r_{set} Based on the Net Difference in Stress

6.10 Step #10 The Equivalent Set Gradient

The r_{set} is conventionally expressed in terms of an equivalent temperature gradient (from bottom to top of the slab) to facilitate correlation to pavement performance. The equivalent temperature gradient is written in:

$$Equivalent\ \Delta T = \frac{2 \times r_{set}(1-\nu) \times MoR}{C.E.\alpha}$$

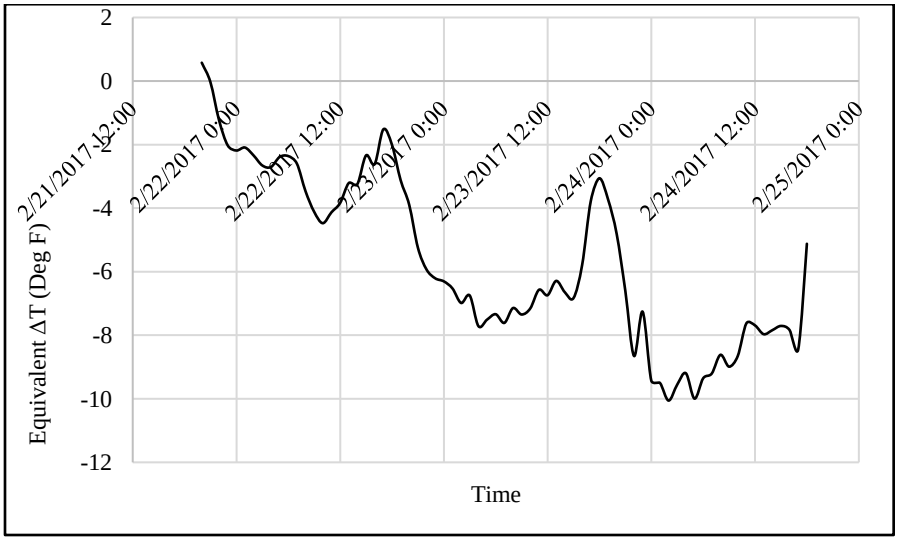

Figure A-14. Calculating the Equivalent Set Gradient in Terms of Temperature

REFERENCES

1. *aashto t 155*, in *STANDARD METHOD OF TEST FOR WATER RETENTION BY LIQUID MEMBRANE-FORMING CURING COMPOUNDS FOR CONCRETE*. 2013, American Association of State Highway and Transportation Officials.

2. Avelar Lezama, I., *Preliminary non-destructive assessment of moisture content, hydration and dielectric properties of Portland cement concrete*. 2007, Texas A&M University.

3. Rao, S. and J.R. Roesler, *Characterizing effective built-in curling from concrete pavement field measurements.* Journal of Transportation Engineering, 2005. **131**(4): p. 320-327.

4. Wells, S., B. Phillips, and J. Vandenbossche, *SR-22 smart pavement phase I: early-age material properties and pavement response characteristics for jointed plain concrete pavements, phase I final report.* Pennsylvania Department of Transportation and the Federal Highway Administration, 2005.

5. Wells, S.A., B.M. Phillips, and J.M. Vandenbossche, *Quantifying built-in construction gradients and early-age slab deformation caused by environmental loads in a jointed plain concrete pavement.* International Journal of Pavement Engineering, 2006. **7**(4): p. 275-289.

6. Armaghani, J.M., T.J. Larsen, and L.L. Smith, *Temperature response of concrete pavements*. 1987.

7. Yu, H. and L. Khazanovich. *Effects of construction curling on concrete pavement behavior*. in *Seventh International Conference on Concrete Pavements. The Use of Concrete in Developing Long-Lasting Pavement Solutions for the 21st CenturyInternational Society for Concrete Pavements*. 2001.

8. Vandenbossch, J., *Premature deterioration of jointed plain concrete pavements.* 2011.

9. Beckemeyer, C., L. Khazanovich, and H. Thomas Yu, *Determining amount of built-in curling in jointed plain concrete pavement: Case study of Pennsylvania 1-80.* Transportation Research Record, 2002. **1809**(1): p. 85-92.

10. Nassiri, S., *Establishing permanent curl/warp temperature gradient in jointed plain concrete pavements*. 2011, University of Pittsburgh.

11. Nassiri, S. and J. Vandenbossche, *Establishing Appropriate Inputs When Using the 26.* MEPDG To Design Rigid Pavements in Pennsylvania-Task 4-Construction Report, 2009. **27**.

12. Coree, B., H. Ceylan, and D. Harrington, *Implementing the mechanistic-empirical pavement design guide: implementation plan.* 2005.

13. Olidis, C. and D. Hein. *Guide for the mechanistic-empirical design of new and rehabilitated pavement structures materials characterization: Is your agency ready*. in *2004 Annual Conference of the Transportation Association of Canada*. 2004. Citeseer.

14. Gutierrez, J.J., *Evaluating the JPCP cracking model of the mechanistic-empirical pavement design guide*. 2008, University of Pittsburgh.

15. Vandenbossche, J., et al., *An evaluation of the built-in temperature difference input parameter in the jointed plain concrete pavement cracking model of the Mechanistic–Empirical Pavement Design Guide.* International Journal of Pavement Engineering, 2011. **12**(03): p. 215-228.

16. Taylor, H.F., *Cement chemistry*. Vol. 2. 1997: Thomas Telford London.

17. Mindess, S., J.F. Young, and D. Darwin, *Concrete*. 2003: Prentice Hall.

18. *ACI Committee 308, Guide to External Curing of Concrete.* 2016.

19. Powers, T.C. *A discussion of cement hydration in relation to the curing of concrete*. in *Highway Research Board Proceedings*. 1948.

20. Powers, T.C., *Structure and physical properties of hardened Portland cement paste.* Journal of the American Ceramic Society, 1958. **41**(1): p. 1-6.

21. Parrot, L. *Prediction of cement hydration*. in *Proceedings of the British Ceramic Society*. 1984.

22. Mindess, S., J.F. Young, and D. Darwin, *Concrete, 2003.* Prentice Hall, Upper Saddle River, NJ, 2003.

23. *Standard Test Method for Water Loss [from a Mortar Specimen] Through Liquid Membrane-Forming Curing Compounds for Concrete*. 2011, ASTM International.

24. Surana, S., R.G. Pillai, and M. Santhanam, *Performance evaluation of curing compounds using durability parameters.* Construction and Building Materials, 2017. **148**: p. 538-547.

25. Jabonero, C., et al., *The analyses of environmental factors for curing concrete pavements inside tunnels.* KSCE Journal of Civil Engineering, 2016. **3**(21): p. 766-773.

26. Uno, P.J., *Plastic shrinkage cracking and evaporation formulas.* ACI Materials Journal, 1998. **95**: p. 365-375.

27. Perenchio, W.F., *The drying shrinkage dilemma.* Concrete Construction, 1997. **42**(4): p. 379-383.

28. Hedenblad, G., *Drying of construction water in concrete.* BFR T-skrift, 1997. **9**(1997).

29. Jackson, F. and W. Kellermann. *Tests of concrete curing materials*. in *Journal Proceedings*. 1939.

30. Hajibabaee, A., *Impact of Different Curing Methods and Drying Conditions on Drying Shrinkage Induced Curling*. 2016.

31. Hajibabaee, A. and M.T. Ley, *Impact of Wet and Sealed Curing on Curling in Cement Paste Beams from Drying Shrinkage.* ACI Materials Journal, 2015. **112**(1).

32. Hajibabaee, A. and M.T. Ley, *The impact of wet curing on curling in concrete caused by drying shrinkage.* Materials and Structures, 2016. **49**(5): p. 1629-1639.

33. Suprenant, B.A., *Why slabs curl.* Concrete international, 2002. **3**: p. 56-64.

34. Wang, L. and D. Zollinger, *Mechanistic design framework for spalling distress.* Transportation Research Record: Journal of the Transportation Research Board, 2000(1730): p. 18-24.

35. Liu, J., *Early age delamination in concrete pavements made with gravel aggregates*. Vol. 68. 2006.

36. Prouty, J., *Sustainable and Durable Infrastructure with Advanced Construction Materials*. 2014.

37. Poole, T.S., *Guide for curing of Portland cement concrete pavements*. Vol. 2. 2006: Turner-Fairbank Highway Research Center, Research, Development, and Technology.

38. Sun, P., *A new protocol for evaluating concrete curing effectiveness*, in *Civil Engineering*. 2013, Texas A & M University: College Station, Texas.

39. Senbetta, E., *Concrete curing practices in the United States.* Concrete international, 1988. **10**(11): p. 64-67.

40. Dhir, R., P. Hewlett, and Y. Chan, *Near-surface characteristics of concrete: abrasion resistance.* Materials and Structures, 1991. **24**(2): p. 122.

41. Gowripalan, N., *Effect of curing on durability.* Concrete International, 1990. **12**(2): p. 47-54.

42. Kosmatka, S. and W.C. Panarese, *Design and control of concrete mixtures.* 1988.

43. Montgomery, F., P. Basheer, and A. Long, *Influence of curing conditions on the durability related properties of near surface concrete and cement mortars.* Special Publication, 1992. **131**: p. 127-138.

44. Ytterberg, R.F., *Shrinkage and Curling of Slabs on Grade--Part 1.* Concrete international, 1987. **9**(4): p. 22-30.

45. Grasley, Z.C., D.A. Lange, and D. Matthew, *Internal relative humidity and drying stress gradients in concrete.* Materials and Structures, 2006. **39**(9): p. 901.

46. Coussy, O., et al., *The equivalent pore pressure and the swelling and shrinkage of cement-based materials.* Materials and structures, 2004. **37**(1): p. 15-20.

47. Wittmann, F.H., *Creep and shrinkage mechanisms.* Creep and shrinkage in concrete structures, 1982: p. 129-161.

48. Murley, J.F., *Florida standard for radon-resistant new commercial building construction.* Florida Dept. of Community Affairs, Tallahassee, Fla, 1996.

49. Curing, E.C.W.M.-F., *Compound: ASTM C 309.* Type I, Class B. **1**.

50. ASTM, C., *Standard specification for liquid membrane-forming compounds for curing concrete.* Annual Book of ASTM StandardsAnnual Book of ASTM Standards, 2007. **4**(2): p. 1-3.

51. Clear, G., M.-F.C. Waterborne, and S. Compound, *ASTM C 1315, Type 1, Class A.* Compatible with penetrating liquid floor treatment for surfaces specified to receive penetrating liquid floor treatment.

52. Wang, K., J.K. Cable, and G. Zhi, *Investigation into improved pavement curing materials and techniques: part 1 (phases I and II)*. 2002, Iowa State University. Center for Transportation Research and Education.

53. C156, A., *Standard Test Method for Water Loss [from a Mortar Specimen] through Liquid Membrane-Forming Curing Compounds for Concrete*. 2011, ASTM International West Conshohocken, PA.

54. Choi, S., J.H. Yeon, and M.C. Won, *Improvements of curing operations for Portland cement concrete pavement.* Construction and Building Materials, 2012. **35**: p. 597-604.

55. Vandenbossche, J.M., *A review of the curing compounds and application techniques used by the Minnesota Department of Transportation for concrete pavements*. 1999.

56. Wang, K., J.K. Cable, and Z. Ge, *Evaluation of pavement curing effectiveness and curing effects on concrete properties.* Journal of Materials in Civil Engineering, 2006. **18**(3): p. 377-389.

57. *Standard Specifications Construction of Transportation Systems, in Georgia Department of Transportation* 2001, Georgia Department of Transportation.

58. *Standard Specifications for Construction of Local Streets and Roads, in California Department of Transportation* 2010, California Department of Transportation.

59. *Standard Specifications for Road and Bridge Construction, in Colorado Department of Transportation* 2011, Colorado Department of Transportation.

60. Ye, D., A. Mukhopadhyay, and D.G. Zollinger, *Laboratory and field evaluation of concrete paving curing effectiveness*. 2009, Texas Transportation Institute.

61. Choi, S. and M.C. Won, *Identification of compliance testing method for curing effectiveness*. 2008.

62. Hajibabaee, A., Z. Grasley, and M. Ley, *Mechanisms of dimensional instability caused by differential drying in wet cured cement paste.* Cement and Concrete Research, 2016. **79**: p. 151-158.

63. Gordon, M., K. Broughton, and M. Hardy, *The assessment of the value of GPR imaging of flexible pavements.* NDT & E International, 1998. **31**(6): p. 429-438.

64. Rhim, H.C. and O. Buyukozturk, *Electromagnetic properties of concrete at microwave frequency range.* Materials Journal, 1998. **95**(3): p. 262-271.

65. Diefenderfer, B.K., *Moisture content determination and temperature profile modeling of flexible pavement structures*. 2002.

66. Lytton, R., *Characterizing asphalt pavements for performance.* Transportation Research Record: Journal of the Transportation Research Board, 2000(1723): p. 5-16.

67. Lin, C.-P., *Time domain reflectometry for soil properties.* 1999.

68. Davis, J.L. and A. Annan, *Ground‐penetrating radar for high‐resolution mapping of soil and rock stratigraphy.* Geophysical prospecting, 1989. **37**(5): p. 531-551.

69. Lim, S., et al., *Characterization of crushed concrete materials for paving and non-paving applications*. 2003, Texas Transportation Institute, The Texas A&M University System College Station, TX.

70. Evans, R.D., et al., *A review of pavement assessment using ground penetrating radar (GPR).* 2008.

71. Nicholls, R.L., *Composite construction materials handbook*. 1976: Prentice Hall.

72. Lee, S.I., *Development of approach to estimate volume fraction of multiphase material using dielectrics*. 2010: Texas A&M University.

73. Ye, D., *Early-age concrete temperature and moisture relative to curing effectiveness and projected effects on selected aspects of slab behavior*. 2007: Texas A&M University.

74. Janoo, V., C. Korhonen, and M. Hovan, *Measurement of water content in Portland cement concrete.* Journal of transportation engineering, 1999. **125**(3): p. 245-249.

75. Lee, S.I., D.G. Zollinger, and R.L. Lytton. *Estimating Volume Fraction of Free Moisture in Fresh Concrete Based on Interpretation of Dielectric Constant Data as a Measure of Curing Quality*. in *Transportation Research Board 89th Annual Meeting*. 2010.

76. Lee, S.I. and D.G. Zollinger, *Estimating volume fraction of free water in hardening concrete by interpretation of dielectric constant.* Journal of Materials in Civil Engineering, 2011. **24**(2): p. 159-167.

77. Lee, S., D. Zollinger, and R. Lytton, *Determining moisture content of soil layers with time domain reflectometry and micromechanics.* Transportation Research Record: Journal of the Transportation Research Board, 2008(2053): p. 30-38.

78. Taylor, H.F., *Cement chemistry*. 1997: Thomas Telford.

79. Shen, P., et al., *Hydration monitoring and strength prediction of cement-based materials based on the dielectric properties.* Construction and Building Materials, 2016. **126**: p. 179-189.

80. Sun, P., *A new protocol for evaluating concrete curing effectiveness*. 2013.

81. Chen, W., P. Shen, and Z. Shui, *Determination of water content in fresh concrete mix based on relative dielectric constant measurement.* Construction and Building Materials, 2012. **34**: p. 306-312.

82. McCarter, W. and P. Curran, *The electrical response characteristics of setting cement paste.* Magazine of Concrete Research, 1984. **36**(126): p. 42-49.

83. Joshaghani, A. and D.G. Zollinger, *Concrete pavements curing evaluation with non-destructive tests.* Construction and Building Materials, 2017. **154**: p. 1250-1262.

84. Bertrand, C., et al., *New Method for Pavement Dielectric Constant Measurement Using Ground-Penetrating Radar*. 2006.

85. Saarenketo, T. and T. Scullion, *Road evaluation with ground penetrating radar.* Journal of applied geophysics, 2000. **43**(2-4): p. 119-138.

86. Evans, R., et al., *Assessment of in situ dielectric constant of pavement materials.* Transportation Research Record, 2007. **2037**(1): p. 128-135.

87. Pérez-Gracia, V., F.G. García, and I.R. Abad, *GPR evaluation of the damage found in the reinforced concrete base of a block of flats: A case study.* NDT & e International, 2008. **41**(5): p. 341-353.

88. Weed, R.M., *Development of multicharacteristic acceptance procedures for rigid pavement.* Transportation Research Record, 1982(885).

89. Fick, G.J., et al., *Field reference manual for quality concrete pavements*. 2012, United States. Federal Highway Administration.

90. Burati, J., et al., *Optimal procedures for quality assurance specifications*. 2003, Turner-Fairbank Highway Research Center.

91. Gee, K., *Use of contractor test results in the acceptance decision, recommended quality measures, and the identification of contractor/department risks.* Technical Advisory T, 2004. **6120**.

92. Burati, J., et al., *Evaluation of procedures for quality assurance specifications*. 2004, Turner-Fairbank Highway Research Center.

93. Gharaibeh, N.G., S.I. Garber, and L. Liu, *Determining optimum sample size for percent-within-limits specifications.* Transportation research record, 2010. **2151**(1): p. 77-83.

94. Cross, S.A. and J.A. Frantzen, *Evaluating percent within limits (PWL) specifications volume 1: HMA specifications*. 2006, Oklahoma State University.

95. Muench, S.T., J.P. Mahoney, and J. Walter, *A Quantification and Evaluation of WSDOT's Hot Mix Asphalt Concrete Statistical Acceptance Specification*. 2001, Citeseer.

96. Trost, S.M., *Evaluation of Percent Within Limits Specifications*. 2003.

97. *Guide for Mechanistic-Empirical Design OF NEW AND REHABILITATED PAVEMENT STRUCTURES, TRANSVERSE CRACKING OF JPCP, National Cooperative Highway Research Program, Transportation Research Board, National Research Council* 2003.

98. Yeon, J.H., *Zero-stress temperature and its implications for long-term performance of continuously reinforced concrete pavements*. 2011.

99. Ren, D., *Optimisation of the crack pattern in continuously reinforced concrete pavements.* 2015.

100. Ioannides, A.M. and L. Khazanovich, *Nonlinear temperature effects on multilayered concrete pavements.* Journal of Transportation Engineering, 1998. **124**(2): p. 128-136.

101. Choubane, B. and M. Tia, *Nonlinear temperature gradient effect on maximum warping stresses in rigid pavements.* Transportation Research Record, 1992. **1370**(1): p. 11.

102. Mohamed, A. and W. Hansen, *Effect of nonlinear temperature gradient on curling stress in concrete pavements.* Transportation Research Record: Journal of the Transportation Research Board, 1997(1568): p. 65-71.

103. Byrum, C.R., *Analysis by high-speed profile of jointed concrete pavement slab curvatures.* Transportation research record, 2000. **1730**(1): p. 1-9.

104. Rao, S. and J. Roesler, *Analysis and estimation of effective built-in temperature difference for North Tangent slabs.* Data Analysis from Palmdale, California Rigid Pavement Test Site. Draft Report for California Department of Transportation, 2004.

105. Hall, K.D. and S. Beam, *Estimating the sensitivity of design input variables for rigid pavement analysis with a mechanistic–empirical design guide.* Transportation Research Record, 2005. **1919**(1): p. 65-73.

106. Kannekanti, V.N. and J.T. Harvey, *Sensitivity analysis of 2002 design guide rigid pavement distress prediction models.* 2005.

107. Khazanovich, L., et al., *Adaptation of Mechanistic-empirical pavement design guide for design of Minnesota low-volume portland cement concrete pavements.* Transportation research record, 2008. **2087**(1): p. 57-67.

108. Mehta, P.K., *Concrete. Structure, properties and materials.* 1986.

109. Soroka, I., *Portland cement paste and concrete*. 1979: Macmillan International Higher Education.

110. Martinez, E.E., *Curling deformations in cement paste slabs and effects of shrinkage reducing admixtures*. 1998, Massachusetts Institute of Technology.

111. Eisenmann, J. and G. Leykauf. *Simplified calculation method of slab curling caused by surface shrinkage*. in *Proceedings, 2nd International Workshop on Theoretical Design of Concrete Pavements*. 1990.

112. Muller, H. and H. Hilsdorf, *Evaluation of the time-dependent behavior of concrete, summary report on the work of general task group 9.* CEB Bulletin d'Information, 1990. **199**: p. 290.

113. Pfeiffer, P.A. and T.-a. Tanabe. *Time-Dependent Behavior*. in *Finite Element Analysis of Reinforced Concrete Structures II*. 1993. ASCE.

114. Rao, C., et al. *Effects of temperature and moisture on the response of jointed concrete pavements*. in *Seventh International Conference on Concrete Pavements. The Use of Concrete in Developing Long-Lasting Pavement Solutions for the 21st CenturyInternational Society for Concrete Pavements*. 2001.

115. Hauggaard, A.B., L. Damkilde, and P.F. Hansen, *Transitional thermal creep of early age concrete.* Journal of engineering mechanics, 1999. **125**(4): p. 458-465.

116. Bazant, Z.P. and P.C. Prat, *Effect of temperature and humidity on fracture energy of concrete.* ACI Materials Journal, 1988. **85**(4): p. 262-271.

117. Carino, N.J., *The Maturity Method,* in *CRC Handbook on Non-destructive Testing of Concrete*, V.M. Malhotra and N.J. Carino, Editors. 1991, CRC Press. p. 101-146.

118. Schindler, A.K. and K.J. Folliard, *Heat of hydration models for cementitious materials.* ACI Materials Journal, 2005. **102**(1): p. 24.

119. Schindler, A.K. and K.J. Folliard. *Influence of supplementary cementing materials on the heat of hydration of concrete*. in *Advances in Cement and*

Concrete IX Conference, Copper Mountain Conference Resort in Colorado. 2003.

120. Hansen, P.F. and E.J. Pedersen, *Maturity computer for controlled curing and hardening of concrete*. 1977.

121. Bažant, Z., *Constitutive equation for concrete creep and shrinkage based on thermodynamics of multiphase systems.* Matériaux et constructions, 1970. **3**(1): p. 3-36.

122. Jeong, *Characterization of Slab Behavior and Related Material Properties due to Temperature and Moisture* in *Civil Engineering*. 2003, Texas A&M University: College Station, Tx.

123. Subcommittee, I. *ACI Committee 209*. in *DE Branson, Chairman," Prediction of Creep, Shrinkage and Temperature Effects in Concrete Structures," Special ACI Publication on Creep, Shrinkage and Temperature Effects in Concrete Structures, Symposium Volume*. 2007.

124. Hansen, W., et al., *Effects of paving conditions on built-in curling and pavement performance.* International Journal of Pavement Engineering, 2006. **7**(4): p. 291-296.

125. Nam, J.-H., *Early-age behavior of CRCP and its implications for long-term performance*. 2005.

126. Schindler, A.K., T. Dossey, and B.F. McCullough, *Temperature control during construction to improve the long term performance of Portland cement concrete pavements*. 2002.

127. Suh, Y.-C., K.D. Hankins, and B.F. McCullough, *Early-age behavior of continuously reinforced concrete pavement and calibration of the failure prediction model in the CRCP-7 program*. 1992, Center for Transportation Research, Bureau of Engineering Research ….

128. Li, Q., et al., *Mechanistic-empirical Pavement Design Guide (MEPDG): a bird's-eye view.* Journal of Modern Transportation, 2011. **19**(2): p. 114-133.

129. Nam, J.-H., S.-M. Kim, and M.C. Won, *Measurement and analysis of early-age concrete strains and stresses: continuously reinforced concrete pavement under environmental loading.* Transportation research record, 2006. **1947**(1): p. 79-90.

130. Byfors, J., *Plain concrete at early ages.* 1980.

131. Meyers, S. *Thermal expansion characteristics of hardened cement paste and of concrete*. in *Highway Research Board Proceedings*. 1951.

132. Hu, C.B., M.L. Du, and L.J. Wang. *Research of Built-In Temperature and Zero Stress Temperature of Cement Concrete Pavement at Early Ages*. in *Advanced Materials Research*. 2014. Trans Tech Publ.

133. Ali, W. and G. Urgessa, *Numerical prediction model for temperature distributions in concrete at early ages.* American Journal of Engineering and Applied Sciences, 2012. **5**(4): p. 282-290.

134. Pinto, R.C. and K.C. Hover, *Application of maturity approach to setting times.* Materials Journal, 1999. **96**(6): p. 686-691.

135. Pinto, R. and A. Schindler, *Unified modeling of setting and strength development.* Cement and Concrete Research, 2010. **40**(1): p. 58-65.

136. *ASTM C403 / C403M-16, Standard Test Method for Time of Setting of Concrete Mixtures by Penetration Resistance, ASTM International, West Conshohocken, PA.* 2016.

137. Schindler, A.K., *Effect of temperature on hydration of cementitious materials.* Materials Journal, 2004. **101**(1): p. 72-81.

138. Ruiz, J.M., et al., *Computer-Based Guidelines For Concrete Pavements Volume II: Design and Construction Guidelines and HIPERPAV II User's Manual*. 2005, United States. Federal Highway Administration. Office of Infrastructure ….

139. Jeong, J.-H. and D. Zollinger, *Early-age curling and warping behavior: insights from a fully instrumented test-slab system.* Transportation Research Record: Journal of the Transportation Research Board, 2004(1896): p. 66-74.

140. Jeong, J.-H. and D.G. Zollinger, *Environmental effects on the behavior of jointed plain concrete pavements*. Journal of Transportation Engineering, 2005. **131**(2): p. 140-148.

141. Wade, S.A., et al., *Effect of temperature on the setting behavior of concrete*. Journal of Materials in Civil Engineering, 2010. **22**(3): p. 214-222.

142. Huang, K., et al., *A developed method of analyzing temperature and moisture profiles in rigid pavement slabs.* Construction and Building Materials, 2017. **151**: p. 782-788.

143. Sun, P. and D.G. Zollinger, *Concepts to Enhance Specification and Inspection of Curing Effectiveness in Concrete Pavement Design and Construction.*

Transportation Research Record: Journal of the Transportation Research Board, 2015(2504): p. 124-132.

144. Springenschmid, R. and E. Hiller. *Influence of temperature during curing on stresses in concrete pavements*. in *8th International Symposium on Concrete Roads*. 1998.

145. McCracken, J.K., *Seasonal analysis of the response of jointed plain concrete pavements to FWD and truck loads*. 2008, University of Pittsburgh.

146. Taghavi Ghalesari, A., et al., *Evaluation of the response from the rigid pavement analysis system (RPAS) program for the characterisation of jointed concrete pavements.* Road Materials and Pavement Design, 2020: p. 1-20.

147. Zollinger, D.G. and E. Fernando, *An Approach to Enhance the Local of Calibration of Concrete Pavement Performance*. 2015.

148. Mukhopadhyay, A.K., D. Ye, and D.C. Zollinger, *Moisture-related cracking effects on hydrating concrete pavement*. 2006, Texas Transportation Institute, Texas A & M University System.

149. Klug, P. and F. Wittmann, *Activation energy and activation volume of creep of hardened cement paste.* Materials science and Engineering, 1974. **15**(1): p. 63-66.

150. Testing, A.S.f. and Materials. *ASTM C778: Standard Specification for Standard Sand*. 2006. ASTM Philadelphia.

151. Standard, A., *C305. Standard Practice for Mechanical Mixing of Hydraulic Cement Pastes and Mortars of Plastic Consistency.* Annual book of ASTM standards, 2006.

152. ASTM C109, A., *Standard test method for compressive strength of hydraulic cement mortars (Using 2-in. or [50-mm] cube specimens).* American Society for Testing and Material, 2002.

153. Setzer, M.J., *A model of hardened cement paste for linking shrinkage and creep phenomena*, in *Fundamental Research on Creep and Shrinkage of Concrete*. 1982, Springer. p. 3-13.

154. Joshaghani, A., et al., *Investigating the effects of curing quality on key concrete pavement surface properties.* Transportation Research Record, 2019. **2673**(11): p. 71-80.

155. Griesel, E. and M. Alexander, *Effect of controlled environmental conditions on durability index parameters of portland cement concretes.* Cement, concrete and aggregates, 2001. **23**(1): p. 44-49.

156. Testing, A.S.f. and M.C.C.-o. Cement, *Standard test method for drying shrinkage of mortar containing hydraulic cement*. 2010: ASTM International.

157. Sebesta, S., et al., *Develop nondestructive rapid pavement quality assurance/quality control evaluation test methods and supporting technology: project summary.* 2017.

158. Joshaghani, A., M. Balapour, and A.A. Ramezanianpour, *Effect of controlled environmental conditions on mechanical, microstructural and durability properties of cement mortar.* Construction and Building Materials, 2018. **164**: p. 134-149.

159. St John, D.A., A.B. Poole, and I. Sims, *Concrete petrography: a handbook of investigative techniques*. 1998: Arnold; Copublished in North, Central and South America by J. Wiley.

160. Inc, M., *Minitab 16 statistical software. Version 16.2. 4*. 2013, Minitab Inc State College, Pennsylvania, USA.

161. Rasband, W.S., *ImageJ*. 1997, Bethesda, MD.

162. Spss, I., *IBM SPSS statistics for Windows, version 20.0.* New York: IBM Corp, 2011. **440**.

163. Bažant, Z. and L. Najjar, *Nonlinear water diffusion in nonsaturated concrete.* Materials and Structures, 1972. **5**(1): p. 3-20.

164. Parrott, L., *Factors influencing relative humidity in concrete.* Magazine of Concrete Research, 1991. **43**(154): p. 45-52.

165. Parrott, L., *Moisture profiles in drying concrete.* Advances in cement research, 1988. **1**(3): p. 164-170.

166. Joshaghani, A. and D.G. Zollinger, *Assessment of Concrete Pavement Set Gradient Based on Analysis of Slab Behavior and Field Test Data.* Transportation Research Record, 2019: p. 0361198119849900.

167. Zollinger, A.J.a.D., *Effect of climatic Factors on the set gradient of newly constructed concrete pavements*, in *Transportation Research Board (TRB)'s 97th Annual Meeting*. 2018: Washington, D.C.

168. C157M-17, A.C., *Standard Test Method for Length Change of Hardened Hydraulic-Cement Mortar and Concrete*, . 2017, ASTM International: West Conshohocken, PA, .

169. Westergaard, H., *Stresses in concrete pavements computed by theoretical analysis.* Public roads, 1926.

170. Huang, Y.H., *Pavement analysis and design.* 1993.

171. Rufino, D. and J. Roesler, *Effect of slab-base interaction on measured concrete pavement responses.* Journal of transportation engineering, 2006. **132**(5): p. 425-434.

172. Guo, E.H. and F. Pecht, *Critical Gear Configurations and Positions for Rigid Airport Pavements–Observations and Analyses*, in *Pavement Mechanics and Performance*. 2006. p. 7-14.

173. Vepakomma, S., J.-H. Jeong, and D.G. Zollinger, *Characterization of cracking restraint at saw-cut joints using the German cracking frame.* Transportation research record, 2002. **1813**(1): p. 28-35.

174. Gao, X., Y. Wei, and W. Huang, *Strain-based equivalent temperature gradient in concrete pavement and comparison with other quantification methods.* Road Materials and Pavement Design, 2017. **18**(6): p. 1460-1472.

175. Lahouar, S., *Development of data analysis algorithms for interpretation of ground penetrating radar data*. 2003, Virginia Tech.

176. Joshaghani, A., *Identifying the problematic areas with structural deficiencies of pavements using non-destructive tests (NDT).* International Journal of Pavement Engineering, 2019. **20**(11): p. 1359-1369.

177. Al-Qadi, I.L., S. Lahouar, and A. Loulizi, *In situ measurements of hot-mix asphalt dielectric properties.* NDT & e International, 2001. **34**(6): p. 427-434.

178. Ward, B., et al., *Evaluating the Effects of Concrete Curing Compounds on Hydration.* COMPENDIUM OF STUDENT PAPERS: 2010 UNDERGRADUATE TRANSPORTATION SCHOLARS PROGRAM, 2011: p. 225.

179. Ye, D., A.K. Mukhopadhyay, and D.G. Zollinger, *Laboratory and field evaluation of concrete paving curing effectiveness*. 2009, Texas Transportation Institute, Texas A & M University System.

180. Leahy, R., *Transportation research circular E-C137: Glossary of highway quality assurance terms.* Transportation Research Board of the National Academies, Washington, DC, 2009.

181. Willenbrock, J.H., *A manual for statistical quality control of highway construction*. Vol. 1. 1976: Department of Transportation, Federal Highway Administration.

182. Freeman, R.B. and W.P. Grogan, *Statistical Acceptance Plan for Asphalt Pavement Construction*. 1998, ARMY ENGINEER WATERWAYS EXPERIMENT STATION VICKSBURG MS GEOTECHNICAL LAB.

183. Circular, A., *Federal Aviation Administration.* US Department of Transportation, AC, 1991(150/5320).

184. Sholar, G.A., et al., *Development of the Florida Department of Transportation's percent within limits hot-mix asphalt specification.* Transportation research record, 2005. **1907**(1): p. 43-51.

185. AASHTO, R., *9-05 "Standard Recommended Practice for Acceptance Sampling Plans for Highway Construction".* American Association of State Highway and Transportation Officials.

186. Lewis, P.A., *Distribution of the Anderson-Darling statistic.* The Annals of Mathematical Statistics, 1961: p. 1118-1124.

187. D'Agostino, R.B., *Goodness-of-fit-techniques*. Vol. 68. 1986: CRC press.

188. Burati, J. and J.H. Willenbrock, *Acceptance Criteria for Bituminous Surface Course on Civil Airport Pavements*. 1979, PENNSYLVANIA TRANSPORTATION INST UNIVERSITY PARK.

189. Burati, J., et al., *FIELD VALIDATION OF STATISTICALLY BASED ACCEPTANCE PLAN FOR BITUMINOUS AIRPORT PAVEMENTS*. 1984.

190. Westergaard, H. *Analysis of stresses in concrete pavements due to variations of temperature*. in *Highway Research Board Proceedings*. 1927.

191. Riad, M., et al., *Curling of concrete slabs on grade: experimental versus theoretical analysis.* Structure and Infrastructure Engineering, 2008. **4**(1): p. 57-72.

192. *Mechanistic-Empirical Pavement Design Guide and AASHTOWare Pavement ME Design Software.* 2017.

193. Poblete, M., *Informe Anual 1986.* Control y Seguimiento de Pavimentos de Hormigon, IDIEM-Direccion de Vialidad, Universidad de Chile, 1986.

194. Yu, H., et al., *Performance of concrete pavements. Volume III: Improving concrete pavement performance*. 1998.

195. Vaysburd, A., et al. *Some aspects of evaluating cracking sensitivity of repair materials*. in *International RILEM Conference on Early Age Cracking in Cementitious Systems*. 2003. RILEM Publications SARL.

196. *Standard Practice for Estimating Concrete Strength by the Maturity Method*.

197. Jeong, J.-H. and D.G. Zollinger, *Finite-element modeling and calibration of temperature prediction of hydrating Portland cement concrete pavements.* Journal of materials in civil engineering, 2006. **18**(3): p. 317-324.

198. Tabatabaeian, M., et al., *Experimental investigation on effects of hybrid fibers on rheological, mechanical, and durability properties of high-strength SCC.* Construction and Building Materials, 2017. **147**: p. 497-509.

199. Easton, V.J. and J.H. McColl, *Statistics Glossary v1. 1*. 1997.

200. Rebba, R. and S. Mahadevan, *Computational methods for model reliability assessment.* Reliability Engineering & System Safety, 2008. **93**(8): p. 1197-1207.